

SQUID-Magnetometry on Fe Monolayers on GaAs(001) in UHV

Vom Fachbereich Physik
der Universität Duisburg-Essen
(Standort Duisburg)

zur Erlangung des akademischen Grades eines
Doktors der Naturwissenschaften
genehmigte Dissertation von

Thomas Kebe

aus Duisburg

Referent : Prof. Dr. rer. nat. Michael Farle

Korreferent : Prof. Dr. rer. nat. Wolfgang Kleemann

Tag der mündlichen Prüfung: 11.12.2006

Jessica, Phil, meinen Eltern

Kurzfassung

Die vorliegende Arbeit beschäftigt sich mit der Charakterisierung des Wachstums und der magnetischen Eigenschaften von ultradünnen Fe Filmen auf GaAs(001). Insbesondere kam hierbei ein im Rahmen dieser Arbeit weiterentwickeltes Raster-SQUID (superconducting interference device) Magnetometer im Ultrahochvakuum (UHV) zum Einsatz. Aus dem mit diesem Gerät gemessenen magnetischen Streufeld eines magnetisierten Films kann die remanente Magnetisierung absolut und mit Submonolagen-Nachweisempfindlichkeit bestimmt werden. Hierzu wurde im Rahmen dieser Arbeit das magnetische Streufeld analytisch berechnet. Die Kombination von SQUID- und Ferromagnetische-Resonanz-Messungen (FMR) am gleichen Film im UHV erlaubt die unabhängige Bestimmung von magnetischen Anisotropien und der Magnetisierung als Funktion der Temperatur, Schichtdicke, Substrat-topographie und Sauerstoffangebot. Die Ergebnisse sind im Einzelnen:

1. Die schichtdickenabhängige remanente Magnetisierung von 2 bis 20 Monolagen Fe auf GaAs(001) wurde als Funktion der Temperatur ohne Deckschichten bestimmt.
2. Eine kontinuierliche Reorientierung der Magnetisierung in der Ebene (von $[1\ 1\ 0]$ nach $[1\ 0\ 0]$) von Fe Filmen mit zunehmender Schichtdicke wurde mit der Raster-SQUID-Technik beobachtet und zeigt gute Übereinstimmung mit FMR-Messungen.
3. Die Änderung der Magnetisierung und der magnetischen Anisotropie wurde als Funktion von Sauerstoffangebot quantitativ untersucht. Es stellt sich heraus, dass bezogen auf den sich bildenden Eisenoxidanteil die Änderung der Magnetisierung in dünneren Filmen (5 und 8 ML) weit größer ist als für dickere Filme (16 ML). Bei geringem Sauerstoffangebot (<10 Langmuir) wird die senkrechte uniaxiale Anisotropiekonstante $K_{2\perp}$ um 40% reduziert wohingegen die anderen Anisotropien nur geringfügig beeinflusst werden. Diese Untersuchungen wurden durch strukturelle IV-LEED Messungen ergänzt.
4. Ein 8.6 ML Fe/GaAs(001) Film, der bei 300 K einem Sauerstoffangebot von 25000 L O_2 ausgesetzt wurde, zeigte eine spontane Magnetisierungsrichtung senkrecht zur Filmebene bei tiefen Temperaturen. Bei Erhöhung der Temperatur dreht sich die Magnetisierung zwischen $175\text{ K} < T < 250\text{ K}$ in die Ebene hinein. Die Reorientierung wird auf die unterschiedliche Temperaturabhängigkeit der Formanisotropie und $K_{2\perp}$ zurückgeführt.

Abstract

This thesis deals with the characterization of the growth and of the magnetic properties of ultrathin Fe films on GaAs(001). In particular, a scanning SQUID (superconducting quantum interference device) magnetometer was used in ultrahigh vacuum (UHV), whose performance has been improved within the scope of this thesis.

By probing the magnetic stray field of a magnetized film, the absolute remanent magnetization can be determined with submonolayer sensitivity. In the context of this thesis the magnetic stray field has been calculated analytically. The combined use of SQUID and ferromagnetic resonance (FMR) on the same film in UHV allows for the independent determination of the magnetization and the magnetic anisotropy constants as a function of temperature, film thickness, topography of the substrate and oxygen exposure. The results of this thesis are:

1. The thickness dependent remanent magnetization from 2 to 20 monolayer (ML) Fe on GaAs(001) without cap layer was measured as a function of temperature.
2. The continuous in-plane reorientation of the magnetization (from $[1\ 1\ 0]$ to $[1\ 0\ 0]$) of Fe films with increasing film thickness was observed using the scanning SQUID technique and showed good agreement with FMR measurements.
3. The influence of controlled oxygen exposure on the remanent magnetization and the magnetic anisotropy constants of 5 to 16 ML Fe was investigated. A faster reduction of the magnetization is found for the thinner Fe films when the volume of the Fe oxide is taken into consideration. At low oxygen exposure (<10 Langmuir), the perpendicular uniaxial anisotropy constant $K_{2\perp}$ is reduced by about 40% whereas other anisotropy contributions remain virtually unchanged. In addition, structural investigations using IV-LEED during the oxygen exposure were carried out.
4. An 8.6 ML Fe/GaAs(001) film which was exposed to 25000 L O₂ exhibits a spontaneous magnetization perpendicular to the film plane at low temperature. As the temperature is increased a continuous reorientation of the magnetization back to the plane of the film was observed from 175 to 250 K. The reorientation can be ascribed to the different temperature dependencies of the shape anisotropy (due to the temperature dependence of the magnetization) and $K_{2\perp}$.

List of Abbreviations

2D / 3D	=	2-dimensional / 3-dimensional
AF	=	antiferromagnet
AFM	=	atomic force microscopy
AES	=	Auger electron spectroscopy
bcc	=	body-centered cubic
CEMS	=	conversion electron Mössbauer spectroscopy
e.a.	=	easy axis
FM	=	ferromagnet / ferromagnetic
FMR	=	ferromagnetic resonance
h.a.	=	hard axis
hcp	=	hexagonal close-packed
IPMA	=	in-plane magnetic anisotropy
i.p.	=	in-plane
L	=	Langmuir = 10^{-6} Torr sec
LEED	=	low energy electron diffraction
MAE	=	magnetic anisotropy energy
ML	=	monolayer(s)
MFM	=	magnetic force microscopy
o.p.	=	out-of-plane
QMS	=	quadrupole mass spectrometer
rf	=	radio frequency
SC	=	semiconductor
SO	=	spin-orbit (coupling, interaction etc.)
SQUID	=	superconducting quantum interference device
STM	=	scanning tunneling microscopy
UHV	=	ultrahigh vacuum
XMCD	=	X-ray magnetic circular dichroism
XPS	=	X-ray photoelectron spectroscopy

Contents

1. Introduction	1
2. Fundamentals	5
2.1. Magnetic and structural properties of Fe/GaAs heterostructures	5
2.2. Magnetic domains	11
2.2.1. Physical origin	11
2.2.2. The magnetic anisotropy energy density	14
2.3. Quantitative magnetometry using the stray field	17
2.3.1. General remarks	17
2.3.2. Square shaped film with in-plane/out-of-plane magnetization	18
2.3.3. Square film with arbitrary magnetization orientation	22
2.3.4. Magnetic stray field of a circularly shaped film	22
2.3.5. Discussion of different stray field geometries	27
2.3.6. Simulation of the stray field of magnetic films including domains	29
3. Experimental methods	33
3.1. UHV system	33
3.2. Magneto-optical Kerr effect	35
3.3. Low energy electron diffraction	37
3.4. Auger electron spectroscopy	40
3.5. rf SQUID magnetometry under ultrahigh vacuum conditions	42
3.6. Technical improvements of the SQUID setup	46
3.7. Calibration of the SQUID	49
3.8. SQUID-magnetometry and Ferromagnetic resonance	51
4. Results and discussion	53
4.1. Quantitative magnetometry: analytical methods and limitations	53
4.1.1. SQUID-sample distance from stray field data	53
4.1.2. SQUID-sample distance using a current loop	57

4.1.3.	The optimal SQUID-sample distance and ultimate sensitivity	62
4.1.4.	Determination of the direction of the in-plane magnetization	63
4.1.5.	Demagnetizing fields of in plane magnetized films	66
4.1.6.	Influence of surface roughness on the magnetic stray field	69
4.1.7.	Asymmetric magnetic stray field shapes of in-plane magnetized films .	71
4.1.8.	Accuracy limitations for the magnetization determination	71
4.2.	Magnetization of Fe monolayers on GaAs(001)	73
4.2.1.	Substrate preparation and growth of Fe films	73
4.3.	Magnetization reversal of Fe films on GaAs	89
4.4.	In-plane spin reorientation transition for Fe/GaAs films	94
4.5.	Influence of oxygen exposure on the magnetic properties of Fe films	97
4.5.1.	Temperature driven reorientation transition of an oxidized Fe film . . .	116
5.	Conclusion and outlook	121
A.	Appendix	125
A.1.	Magnet used for magneto-optic Kerr effect	125
A.2.	Magnetic field pulse box	127
A.3.	Analytic expressions for the magnetic stray field	128
A.3.1.	Rectangular shaped current loop	128
A.3.2.	In-plane magnetized square shaped film	129
A.3.3.	Out-of-plane magnetized square shaped film	130
A.3.4.	In-plane magnetized circular film	130
A.3.5.	The demagnetizing field of a square shaped film	131
A.4.	Calculation of the magnetostatic potential for periodic surface charges	132
A.5.	Remarks on phase transitions and the critical exponent β	133
A.6.	Details of the sample holder	134
	List of Figures	139
	List of Tables	143
	Bibliography	145
	Publications	155
	Curriculum vitae	159
	Acknowledgment	161

1. Introduction

In the field of spintronics, the spin degree of freedom is added to conventional charge-based electronic devices to open new avenues of device conception and performance [1,2]. The technical issues for exploiting the spin include the basic aspects of efficient spin injection, spin transport, controlled manipulation and detection of the spin polarization. An economically successful spintronic device is the giant magnetoresistance (GMR) sensor [3,4] which is used nowadays in the read heads of hard disc drives. Another famous example is the spin transistor, proposed by DATTA and DAS [5], which has the potential of revolutionizing today's integrated circuits. However, its experimental realization has not been accomplished yet. Currently, two routes for the realization of spin injection devices are under intensive investigation. (i) Para- or Ferromagnetic semiconductors were employed to yield spin-injection efficiencies of up to 90% [6,7]. The drawback of this approach, though, is the necessity of low temperatures and high magnetic fields for the device operation, which limits its technological applicability. Hence, the use of (ii) ferromagnetic metals/semiconductor heterostructures seems more promising. Ferromagnetic (FM) metals on semiconductor (SC) substrates are attractive for spin injection contacts due to their high Curie temperature T_C and high spin polarization at the Fermi level. With regards to these requirements the Fe/GaAs system is a promising candidate.

The spin-injection efficiency of Fe/GaAs was measured by HAMMAR *et al.* [8] and ZHU *et al.* [9] and yielded values of 1% and 2%, respectively, at room temperature. A spin-injection efficiency of 30% at low temperature and of 9% at room temperature has been measured for Fe/AlGaAs(001) using optical methods [10]. However, a detailed and quantitative study on the magnetic properties of the injector has not been carried out in any of these studies.

Other earlier works (e.g. Ref [11]) report reduced interfacial magnetic moments at the Fe/GaAs interface. However, the samples were grown at 175° C which probably induced the formation of a thick interdiffused layer with reduced magnetization. To reduce interfacial interdiffusion ZÖLFL *et al.* [12] and XU *et al.* [13] deposited Fe at room temperature on As depleted GaAs(001) and capped the Fe films with a protective Au layer. Both studies by *ex situ* magnetometry, find that the average Fe magnetic moment in these films is bulk-like. On the other hand DOI *et al.* [14] and Cuenya *et al.* [15] probed interfacial Fe magnetic moments of several nm thick Fe/GaAs(001) films using conversion Mössbauer spectroscopy (CEMS) and found reduced interfacial magnetic moments of down to 0.5 μ_B . These authors attribute their finding to

the formation of dilute Fe-based FeGa or FeAs alloys.

Despite these results, the absolute magnetization of Fe films has never been measured under ultrahigh vacuum conditions. These measurements are systematically carried out and are reported in this thesis.

These measurements are supplemented by a detailed study of the magnetic properties of Fe/GaAs heterostructures during exposure to oxygen. Literature on this topic is rarely found. This investigation is motivated by the fabrication of future spin electronic devices which requires microscale or even nanoscale patterning of suitable heterostructures [16]. Fe microstructures which are protected by capping layers against oxidation before patterning are subject to oxidation at the edges. For small structures (nm regime) the oxide formation will alter the magnetic properties which influence the spin transport undesirably. For instance, it was shown in Ref. [17] that Fe films grown on InAs which were insufficiently capped with Ag, and were therefore partly oxidized at the surface, showed a significant exchange bias effect at low temperature. This was attributed to a non-collinear spin order at the Ag capping layer/Fe interface.

The magnetic remanent state of thin films is of great importance for storage applications and device performance. Therefore, in this thesis the absolute remanent magnetization of ferromagnetic monolayers under ultrahigh vacuum (UHV) conditions is measured by a high-temperature superconducting (HTS) SQUID (Superconducting QUantum Interference Device). The HTS-SQUID which resides outside the UHV in a dewar is only separated by a thin walled non-magnetic metal sheet and is kept at operating temperature by using liquid nitrogen (ℓN_2). A saturated ferromagnetic film can then be scanned below the HTS-SQUID to monitor the z -component of the magnetic stray field \vec{B} as a function of position which allows the extraction of the sample magnetization. The arrangement of this thesis is as follows:

In Sec. 2 the fundamentals are presented starting with an overview of the Fe/GaAs system. Subsequently, the physical mechanisms which lead to the formation of domains are discussed. In this context the magnetic anisotropy energy density is introduced which determines the direction of the magnetization in the absence of an applied magnetic field (magnetic remanent state). The calculation for the magnetic stray field of different sample shapes is presented which is necessary for extracting the magnetization from the stray field measurements using the HTS-SQUID. In addition, the influence of magnetic domains on the magnetic stray field is simulated and limitations for the evaluation of these multi-domain films are given.

Section 3 deals with the experimental methods which were used throughout this thesis where special attention is paid to the rf (radio frequency) SQUID operation. The advanced SQUID setup now includes scanning ability in virtually 3 dimensions, which (i) reduces errors in the determination of M and (ii) enables us to analyze the in-plane angle of the magnetization. The unique combination of *in situ* SQUID and FMR on the same sample is illustrated as well.

In Sec. 4 the results are discussed. This begins with a description of analytical methods

in Sec. 4.1 for the stray field analysis. Also included is an experimental approach to find the SQUID to sample distance by using the magnetic field from a current loop. It is shown that the outstanding sensitivity of the scanning SQUID can resolve M with sub monolayer resolution. Moreover, a technique to derive the equilibrium angle of magnetization is introduced. Furthermore, it is proven by calculations that both demagnetizing effects in remanence, and a rough surface of the ferromagnetic film (typical for the Fe/GaAs system) do not influence the magnetic stray field in a distance of a few nm. This section ends with a summary of factors limiting the accuracy. In Sec. 4.2 the remanent magnetization and interplanar distance of Fe/GaAs(001) was characterized as a function of film thickness. Additionally, temperature dependent measurements ($40 \text{ K} < T < 400 \text{ K}$) for 2.3, 3.7 and 6.5 ML Fe films are presented which show a significantly reduced Curie temperature for the thinner films. The temperature dependence of M of these films was quantitatively analyzed in terms of the classical $T^{3/2}$ -law. Sec. 4.3 deals with the reversal of magnetization of a 15 ML Fe/GaAs(001) film capped with Pt which shows no magnetic domains in remanence by using Kerr microscopy. Subsequently, the SQUID is used to study the in-plane reorientation transition of Fe/GaAs(001) (from $[1 \ 1 \ 0]$ to $[1 \ 0 \ 0]$) with increasing film thickness (Sec. 4.4). A detailed study on the oxidation of Fe/GaAs heterostructures and the concomitant evolution of the magnetic parameters follows in Sec. 4.5 where also chemical and structural properties are addressed. In the last section 4.5.1 the temperature driven reorientation transition from out-of-plane to in-plane of a heavily oxidized 8.6 ML Fe film is shown. This is explained in terms of the temperature dependence of the uniaxial out-of-plane anisotropy constant $K_{2\perp}(T)$ and the magnetization $M(T)$.

2. Fundamentals

2.1. Magnetic and structural properties of Fe/GaAs heterostructures

The Fe/GaAs heterostructure, whose magnetism and structure has been intensively studied over the last decade [18,19,20,21,22,23,24,11,25,12,13,26,27,28,29], has been considered as a material system for future spintronic applications. Such applications may become possible due to the high Curie temperature of Fe ($T_C=1043$ K) and the fact that Fe atoms have a large magnetic moment of $2.22 \mu_B$, exceeding the values of Co ($1.72 \mu_B$) and Ni ($0.606 \mu_B$) [30] for instance. Further benefit stems from the epitaxial growth of Fe on GaAs by molecular beam epitaxy, which is supported by similar lattice constants of the Fe bcc phase ($a_0 = 2.866 \text{ \AA}$) and the zinc-blend-type GaAs crystal ($a_0 = 5.654 \text{ \AA}$) with a lattice mismatch of only 1.4 % [31]. An important parameter of such FM/SC structures is its magneto-crystalline anisotropy, which is absent in polycrystalline or amorphous films.

First attempts to measure spin-injection efficiencies of Fe/GaAs heterostructures yielded disappointingly low values below 1% (e.g. [8]). SCHMIDT *et al.* [32] found that a fundamental obstacle exists for electrical spin injection in the diffusive regime from a FM metal into a semiconductor. They calculated that the spin injection efficiency from a ferromagnet into a semiconductor depends linearly on the ratio of their conductivities σ_{sc}/σ_{fm} , which is in the order of $\sim 10^{-4}$ for Fe and GaAs. Due to the high conductivity mismatch between those candidates, a maximum spin-injection efficiency of 1 % could be derived. One possibility to circumvent these difficulties is the use of Schottky barriers which leads to tunnel contacts. In the case of Fe on GaAs, ZHU *et al.* [9] demonstrated an efficiency of 2% at room temperature (detected optically). Recently, a spin-injection efficiency of 30% has been measured for Fe/AlGaAs(001), using optical methods at low temperature and of 9% at room temperature [10]. In both cases a detailed analysis of the magnetic properties was not reported.

The growth of Fe on GaAs at elevated temperatures ($70^\circ - 100^\circ$ C) results in flat Fe films as demonstrated by atomic force microscopy (AFM) [33]. PRINZ *et al.* [31] checked the quality of the films' crystallinity with FMR, revealing line widths even narrower than the line width of Fe whiskers, which normally serve as a benchmark for excellent crystalline quality. Unfortunately, 'magnetic dead' layers at the interface evolve due to the formation of intermetallic compounds

(e.g. iron-arsenides) at elevated growth temperatures. The terminology 'magnetic dead layer', which is used throughout the literature, is sometimes misleading. Although the layer is non-ferromagnetic it is paramagnetic or anti-ferromagnetic.

Since chemical and magnetic disorder, as well as surface segregation at the interface, disturb spin polarized electron transport across the interface, the film growth has to be carried out at lower temperatures to prevent interfacial mixing. Admittedly, one has to accept a poorer crystalline quality of the Fe layers, which, however, is still sufficient for spin injection applications. For epitaxial interfaces, the inhomogeneities, which emerge on large length scales, do not significantly influence the spin injection. In order to obtain high spin injection efficiency, the spin polarization needs to be high, not only *in* the FM metal, but also *at the interface* of the heterostructure. Therefore, the quality and sharpness of the FM/SC interface becomes an important factor. It has been shown in Ref. [34] that a defective interface of a ZnMnSe/AlGaAs-GaAs(001) spin-LED will reduce the spin injection efficiency. It was proven theoretically and experimentally that spin scattering at defects was the decisive cause for this finding. It was confirmed by means of Mössbauer spectroscopy (CEMS) that Fe can be deposited on GaAs(001) at room temperature such that the Fe interface does not contain any 'magnetic dead' layers. From the analysis of the magnetic hyperfine field distribution, an average Fe magnetic moment of 1.7-2.0 μ_B was deduced [14]. X-ray magnetic circular dichroism (XMCD) measurements of 0.25-1 ML Fe capped with 9 ML Co showed Fe spin moments of (1.84-1.96) μ_B and a large enhancement of the orbital magnetic moment at the Fe/GaAs(001)-4 \times 6 interface [35].

The growth of Fe on GaAs has been investigated on Ga-rich and As-rich surfaces using LEED, RHEED and STM by numerous authors (e.g. [36,13,37]). Although the exact thicknesses of the growth stages vary by about 2 ML from study to study, the growth of Fe on Ga rich surfaces can be divided in two steps. In a first step the growth proceeds via a Volmer-Weber growth (nucleation of 3D islands) between 3 and 5 ML Fe, followed by quasi-layer-by-layer growth from coverages around 5 ML onwards. THIBADO suggested that the preferential bonding of Fe to As influences the growth mode, since Fe tries to minimize its contact with the Ga-rich surface [23].

On As-rich surfaces, the growth at 175°C proceeds via nucleation of 2D islands and subsequent layer-by-layer growth [38]. Here it is noteworthy, that the growth front for thin Fe films is approximately 2 ML thick and even for a 35 ML Fe film it does not exceed 3 Fe layers [23]. However, it has been reported by LALLAIZON that at a lower growth temperature (T=RT), a more 3D like growth mode was observed on GaAs(001)-(2 \times 4) [39], which was thought to result from the lower Fe mobility on the surface. A first-principles study by ERWIN *et al.* [40] found that at low Fe coverage the following factors influence the growth: At first, the bonding of Fe to As is favored over Ga. Secondly, Fe atoms prefer to be highly coordinated which enables a single adatom to break spontaneously surface Ga-Ga and Ga-As bonds in order to form Fe-As

bonds. Interestingly, these authors showed that the initial intermixing of Fe with the GaAs interface becomes energetically less favorable for increasing film thickness. Hence, above a film thickness of 2 ML abrupt interfaces are energetically favored. Furthermore, the outdiffusion of As or Ga atoms which can segregate to the top of the growing Fe film significantly reduces its formation energy [41].

Although the use of As rich GaAs surface reconstructions reduces the density of defects in the Fe overlayers [33], non-magnetic Fe-As compounds with undesired magnetic properties tend to form at the surface. Therefore, Fe deposition on As depleted surfaces is preferred. Throughout this thesis only GaAs substrates with a $\{4\times 6\}$ -reconstructed surface were used since this is one of the most Ga rich surfaces.

The magnetism of bulk α -Fe is well understood. Some fundamental properties are listed in Tab. 2.1 which has been adapted from Ref. [28]. It is important to note that the structural and magnetic properties of epitaxially grown transition metal films are not exclusively defined by their bulk properties. They can be altered significantly by the substrate [42]. In the first magnetic characterization of Fe/GaAs by JANTZ *et al.* [43] in 1983, the authors find non-equivalent FMR spectra along the different $\langle 110 \rangle$ in-plane directions. The cubic fourfold anisotropy, K_4 , cannot explain this finding from the symmetry of bulk α -Fe. A further study by KREBS *et al.* [19] clarifies that the $[110]$ -direction is always less hard than the $[1\bar{1}0]$ -direction, and the in-plane $\langle 100 \rangle$ directions are magnetically equivalent. Based on this fact the existence of a uniaxial in-plane magnetic anisotropy (IPMA) was suggested which has been investigated in the course of further research (e. g. [24,21,44,45]). The physical origin of the IPMA has not been entirely clarified. According to Ref. [28] the total IPMA consists of different contributions, a magnetocrystalline interface anisotropy which is related to interfacial bondings (predominately Fe-As bonds), a magnetoelastic anisotropy due to anisotropic (in-plane) film strain, and a smaller dipolar contribution which is related to anisotropic surface roughness.

The evolution of the FM phase at room temperature of Fe on $\{4\times 6\}$ -reconstructed GaAs(001) proceeds in 3 distinct steps as identified by XU *et al.* using *in situ* MOKE [13]. Below 3.5 ML an Fe film is found to be non ferromagnetic at room temperature. The absence of

Lattice constant	a_0	2.8664	Å
Curie temperature	T_C	1043	K
Saturation magnetization	M_s	1714	kA/m
	$\mu_0 M_s$	2.15	T
Magnetic moment per atom		2.22	μ_B
Lowest order			
Anisotropy constant	K_4	4.81×10^4	J/m ³

Table 2.1.: Properties of bulk α -Fe at room temperature taken from Ref. [28]

a magnetic signal might arise from the formation of smaller clusters, which inhibits magnetic ordering, or the ordering at room temperature. During further Fe deposition, the small clusters increase in size and coalesce to form larger clusters. Hence, in the thickness range between 3.5 and 4.8 ML Fe a superparamagnetic regime was found. This means that the magnetization starts to fluctuate within the experimental time scale, although the temperature is far below the Curie temperature. Above the critical thickness of 4.8 ML, a continuous Fe film evolves which exhibits a FM phase which could be identified by a rectangular hysteresis loop measured in the [1 1 0]-direction. The superparamagnetic-to-ferromagnetic phase transition has been confirmed in Ref. [46] to occur at ~ 4 ML. The onset of ferromagnetism of Fe films has been investigated on (4×2) and (2×6) GaAs(001), and the same T_C as a function of film thickness was found [47]. Apparently the critical thickness, below which the film loses its ferromagnetism at all temperatures does not depend on the surface reconstruction, at least for Ga-rich surfaces. According to Ref. [29] the FM and the IPMA both appear at 2.5 ML Fe in the ground state. The appearance of the IPMA was suggested to be induced by a structural transformation from an amorphous state to a crystalline state. Furthermore, this structural transformation is most likely linked to the island percolation which indirectly relates the onset of FM and IPMA.

With regards to structure, magnetism and the origin of the uniaxial magnetic anisotropy, the influence of surface reconstruction of the GaAs substrate has been a matter of debate. However, reports by various authors substantiate that in the initial growth stage (up to 2 ML) interfacial bonding between Fe and As occurs whereas As-Ga bonds are broken up. Thereafter (above 2 ML), Fe atoms displace substrate atoms in order to form the preferential Fe-As bonds. As a consequence it was suggested that a common Fe-GaAs interface forms irrespective of the surface termination (Ga- or As-rich) [33,48,49]. Furthermore, the substrate surface reconstruction will be disassembled such that it finally results in an interface that is likely to be neither flat nor sharp. Note that disassembled substrate atoms can float on top of the Fe film or can even be incorporated into the film.

Since in theoretical studies often ideally flat surfaces are assumed, the prediction of these studies concerning electronic and magnetic properties of the Fe interface should be handled with caution. Notwithstanding, in the discussion of the magnetic moments, theoretical works with ideally flat interfaces are also summarized in the next section.

Magnetic moments of Fe monolayers on Ga-rich surfaces deposited at room temperature

In magnetic monolayers the magnetic moments can significantly differ from the values of the bulk. Due to a reduced coordination number in 2D, assuming flat interfaces, the narrowing of the d -band width enhances the density of states, $n_0(E_F)$, near the Fermi-level and consequently can lead to increased magnetic moments [50]. Besides, the magnitude of the magnetic mo-

ment depends on the details of the electronic structure of the ferromagnet-substrate interface and can be enhanced or decreased. An overview of the underlying principles has been given by ELMERS [51]. The situation with the Fe/GaAs structure, on the one hand, might be complicated by a corrugated interface and, on the other hand, by the presence of Ga and As at the interface, incorporated in the Fe film or floating on top of the Fe film as a segregated layer. It was theoretically shown that the presence of As and Ga ad-layers can suppress the interfacial magnetic moments by as much as $1 \mu_B$ [40]. *Ab initio* calculations by CRISAN and ENTEL [52] have shown an enhanced magnetic moment for a 1 ML Fe film on Ga-terminated GaAs of $2.82 \mu_B$ for an ideally flat surface. The average magnetic moments as a function of Fe film thickness for relaxed Fe films by these authors are listed in Tab. 2.2. The authors found a gradual decrease of the magnetic moment to the Fe bulk value at a thickness of around 7 ML Fe, with a superimposed oscillation. This oscillation was attributed to the different Fe positions in adjacent Fe layers with respect to the GaAs. A theoretical study by ERWIN *et al.* [40] even showed an increased surface Fe magnetic moment of $\sim 3.0\mu_B$.

Besides theoretical considerations, magnetic moments have also been investigated experimentally. Using CEMS measurements, the interfacial Fe magnetic moments of 1.7 to $2.0 \mu_B$ on GaAs(001)-(4 \times 6) were derived from the hyperfine field distribution. Using the same technique on Fe/GaAs/Al_{0.35}Ga_{0.65}As(001) 2D electron gas heterostructures yielded interface magnetic moments between 1.8 and $2.1 \mu_B$ [15]. Both CEMS investigations indicate a reduction of the interface magnetic moment of up to $0.5 \mu_B$. From a Au capped Fe film of 7 ML thickness which was measured with *ex situ* SQUID magnetometry, ZÖLFL *et al.* [12] deduced an Fe interface magnetic moment of $2.1 \mu_B$. However, the authors made assumptions about the magnetic moments of Fe/Au interface atoms and also about the inner layers of the Fe film which may raise doubts about the accuracy of their results. In addition, X-ray magnetic circular dichroism (XMCD) measurements were conducted on 0.25 to 33 ML Fe films on GaAs(001)-(4 \times 6) [53,54,35] to find the spin and orbital contributions of the magnetic moments by applying

Fe ML	magnetic moment [$\mu_B/atom$]
1	2.82
2	1.89
3	2.46
4	2.03
5	2.30
6	2.13
7	2.26

Table 2.2.: Average magnetic moment for relaxed Fe layers on Ga-terminated GaAs(001) from Ref. [52].

Fe thickness [ML]	m_{spin} [μ_B]	m_{orb} [μ_B]	m_{total} [μ_B]
bulk bcc Fe ^a	1.98	0.085	
33 ^b	2.07 ± 0.14	0.12 ± 0.02	2.19 ± 0.16
8 ^b	2.03 ± 0.14	0.26 ± 0.03	2.29 ± 0.17
5 ^c	2.53 ± 0.29	0.25 ± 0.04	2.78 ± 0.33
4 ^c	2.21 ± 0.23	0.22 ± 0.03	2.43 ± 0.26
1 ^d	1.84 ± 0.11	0.23 ± 0.04	2.07 ± 0.15
0.5 ^{c,d}	1.84 ± 0.21	0.25 ± 0.05	2.09 ± 0.26
0.25 ^d	1.96 ± 0.5	0.23 ± 0.1	2.19 ± 0.6

Table 2.3.: Fe spin, orbital and total magnetic moments measured with XMCD. Values were taken from Refs. ^a [58], ^b [53], ^c [54] and ^d [35].

the sum-rules [55,56]. The data are presented in Table 2.3, where bulk bcc Fe values are also given for comparison. The data show bulk-like spin moments at all thicknesses and a giant enhancement of the orbital moment of up to 300% for a thickness below 8 ML.

Substrate temperatures larger than room temperature and Fe deposition on As rich surfaces can also decrease interfacial magnetic moments. Deposition of Fe on sputter annealed GaAs(001)¹ at 175° C results in a reduced magnetization of the films (90-330 Å) which is especially so the thinner the films are [19]. Fe films up to 100 Å show a saturation magnetization which is only about 60% of the bulk value which indicates that 40% of all Fe atoms are magnetically inactive. It was suggested that this behavior is due to the formation of antiferromagnetic Fe₂As ($T_N = 353$ K [57]) resulting from As out-diffusion. A reduced magnetization with respect to the bulk value is also observed in Ref. [11] which was explained by the formation of a nearly half-magnetized Fe₃Ga_{2-x}As_x (with 0.52 M_{Fe}^{bulk}) sandwiched between GaAs and bulk-like Fe. The width of this layer increases with substrate temperature during growth from 0.8 nm at 50° C to 5.7 nm at 250°C.

Theoretical work by MIRBT *et al.* [49] suggests that As from the GaAs substrate segregates to the top of the Fe layers, while most likely Ga is incorporated in the Fe film (in agreement with experimental studies). They found that the Fe-Ga interaction is very weak and therefore the presence of Ga in the Fe film does not influence the magnetic moment. On the other hand, 1 ML As on top of the Fe film will quench the magnetic moment of the top Fe layer to almost zero. If only 0.5 ML As is present, the Fe magnetic moment is not influenced, since the Fe-Fe interaction is stronger than the Fe-As interaction. The segregation of As is independent of temperature, whereas the segregation of Ga depends on T .

¹the reconstruction of the GaAs(001) substrate was not stated in this work

2.2. Magnetic domains

2.2.1. Physical origin

The idea of magnetic domains was first proposed by WEISS in 1907 who gave an explanation for the fact that a ferromagnet can appear non-magnetic [59]. Although single domains of a magnetic sample are uniformly magnetized their alignment across a large volume of material can be more or less random. Motivated by experimental observations of domains LANDAU and LIFSHITZ argued that magnetic domains form to minimize the total free energy of a FM [60]. Generally, the total free energy of a FM is given by the integral over different free energy contributions:

$$F_{tot} = \int (F_{exchange} + F_{anisotropy} + F_{Zeeman} + F_{strayfield} + F_{ext.stress} + F_{magnetostriction}) dV \quad (2.1)$$

The last two terms of this equation refer to magneto-elastic interactions and magnetostriction effects and will not be discussed in the following.

Exchange energy $F_{exchange}$ describes the change of energy depending on the relative orientation of two neighboring magnetic moments and is the origin of magnetic order. Phenomenologically, the Heisenberg exchange interaction can be written as $F_{exchange} = A_{ex}[(\nabla \vec{M}_x)^2 + (\nabla \vec{M}_y)^2 + (\nabla \vec{M}_z)^2]/M^2$. [61]. Here A_{ex} is a material constant the so-called exchange stiffness constant and M_i (i=x,y,z) are the cartesian components of the magnetization vector \vec{M} . For $A_{ex} > 0$ the interaction favors a collinear alignment of magnetic moments (ferromagnetic state) whereas for $A_{ex} < 0$ an antiferromagnetic order is preferred. It is obvious that in the FM state any deviation from a uniform magnetization, e.g. a spacial variation of the direction of \vec{M} , will give rise to an increased energy contribution. In ultrathin structures the exchange energy between electrons maintains the same orientation of atomic moments across the film thickness. Therefore, the question is at what film thickness d magnetic domains can form across the thickness of the film. The spacial variation of the magnetization is most likely of Bloch type, i.e. a rotation of \vec{M} perpendicular to the domain wall, to avoid dipolar stray fields. The exchange length is generally estimated by $\delta_{ex} = \sqrt{A_{ex}/K}$, where K is the magnetic anisotropy constant of the material [62]. For the Fe bulk anisotropy constant $K_4 = 4.81 \times 10^4$ J/m³ [28] and $A_{ex} = 21$ pJ/m [63] δ_{ex} is about 21 nm which is much larger than all investigated film thicknesses in this thesis. This finding implies that for $d < \delta_{ex}$ magnetic domains can only be found laterally and never across the thickness of the films, i.e. the z -direction.

Magnetic anisotropy energy (MAE) $F_{anisotropy}$ describes the energy dependency of a FM on the direction of its magnetization. There are two causes for magnetic anisotropy, namely (i) dipole interaction and (ii) spin orbit interaction (SO coupling). The (i) dipole interaction energy (Eq. (2.15)) depends on the magnitude and direction of two dipole moments $\vec{\mu}_i$ and $\vec{\mu}_j$ and their

separation \vec{r}_{ij} . Due to the regular arrangement of the magnetic dipoles on the lattice sites the distance r_{ij} is connected to crystallographic axes. Thus, the MAE depends on the orientations of the magnetization with respect to the crystal axes. The second contribution is given by the spin orbit interaction, which couples the isotropic spin of an electron to the lattice of a crystal. The regular arrangement of atoms in a crystal gives rise to periodically arranged crystal fields. These electric fields will influence the orbital motion of electrons, i.e. the orbital magnetic moment will become direction dependent. Without external magnetic field applied the magnetization of a sample will adjust along directions where the MAE is lowest. These directions denote the easy axes of a system whereas magnetization directions with the highest MAE are called hard axes. Expressions of the MAE for different symmetries are presented in Sec. 2.2.2.

The **Zeeman energy** F_{Zeeman} is the interaction energy of an external magnetic field \vec{H}_{ext} with the magnetization vector field of a sample and can be written as

$$F_{Zeeman} = -\mu_0 \int \vec{H}_{ext} \cdot \vec{M} dV \quad (2.2)$$

A parallel alignment of the magnetization with the magnetic field is hence energetically favorable.

Stray field energy [64]: Demagnetizing fields emanate from spaces where the magnetization is not solenoidal. Maxwell's equation $\nabla \cdot \vec{B} = \nabla \cdot (\mu_0 \vec{H} + \vec{M}) = 0$ can be transformed into

$$\nabla \cdot \vec{H}_d = -\frac{1}{\mu_0} \nabla \cdot \vec{M} \quad (2.3)$$

Here \vec{H}_d is identified with the demagnetizing field and one sees that its source are divergences of the magnetization, the magnetic poles of a sample. The potential energy of the magnetic moments of a sample with the demagnetizing field is often referred to as *magnetostatic self energy*, i.e. magnetic moments themselves give rise to the demagnetizing field. We write this energy as:

$$E_d = -\frac{\mu_0}{2} \int \vec{H}_d \cdot \vec{M} dV \quad (2.4)$$

An important fact of the self energy is its *non-locality*, since it contains the interaction of any dipole with all remaining ones.

The demagnetizing field can be depicted by the gradient of a scalar potential:

$$\vec{H}_d = -\nabla \phi \quad (2.5)$$

It is a consequence of $\nabla \times \vec{H}_d = 0$ and it is treated in potential theory. For a given magnetization within a sample volume V and the assumption of an abrupt decrease of the magnetization to zero 'outside' V the scalar potential can be solved [65]:

$$\phi(\vec{r}) = \frac{1}{4\pi} \left(-\int_V \frac{\nabla' \cdot \vec{M}(\vec{r}')}{|\vec{r} - \vec{r}'|} dr'^3 + \int_{\partial V} \frac{\vec{n}(\vec{r}') \cdot \vec{M}(\vec{r}')}{|\vec{r} - \vec{r}'|} dS' \right) \quad (2.6)$$

This is the Poisson potential equation and gives the volume and surface contributions separately. In the special case of a uniform sample magnetization $\nabla' \cdot \vec{M}(r')=0$ the first term, i.e. the volume contribution of Eq. (2.6) vanishes. In addition, \vec{M} is not a function of the position r' . The Poisson equation then simplifies to:

$$\phi(\vec{r}) = \frac{1}{4\pi} \int_{\partial V} \frac{\vec{n}(r') \cdot \vec{M}}{|\vec{r} - r'|} dS' \quad (2.7)$$

Equation (2.7) is used in section 4.1.5 to calculate the demagnetizing field of an in-plane magnetized film in order to estimate whether or not the formation of magnetic domains in a ferromagnetic film is favored after it has been saturated in an external magnetic field.

As the demagnetizing field linearly depends on the magnetization \vec{M} , it is common practice to express the field with the demagnetizing tensor $\tilde{\mathbf{N}}$

$$\vec{H}_d(r') = -\tilde{\mathbf{N}}(r') \cdot \vec{M} \quad (2.8)$$

It is interesting to note that Eq. (2.8) can be directly related to Eq. (2.7) which is inserted into Eq. (2.5). The demagnetizing tensor $\tilde{\mathbf{N}}$ can therefore be identified with the vector gradient arising from the combination of the latter two equations [66].

If a sample has a ellipsoidal shape then the demagnetizing tensor, and therefore the demagnetizing field, is independent of the position inside the sample [64]. It is always possible to convert the tensor to a diagonalized form.

$$\vec{H}_d = - \begin{pmatrix} N_x M_x \\ N_y M_y \\ N_z M_z \end{pmatrix} \quad (2.9)$$

Moreover it is essential that trace $\text{tr}(\tilde{\mathbf{N}}) = 1$ or in other words $N_x + N_y + N_z = 1$ in the SI-system. For simple sample geometries the demagnetizing factors can be calculated. For a thin film with infinite dimensions the demagnetizing factors are $N_x = N_y = 0$ and $N_z = 1$. It means that the demagnetizing field for an out-of-plane magnetized sample is maximal and opposed to the magnetization direction, whereas no demagnetizing field exists for a film with in-plane magnetization. The magneto static energy (Eq. (2.4) is maximal for the out-of-plane case and hence, this situation is unfavorable. The shape anisotropy for a flat cylinder, i.e. a good approximation for a thin film, can explicitly be expressed by $F_{shape} = \mu_0 M^2 \cos^2(\theta)/2$ where θ is the polar angle. It means that the dipole-dipole interaction always constrains the magnetization in the film plane ($\theta = \pi/2$). The out-of-plane alignment of the magnetization becomes the less favored the bigger the magnitude of the magnetization is. Thus most FM films have an easy axis of magnetization in the plane of the film unless out-of-plane magnetocrystalline anisotropy contributions become dominant. However, in the case of very thin magnetic layers the discreteness of the lattice becomes evident and a continuum approximation is not an appropriate description [67,42].

The average demagnetizing factor N_{\perp} for a film of n layers is reduced to $N_{\perp} = 1 - A/n$, where $A = 0.4245$ ($n \geq 2$) for a bcc(001) structure, $A = 0.2338$ ($n \geq 2$) for fcc(001) and $A = 0.15$ ($n \geq 3$) for hcp(0001). In addition, it was demonstrated that a surface roughness can considerably influence the effective dipolar energy [68]. The positive dipolar roughness contribution favors an out-of-plane alignment and behaves as $1/d$.

In an in-plane magnetized film with finite lateral size, magnetic poles at the edges appear which are sources of inhomogeneous demagnetizing fields. The demagnetizing field for an in-plane magnetized film is calculated in Sec. 4.1.5. It will be shown that the demagnetizing effects of typical films investigated in this thesis ($d < 10$ nm, $a=4$ mm) are negligible.

2.2.2. The magnetic anisotropy energy density

The theorem of MERMIN and WAGNER [69] states that a two-dimensional system cannot develop ferromagnetic order at finite temperature $T > 0$, if the magnetic interactions are isotropic and short-range. The magnetic anisotropy is the decisive quantity to stabilize ferromagnetic order in the 2D Heisenberg system at finite temperature [70]. Note, that in addition, the dipole-dipole interaction between the magnetic moments at the lattice sites might be anisotropic (e.g. for a non cubic system) and can stabilize ferromagnetic order.

Phenomenologically, it is customary to develop the free energy of cubic systems in direction cosines $\alpha_i = (\vec{M}/M)\vec{e}_i$ ($i=1,2,3$) of the magnetization with respect to the cubic $\langle 100 \rangle$ crystal axes. Due to cubic symmetry all mixed terms of α_i (e.g. $\alpha_1\alpha_2$) and all α_i of odd power have to vanish as these terms do not reflect the cubic symmetry of the system. Additionally, the free energy has to be invariant considering exchange of any α_i with one another. Eventually, the anisotropy energy density of cubic systems is given by [71]:

$$F_{cub} = K_4 (\alpha_1^2\alpha_2^2 + \alpha_1^2\alpha_3^2 + \alpha_2^2\alpha_3^2) + K_6 (\alpha_1^2\alpha_2^2\alpha_3^2) + K_8 (\alpha_1^2\alpha_2^2 + \alpha_1^2\alpha_3^2 + \alpha_2^2\alpha_3^2)^2 \quad (2.10)$$

Here K_4 , K_6 and K_8 are the anisotropy constants. The lowest order term is of the order four. Terms higher than the K_4 term are small and generally neglected. If all direction cosines are expressed in spherical coordinates $\alpha_1 = \sin(\theta) \cos(\phi)$, $\alpha_2 = \sin(\theta) \sin(\phi)$ and $\alpha_3 = \cos(\theta)$, the free energy of a cubic system is written as:

$$F_{cub} = K_4 \sin^2(\theta) - \frac{1}{8}K_4 (\cos(4\phi) + 7) \sin^4(\theta) \quad (2.11)$$

It should be noted that θ is measured against the $[0 0 1]$ - and ϕ against the $[1 0 0]$ -direction. Eq. (2.11) is appropriate for the symmetry of α -Fe in the bulk.

Besides the fourfold anisotropy, there may also exist two uniaxial anisotropies in a thin film. The out-of-plane uniaxial anisotropy is given by

$$F_{uni}^{o.p.} = K_{2\perp} \sin^2(\theta) \quad (2.12)$$

whereas the in-plane uniaxial anisotropy can be described by

$$F_{uni}^{i.p.} = -K_{2\parallel} \sin^2(\theta) \cos^2(\phi - \delta) \quad (2.13)$$

where δ is the angle between the easy axis of the twofold in-plane anisotropy with respect to the easy axis of the fourfold anisotropy. Figure 2.1 shows polar plots of the free energy surface for the fourfold anisotropy and the uniaxial in-plane anisotropy. For better visualization of the energy surfaces a sphere is added in the polar plots. Figure 2.1 (a) shows the fourfold anisotropy for $K_4 < 0$ with the easy axes of magnetization along the $\langle 111 \rangle$ -directions. Anisotropy energy plots for $K_4 > 0$ are plotted in (b) and here the e. a. are along $\langle 100 \rangle$. In (c) a cut of (b) is presented, since the cross section in the film plane is relevant for the alignment of magnetization in the in-plane case.

Taking into account both uniaxial anisotropies the in-plane case is of particular importance when considering Fe films on III/V semiconductor substrates. A cross section of the polar plots of free energies along a plane parallel to the film surface is plotted for $K_{2\parallel} > 0$ with e. a. along the $[1\bar{1}0]$ -direction in (d) and for $K_{2\parallel} < 0$ with e. a. along $[110]$. Note that $\delta = \pi/4$ in Eq. (2.13) has been chosen to reflect the experimental situation. A change of sign of the uniaxial anisotropy constant $K_{2\parallel}$ will rotate the in-plane easy axis by $\pi/2$.

Uniaxial anisotropy contributions become more and more important in the limit of thin films, since they originate from strains and the interfaces of the films, i.e. vacuum-Fe and Fe-substrate interface. In a phenomenological way the surface and the volume contributions of the anisotropy constants for ultrathin films can be separated by the ansatz [72]:

$$K_i = K_i^v + \frac{K_i^{s,eff}}{d} \quad (2.14)$$

Here, it is important to note that $K_i^{s,eff} = K_i^{s,vac} + K_i^{s,GaAs}$ contains both the Fe-vacuum and the Fe-GaAs interface contribution to the magnetic anisotropy. Eq. (2.14) can be used to separate the volume and interface contributions from thickness dependent measurements. In Eq. (2.14) one often writes $2 K_i^{s,eff}$ when the two surface anisotropies cannot be separated properly. If they are separable they can be given explicitly.

In thin magnetic films anisotropy contributions also arise from dipole-dipole interactions as has been discussed in the previous section. This interaction supports the alignment of the magnetization in the plane of a magnetic film. It is worth mentioning that this *shape anisotropy* has the same angular dependency as the out-of-plane uniaxial anisotropy described by $K_{2\perp}$.

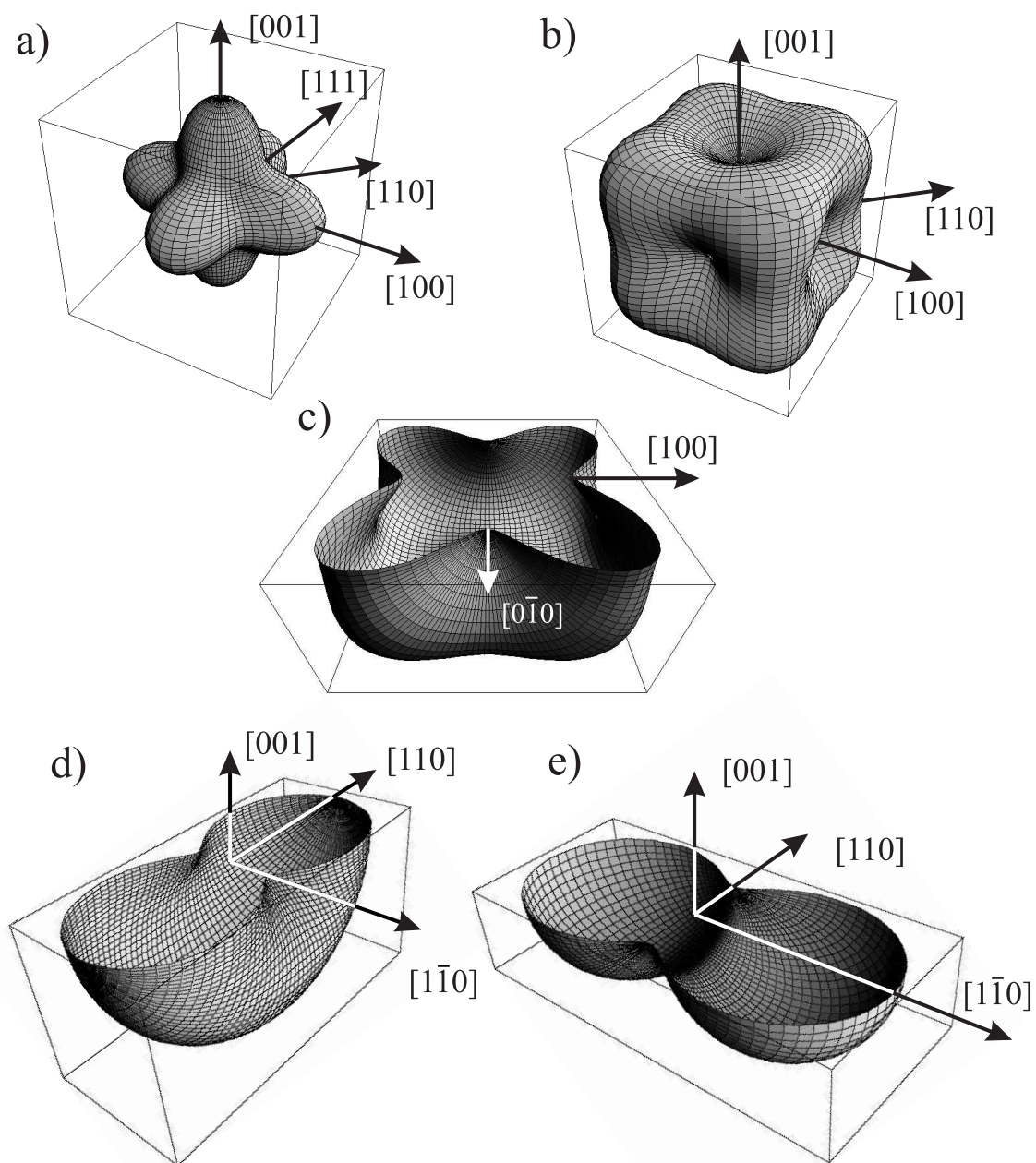


Fig. 2.1.: Polar plots of the magnetic anisotropy energy density for fourfold anisotropy with (a) $K_4 < 0$, (b) and (c) $K_4 > 0$, where (c) is a cross section of (b). (d) and (e) show cross sections of the uniaxial in-plane anisotropy for $K_{2||} > 0$ and $K_{2||} < 0$, respectively, in the plane of the film.

2.3. Quantitative magnetometry using the stray field

Measuring the magnetic stray field emanating from a ferromagnetic sample has become a standard to determine its magnetization. ZIEBA and FONER investigated the effects of the sample geometry on the output of a vibrating sample magnetometer (VSM) [73]. They found that two samples with different shapes and the same sample volume can alter the magnetic signal considerably, thus leading to erroneous magnetization values. Therefore, the exact sample geometry has to be taken into consideration to obtain quantitative magnetization values. The scanning SQUID-magnetometry technique has an outstanding sensitivity to measure the magnetization of ferromagnetic monolayers (10^{-7} emu) [74] and can even be used for measurements under UHV conditions at a high speed [75]. However, in these studies either no *analytical* solution for the magnetic field fields were given, or the solutions were restricted to special cases. Instead, numerical calculations were used, which makes the evaluation of experimental data impractical and limits the adaptability. In this work *analytical* stray field expressions are derived for thin magnetic films of different shapes and magnetization orientation (guidance can be found e.g. in Ref. [76]). Special focus will be given to the derivation of the experimental z -component of the magnetic stray field, B_z . An important requirement for the subsequent calculations is a homogeneously magnetized film, which resides in the x, y -plane of a cartesian coordinate system. Since the films referred to in Sec. 4 have different lateral dimensions, the calculations for a square shaped film with in- and out-of-plane magnetization and for circular shaped films with in-plane magnetization directions are presented. Nevertheless, it will be shown that the derived stray field expressions converge to the same description below a distance which is ten times the samples' dimension. This is the typical distance where a dipole approximation describes a magnetization distribution in the far field. In the in-plane cases, the magnetization orientation includes arbitrary angles with respect to the x -axis.

Section 2.2 discusses the influence of simulated magnetic domains on the magnetic stray field. In order to find more generalized solutions, length scales are expressed in units of sample dimensions, the so-called rescaled units.

2.3.1. General remarks

The dipole-dipole interaction energy of two magnetic dipoles $\vec{\mu}_i$ and $\vec{\mu}_j$ at a distance \vec{r}_{ij} in SI-units is given by:

$$E_{dip} = \frac{\mu_0}{4\pi} \left(\frac{\vec{\mu}_i \cdot \vec{\mu}_j}{(\vec{r}_{ij} \cdot \vec{r}_{ij})^{3/2}} - \frac{3(\vec{r}_{ij} \cdot \vec{\mu}_i)(\vec{r}_{ij} \cdot \vec{\mu}_j)}{(\vec{r}_{ij} \cdot \vec{r}_{ij})^{5/2}} \right) \quad (2.15)$$

To calculate the magnetic field \vec{B}_i which is generated by the dipole $\vec{\mu}_j$ at the position of $\vec{\mu}_i$ one differentiates $\vec{B}_i = -\partial E_{dip}/\partial \vec{\mu}_j$. This then gives:

$$\vec{B}_i = -\frac{\mu_0}{4\pi} \left(\frac{\vec{\mu}_i}{r_{ij}^3} + \frac{3(\vec{r}_{ij} \cdot \vec{\mu}_i)(\vec{r}_{ij})}{r_{ij}^5} \right) \quad (2.16)$$

Furthermore one substitutes

$$\vec{\mu} = \mu \vec{S} \quad \text{with} \quad |\vec{S}| = 1 \quad (2.17)$$

Here, \vec{S} represents the direction of the magnetic moment and is defined as $\vec{S} = (\sin \theta \cos \phi, \sin \theta \sin \phi, \cos \theta)$ where ϕ is the angle between \vec{M} and the x -axis and θ is the angle between \vec{M} and z . Although Eq. (2.16) refers to discrete magnetic dipoles one assumes a homogenously distributed magnetization $\vec{M} = \sum_i^N \vec{\mu}_i/V$ which is true concerning the lateral dimensions of the samples (a few mm) in relation to interatomic distances. One can physically interpret μ as an area magnetization, in which $\mu = M_{Vol} \cdot d$, where M_{Vol} is the volume magnetization and d is the thickness of the film. Note that for thin films where $d \ll L$ the posterior integration is carried out over the lateral dimensions, neglecting the film thickness. Furthermore, the magnetic field probing device, the SQUID, will measure the flux penetrating through the superconducting loop, which is aligned with the area normal pointing in z -direction and thus makes it sensitive solely to the z -component of the magnetic field vector \vec{B} . The choice of the used coordinate system can be gathered from Fig. 2.2, shown for the instance of a square shaped film. With $\vec{r} = (x - x', y - y', z)$ using Eq. (2.16) and the above mentioned premises, one gets the z -component of \vec{B} from the i -th dipole element for an in-plane magnetization ($\theta = 90^\circ$):

$$B_{z,i}(\vec{r}, \vec{r}') = \frac{3\mu_0\mu}{4\pi} \frac{[(x - x') \cos \alpha + (y - y') \sin \alpha] z}{[(x - x')^2 + (y - y')^2 + z^2]^{5/2}} \quad (2.18)$$

with $\vec{r} = (x, y, z)$ as the position vector of the stray field, and $\vec{r}' = (x', y', z')$ as the position vector of the magnetic dipole element. To obtain the total magnetic field $B_{z,tot}$ at position \vec{r} one has to integrate over the dipole distribution, i.e. the shape of the film.

2.3.2. Square shaped film with in-plane/out-of-plane magnetization

In-plane magnetization with arbitrary in-plane angle

Figure 2.2 shows a schematic drawing of a square shaped film of length L , thickness d and the involved variables. The origin of the coordinate system lies in the center of the film for symmetry reasons. The total magnetic field in the z -direction can be calculated from Eq. (2.18):

$$B_{z,square}^{\text{in-plane}}(\vec{S}, \vec{r}) = \frac{3\mu_0\mu}{4\pi} \underbrace{\int_{-L/2}^{L/2} \int_{-L/2}^{L/2} dx' dy' \frac{[(x - x') \cos \alpha + (y - y') \sin \alpha] z}{[(x - x')^2 + (y - y')^2 + z^2]^{5/2}}}_{B_{z,square}^{\text{resc.i.p.}}(\vec{S}, \vec{r})} \quad (2.19)$$

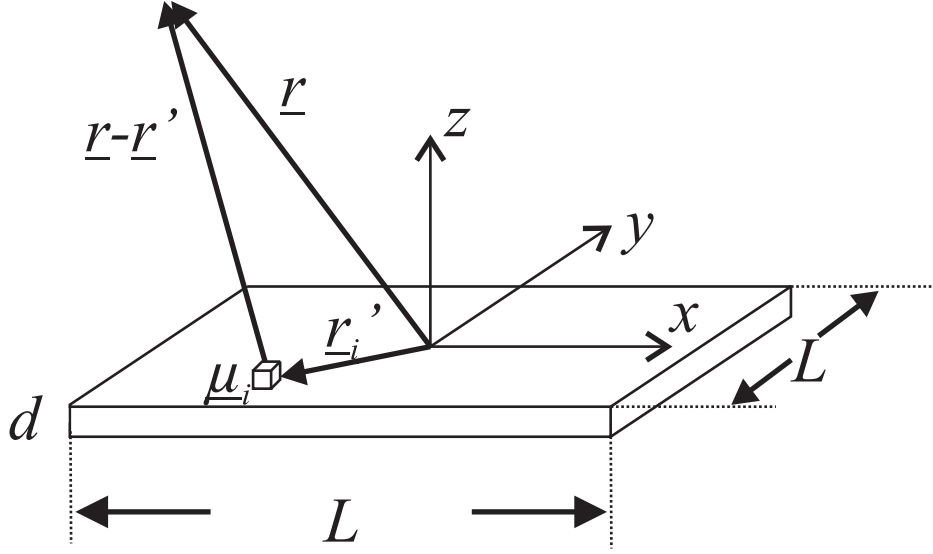


Fig. 2.2.: Square shaped film of length L and thickness d . A magnetic dipole element μ_i gives rise to a magnetic field element at \vec{r} .

In the further calculations we will turn our attention to $B_{z,\text{square}}^{\text{resc,i.p.}}(\vec{S}, \vec{r})$ and introduce rescaled variables \tilde{r} and \tilde{r}' . One substitutes

$$\tilde{r}^{(\prime)} = \frac{\vec{r}^{(\prime)}}{L/2} \Leftrightarrow \vec{r}^{(\prime)} = \frac{L}{2} \tilde{r}^{(\prime)} \quad (2.20)$$

and change the integration boundaries such that

$$B_{z,\text{square}}^{\text{resc,i.p.}}(\vec{S}, \tilde{r}) = \frac{2}{L} \int_{-1}^1 \int_{-1}^1 d\tilde{x}' d\tilde{y}' \frac{[(\tilde{x} - \tilde{x}') \cos \alpha + (\tilde{y} - \tilde{y}') \sin \alpha] \tilde{z}}{[(\tilde{x} - \tilde{x}')^2 + (\tilde{y} - \tilde{y}')^2 + \tilde{z}^2]^{5/2}} \quad (2.21)$$

The result of this calculation is a lengthy expression that just depends on

$$B_{z,\text{square}}^{\text{resc,i.p.}} = f(\alpha, L, \tilde{x}, \tilde{y}, \tilde{z}) \quad (2.22)$$

Here α represents the magnetization direction with respect to the x -axis. Interestingly, $B_{z,\text{square}}^{\text{resc,i.p.}}$ is inversely proportional to the square length L . If one compares two films of $L = a$ and $L = 2a$ the stray field at the rescaled heights $z = a$ and $z = 2a$, respectively, is smaller by a factor of two for the larger film. The whole formula is fully displayed in the appendix of this thesis (see Eq. (A.4)).

Figure 2.3 displays the distributions of the magnetic stray field component $B_{z,\text{square}}^{\text{resc,i.p.}}$ at different heights $z = h$ above the samples as density plots. In the case of Fig. 2.3 (a)-(c) the magnetization \vec{M} of the film is pointing along the x -direction, whereas in Fig. 2.3 (d)-(f) it is oriented $\alpha = 45^\circ$ away from it. Bright coloring in the density plot corresponds to positive values of the stray field, whereas a dark contrast level marks negative values. At a height $h = 0.1L$ the

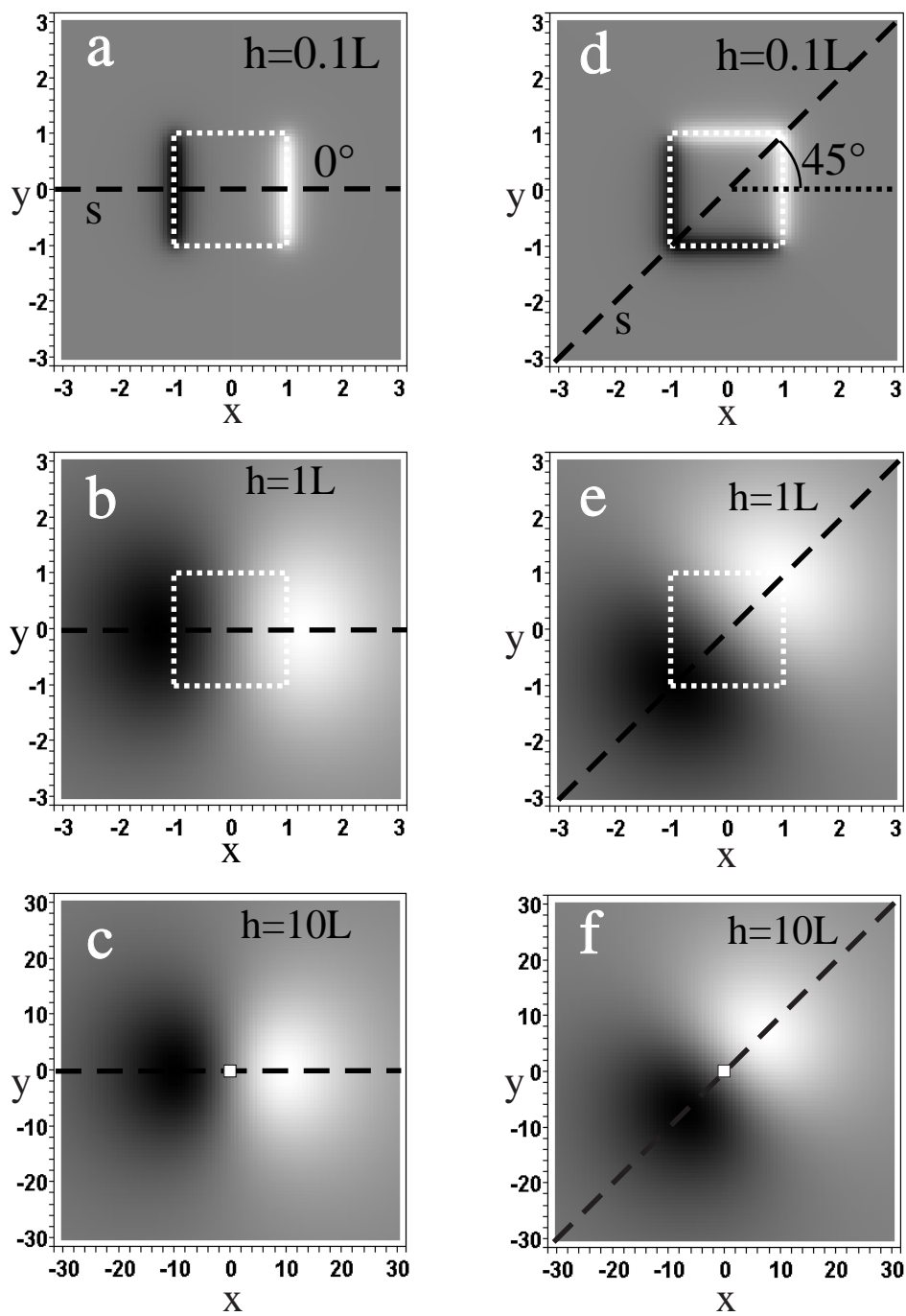


Fig. 2.3.: Density plot of B_z in rescaled units for three different heights $z = h$ above the sample with the magnetization lying parallel to the x -axis ((a)-(c)) and diagonal with respect to the square magnetic film ((d)-(f)). The white dotted squares in (a), (b), (d), and (e) indicate the position of the magnetic film. At a height ten times the distance of the sample length $h = 10L$ ((c), (f)) the film position is depicted as a small white square.

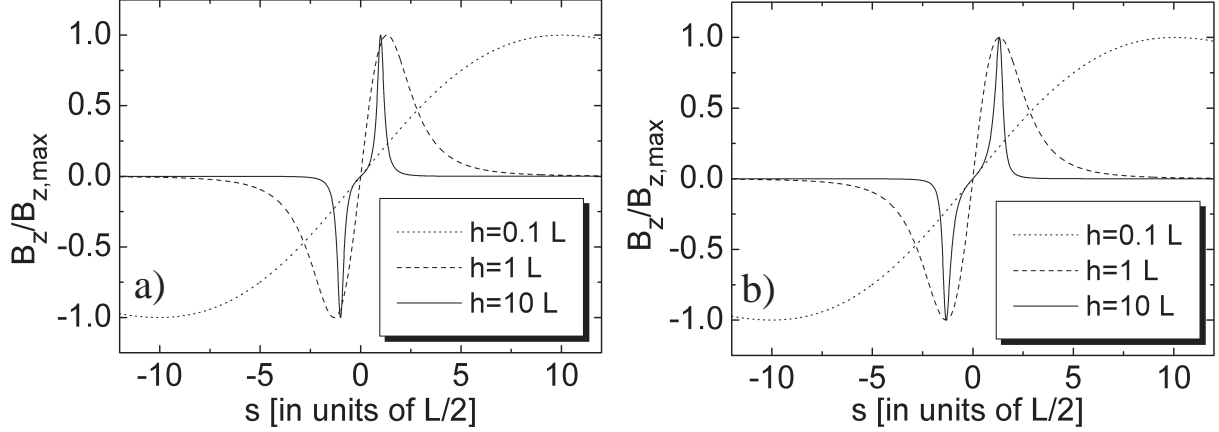


Fig. 2.4.: Line scans of the z -component of the magnetic stray field along the dashed lines of Fig. 2.3. (a) refers to the three different heights above the sample from Fig. 2.3 (a),(b) and (c). (b) refers to Fig. 2.3 (d), (e) and (f).

field distribution clearly reflects the contours of the sample boundary since the magnetic flux density emerges at the edges of the in-plane magnetized film. When the distance increases to $h = L$ (see Fig. 2.3 (b), (d)), the stray field distribution does not any longer mirror the shape of the film, but still unambiguously reveals the orientation of the magnetization. Increasing the distance to $h = 10L$ (see Fig. 2.3 (c), (f)) further separates the stray field's extremal values. Note that the x and y scales extend by a factor of 10. Figure 2.4 shows line scans along the dashed lines s of Fig. 2.3 whose directions all coincide with the magnetization directions across the center of the films. All graphs have been normalized to the respective maximum field value because increasing the distance from $h = 0.1L$ to $h = 10L$ reduces the magnitude of magnetic field B_z by a factor of more than 2×10^4 . Note, that for the lowest distance $h = 0.1L$ the change in both scan lines (respective curves in Fig. 2.4 (a) and (b)) are visible. The extremal values of the diagonal scan from Fig. 2.4 (b) reside approximately above the film edges at a further distance than in figure 2.4 (a) because of the film geometry. For a distance $h = 1L$, the extremal position deviates less than 1% and comparison of absolute values at this position gives an accordance of better 0.3%. At a distance of $h = 10L$, the discrepancy between different magnetization directions almost vanishes (10^{-6}) and measurements of the far field of a magnetic charge distribution can be described by a point dipole. We will refer to this in Sec. 2.3.5.

Out-of-plane magnetization

If one assumes an out of plane magnetization direction ($\theta = 0$), one can write for \vec{S} in Eq. (2.17) $\vec{S} = (0, 0, 1)$. Together with Eq. (2.16), this yields for the magnetic field component B_z

generated by a dipole element:

$$B_{z,i}(\vec{r}, \vec{r}') = \frac{3\mu_0\mu}{4\pi} \frac{[-(x-x')^2 - (y-y')^2 + 2(z-z')^2]}{[(x-x')^2 + (y-y')^2 + z^2]^{5/2}} \quad (2.23)$$

where once again \vec{r} is the position vector of the considered magnetic field and \vec{r}' is the position of a single dipole element of the magnetic film. The integration is performed in a similar manner to the way it was done in the previous section. Appendix (Eq. (A.5)) explicitly shows the result of the analytic expression of B_z . Figure 2.5 shows the B_z distribution for the out-of-plane case at two distinct distances. On the left hand side of the figure, contour plots of B_z are shown for distances $h = 0.1L$ and $h = 1L$. The right hand side presents a 3D view of B_z plotted against x and y for the stated heights. The closer the distance, the more the stray field illustrates features of the film's lateral dimensions. Figure 2.5 (e) shows line scans of the B_z distribution along the x -axis for $y = 0$ and the given heights. Both scans have been normalized to their maximum field value in order to display them in the same graph. For small distances (e.g. $h = 0.1L$) the maxima are positioned close to the sample edges, whereas for greater distances (here $h = 1L$) a single maximum evolves in the middle above the film.

2.3.3. Square film with arbitrary magnetization orientation

As shown in the previous sections, analytic expressions for the magnetic stray field of square shaped films exist for in-plane, as well as out-of-plane magnetized samples. Using these results, the stray field of arbitrary uniform magnetization orientations can be derived by a suitable superposition:

$$B_z(x, y, z, \varphi, \theta) = \frac{\mu_0\mu}{4\pi} [\sin(\theta)B_{z_{ip}}(x, y, z, \varphi) + \cos(\theta)B_{z_{op}}(x, y, z)] \quad (2.24)$$

Here, θ denotes the polar angle of the magnetization and φ denotes the azimuth. $B_{z_{ip}}$ is the rescaled in-plane contribution to B_z and represents Eq. (A.4), while $B_{z_{op}}$ has to be substituted by Eq. (A.5). Equation (2.24) satisfies the condition that the absolute value of the magnetization does not change if θ and φ vary. If the polar angle is $\theta = 0$, then Eq. (2.24) results in the out-of-plane case since the first term disappears. One obtains the in-plane case when $\theta = \pi/2$ and the second term becomes zero.

2.3.4. Magnetic stray field of a circularly shaped film

Once again Eq. (2.18) is the starting point of the calculation. For the rotational symmetry of the problem one chooses a fixed angle of the magnetization, e. g. $\alpha = \pi/2$. The coordinate system resides in the center of the circular film as can be seen in Fig. 2.6. Eventually, one has to carry out an integration over a circle with radius R .

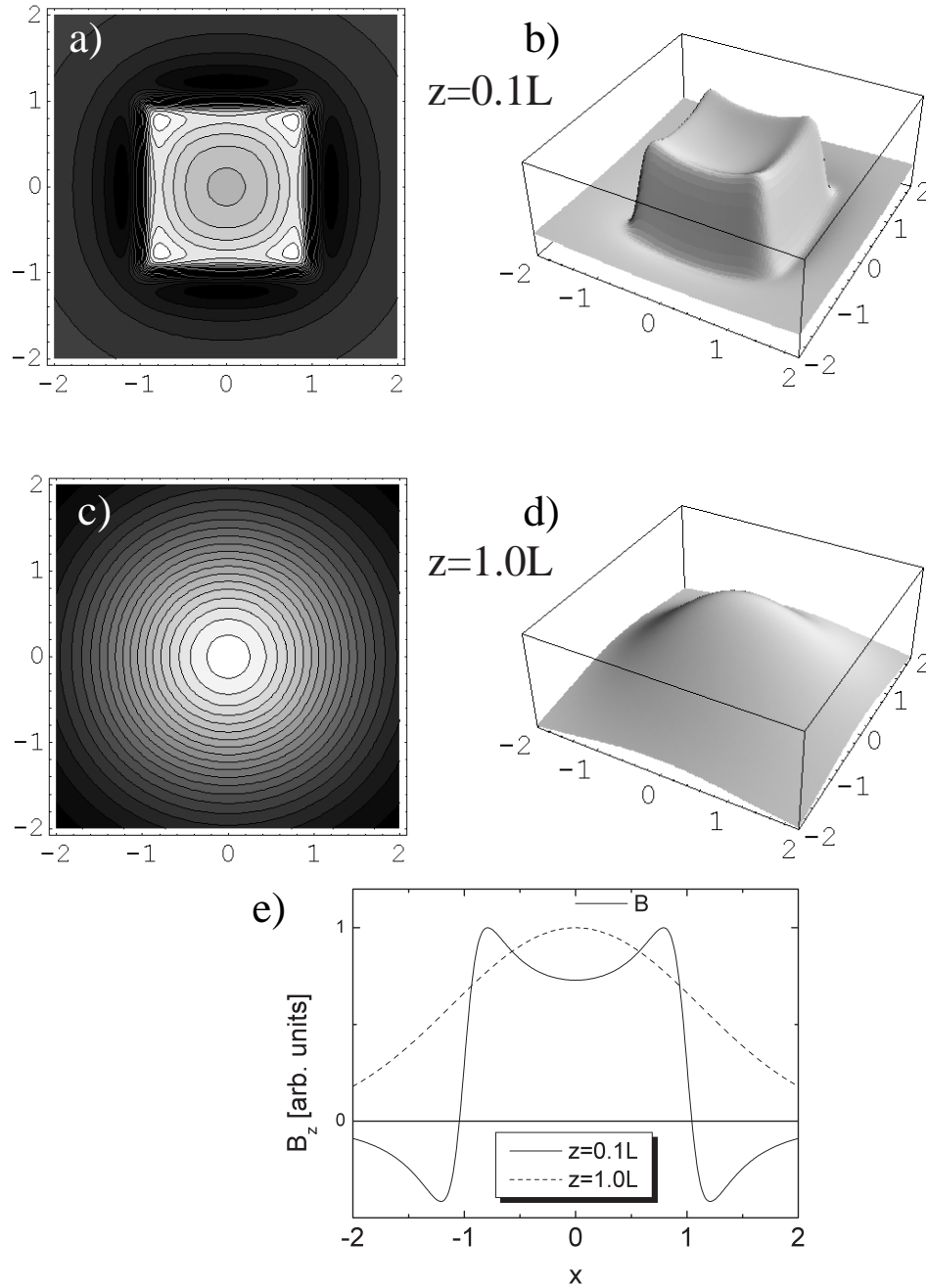


Fig. 2.5.: (a) and (b) respectively show the rescaled B_z field in a contour plot and a 3D-plot at a height $z = 0.1L$, (c) and (d) show the same plots for height $z = 1.0L$. (e) presents two line scans at the previously discussed heights for $y = 0$.

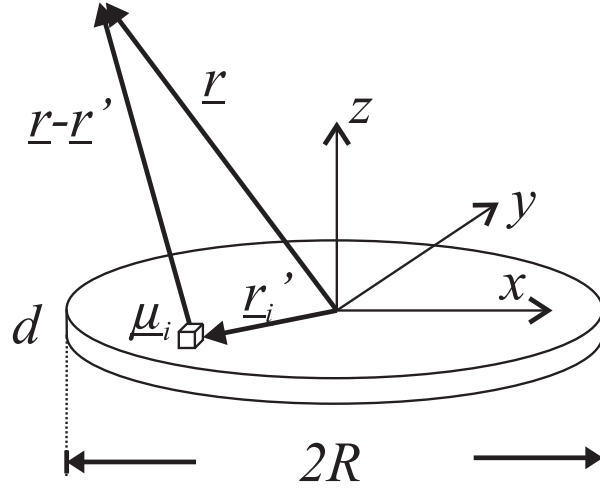


Fig. 2.6.: Circular shaped film of Radius R and thickness d . A magnetic dipole element μ_i gives rise to a magnetic field element at \vec{r} .

$$B_{z,circle}^{\text{in-plane}}(x, y, z, R) = \frac{3\mu_0\mu}{4\pi} \underbrace{\int \int_{\text{circle area}} \frac{(y-y')z}{[(x-x')^2 + (y-y')^2 + z^2]^{5/2}} dx' dy'}_{B_{z,circle}^{\text{resc,i.p.}}(x,y,z,R)} \quad (2.25)$$

Now it is useful to employ cylindrical coordinates, due to the sample geometry: $x = r \cdot \cos \theta$ and $y = r \cdot \sin \theta$ on the one hand, and $x' = r' \cdot \cos \theta'$ and $y' = r' \cdot \sin \theta'$ on the other hand. Subsequently, one integrates θ' from 0 to 2π and r' from 0 to R . In cylindrical coordinates, the result is:

$$B_{z,circle}^{\text{resc,i.p.}}(R, \beta, r, z) = \frac{1}{Rr[(r-1)^2 + z^2]^{3/2}} \cdot \left\{ 2z \sqrt{1 - \frac{4r}{(r+1)^2 + z^2}} \left[(1 + r^2 + z^2) \text{EllipticE} \left(\frac{4r}{(r+1)^2 + z^2} \right) - [(r-1)^2 + z^2] \text{EllipticK} \left(\frac{4r}{(r+1)^2 + z^2} \right) \right] \sin(\beta) \right\} \quad (2.26)$$

where R is the radius of the film and β , r , and z are the cylindrical coordinates. *EllipticK* and *EllipticE* are analytic expressions respectively known as the complete elliptic integrals of the first and second kind. By definition [77]:

$$\begin{aligned} \text{EllipticK}(m) &= \int_0^1 [(1-t^2)(1-mt^2)]^{-1/2} dt \\ \text{EllipticE}(m) &= \int_0^1 (1-t^2)^{-1/2} (1-mt^2)^{1/2} dt \end{aligned} \quad (2.27)$$

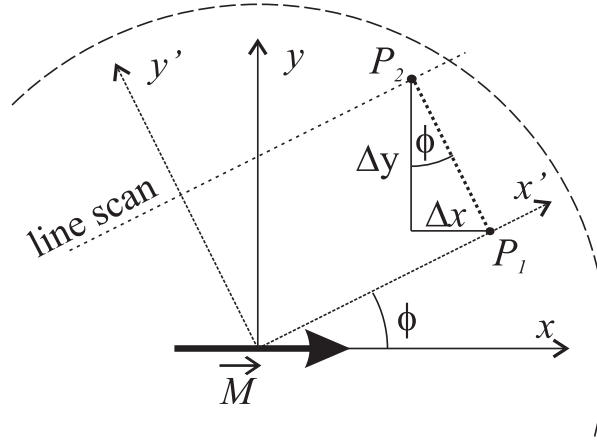


Fig. 2.7.: Auxiliary chart for the transformation of the coordinate system to account for an arbitrary in-plane orientation of the magnetization.

Elliptic integrals arise, e.g. in solving the equation of motion for a simple pendulum. Because cartesian coordinates are used in the experiments, the expressions must be transformed back to cartesian coordinates. The substitution instruction is:

$$\begin{aligned}\beta &= \arctan(y/x) \\ r &= \sqrt{x^2 + y^2} \\ z &= z\end{aligned}\tag{2.28}$$

The analytic cartesian expression is explicitly written in (A.6).

Although Eqs. (2.26) and (A.6) do not include an arbitrary in-plane angle for the alignment of the magnetization vector \vec{M} , one can describe this situation by rotating the coordinate system in the film plane. The circular shape of the sample is suitable for rotation of the coordinate system around its center in the film plane. Figure 2.7 helps to derive an appropriate coordinate transformation. In the initial coordinate system (x, y) , the magnetization is aligned in the x -direction. Now one expresses point $P_2 = (x, y)$ in terms of x' and y' . From basic geometric considerations, the transformation instruction reads as follows:

$$x = x' \cos(\phi) - y' \sin(\phi)\tag{2.29}$$

$$y = x' \sin(\phi) + y' \cos(\phi)\tag{2.30}$$

Consider that the new coordinate system (x, y) in Fig. 2.7 is turned counter-clockwise by an angle ϕ . The magnetization \vec{M} viewed from this new coordinate system rotates thereupon vice-versa ($\alpha = -\phi$).

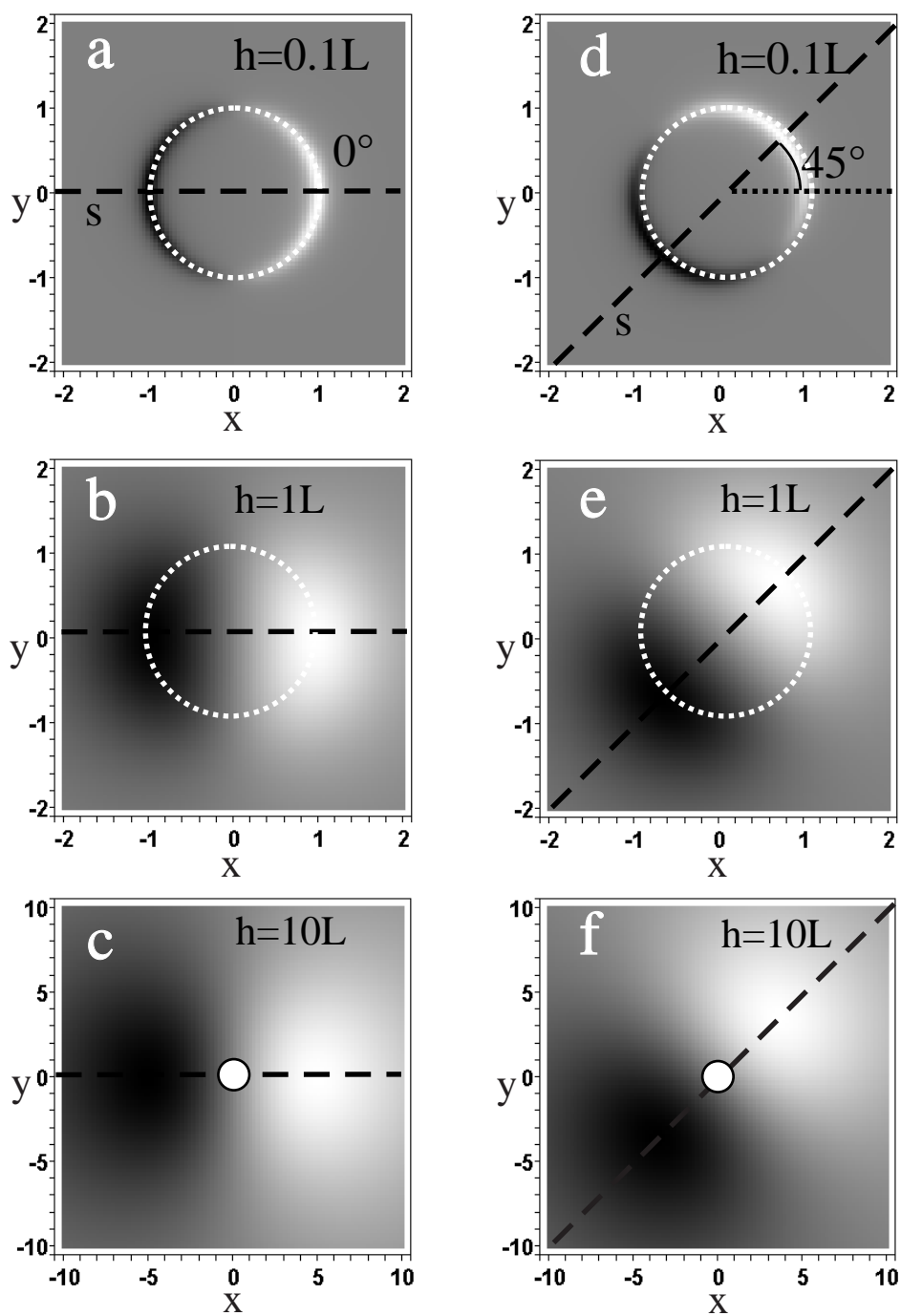


Fig. 2.8.: Contour plot of B_z in the $x-y$ plane for three different heights $z = h$ above the sample. (a),(b) and (c) represent cases with \vec{M} parallel to the x -axis. (d),(e) and (f) show the same plots for an in-plane angle $\alpha = 45^\circ$. The white circles represent the boundaries of the sample.

2.3.5. Discussion of different stray field geometries

To get the magnetic stray field in absolute values the rescaled stray fields (Eqs. (A.4),(A.5) and (A.6)) have to be multiplied by $3\mu_0 \cdot \mu/4\pi$. Here the magnetic moment per area $\mu = M \cdot d$, where d is film thickness, is connected with the volume magnetization M by

$$\mu = M \cdot n \cdot d_{inter} \quad (2.31)$$

with n the number of monolayers and d_{inter} the interplanar distance of the sample atoms. Additionally, one must re-substitute the rescaled position variable from Eq. (2.20), i.e. $\tilde{x} = 2x/L$, $\tilde{y} = 2y/L$ and $\tilde{z} = 2z/L$.

Convergence of analytic description for extended sample geometries and depiction with point dipole

In contrast to the calculation of the stray field of a magnetic charge distribution, the magnetic field originating from a single point dipole can be calculated much more simply using Eq. (2.16):

$$\vec{B}(\vec{r}) = \frac{3\mu_0}{4\pi} \left\{ \frac{1}{r^5} \left[\begin{pmatrix} x \\ y \\ z \end{pmatrix} \begin{pmatrix} \mu_x \\ \mu_y \\ \mu_z \end{pmatrix} \right] \begin{pmatrix} x \\ y \\ z \end{pmatrix} - \frac{1}{r^3} \begin{pmatrix} \mu_x \\ \mu_y \\ \mu_z \end{pmatrix} \right\} \quad (2.32)$$

where the magnetic moment $\vec{\mu}$ can have any spatial direction. Reasonably, one uses spherical coordinates to define the moment's direction: $\vec{\mu} = \mu(\sin \vartheta \cos \phi, \sin \vartheta \sin \phi, \cos \vartheta)$. Just considering a magnetic moment aligned along x (i. e. $\vartheta = 0$) the B_z -component in cartesian coordinates results in:

$$B_z(\vec{r}) = \frac{3\mu_0}{4\pi} \frac{x \cdot z \cdot \mu}{(x^2 + y^2 + z^2)^{5/2}} \quad (2.33)$$

Let's now compare the magnetic stray field of a point dipole, a square shaped film and a circular film where all have a magnetic moment along x . In order to adequately evaluate the stray fields, it is necessary to assume the same magnetic moments for all three cases. For the square film, we consider a sample length of $a = 3$ mm and a thickness of 10 ML Fe with bulk magnetization. In contrast, the circle radius is chosen $r = a/2$ which makes the sample boundaries lie onto the ones of the square. But as the areas of the square (a^2) and the circle ($a^2\pi/4$) differ, the magnetic moments differ as well, and the circle's stray field is multiplied by a correction factor $4/\pi$. This reflects the ratio of the respective areas. The point dipole unifies the total magnetic moment (of the square) in a singular point $\mu = M \cdot V = M \cdot a^2 \cdot d$, where d is the thickness of the film. In Fig. 2.9 (a), (b) and (c), the stray field component, $B_z(x)$, is plotted at heights $h = 3, 5$ and 10 mm above the film's center ($y = 0$). The point dipole shows the biggest stray field amplitude, followed by the circular film's for all heights. The greater the distance from the film the more quickly all three line scans approach each other. Note that the far field of a (magnetic) charge

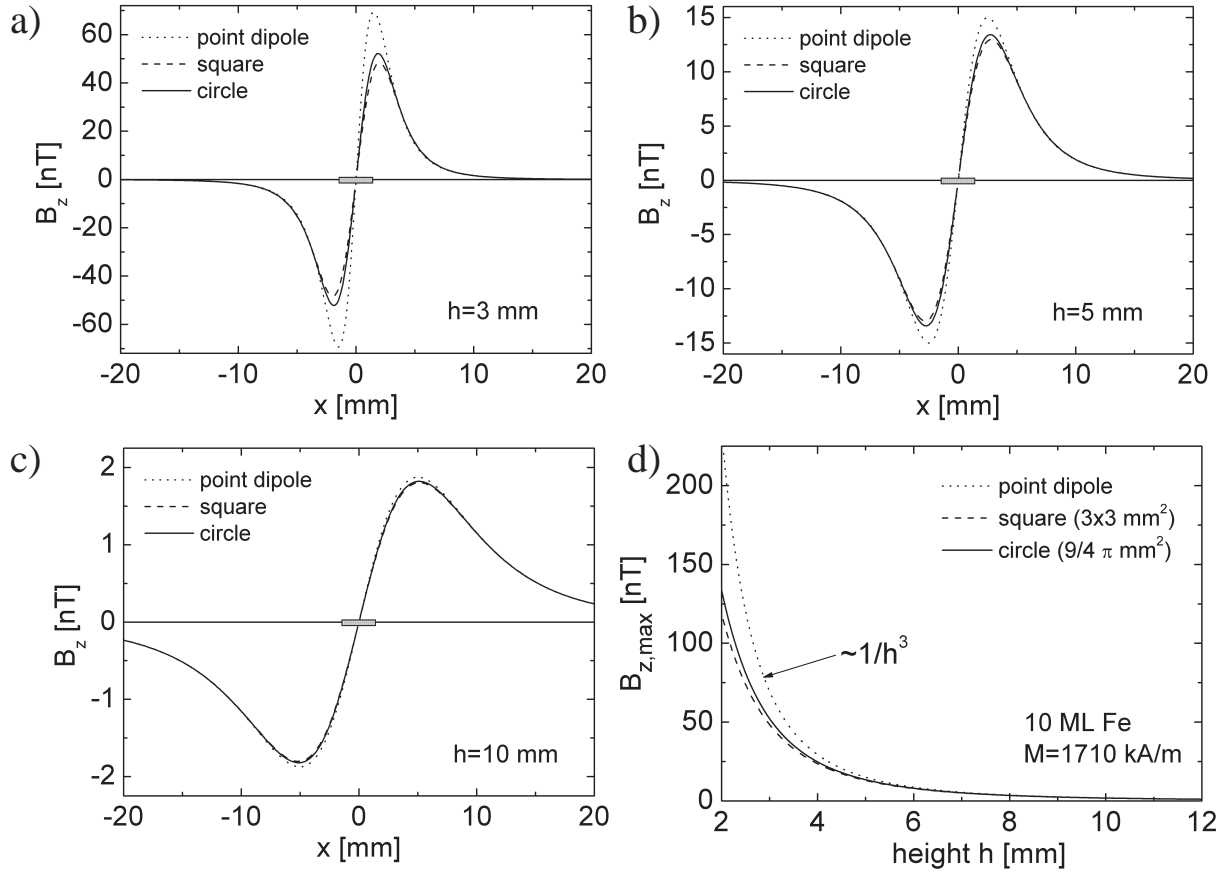


Fig. 2.9.: (a), (b), (c) Comparison of $B_z(x)$ at $h=3, 5, 10$ mm for a square shaped (3×3 mm²) and circular sample ($\varnothing=3$ mm) and a point dipole. (d) Stray field amplitude as a function of height h for the different sample geometries.

distribution ($distance \gg sample\ dimensions$) always describes a dipole approximation. In Fig. 2.9 (d), the maximum values of B_z as a function of height, h , are numerically calculated by solving $dB_z/dx = 0$ for $x > 0$. In the limit of $h \rightarrow 0$ the stray field diverges in all three cases. As seen in (a)-(c), the $B_{z,max}$ value of the point dipole deviates more at smaller distances and drops with h^{-3} . At great distances, all three curves merge. At heights around 5 mm, as typically used in the experiments, the stray field amplitudes of the circle and the square differ only by about 3 %. Therefore, a description with both stray field formulas, including a small correction factor, will yield acceptable accordance.

2.3.6. Simulation of the stray field of magnetic films including domains

Magnetic domains will alter the magnetic stray field \vec{B} of a ferromagnetic sample in comparison to a homogeneously magnetized film. Having illustrated the physical origins for the evolution of magnetic domains in a previous section we will now describe the effects of a given magnetic domain configuration on the measured magnetic signal B_z . This is important for the quantitative determination of the sample magnetization M from the effective stray field.

In Sec. 2.3.5 an expression for square shaped magnetic films has been given for homogeneous in-plane magnetized films. In a simplified approach we will simulate magnetic domains by summing the stray fields of magnetic films with different in-plane magnetization direction. A simple domain arrangement can be seen in Fig. 2.10. A square film of length $L = 3a$ is divided into nine smaller patches of length $L = a$ representing the domains. Each film's center position is given by the coordinates (na, ma) with $n, m = -1, 0, 1$. Of course the shape and size of the domains lack physical reality. Nonetheless it will help to improve our understanding of the SQUID data which senses the stray field in a distance comparable to the lateral sample dimensions. With Eq. (A.4) (see appendix) we can calculate $B_z^{nm}(\alpha_{nm}, x + na, y + ma, z)$ of

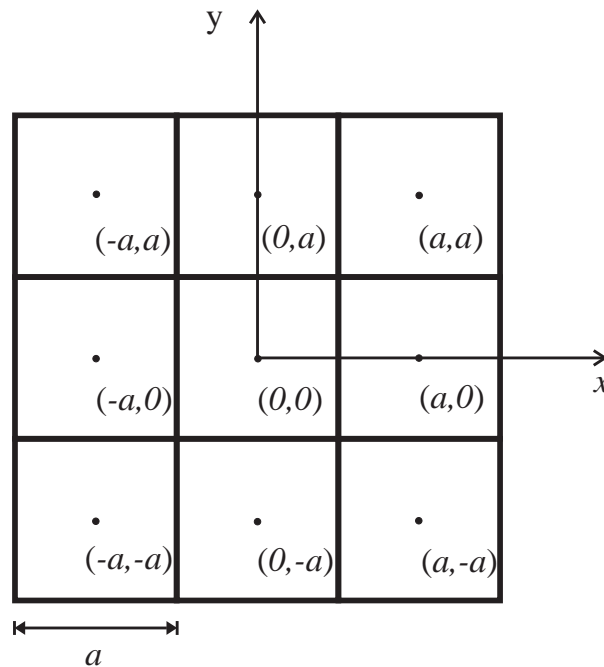


Fig. 2.10.: Square film of length $L = 3a$ divided in 9 square 'sub'-films of length a . Each film position is given by the coordinates shown above and can be addressed with an arbitrary in-plane magnetization direction.

the sections with individual magnetization directions α_{nm} and obtain the total magnetic field by

$$B_z^{tot}(x, y, z) = \sum_{n,m} B_z^{nm}(\alpha_{nm}, x + na, y + ma) \quad (2.34)$$

Exemplary, we chose a multi domain state of a square film with 4 of the 9 sections having a magnetization direction turned in-plane by -45° from x and the other 5 sections turned by $+45^\circ$. This situation is sketched in Fig. 2.11 (a). The stray fields B_z at various heights h are presented in density plots. At close distance $h = 0.2$ mm (b) the individual sections can be identified in the stray field distribution. At $h = 1$ mm (c) the stray field looks more blurred but still reflects the domain arrangement. Further increasing the distance to $h = 5$ mm (d) makes the stray field look typical dipolar where all individual stray field contributions of the individual domains have merged. Since there was an imbalance of magnetization contributions (by 5 to 4) with respect to the x -direction the stray field amplitudes appear rotated by some angle. Consequently, one can state that magnetic domains in the ferromagnetic film cannot clearly be identified, since at a typical measuring distance of the scanning SQUID of $h = 5$ mm their contribution will be smeared out. Domains alter the appearance and also the magnitude of the stray field. But it is impossible to deduce the detailed domain configuration from SQUID measurements when measuring in the far field regime. Nevertheless, if one knew that the magnetization is aligned along the diagonal directions (see Fig. 2.11 (a)) then statements could be made on how much of the film was magnetized at 45° and -45° . From Fig. 2.11 one can conclude that domains can be resolved when the distance h is smaller than the domain size. Finally the special case of a thin film with biaxial anisotropy (90° symmetry) shall be discussed, where the easy axes of magnetization are turned by 45° from the scanning direction x which is very similar to the situation in Fig. 2.11 (a). We assume, however, that the film magnetization after being magnetized along x decomposes in a great number of magnetic domains, but on average equally distributed in 45° and -45° direction. From the magnetic stray field distribution at a height h greater than the maximum domain size the existence of domains cannot be deduced, and the film seems to be magnetized along x . If one assumes a single domain magnetic state with M along x and follows the fit procedure which is explained later one would obtain an erroneous magnetization which is reduced by a factor $\cos(45^\circ) = 1/\sqrt{2}$. Only the x component of M is measured whereas the components in y and $-y$ cancel out. Therefore, care should be taken to saturate the sample in a magnetic field which is parallel to an easy axis of the film to avoid domain formation and ambiguous stray fields.

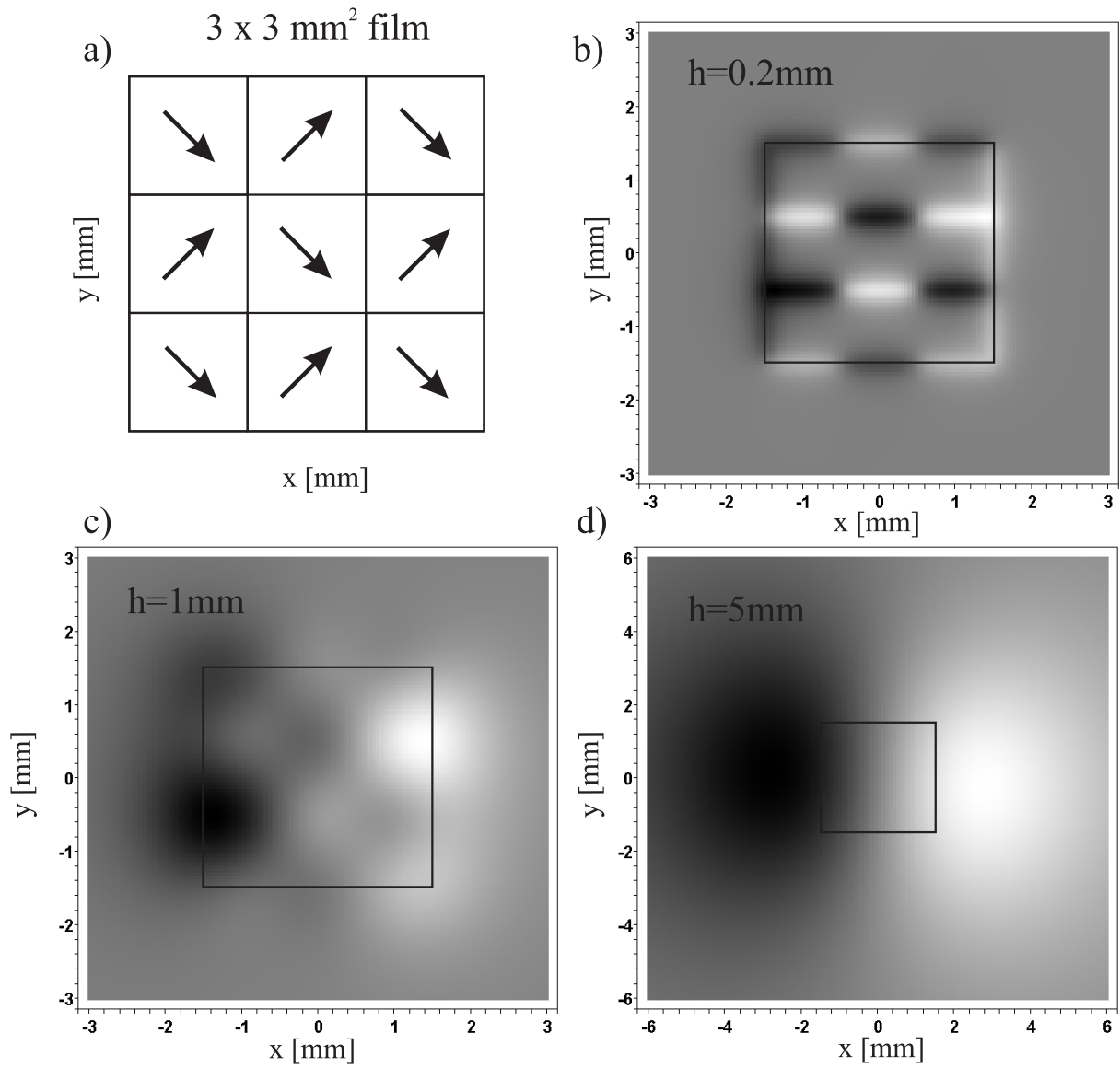


Fig. 2.11.: Calculated density plots of B_z for 9 domains including angles of 45 degree with respect to x at various distances. The domain configuration is shown in the upper left panel.

3. Experimental methods

3.1. UHV system

The experiments are carried out in an ultrahigh vacuum chamber with a base pressure of 2×10^{-10} mbar, along with a combination of an ion getter pump (300 l/sec), a titanium sublimation pump (TSP) and a turbo molecular pump (300 l/sec). A rotary vane pump serves as a forepump for the turbo molecular pump with a base pressure below 10^{-2} mbar. An ion gauge measures the absolute pressure in the UHV chamber. A manipulator allows sample movement along the main axis (x direction) by 600 mm and rotates the sample about the x axis by using computer-controlled stepper motors. Two micrometer screws move the sample manually in the y - z -plane within a circle of radius $R=25$ mm. The manipulator is equipped with a flow cryostat for liquid He cooling and a resistive heater to control the temperature, allowing a sample temperature variation from 40 to 500 K. Since the sample preparation requires temperatures of $T = 870$ K, an integrated current loop inside the sample holder can be used to heat the sample above 900 K. A K-type thermocouple integrated in the Cu sample holder (see appendix Fig. A.5) measures the sample temperature. Additionally, the UHV-chamber contains an Ar^+ ion gun to clean the sample surfaces by argon ion bombardment. A cylindrical mirror analyzer (CMA) with an axial electron gun is used for Auger electron analysis to obtain chemical information on the sample surfaces. Structural investigations are carried out with a low energy electron diffraction (LEED) unit which is mounted opposite to the CMA. Residual gas analysis is performed with a quadrupole mass spectrometer (QMS). A sketch of the setup of the SQUID measurement system is shown in Fig. 3.1. The cryostat which contains the SQUID is filled with liquid nitrogen. It can be shifted along the z -axis by means of a translator such that the sample can be scanned along the x -axis at a fixed distance to the SQUID. While the sample is scanned along the x -direction, the SQUID measures the z -component of the magnetic field B_z . The non-magnetic steel finger which separates the liquid nitrogen from the vacuum is surrounded by two μ metal cylinders with holes to let the sample holder pass through. If the SQUID is not in use, the z -translator is retracted upwards. Prior to SQUID experiments the sample is moved in the glass finger where a (pulsed) magnetic field can be applied along the x , y or z direction to saturate the magnetic film along its easy axis of magnetization. The appendix (see A.2) describes the electric circuitry of the device, which is used to generate pulsed magnetic fields

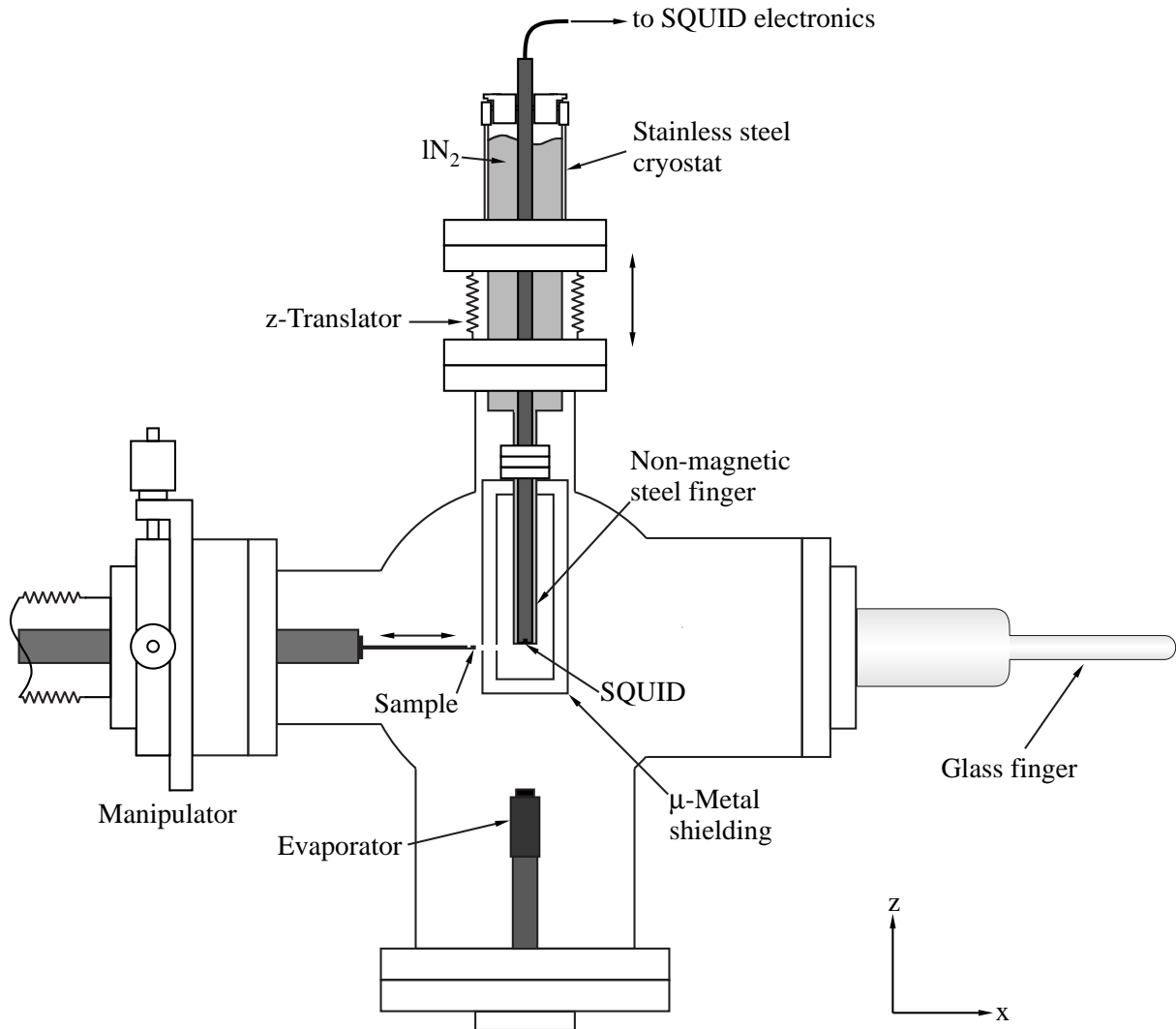


Fig. 3.1.: The UHV-SQUID setup shows the basic elements in a cross section of the vacuum chamber along the x - z -plane. (From [78])

(‘Pulse box’). The glass finger’s location shown in Fig. 3.1 is also the sample position for the *in situ* Ferromagnetic Resonance (FMR) measurements. A 4 pocket e-beam evaporator is mounted at the bottom side of the chamber. Flux electrodes measure the ion flux during evaporating and feed back the signal into the power supply of the evaporator. A PID controller uses this signal to stabilize the ion flux (\propto evaporation rate). Figure 3.2 shows the aperture which is fixed to a water-cooled quartz micro balance. It is 20 mm wide and 80 mm long to prevent the sample holder from being contaminated by the evaporating material. Through the apertures a film of square ($4 \times 4 \text{ mm}^2$) or circular shape (4 mm diameter) can be deposited on the substrate. This experimental configuration permits *simultaneous* evaporation and thickness determination.

A substrate ($20 \text{ mm} \times 5 \text{ mm}$) is mounted on the front part of the sample holder whose detailed drawings and a photograph are shown in the appendix (see Figs. A.5, A.6, A.7, A.8). The length of the substrate offers the possibility to fix it with a screw ‘far’ away from the Fe

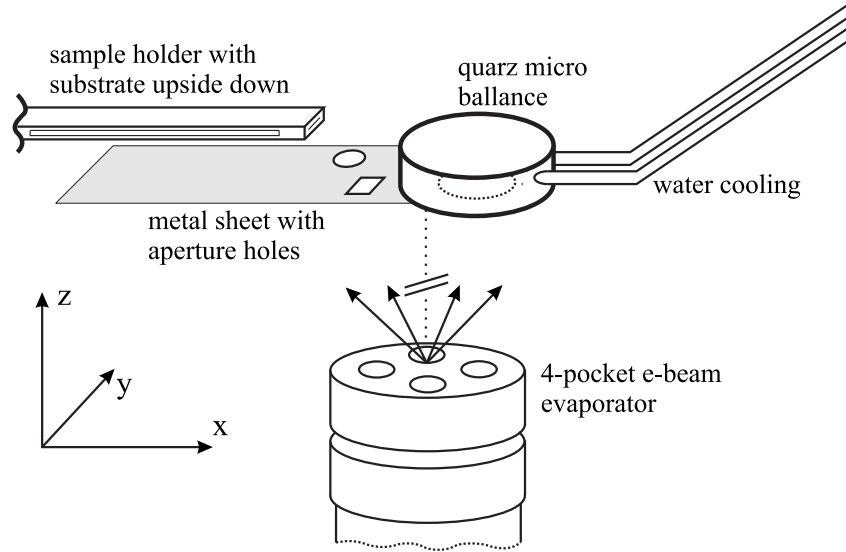


Fig. 3.2.: Experimental configuration during the deposition of thin films on a substrate. A metal sheet with well defined holes is attached to a quartz micro balance which can be retracted with a z-bellow. The evaporant is simultaneously deposited on the quartz crystal and on the substrate through the aperture.

film's position. This is advantageous because sometimes the Cu screw shows a ferromagnetic signal. Due to the lateral spacing the signal from the film and the undesired background signal can be distinguished. In addition, this method ensures good thermal contact of the substrate and the Cu sample holder. Another important issue is a good electrical contact since LEED and Auger measurements would otherwise charge the substrate and make investigations with electrons - especially at low energy - difficult.

3.2. Magneto-optical Kerr effect

Magneto-optical effects include the magneto-optical *Kerr* effect (MOKE) [79] in reflection geometry and the *Faraday* effect [80] in transmission. In principle they are based on the dependence of the optical constants on the direction of the magnetization. Besides, the much smaller *Voigt* effect [81] is quadratic in its magnetization components and is also called *linear birefringence* or *Cotton-Mouton* effect. On the other hand, the *Kerr* effect and the *Faraday* effect, which are both linear in the components of magnetization, are referred to as *circular magnetic birefringence*.

Three possible configurations for the MOKE are defined by the direction of the applied magnetic field \vec{B} . In polar geometry \vec{B} is applied in a direction normal to the film plane whereas in longitudinal (transverse) geometry \vec{B} lies in the film plane parallel (perpendicular) to the plane of incidence. It is helpful to consider the incident linearly polarized light as a superposition of a left and a right circularly polarized wave of equal phase and amplitude. The change of its

polarization state is considered to be a birefringence at the interface, i.e. both components have different absorption coefficients and phase shifts. In general, the reflected light is elliptically polarized where the Kerr rotation θ_K is the angle between the polarization plane of the incident light and the major axis a of the ellipse. The ellipticity is by definition $\epsilon_K = a/b$, where a and b are the major and minor (principal) axes of the ellipse. Consequently, both angles may be combined to form the complex Kerr angle:

$$\Phi_K = \theta_K + i\epsilon_K \quad (3.1)$$

At optical frequencies the influence of the magnetic field of the light on MO effects can generally be neglected [82]¹. Therefore, the response of a magnetized solid to the perturbation of an electromagnetic wave is described by the frequency-dependent conductivity tensor σ . For a cubic system with $\vec{M}||[0\ 0\ 1]$, symmetry considerations lead to [83]:

$$\sigma(\omega) = \begin{pmatrix} \tilde{\sigma}_{xx} & \tilde{\sigma}_{xy} & 0 \\ -\tilde{\sigma}_{xy} & \tilde{\sigma}_{xx} & 0 \\ 0 & 0 & \tilde{\sigma}_{zz} \end{pmatrix} \quad (3.2)$$

with complex elements $\tilde{\sigma}_{ij}$. The off-diagonal elements are caused by the symmetry breaking property of the magnetization. Generally, the $\tilde{\sigma}_{xy}$ are small in comparison to the diagonal element and depend linearly on the magnetization. Instead of using the optical conductivity tensor, the dielectric tensor ϵ can be applied, both of which are related by $\tilde{\epsilon}_{ij} = 1 + \frac{i}{\omega \epsilon_0} \tilde{\sigma}_{ij}$ (ω = frequency). In addition, the index of refraction can be used to describe the interaction by $\tilde{n}_{ij} = \sqrt{\tilde{\epsilon}_{ij}}$.

For thin magnetic films with a thickness d , the complex Kerr angle in polar configuration can be calculated if d is much smaller than the wavelength λ of the polarized light [84]:

$$\Phi_K = \frac{i\tilde{\sigma}_{xy}}{\tilde{\sigma}_{xx}^s} \frac{4\pi d}{\lambda} \quad (3.3)$$

The Kerr angle is proportional to the off-diagonal element of the conductivity tensor $\tilde{\sigma}_{xy}$ and to the film thickness d . It scales reciprocally with both the wavelength λ and $\tilde{\sigma}_{xx}^s$ which describes the optical properties of the substrate. Equation (3.3) is also valid for longitudinal MOKE when multiplied with a factor $f(\theta_{\text{incidence}})$ which depends on the angle of incidence $\theta_{\text{incidence}}$.

In an atomistic picture the magneto-optical Kerr effect is explained from the interplay of magnetic ordering and the spin-orbit interaction Δ_{SO} [85]. Generalized analytical formulae for the magneto-optical Kerr effects including thick and ultrathin magnetic films are elaborated in Refs. [86,87].

Fig. 3.3 illustrates the experimental setup for the longitudinal *in situ* magneto-optical Kerr effect measurement. A diode Laser emits light at a wavelength of $\lambda = 675$ nm with a power of 3

¹usually the relative magnetic permeability μ is set to unity, since the magnetic interactions of the light with the medium is about 2 orders of magnitude smaller than the electric ones.

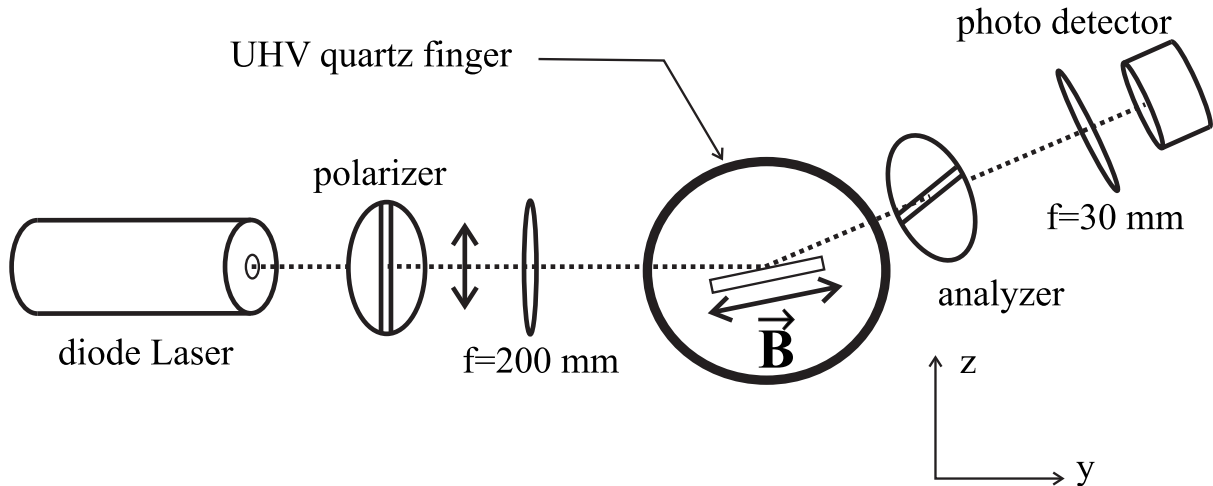


Fig. 3.3.: *in situ* setup of the longitudinal magneto-optic Kerr effect.

mW. The light passes a Glan-Thompson prism with an extinction ratio of 10^{-6} to obtain linearly polarized light. By rotating the polarizer (and the laser simultaneously), s-polarized light, i.e. the electric field vector \vec{E} of the laser light lies in the plane of incidence, or p-polarized light ($\vec{E} \perp$ plane of incidence) can be selected. A lens of focal distance $f = 200$ mm focuses the light beam through the glass finger at grazing incidence on the sample surface where it is reflected. Having prepared the sample under UHV conditions, it is then moved inside the glass finger along the x -direction. The analyzer (also a Glan-Thompson prism) is turned approximately 1° away from extinction such that a small intensity falls onto the photo detector. A change of sample magnetization gives rise to a Kerr rotation, which the photo detector reads as an intensity variation. The voltage output of the photo detector is recorded as a function of the magnetic field of the computer controlled electromagnet. A software is used to control favored measuring parameters like the magnetic field steps, the maximum magnetic field ($B_{max} = 60$ mT), the time at each measuring point and the number of loop averages. The maximum angle of incidence is given by the MOKE magnet (Appendix A.1) and is about 75° from the film normal.

3.3. Low energy electron diffraction

Low energy electron diffraction is used to determine the structure of thin films and surfaces. The vertical position of surface atoms can be measured by IV curves, i.e. the intensity variation of the diffraction spots as a function of primary kinetic energy of the electrons.

A beam of electrons of kinetic energy E incident on a sample surface is elastically scattered. The observed diffraction pattern is directly connected to the crystal reciprocal lattice by the scattering condition [30]:

$$\vec{k} - \vec{k}_0 = \vec{G}_{hkl}, \quad (3.4)$$

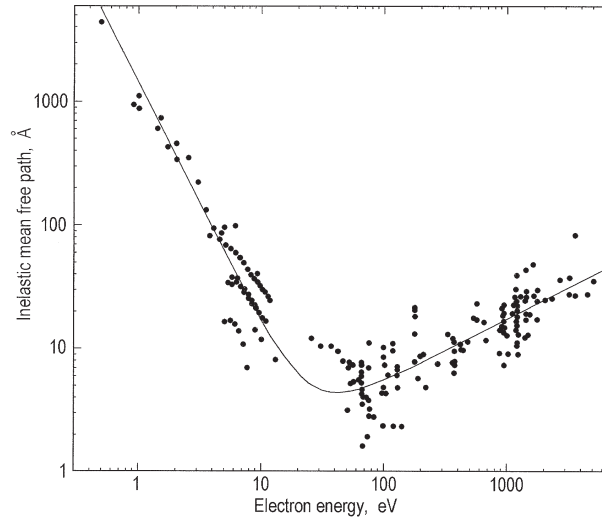


Fig. 3.4.: Experimental inelastic mean free path as a function of energy for different materials. The full line is a least square fit of all points in the graph. The graph has been taken from [88] (and references therein).

where \vec{k} is the scattered wave vector, \vec{k}_0 is the incident wave vector, and \vec{G}_{hkl} represents the reciprocal lattice vector. Here h, k, l are integers which do not necessarily have to coincide with the indices of real crystal planes.

As scattering occurs elastically one can write

$$|\vec{k}| = |\vec{k}_0| \quad (3.5)$$

which means energy as well as momentum is conserved. If diffraction is performed using electrons one has to consider their penetrating depth in a solid. In the case of low energy electrons, diffraction occurs in the range of a few atomic layers as can be seen from Fig. 3.4. A compilation of experimental data shows that the universal behavior of the mean free path, due to inelastic scattering of electrons, is independent of material type. Fig. 3.4 also demonstrates that low energy electrons have certain surface sensitivities. Thus, the diffraction pattern mainly originates from the 2D periodicity of the surface. In this case, Eq. (3.4) can be rewritten in the form:

$$\vec{k}_{\parallel} - \vec{k}_0^{\parallel} = \vec{G}_{hk} \quad (3.6)$$

This means, that the scattering wave vector ($\vec{k}_{\parallel} - \vec{k}_0^{\parallel}$) must coincide with the reciprocal lattice vector \vec{G}_{hk} (both lying in the film plane) in order to obtain LEED spots. Contrary to the parallel scattering wave vector, the one perpendicular to the surface does not conserve momentum. The lack of periodicity in the film normal direction can formally be written as an infinite periodicity length $c \rightarrow \infty$, which results in $c^* \rightarrow 0$. The reciprocal lattice points are arranged infinitely close along the normal direction forming *lattice rods* at the sites of the 2D reciprocal lattice points. This situation can be graphically visualized (Fig. 3.5 (a)). In addition to the shown

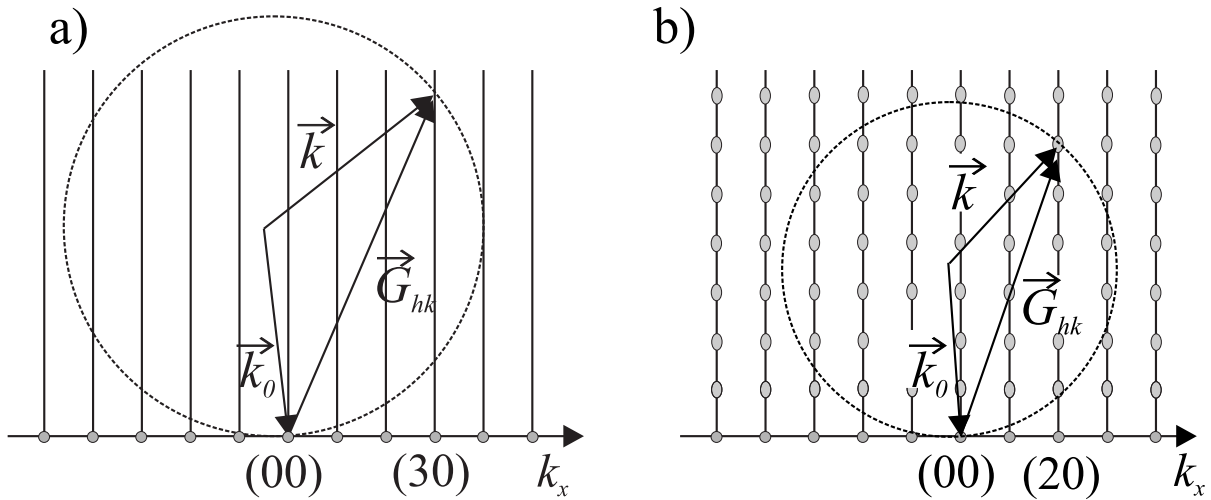


Fig. 3.5.: (a) Ewald construction for diffraction from a 2D surface lattice along the k_x -direction. (b) Ewald construction for diffraction from a 2D surface with lattice periodicity along z in addition.

lattice rods, there also exist rods along the k_y direction. By the simple Ewald construction the direction of the scattered wave vector can be determined (see Fig. 3.5). First the incident wave vector \vec{k}_0 is plotted into the reciprocal lattice in such a way that it terminates at a reciprocal lattice point. Then a sphere of radius $k = 2\pi/\lambda$ is drawn with the origin of \vec{k}_0 to be its center point. Now all intercepts of the sphere with the reciprocal lattice points correspond to scattered wave vectors which start from the center of the sphere. Along these directions of \vec{k} , diffraction spots at the LEED screen may appear as shown for the (0,3) reflex in Fig. 3.5 (a). A diffraction pattern will only originate from an area of the electron spot which is within the transfer width (corresponding to the coherence length) of the electron beam, i.e. typically 100 Å [89]. Although the penetration depth of the electrons in the solid is small, the electrons only slightly 'feel' the vertical periodicity. This gives rise to periodic swellings of the vertical lattice rods along the z -direction as indicated in Fig. 3.5 (b) and therefore, is a further constriction for possible diffraction spots. It explains the experimentally observed intensity variation of LEED spots in consequence of electron energy variation and is exploited to investigate the vertical interplanar spacing.

IV-LEED

Another way to write Eq. (3.4) is the Bragg equation $2d_{hkl} \sin \theta = n\lambda$ [30], where d_{hkl} is the interplanar spacing, θ the angle of incident of the wave, n the order of the Bragg reflexes and λ the wavelength of the incident wave. This situation is presented in Fig. 3.6. In a simple IV-LEED experiment, the intensity variation of the (0,0)-LEED spot is analyzed as a function of the primary electron energy. The sample alignment is $90^\circ - \theta \approx 3^\circ$ off normal incidence to reveal the (0,0) spot, which at normal LEED operation is covered by the electron gun of the

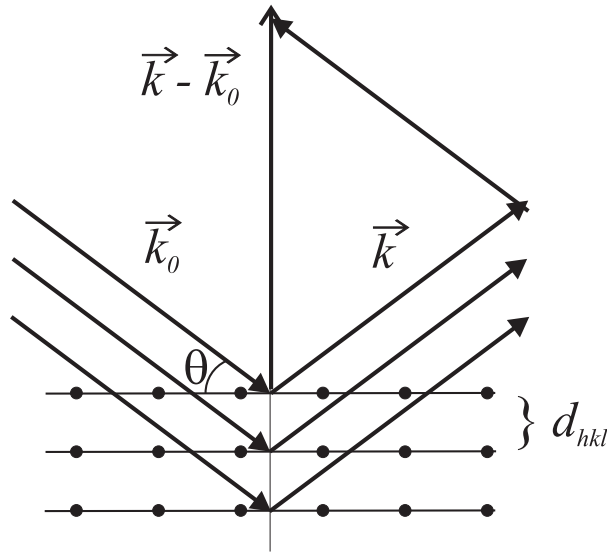


Fig. 3.6.: Bragg reflection: An incident wave, with wave number \vec{k}_0 , is reflected along the atomic planes of a single crystal, which has an interplanar lattice spacing d_{hkl} with a scattering wave vector \vec{k} .

LEED. In a simplified approach the intensity of the diffracted (0,0) spot is brightest when the Bragg condition is fulfilled. Thus one gets:

$$E = \frac{h^2}{8d^2m_e e \sin^2(\theta)} \cdot n^2 + V \quad (3.7)$$

where h is Planck's constant, $d = d_{001}$ is the vertical interplanar distance along the z -direction, θ is the angle of incidence (as indicated in Fig. 3.6), m_e is the electron's mass, e is the electron's charge, n is the order of the Bragg peak and V reflects the inner potential of the sample. In the experiment the peak energy is plotted over n^2 . The slope of the linear fit can then be used to calculate the vertical interplanar spacing using Eq. (3.7) [90]. The lowest order Bragg peak to be evaluated is $E = 140\text{eV}$ ($n=3$) since for high energy electrons the influence of the inner potential V is negligible. Their band structure approaches the one of free electrons. The IV-spectra can also be calculated using full dynamic computer codes [89] to include, e.g., temperature effects on the shape of the curves in order to evaluate interplanar spacings between individual surface layers or even individual atom positions. However, the above presented method, only gives an averaged vertical interplanar distance of the surface layers from the energy positions of the Bragg peaks. The accuracy of the measurements is about 1-2 %.

3.4. Auger electron spectroscopy

Auger electron spectroscopy (AES) is a surface specific spectroscopic technique which reveals information about the chemical composition of e.g. thin films. For a review, the reader should refer to Ref. [91]. By an arbitrary excitation process, (Fig. 3.7 (a),(b)) a core-level atomic ion-

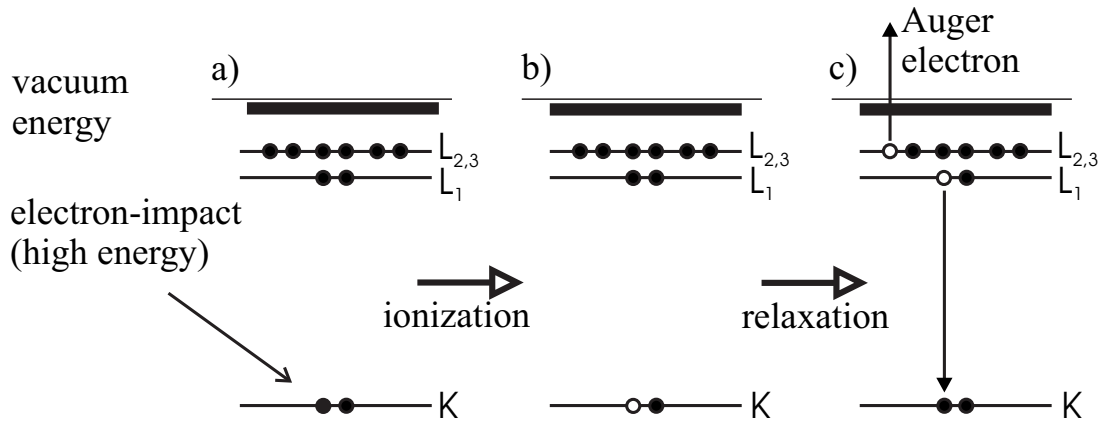


Fig. 3.7.: (a) A high energy electron impacts on an atom and (b) ionizes a core level. (c) An outer level electron fills the hole and the excess energy is transferred to another outer-shell electron, which then leaves the atom.

ization occurs, which is followed by a de-excitation of an outer electron to fill the core hole. The energy difference either generates an X-ray photon (X-ray fluorescence) or is transferred to another outer-level electron (Auger electron) which leaves the specimen at a defined kinetic energy (Fig. 3.7 (c)). This energy can be calculated by the differences in binding energies of the three energy levels whereupon a correction term for the work function and electron wave function relaxation has to be taken into consideration. Due to the involved energy levels one denotes the Auger process by e.g. KL_1L_{III} . There is experimental proof from a variety of experiments that the mean free path of electrons with kinetic energies ranging from 0 to 3000 eV lies within the range of 5 to 30 Å (as already shown in Fig. 3.4). The escape probability of Auger electrons decays exponentially with overlayer thickness and explains the high surface sensitivity of AES.

To excite electron core states one employs a primary electron beam energy of 3 keV which is substantially larger than the binding energy of the states involved. Consequently, not only does the primary energy give rise to excitation processes, but also backscattered primary electrons can contribute to the generation of Auger electrons. One obtains a maximum of the Auger electron yield if the excitation energy is 3 to 5 times larger than the core energy levels.

To analyze the energies of the Auger electrons, one employs a cylindrical mirror analyzer (CMA) with coaxial electron gun, whose mode of operation is explained e.g. in Ref. [92]. The electron beam is focused to a small point ($d \approx 1$ mm) and hits the sample at perpendicular incidence. Ejected electrons from the excited surface enter the analyzer through an aperture. By applying a suitable voltage between the inner and outer cylinder of the CMA, electrons of proper energy are deflected in such a way that they can pass through a set of apertures to finally hit an electron multiplier. The amplified signal is fed in a computer and is recorded as a function of pass Energy E .

Inelastically scattered electrons dominate the secondary electron energy distribution $N(E)$.

The Auger peaks only contribute by a factor of 10^{-4} to 10^{-3} . Therefore, it is common practice to evaluate the derivative signal dN/dE which can clearly identify the Auger peaks. The peak to peak signal strength is used as a relative measure of the investigated element concentration. To identify the Auger transition energies one employs the negative peak value in the derivative spectrum. As three energy levels are involved in the Auger process, lithium is the first element in the periodic table of the elements that can be detected. For higher atomic numbers of the elements the probability of the Auger process decreases and it is more likely to observe the de-excitation of electron core levels via photo emission.

3.5. rf SQUID magnetometry under ultrahigh vacuum conditions

The Superconducting QUantum Interference Device (SQUID) is known to be the most receptive tool for probing magnetic fields. In comparison to the earth's magnetic field which is in the order of $50 \mu\text{T}$ (in middle Europe) [93], its sensitivity is a factor of more than 5×10^5 higher. The SQUID used in this work consists of an Yttrium-Barium-Cuprate-compound ($\text{YBCO} \equiv \text{YBa}_2\text{Cu}_3\text{O}_{7-x}$) on a SrTiO_3 substrate. YBCO is a so-called high T_C superconductor, which becomes superconducting above ℓN_2 temperature. A high T_C SQUID is much easier to handle in contrast to a low T_C SQUID, which needs ℓHe for cooling.

A SQUID exploits two physical principles: (i) quantization of magnetic flux in superconducting rings, and (ii) the Josephson-effect. (i) When a magnetic field is applied to a superconducting loop, a superconducting shielding current is generated inside the loop. These currents can be described by a macroscopic wave function, whose stationary states obey quantized boundary conditions. Consequently the generated current in the ring will have discrete values. The Bohr-Sommerfeld quantization condition has the form:

$$\oint \vec{p}_c \cdot d\vec{s} = nh, \quad (3.8)$$

where n is an integer. The momentum p_c of a cooper-pair is an integer multiple of h (Planck's constant). Taking the canonical momentum with a vector potential A (magnetic field) one obtains:

$$\Phi = \frac{nh}{q} = n\Phi_0, \quad \Phi_0 = \frac{h}{2e} \quad (3.9)$$

Φ_0 is a flux quantum or fluxoid and has a value of $\Phi_0 = 2.07 \cdot 10^{-15} \text{Vs}$ and is the elementary flux. As the supercurrent is carried by cooper pairs one writes $q = 2e$ for the charge. When a transition in the superconducting ring between two states occurs, which differs by a single flux quantum, the wavefunction changes its phase by 2π .

(ii) A Josephson junction is a thin insulating barrier which separates two superconductors. The electrical properties of this junction are described by the two Josephson equations [94].

Since the junction is normal conducting, only a tunneling current of cooper pairs is able to flow through it. The superconducting order parameter is given by $\Psi = \Psi_0 e^{i\Theta_i}$, where Θ_i are the phases of the wave functions on each side of the junction. Consequently, the current through the junction is governed by the phase difference $\delta = \Theta_1 - \Theta_2$ of the superconductors resulting in a current

$$I = I_{max} \sin \delta \quad (3.10)$$

where I_{max} is the maximum current. This equation is the dc (direct current) Josephson equation, which describes a stationary state as δ is time independent. The situation changes if a voltage U is applied across the Josephson junction which gives the second Josephson equation:

$$U = \frac{\hbar}{2e} \left(\frac{d\delta}{dt} \right) \quad (3.11)$$

Consequently, this causes a high frequency ac (alternating current) with frequency $\nu = 2eU/h$.

Figure 3.8 shows a dc SQUID which contains two Josephson contacts. If the SQUID is exposed to a changing magnetic field the maximum supercurrent oscillates with a periodicity of Φ_0 . However, a dc SQUID requires two Josephson junctions which need to be nearly identical. This problem of fabrication is overcome by using an rf SQUID which works with a single Josephson junction.

rf SQUID operation

The basics of an rf superconducting quantum devices have been described by several authors [95,96,97]. Here a brief and simplified overview about the underlying principles is presented. Figure 3.9 shows an rf-SQUID with a single weak link, which is driven by a tank circuit

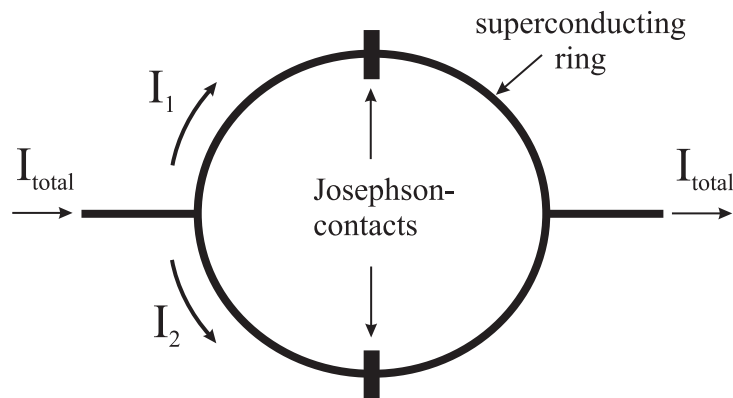


Fig. 3.8.: A dc (direct current) SQUID consists of a closed loop with two Josephson junctions (Josephson contacts). A current I_{total} splits in I_1 and I_2 . Without magnetic field applied, both currents oscillate in phase. If a magnetic field smaller than the critical field is switched on, a phase shift occurs between the two currents. Then the current I_{total} exhibits interferences. The phase difference is proportional to the external magnetic field.

3. Experimental methods

consisting of a capacitor C_T and a loop with induction L_T , operating at frequencies ranging from 100 MHz to 1 GHz. The tank circuit is inductively coupled to the SQUID loop and can be used to couple alternating and constant magnetic fields into the SQUID ring. A direct voltage V across the tank circuit can be used to determine changes in the penetrating flux through the SQUID loop. The flux is obtained by demodulating the ac voltage V_{rf} from the excitation current I_{rf} of the tank circuit.

Firstly, the flux quantization inside the SQUID loop has to be considered. If an external flux does not satisfy the quantization constraint, the missing flux is instantaneously compensated by a supercurrent I_s , which has to run through the weak link. An ac current I_{rf} will drive the tank circuit at its resonant frequency ω_0 . Consequently, an alternating flux $\Phi_{rf} \propto \sin(\omega_0 t)$ is generated inside the SQUID which superimposes the external flux. This flux depends on the quality factor of the tank circuit, a coupling constant k and the inductances L_T of the tank circuit, and the SQUID loop respectively. k reflects the SQUID geometry and position with respect to the inductance of the tank circuit.

Now one can visualize the process of measuring with the SQUID. The weak link of the SQUID is designed such that it can approximately compensate a single flux quantum Φ_0 before the supercurrent I_s will exceed the critical value I_c of the Josephson junction. If one assumes an external magnetic field, which causes a flux $\Phi_{ext} = n\Phi_0$ in the SQUID, then an integer number n of flux quanta are kept inside. In this case, no supercurrents are needed to correct the deficiency of the total flux through the ring in order to satisfy the quantization constraint. If the tank circuit is driven with a small amplitude I_{rf} , the SQUID will shield this additional flux by a supercurrent I_s . As long as the supercurrent does not overcome I_c an increase of the pumping current I_{rf} , linearly raises the voltage V of the tank circuit. Once the critical flux Φ_c , which is

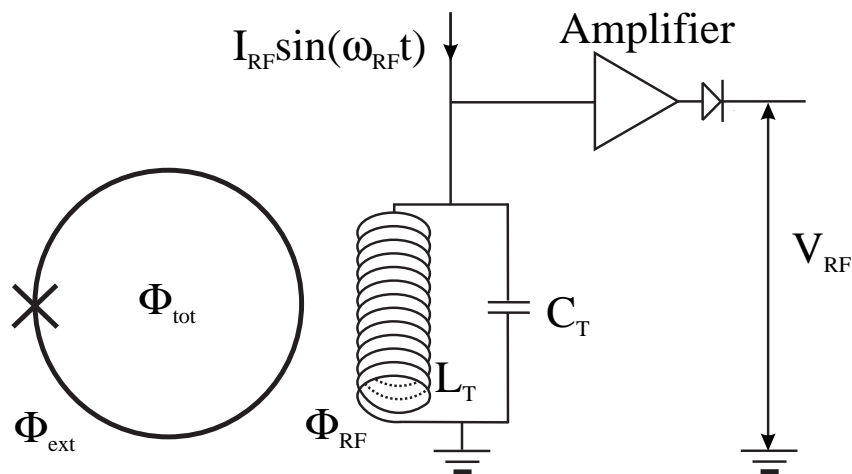


Fig. 3.9.: A SQUID loop contains a single weak link, which is inductively coupled to an inductance L_T . It is powered by a driving current I_{rf} , which produces an ac flux in the SQUID. The voltage V_{rf} detects external magnetic flux changes through the SQUID loop.

connected to the critical supercurrent I_s is established, the tank circuit voltage V approaches a limit. At this threshold, the weak link of the SQUID becomes locally normal conducting and dissipates energy. A flux quantum leap occurs and the state of the SQUID changes from n to $(n + 1)$ or $(n - 1)$, which allows a flux quantum to penetrate through the weak link inside the SQUID or escape it. The dissipated energy, which is about $\Delta E = I_c \times \Phi_0$ [98], is withdrawn from the tank circuit. If ΔE approximates the stored energy of the tank circuit, it means that it is significantly damped and its amplitude is immediately reduced. The external oscillator needs several periods to recover the tank circuit's amplitude to the critical voltage V_c before the dissipating process takes place again. The sharp threshold of this process, effectively limits V . Further increase of the pumping current I_{rf} recovers the amplitude of the resonant circuit faster and consequently, the dissipating processes occur in shorter time periods. For a wide range of I_{rf} the voltage V does not increase, forming the plateau B, C in Fig. 3.10. If I_{rf} grows such that every high frequency period causes a flux quantum jump, the voltage V will rise linearly with I_{rf} once more. If I_{rf} is high enough, even a second flux quantum leap takes place, which leads to another plateau similar to the previous case. In the section above the influence of an external flux $\Phi_{ext} = n\Phi_0$ was discussed, which is an extreme case since no supercurrent at all flows while there is an absence of flux deficiency (not regarding the rf-flux). The other extreme case is found when $\Phi_{ext} = (n + 1/2)\Phi_0$. Here, a superconducting shielding current already exists to satisfy the flux quantization condition. As a consequence the critical current I_c is reached earlier when the pumping current I_{rf} is increased. In this case, the voltage V of the tank circuit as a function of the pumping current I_{rf} is plotted as a dashed line in Fig. 3.10. Note that it will never be necessary to compensate more than $1/2\Phi_0$ to fulfill the quantization condition. Having discussed the two extreme cases, it is worth mentioning that any external flux apart from those cases causes a shielding current and therefore, a tank circuit voltage between the discussed values.

A real rf-SQUID system operates with a fixed pumping current I_{rf} , which is advisably adjusted slightly above I_B (in practice this means to adjust the operating point). The measured voltage amplitude V can vary between V^n and $V^{(n+1/2)}$. The voltage value only depends on the external flux Φ_{ext} . Fig. 3.10 (b) displays the corresponding flux-voltage transfer function. It also describes the direct sensor characteristics of a SQUID and has a periodicity of exactly Φ_0 .

With the described setup, magnetic field changes up to $1/2\Phi_0$ maximum can be measured. Greater field values lead to ambiguous signals due to the periodicity of the flux-voltage transfer function. For an effective loop area of 0.2 mm^2 , $1/2\Phi_0$ corresponds to a magnetic field range of about 5 nT, which is much too narrow to be applied. To overcome this limitation an electrical loop instantly compensates for a change in the external magnetic field. In this configuration the SQUID will be a null field detector. This mode of operation is called 'flux locked mode' since the total flux inside the SQUID does not change. The 'flux-locked-mode' easily increases

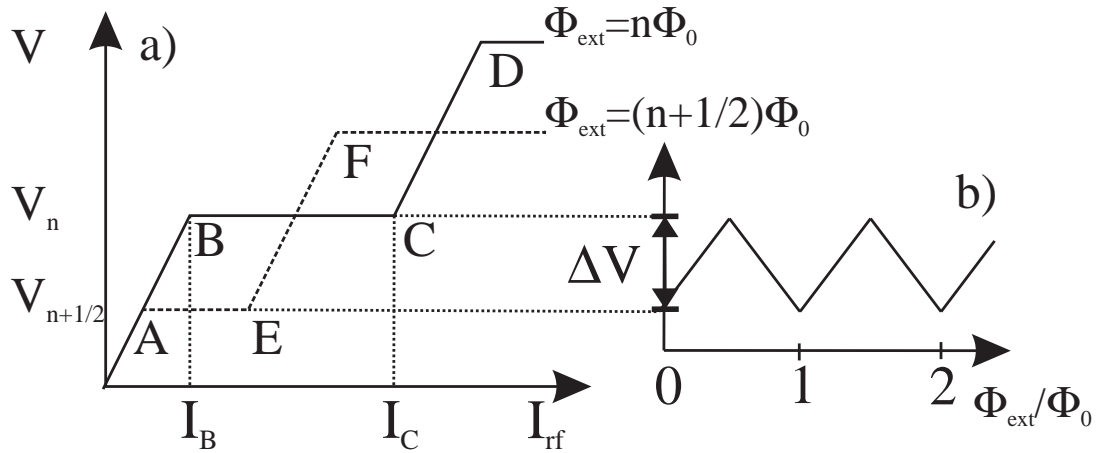


Fig. 3.10.: (a) Dependence of the voltage V across the resonant circuit as a function of pumping current I_{rf} for the two extremal quantum states. (b) flux-voltage transfer function of an rf-SQUID.

the measuring range of the SQUID by orders of magnitude without significantly reducing its resolution.

3.6. Technical improvements of the SQUID setup

During this thesis the setup of the SQUID (originating from a former PhD thesis [78]) has been modified considerably. On the one hand, the stability of the SQUID operation has been increased such that it can be operated in the flux locked mode for up to several hours without the need for a reset. On the other hand, the hole in the μ -metal shielding has been enlarged for sophisticated stray field analysis without affecting the magnetic shielding ability. Furthermore, the software for recording the stray field data, now has the capability to average a number of single scans, which is helpful for low level magnetic signals, and automatically displaces the averaged curve to the 'zero' line. This latter feature enables the user to quickly analyze stray field data.

Electrical shielding and μ -metal screening

The electrical signal from the rf tank circuit (frequency of about 800 MHz) is conducted through a coaxial cable to the electrical SQUID controller unit (JSQUID HTSL-RF-SQUID-Elektronik, model 1000, vers. 2.0), which resides right above the support-stick in which the SQUID chip is located. However, it is very sensitive to hf (high frequency) electromagnetic environmental noise and pulsed electromagnetic fields, which can be generated by e.g. cellular phones, WLAN access points, CPUs of laboratory PCs, or even passing trams. We found that the best possibility to shield the signal cable is to put it in a Faraday-like cage which is *properly* grounded. Fig. 3.11 presents a photograph of the current setup. A stainless steel cylinder can be attached to

the bottom aluminum plate where the SQUID electronics is mounted with two M3 screws. The shielding can be lowered to refill the dewar with liquid nitrogen, as illustrated in Fig. 3.11. A hole in the aluminum plate is used to put through the signal cable which also needs to be shielded above this plate. This is achieved by putting an aluminum cover box over the cable and connector of the SQUID electronics (not shown in the image). The SQUID electronics itself is completely covered by a full aluminum housing which has same ground potential as is the stainless steel cylinder. Fortunately, the position of the SQUID sensor is inside the stainless steel UHV chamber which minimizes disturbing electrical field influence directly acting on the SQUID and tank circuit.

A critical issue to the SQUID operation is the influence of ac magnetic fields arising from power consuming devices with typical 50 Hz characteristics. Here the SQUID itself is solely influenced by the magnetic part of the electromagnetic noise. These effects will be attenuated by employing a μ -metal shield whose inner space is free of magnetic fields to some extent. Static magnetic fields that originate from ferromagnets, like in the ion getter pump of the UHV system, do not affect the SQUID operation. The μ -metal screening used in this thesis consists of two cylinders with diameters of $d_1 = 41.5$ mm and $d_2 = 61.5$ mm and a wall thickness of 0.7 mm. A scanning SQUID requires a relative motion of the sensor with respect to the sample. This relative movement is found by moving the sample underneath the SQUID resting in the dewar.



Fig. 3.11.: SQUID electronics and the electrical shielding, which has been lowered for the photograph.

3. Experimental methods

The sample holder enters the μ -metal shield through rectangular holes in both cylinders, which have been further countersunk in this study. Previously, its size was 4 mm in height and 7 mm wide. In comparison to the cross section of the sample holder (3 mm \times 6.5 mm, see Appendix A.6) variations were not possible. This encouraged us to scale up the hole dimension to 5.5 mm \times 13.5 mm. We tried to leave some distance between the shield and the sample holder during the measurements because thermal effects may alter the relative distance, which could end up in crashing the sample holder into the μ -metal shielding. To ensure that the sample holder does not touch the magnetic shield, an ohmmeter (with acoustic alarm at an emerging short-circuit) measures the resistance between the μ -metal, which is on ground potential, and the sample holder, which is electrically isolated from ground. Height variations of the sample holder of 2 mm are easily achievable (by lifting up the SQUID, the distance can be increased arbitrarily), as well as a 6 mm variation in the y -direction. Figure 3.12 shows how a discontinuous variation of the y -position is used to monitor the B_z distribution in a plane of distance $h = 5.6$ mm with respect to the sample surface of a 3×3 mm² 20 ML Fe film. Prior to the experiment, the film had been magnetically saturated in a magnetic field along the x -direction, which is one of the film's easy magnetic axes. The curve with the greatest maximum is located at $y = 28.3$ mm. The variation ability in the y -direction gives one the opportunity to find the in-plane equilibrium

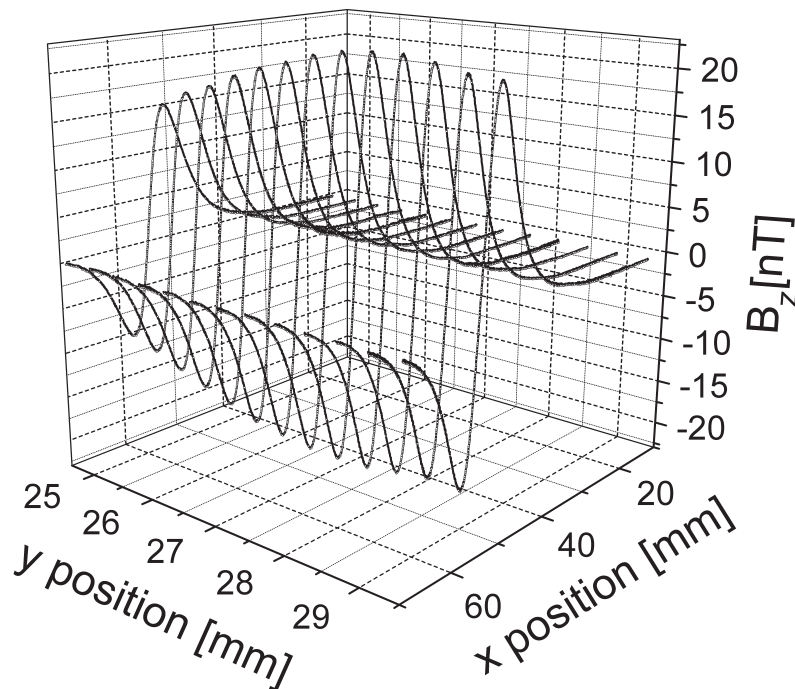


Fig. 3.12.: Measured B_z scans above a 20 ML Fe film of 3×3 mm² size with the magnetization lying parallel to the scanning direction x in the plane of the film at a height $h = 5.6$ mm. Lines were continuously recorded in x -direction whereas the y -position is varied in steps of 0.4 mm, covering a range of $\Delta y = 5.2$ mm.

angle of the magnetization with respect to the scanning direction x (see Sec. 4.1.4) and allows one to minimize errors when fitting the magnetization (see Sec. 4.1.8).

Software improvements

Besides the hardware improvements of the last section, the data acquisition software was also modified. Basically, two features were added, which help to simplify the routine work. First, to reduce the noise in the $B_z(x)$ -scans, an optional number of single scans can be averaged by a few mouse clicks and data is recorded in both scanning directions (x -direction and $-x$ -direction). A series of scans is then graphically displayed, and by activating the respective tabs, the desired graphs can be included in an average procedure. This is necessary as there is a temporal drift in the SQUID output voltage due to the SQUID electronics. This results in a tilted curve with a slight negative slope as scanning is performed in $+x$ -direction and the same slope with opposite sign is obtained in $-x$ -direction. By averaging an equal number of $+x$ and $-x$ -scans, the individual slopes of the data curves are compensated. Secondly, the software offers the chance to displace the $B_z(x)$ line scans along the B_z axis. One should reconsider that the SQUID electronics measures absolute *changes* of the magnetic flux through the ring and cannot give the magnetic field with respect to an absolute zero field. One defines the zero field far away from the sample where the stray field has decayed to a non-measurable value. Now one can choose a range of the x -axis (presumably when the sample is outside the μ -metal screening) of the B_z scans where all data points are averaged and subsequently the averaged value is subtracted from all data points. Thus, one shifts the signal along the B_z -axis in order to define a 'zero line'.

3.7. Calibration of the SQUID

The output voltage of the SQUID electronics varies linearly with the magnetic flux within the SQUID loop. The proportionality constant depends on the area of the SQUID loop and the intrinsic gain factors of the SQUID electronics. Furthermore, the sensitivity of the SQUID, i.e. the voltage to flux transfer coefficient, can be set manually to get either a low sensitivity and consequently bigger field range, or high sensitivity for better field resolution. We choose the latter setting since we are interested in detecting small stray field signals with sub-nT resolution. The calibration procedure is carried out with the SQUID operating in the μ -metal shielding inside the UHV chamber. A single turn Cu wire around the SQUID support stick, such that the loop axis coincides with the SQUID, generates a well defined magnetic field at the SQUID's position. The schematic experimental situation is shown in Fig. 3.13 (b). Additionally, one can connect a low pass (RC) filter between the leads and the high precision current source (*D. C. Current Calibrator (Type 609), Time Electronics Limited*) to eliminate high frequency

3. Experimental methods

noise. The use of the RC filter turns out to be necessary, as the input leads outside the μ -metal and electrical shield act as an antenna. This reduces electric oscillations (noise), which are conducted to the calibration loop, and in turn generate time varying magnetic fields at the SQUID, which makes stable SQUID operation impossible. We choose a cut-of frequency of the RC filter of about 15 Hz to eliminate the predominating 50 Hz environmental perturbation. The feed wires are tightly twisted to eliminate stray fields from the leads when a current flows. Then the axial magnetic field (in z -direction) of a single turn loop is expressed by

$$B_z = \mu_0 \frac{I}{2R} \quad (3.12)$$

with I the current and R the radius of the loop. One uses a high precision current source for currents up to 1.4 mA which are converted in magnetic fields employing Eq. (3.12). Fig. 3.13 (a) presents the result of the calibration. The slope of the linear fit defines the calibration factor (15.289 nT/V). After the calibration, slight shifts of the calibration loop along the axial direction result in only smaller SQUID output signals for a given current. Hence, one can concluded whether the calibration loop is at an ideal position during the calibration procedure. The maximum error of the SQUID calibration is estimated to be around 1%. The noise of the SQUID limits its sensitivity, which is below 0.2 nT. Sec. 4.1.3 discusses the sensitivity with respect to the smallest detectable amount of material.

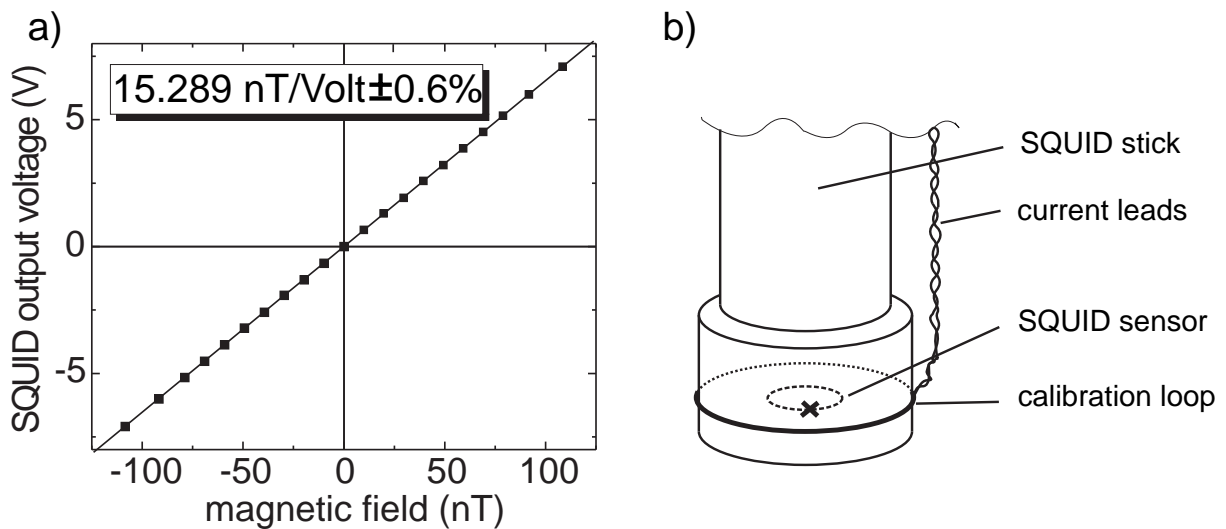


Fig. 3.13.: (a) Experimental determination of the calibration factor of the SQUID which converts the SQUID output voltage to a magnetic field. (b) Schematics of the calibration loop arrangement.

3.8. SQUID-magnetometry and Ferromagnetic resonance

Ferromagnetic resonance (FMR) is a powerful technique to study the magnetic properties of ultrathin magnetic films [71]. Its high sensitivity and energy resolution allows one to measure a set of magnetic parameters in the ferromagnetic ground state (wave vector $k \approx 0$), such as magnetic anisotropy, magneto-elastic coupling effects (see e. g. [99]) and relaxation mechanisms of the magnetization. Moreover, in superlattices one can obtain the interlayer exchange coupling strength [100,101]. It is also possible to determine the spectroscopic splitting factor (g-factor), which comprises information on the orbital contribution to the magnetic moment. However, an absolute measurement of the total magnetic moment is not possible.

In an FMR experiment, one places a ferromagnetic sample in a microwave resonant cavity, in which forms a standing wave with a magnetic part \vec{h}_{mw} perpendicular to the external field \vec{H}_0 . The magnetization of the sample precesses around the effective magnetic field \vec{H}_{eff} , which not only comprises the externally applied field \vec{H}_0 but also the microwave \vec{h}_{mw} and other internal fields \vec{H}_{int} inside the sample that account for anisotropies and the strong interaction of individual spins in a ferromagnet: $\vec{H}_{eff} = \vec{H}_0 + \vec{h}_{mw} + \vec{H}_{int}$.

The frequency of this precession is the Larmor frequency:

$$\omega_L = \gamma H_{eff} \quad (3.13)$$

with the gyromagnetic ratio $\gamma = g\mu_B/\hbar$. At $\omega = \omega_L$ energy is absorbed by the spin system and one can measure a detuning of the system by the change of microwave power reflected by the cavity. It should be noted that in most experimental setups, the microwave frequency ω is held constant and the external field \vec{H}_0 is varied.

The equation of motion of the magnetization vector \vec{M} in a magnetic field is given by the Landau-Lifshitz equation:

$$\frac{d\vec{M}}{dt} = -\gamma \left(\vec{M} \times \vec{H}_{eff} \right) \quad (3.14)$$

This equation describes the precession of the magnetization around the direction of \vec{H}_{eff} caused by the torque $\vec{M} \times \vec{H}_{eff}$.

Joint research done by SMIT and BELJERS, as well an independent study by SUHL [102, 103] derive the resonance condition for a ferromagnet with free energy density F :

$$\frac{\omega}{\gamma} = \frac{1}{M_s \sin(\theta^0)} \sqrt{(F_{\theta\theta} F_{\phi\phi} - F_{\theta\phi}^2)} \quad (3.15)$$

θ and ϕ denote the the polar and azimuthal angles of the used coordinate system and $F_{\theta\theta}$, for instance, is the second derivative with respect to θ .

For the samples examined here, the main contributions to the free energy density (in terms of magnetic properties) are the magnetocrystalline anisotropy F_{MCA} , the dipolar interactions

3. Experimental methods

(giving rise to shape anisotropy) F_{shape} and the Zeeman energy: $F = F_{MCA} + F_{shape} + F_{Zeeman}$. Please note that in comparison to Eq. (2.1) $F_{anisotropy}$ is now split into two terms. One term refers to its magnetocrystalline origin (F_{MCA}), and the other refers to its long range dipolar interaction (F_{shape}).

The values of the anisotropic terms F_{MCA} and F_{shape} are given by the anisotropy constants K_i [104]. One can calculate K_i from the anisotropy fields $H_{ani} = K_i/M_s$, which can be obtained from angular dependent FMR. The anisotropy constants K_i can only be given in absolute values if one knows the saturation magnetization of the sample. As a consequence, authors often assume M_s from bulk values. Especially in the ultrathin film regime, the magnetization can be different from bulk values, or change in a non-predictable manner, e.g. as a function of temperature or oxygen exposure, respectively. Thus, the measurement of the absolute magnetization is of extreme value to get a description of the system *in extenso*. In conclusion, the combination of (*in situ*) FMR and SQUID magnetometry is unique to study the magnetic properties of thin magnetic films under ultra high vacuum conditions.

4. Results and discussion

4.1. Quantitative magnetometry: analytical methods and limitations

The analysis of the sample magnetization requires the following: a) The film must be in a magnetic single domain state. b) The SQUID must be scanned above the *center* of the sample ($y = 0$). c) The film thickness d must be known. d) The lateral dimensions (shape) of the films must be known. e) The sample to SQUID distance h must be known.

Since the latter point is not given *a priori*, the following two sections deal with two independent methods for the determination of h . This is the most crucial quantity in fitting the experimental stray fields in order to determine M . The first method is discussed in detail for in-plane magnetized samples; and it makes use of the intrinsic property of the stray field to change the peak positions and also their shape when the height h is varied. The second method uses the stray field of a current loop to determine the sample to SQUID distance. A further method presented below deals with the finding of the in-plane magnetization angle with respect to the scanning direction of the sample. Shown below is the necessity of this feature in order to find the correct values of sample magnetization. It is not merely an additional piece of information the scanning SQUID can provide.

Also discussed is the possibility of magnetic domain formation in magnetic remanence and the magnitude of its influence on the magnetic stray field. Sec. 4.1.6 discusses how the sizeable surface roughness of Fe films on GaAs influences the magnetization determination. Finally, Sec. 4.1.8 summarizes all the limiting factors for quantitative SQUID magnetometry in UHV.

4.1.1. SQUID-sample distance from stray field data

Figure 4.1 shows the z -component of the magnetic stray field of a 40 ML Fe film which was saturated in the film plane in a pulsed magnetic field along the x -direction before the experiment. The line scans were measured above the film center along the magnetization direction in x for various heights h . The curve with the biggest amplitude was measured at a height $h = 4.8$ mm. This height was obtained from fitting the stray field data as described in the following. We denote the distance between the minimum and the maximum peak positions of the scan trace with

p. When the distance changes, two things become evident. An increase of distance h (i) reduces the stray field amplitude and (ii) shifts the peak positions farther apart. Note that the line scans of Fig. 4.1 are slightly asymmetric. For this measurement that can be explained by a slightly tilted sample surface with respect to the scanning direction. If one tries to fit the analytic expression for the magnetic stray field to experimental data, one can basically change two parameters to find good accordance, i.e. the magnetization M and the distance h between sample and SQUID. The stray field is proportional to the sample magnetization $B_z \propto M$. Therefore, changing M will only change the amplitude of the B_z fit. On the other hand, changing the height h will have two effects that were already illustrated in Fig. 4.1. The magnetization M can always be chosen such that the stray field amplitude matches the experimental data. But only if the height h is chosen correctly will the shape of the calculated stray field fit the experiment. Figure 4.2 shows calculated B_z line scans normalized to the peak values of a $3 \times 3 \text{ mm}^2$ film with magnetization in the film plane along x (a) and out of the film plane along z (b). The insets present the same graphs without normalization for a 10 ML Fe film with the bulk magnetization value. The normalization takes into account that M is adjusted to match the stray field peaks and only the effect of h on the stray field shape can be examined. The greater the sample to SQUID distance, the broader the curves are in the in-plane case as well as in the out-of-plane case. Following this approach, the sample-SQUID distance can be obtained for sufficiently smooth curves with an accuracy of 0.1 mm. A systematic and quantitative study of the evolution of the stray field shape as a function of h is shown in Fig. 4.3. For an in-plane magnetized film along x of 3×3

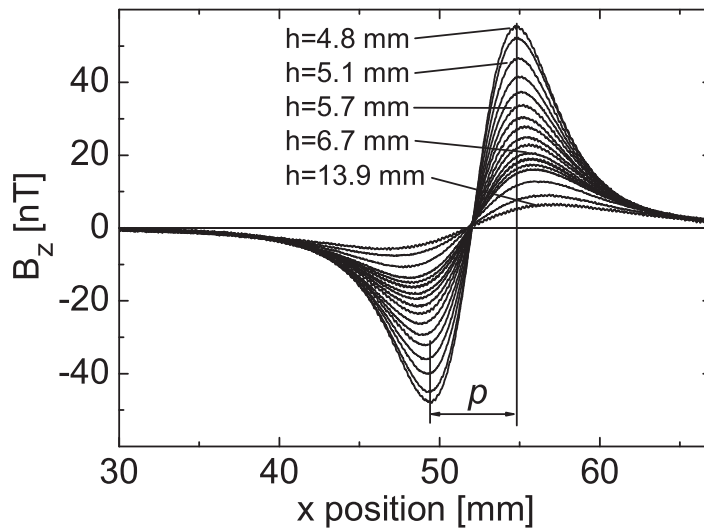


Fig. 4.1.: $B_z(x)$ of a 40 ML Fe film magnetized along x across the film's center for various SQUID-sample distances h .

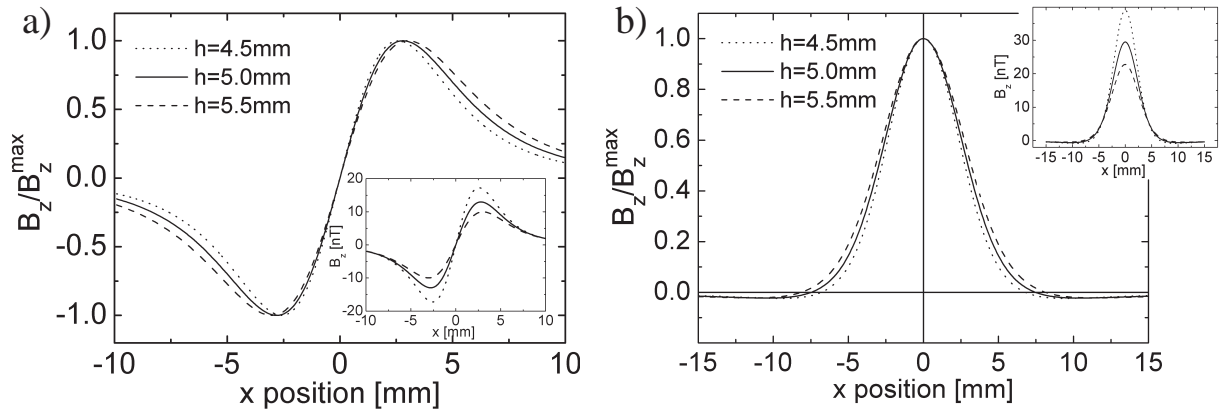


Fig. 4.2.: (a) normalized $B_z(x)$ above the center ($y = 0$) of a square film ($3 \times 3 \text{ mm}^2$) with in-plane magnetization along x at three given distances. The insets shows B_z of the three curves without normalization for a 10 ML Fe film with bulk magnetization. (b) as in the left figure for an out-of-plane magnetized film along z .

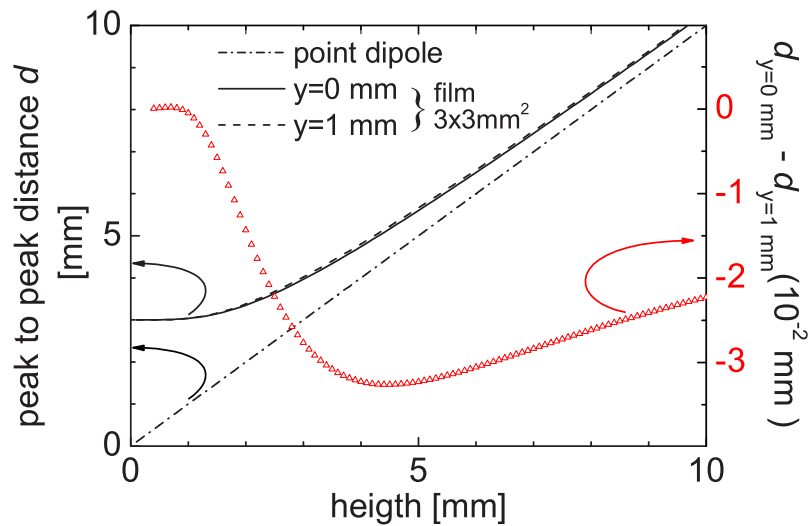


Fig. 4.3.: Peak to peak distance p of $B_z(x)$ line scans as a function of height h for a $3 \times 3 \text{ mm}^2$ film with magnetization lying along the x -direction.

mm² size, the peak to peak distance p was calculated as a function of height $z = h$ by finding $dB_z(x, y, z = h)/dx = 0$ of the analytic stray field numerically. The solid (dashed) line represents the result for a line scan across the sample center $y = 0$ (1 mm displaced in y). In the limit as $h \rightarrow 0$ the peak to peak distance equals the sample length $a = 3$ mm since the stray field emerges from the sample poles. In the limit of great distances, p approaches the peak to peak spacing of a point dipole (dashed-dotted line), i.e. $d = h$. There is good agreement between the solid and the dashed line, indicating that this is a robust method to determine p . Regardless of this finding, the deviation of $d_{y=0}$ and $d_{y=1mm}$ have been plotted (Δ) in the same graph but with a different scale (see right axis). The deviations are largest at h between 3 and 7 mm. This covers the range of typical experimental sample-SQUID distances. Nevertheless, the absolute deviation is only 0.03 mm which is below the resolution limit of the measurement.

4.1.2. SQUID-sample distance using a current loop

Another possible method of finding the SQUID-sample distance makes use of the distance dependence of a magnetic field from a current loop. An insulated tungsten wire loop of rectangular shape inside the sample holder is used for sample heating at currents of a few Amperes. At a lower current of 5 mA the induced magnetic stray field at a typical distance of 5 mm is in the range of 100 nT and can easily be detected by the SQUID. In this section, an analytic expression for the magnetic stray field of this wire geometry is derived followed by the experimental approach to find the distance h .

To calculate the stray field of a current carrying wire, the Biot-Savart law is used:

$$d\vec{B} = \frac{\mu_0 I}{4\pi} \frac{d\vec{l} \times \vec{r}}{r^3} \quad (4.1)$$

Consider a straight wire of small diameter and finite length L (see Fig.4.4). Let S be the starting point and E be the end point of this wire with a constant current I running through it. P is a point at a distance \vec{r} where the line element $d\vec{l}$ causes the magnetic flux element $d\vec{B}$. Expression of dB in terms of ϑ_1 yields:

$$dB = \frac{\mu_0 I}{4\pi} \frac{\cos \vartheta_1}{r^2} dl \quad (4.2)$$

Thus,

$$\begin{aligned} B &= \frac{\mu_0 I}{4\pi} \int_{\vartheta_1}^{\vartheta_2} \frac{d\vartheta'_1 \cos \vartheta'_1}{h} \\ &= \frac{\mu_0 I}{4\pi h} (\sin \vartheta_2 + \sin \vartheta_1) \end{aligned} \quad (4.3)$$

where $0 \leq \vartheta_1, \vartheta_2 \leq \frac{\pi}{2}$. Note that B points out of the plane of the page due to the cross product of Eq. (4.1). For an infinitely long wire ($\vartheta_1, \vartheta_2 \rightarrow \frac{\pi}{2}$) Eq. (4.3) transforms to $B = \mu_0 I / (2\pi r)$,

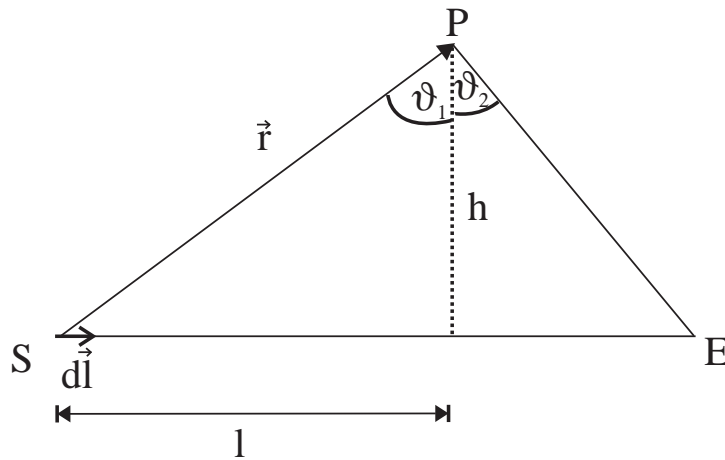


Fig. 4.4.: A line element $d\vec{l}$ with a current I produces a magnetic flux element $d\vec{B}$ at a distance \vec{r} which is perpendicular to the \overline{SPE} plane

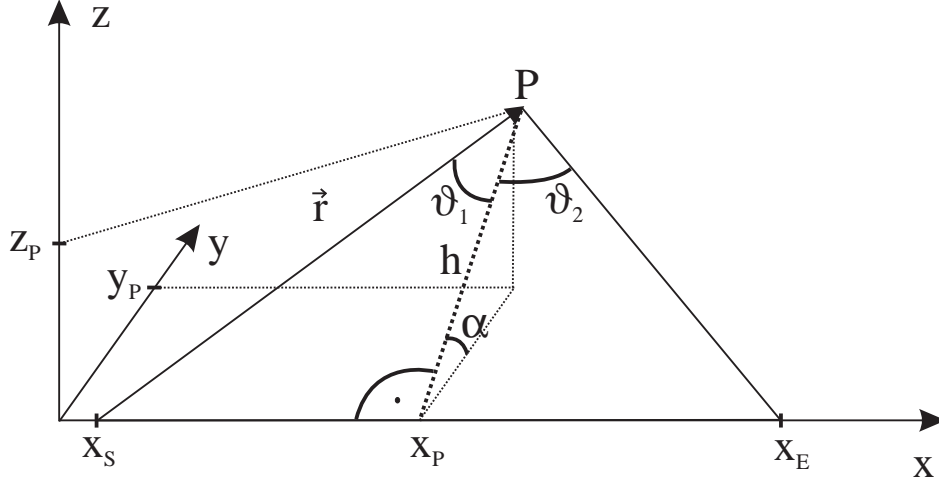


Fig. 4.5.: Triangle \overline{SPE} of Fig. 4.4 with P being an arbitrary point in the cartesian space. The wire coincides with the x axis.

where r is the distance from the wire. In the next step, the stray field is expressed in Cartesian coordinates. In Fig.4.5, one finds the triangle tilted in three dimensional space and the straight wire lies along the x -axis with x_s located at the starting point and x_E at the end point of the wire, respectively. The height h in the triangle \overline{SPE} can be expressed in Cartesian coordinates (see Fig.4.5) $h = \sqrt{y_p^2 + z_p^2}$. The next step is to find an expression for ϑ_1 and ϑ_2 :

$$\begin{aligned} \frac{x_a - x_p}{h} &= \tan \vartheta_1 \Rightarrow \vartheta_1 = \arctan \left(\frac{x_a - x_p}{\sqrt{y_p^2 + z_p^2}} \right) \\ \frac{x_e - x_p}{h} &= \tan \vartheta_2 \Rightarrow \vartheta_2 = \arctan \left(\frac{x_e - x_p}{\sqrt{y_p^2 + z_p^2}} \right) \end{aligned} \quad (4.4)$$

Inserting the latest relations (Eq. (4.4)) into Eq. (4.3) yields¹:

$$B = \frac{\mu_0 I}{4\pi \sqrt{y_p^2 + z_p^2}} \left\{ \sin \left[\arctan \left(\frac{x_e - x_p}{\sqrt{y_p^2 + z_p^2}} \right) \right] - \sin \left[\arctan \left(\frac{x_a - x_p}{\sqrt{y_p^2 + z_p^2}} \right) \right] \right\} \quad (4.5)$$

As the experiment is only sensitive to the z -component of the stray field, we need to determine the projection of \vec{B} onto the z axis. For α one finds the expression $\alpha = \arctan(z_p/y_p)$ and using the identity $\cos[\arctan(x)] = 1/\sqrt{1+x^2}$ one gets:

$$B_z = B \frac{1}{\sqrt{1 + \frac{z_p}{|y_p|}}} \quad (4.6)$$

Note that in the last equation the absolute value of y_p is taken to get consistent values for B_z when y_p changes sign.

¹note that using the identity $\sin[\arctan(x)] = x/\sqrt{1+x^2}$ this equation can be rewritten. However, it is shown in the present form since it is shorter

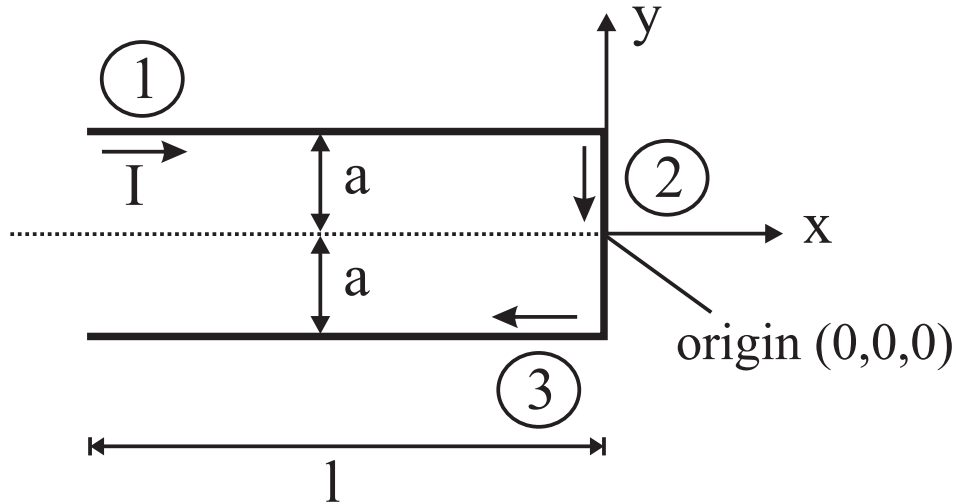


Fig. 4.6.: Arrangement of three straight wires as used in the experiment. The distance of the two parallel wires is $2a$ and the the origin of the cartesian coordinate system is located as indicated.

Figure 4.6 shows an arrangement of three straight wires of finite length denoted with 1, 2 and 3. The z -component of \vec{B} of the individual wires is labelled as B_{z_1}, B_{z_2} and B_{z_3} . The total field is obtained by superposition $B_{z_{tot}} = B_{z_1} + B_{z_2} + B_{z_3}$, where the individual expressions are adapted to the geometry of each wire section. The explicit expression can be reviewed in the Appendix A.3.1.

The stray field $B_{z_{tot}}$ can be viewed in the 3D plot in Fig. 4.7 (a). The rectangular wire configuration with the given dimensions is also drawn below the stray field distribution. Across the center of the loop along the x -direction the B_z peak values are largest and at a distance of $h=5$ mm reach a value of about 100 nT for $I = 5$ mA. The coordinate system was chosen such that it coincides with Fig. 4.6. Figure 4.7 (b) shows measured B_z line scans in a 3D plot along x for step-wise variations of y measured at a distance $h = 5 \pm 0.2$ mm. Projections of the line scans at $y = 25, 27,$ and 29 mm, marked as bold lines on the x - y -plane, illustrate the site of the line scans. The absolute x and y positions in (b) are given in the lab frame (using the absolute positions of the manipulator). The qualitative good agreement between the calculated and measured stray fields is demonstrated when comparing (a) and (b). Experimentally one can easily find the center line scan by varying y until the peak of $B_z(x)$ is the largest. Then, experimental and calculated stray fields can be compared. The height h in the calculation can be adapted in order to find the best agreement. As the loop position is not at the substrate's position, the distance between both must be considered. It is specified by the dimensions of the sample holder (see Appendix Fig. A.5,A.8).

However, it turns out that the experimentally attained height h using the calibration loop by fitting the calculated stray field can differ by ± 0.2 mm. This is inferior to the formerly method which determines f from the geometry of the sample stray fields (Sec. 4.1.1). Reasons for it, on

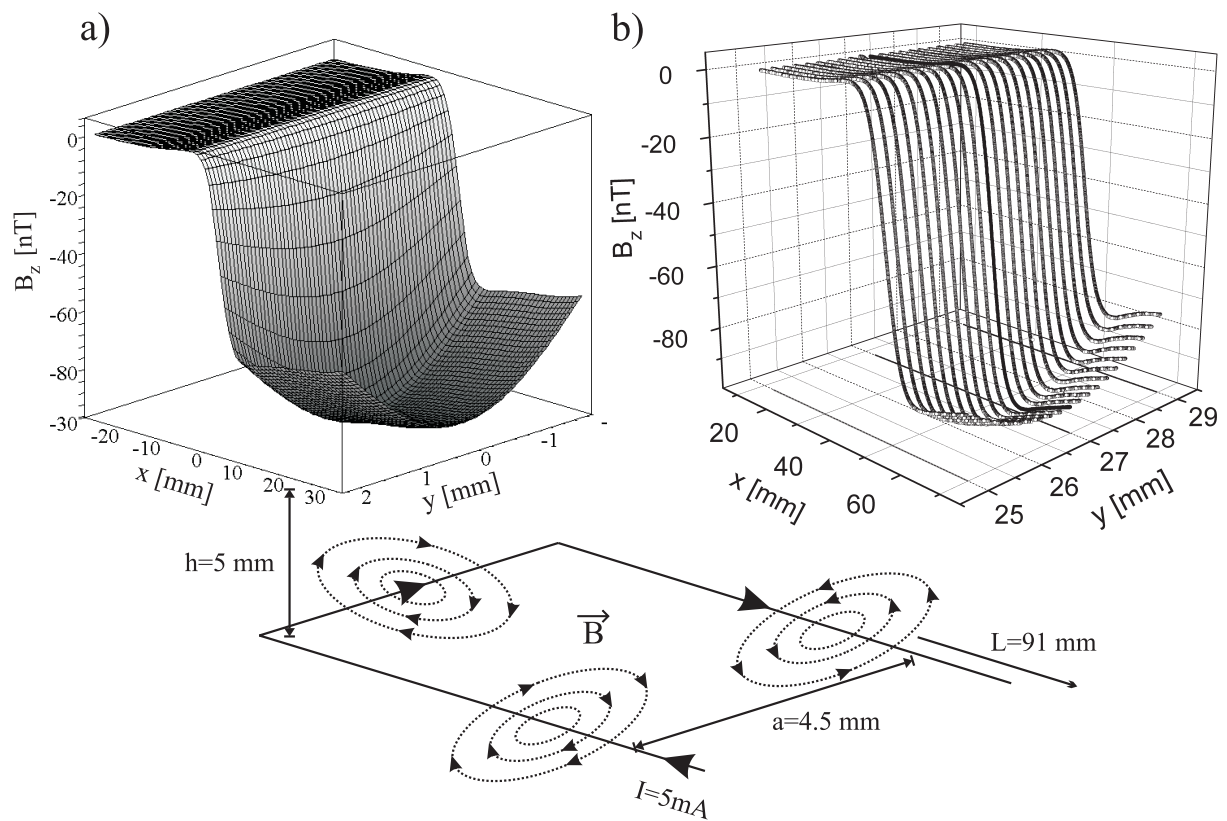


Fig. 4.7.: Comparison of calculated (a) and experimental (b) $B_z(x, y)$ distribution of the rectangular calibration loop in the x - y -plane at a distance $h=5$ mm as a 3D plot. A schematic plot of the rectangular wire configuration with dimensions reflecting the experimental situation is given beneath. The experimental scans (b) were performed for $I=5$ mA.

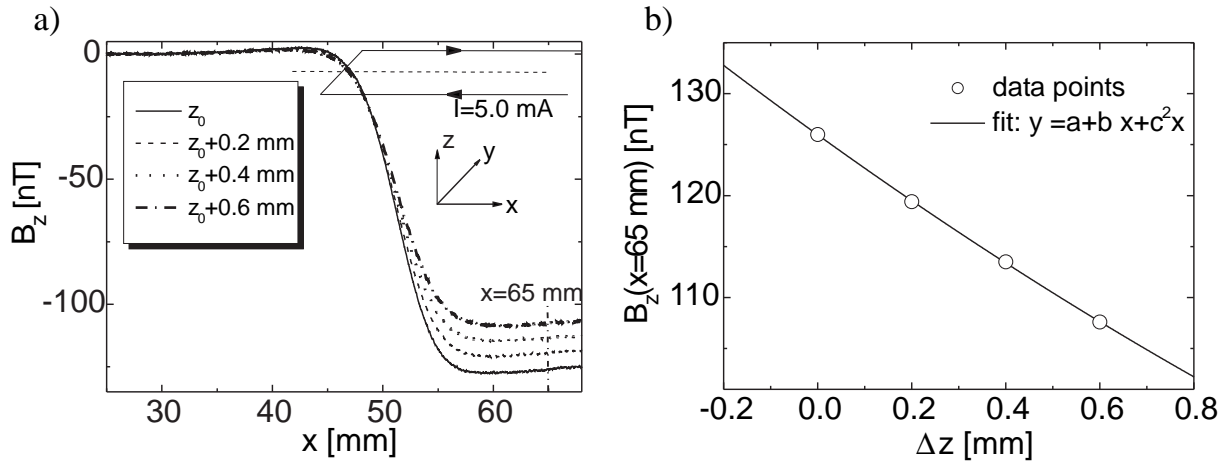


Fig. 4.8.: (a) Experimental line scans above the center of the calibration loop at various distances and a current of $I = 5$ mA. Schematic drawing of the wire arrangement which resides in the x - y -plane below the SQUID at a distance $z_0 + \Delta z$. (b) B_z values at a fixed position $x = 65$ mm. The solid line represents a polynomial fit.

the one hand, stem from the deviation of the experimental wire shape, such as curved bending edges of the wire and uncertainty in the absolute position from the substrate. On the contrary, it is unlikely that the entire sample holder of length $L = 91$ mm is perfectly aligned along the x -direction. Small tilt angles of only 0.5° can visibly change the B_z line scans of the calibration loop.

Nonetheless, the calibration loop can be used as a very sensitive tool for measuring slight *deviations* of the SQUID sample distance since the stray field of a current carrying wire drops with $1/r$. It was observed that during SQUID measurements there is always a continuous drift in the SQUID sample distance which is attributed to a continuous evaporating of liquid nitrogen from the dewar which contains the SQUID. Consequently, the upper part of the dewar warms up and elongates, thus decreasing the distance between the SQUID and the sample (typically $\Delta h > 1$ mm in 2 hours). By this method, absolute *changes* of the distance of about 0.01 mm are resolvable. Stray field evaluation using this method yields more consistent magnetization values with much less scattering in contrast to magnetization values extracted from sample stray fields alone. This method can determine relative changes of magnetization of only 1%.

Figure 4.8 illustrates how relative distance changes can be monitored. In (a) four line scans above the calibration loop at different heights are presented starting from an arbitrary height $z_0 \approx 4.5$ mm and a current of $I = 5$ mA. Then, the micrometer screw of the UHV manipulator is used to adjust well-defined increases of distance in steps of 0.2 mm. The farther the SQUID is away from the sample holder, the smaller the B_z values become. At a fixed position, e.g. $x = 65$ mm, the B_z values are taken and plotted against the height variations Δz . They are found in (b) where the data points are additionally fitted by a polynomial of second order. The

error bars of the data points are much smaller than the symbol size. Now absolute changes of the SQUID sample distance can be measured with the following procedure (Fig. 4.8 (a)). A first measurement of the ferromagnetic film is performed without a current through the rectangular loop thus revealing the stray field of the film. In a second measurement, a calibrated current is sent through the loop. In a subsequent step, both measurements can be subtracted in order to find the stray field of the current loop alone. By comparing the stray field B_z at an unknown height with a calibration plot shown in Fig. 4.8, height *changes* can instantaneously be detected and incorporated in the analysis.

This method also proves helpful in measuring magnetic films below 5 ML since the magnetic stray field decreases with decreasing film thickness. In this case, finding the height from the stray field shape is much more inaccurate. Admittedly, this procedure requires knowledge of the absolute distance which can be extracted from sample stray fields of previous measurements on thicker Fe films.

Additionally, the use of the calibration loop allows for the *immediate* correction of changes of the SQUID-sample distance. This feature is necessary, e.g., in temperature dependent measurements which might lead to a change of the sample-SQUID distance h resulting in an apparent change of the magnetization.

4.1.3. The optimal SQUID-sample distance and ultimate sensitivity

Since we are interested in ultrathin films, we assume a homogenous magnetized square Fe film of 4 mm length and a thickness of a single atomic layer. This film contains about 1.963×10^{14} (1.227×10^{15} atoms/cm²) Fe atoms, each with a bulk magnetic moment of $2.22 \mu_B$. A line scan across the center of the film at a height $h = 5$ mm would yield a peak to peak B_z^{pp} value of 4.17 nT. The magnetic field of a point dipole scales with $1/r^3$ with \vec{r} being the position vector (see Eq. (2.16)). Consequently, a reduction of the distance r by a factor of two will increase the magnetic field eight-fold. Yet in the case of the finite extended film the increment will be smaller than for the point dipole. A line scan above the previously mentioned film at half distance $h = 2.5$ mm yields $B_z^{pp} = 20.20$ nT. At first glance, one would conclude that the most accurate determination of M would be obtained for h as small as possible. That, however, requires that the height h is known exactly. From the experimental point of view the SQUID-sample distance is determined with an error bar of approximately ± 0.1 mm. As it follows, the error in M is for $h = 5$ mm, 5.1%, and for $h=2.5$ mm already 7.8%. That is an increase of the uncertainty by more than 50%. Within the SQUID setup, the typical noise of B_z (four averaged scans) is about 0.1 nT. Consequently, even at a distance of 5 mm fractions of a monolayer Fe can be detected easily without increasing the error in the magnetization which arises from a smaller distance h , provided that the ferromagnetic film is in a single domain magnetic state. The ultimate sensitivity of the present setup is estimated to be around 10^{-7} emu when taking

into consideration a signal to noise ratio of 1:1. In conclusion, a distance of about 5 mm is a good compromise between high sensitivity on the one hand and higher accuracy with regard to height uncertainties on the other hand.

In principle, one could also scan the stray field with high lateral resolution at a distance $h < 0.1$ mm. Since the size of the SQUID loop is $100 \times 100 \mu\text{m}^2$, this is the maximum attainable spacial resolution. However, as shown before, the magnetic analysis of 10% of a monolayer can already be performed with our setup. To decrease h to 0.1 mm would have required bringing the SQUID sensor into UHV with all cooling and other technical problems during bake-out processes and measurements. Hence, in this work we always worked with the easy-to-handle setup described before. For completeness we note that KITLEY *et. al* built a scanning SQUID microscope which can resolve small magnetic fields down to the μm scale, but it is only functional under ambient conditions [105].

4.1.4. Determination of the direction of the in-plane magnetization

Besides the absolute magnetization determination with the scanning SQUID, it is also possible to find the in-plane easy axis of a homogeneously magnetized film, if the remanent magnetization direction does not coincide with the scanning direction. Since the stray field geometry is independent of the magnetization value, the thickness or the lateral size of the film, the rescaled stray field (as introduced in Sec. 2.3.1) is used for the analysis.

In Fig. 4.9 (a) and (c), contour plots of the B_z component are presented for a square shaped film at a distance $h = 1L$ (L : square length) for in-plane angles of the magnetization $\alpha = 0^\circ$ and $\alpha = 30^\circ$, respectively. For $\alpha = 0^\circ$, the magnetization direction is parallel to the x axis. (b) shows line scans along the dashed lines of the contour plot in (a). The stray field is largest across the film's center, i.e. $y = 0$. All other B_z scans (in (b) and (d)) have been normalized to this maximum field value. The farther one moves away from the center scan in y -direction the smaller the maximum (minimum) values of B_z becomes.

The case is more interesting, if the scanning direction is not parallel to the magnetization direction (see (c) and (d)). A scan at $y = 0$ yields B_z scans which are reduced by a factor $\cos \alpha$. In the extreme case that $\alpha = 90^\circ$ at $y = 0$ there will not be any z -component of the magnetic stray field. A variation of y for $\alpha \neq 0$ has two effects on the line scans: (i) the B_z line scan becomes asymmetrical and (ii) the zero line shifts.

Fig. 4.10 shows how to extract the in-plane angle α from stray field data. In (a), a cross section of an in-plane magnetized film in the x - z -plane is shown. Sources of the magnetic field are the edges of the magnetized film so that the magnetic flux forms closed lines between the two poles of the film. Along the dotted line the magnetic field does not possess a z -component of the magnetic field. The z -component of the stray field of a point dipole, which is normal to the dipole orientation, is generally zero in a plane which is orthogonal to the dipole and includes

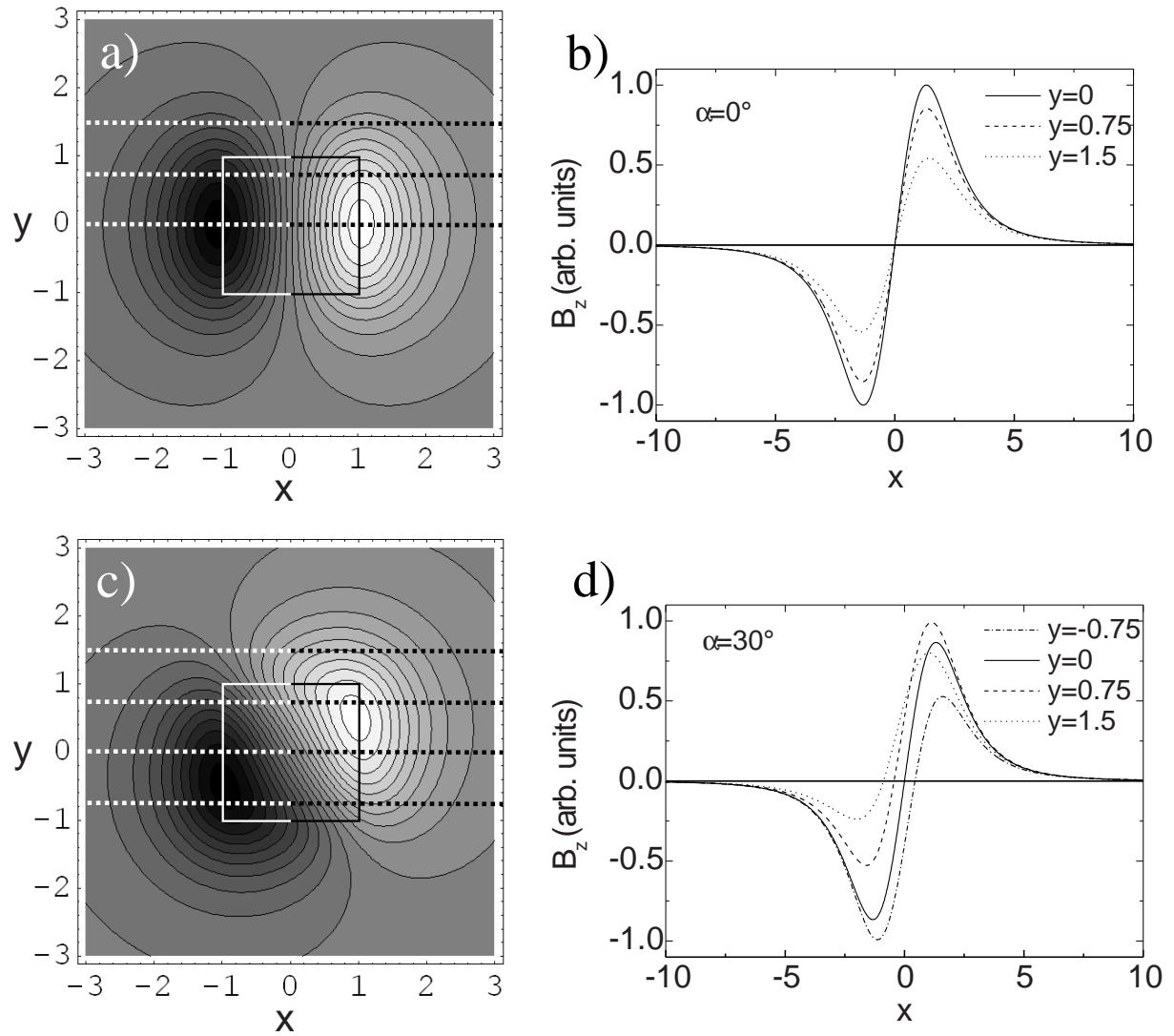


Fig. 4.9.: Contour plots of the rescaled stray field component B_z at a distance $z = L$ in the x - y -plane at the different in-plane angles $\alpha = 0^\circ$ (a) and $\alpha = 30^\circ$ (c). The square indicates the boundaries of the magnetic film below. (b) and (d) show respective line scans along the dashed lines in (a) and (c).

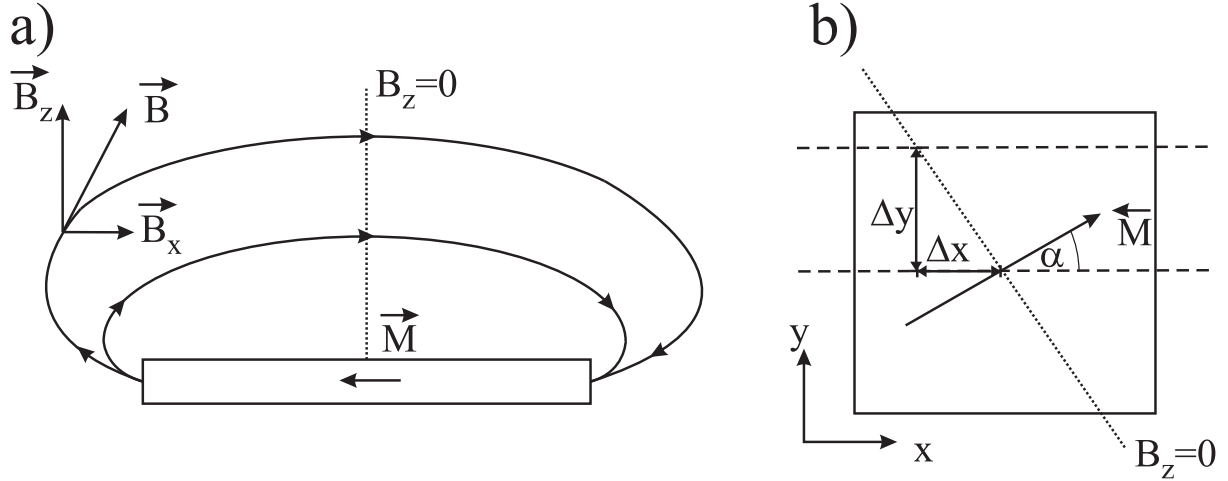


Fig. 4.10.: (a) Side view of the magnetic flux of an in-plane magnetized film. Along the dotted line B_z vanishes. (b) Top view.

it. Consequently, in every x - y -plane one finds a 'zero line' (dotted line) perpendicular to the magnetization vector. This situation is depicted in Fig. 4.10 (b) where \vec{M} and the x -direction include an angle α . This sketch shows a top view of a square shaped sample with two dashed lines indicating the scan direction. Apparently, a shift of the y -position will change the position of $B_z(x, y, z = h) = 0$ line profiles along x (Fig. 4.9 (d)). Since experimentally the y -position can be set by means of a micrometer screw one only needs to extract the null position x from the B_z scans. One can show easily that

$$\alpha = \arctan\left(\frac{\Delta x}{\Delta y}\right) \quad (4.7)$$

with Δx and Δy being the differences of two respective x and y positions. The experimental uncertainty of Δy is assumed to be negligible where Δx is limited by the observational accuracy in the B_z scans. For typical line scans the x position can be determined with an accuracy of 0.1 mm. This leads to an error bar of $\pm 3^\circ$ for angles $0^\circ < \alpha < 45^\circ$ (fixed $\Delta y = 2$ mm). For $45^\circ < \alpha < 90^\circ$ the accuracy even becomes better ($< \pm 1.5\%$).

Fig. 4.11 gives an example for the determination of the in-plane angle. In (a), the $B_z(x, y = y_i, h = 5\text{mm})$ profiles of an 8 ML Fe film on GaAs(001) are shown for different y_i . The x and y coordinates are given in the laboratory reference frame. The [100]-direction of the GaAs(001) substrate is oriented parallel to the scanning direction x of the sample. As an 8 ML Fe film has its easy axis along the [110]-direction (compare Sec. 4.4), an in-plane angle of $\alpha = 45^\circ$ is expected with respect to the [100]-direction. In Fig. 4.11 (b), the 'zeros' of the B_z profiles are plotted versus the corresponding y_i positions. In Eq. (4.7), α is determined by $x(y_i)$, i.e. how much x changes when y is shifted. Therefore, the linear fit in Fig. 4.11 (b) corresponds to $\Delta x/\Delta y$ and yields an angle $\alpha = 45.7^\circ$ which is in good agreement to the expected easy axis along the [1 1 0]-direction ($\alpha = 45^\circ$). Here the error in the angle determination is quite small

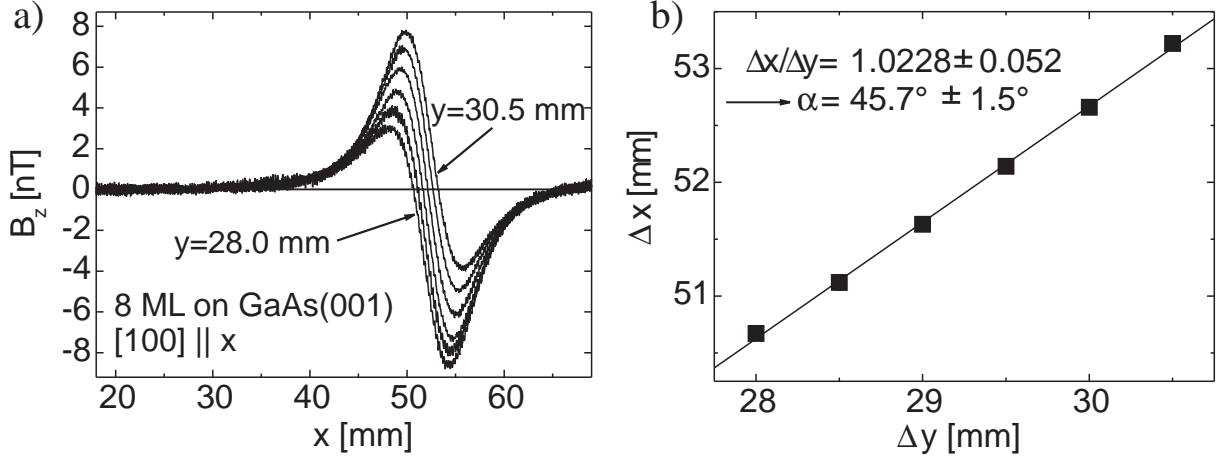


Fig. 4.11.: (a) Experimental $B_z(x, y, h = 5 \text{ mm})$ line scans for $y = 28\text{-}30.5 \text{ mm}$ with 0.5 mm spacing. (b) Zero crossing of the B_z line scans as a function of y position. The in-plane magnetization angle of \vec{M} is determined according to Eq. (4.7).

($\Delta\alpha = \pm 1.5^\circ$), since 5 line scans at different y_i are taken into consideration. Yet in a typical experiment, only 2 discrete y positions are used which gives an error bar of typically 5 %.

One should note that at a closer distance $h \ll L$ there is no straight 'zero line' ($B_z = 0$), perpendicular to the sample magnetization but the x, y position where $B_z = 0$ changes with height ('null curve'). Only along the high symmetry directions, i.e. magnetization parallel to a sample edge or diagonal to the square sample, one obtains an exact 'zero line'. Fortunately, at distances $h \approx L$ the curve is quite well approximated by a line perpendicular to \vec{M} such that the above presented method yields an accurate result within the assumptions of Eq. (4.7). The reading inaccuracy of the determination of the x -position at which $B_z = 0$ yields the biggest contribution to the error of the in-plane angle α .

4.1.5. Demagnetizing fields of in plane magnetized films

Using Eqs. (2.6) and (2.5), the demagnetizing field of a sample with uniform magnetization can be calculated. The result for a square shaped film with magnetization lying in the film plane along the x -direction is shown in Fig. 4.12. The two poles give rise to pseudo magnetic surface charges and generate fields which are opposed to \vec{M} . Furthermore, we neglect the y -component of the demagnetizing field and focus on the x component because (i) its magnitude is much larger and (ii) it is the relevant component which can force the magnetization near the poles to align along $-x$ (i.e. demagnetizing the sample). Under these assumptions, Eq. (2.7) simplifies to:

$$\vec{H}_d(x, y, z) = M_x \nabla \left(\int_{-L/2}^{L/2} \int_{-L/2}^{L/2} \int_{-d/2}^{d/2} \frac{\delta(x' - L/2) - \delta(x' + L/2)}{|\vec{r} - \vec{r}'|} dx' dy' dz' \right) \quad (4.8)$$

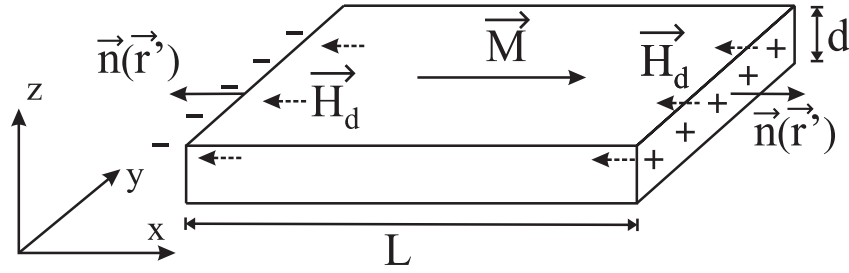


Fig. 4.12.: A uniform magnetization causes magnetic poles at the sample edges which give rise to demagnetizing fields.

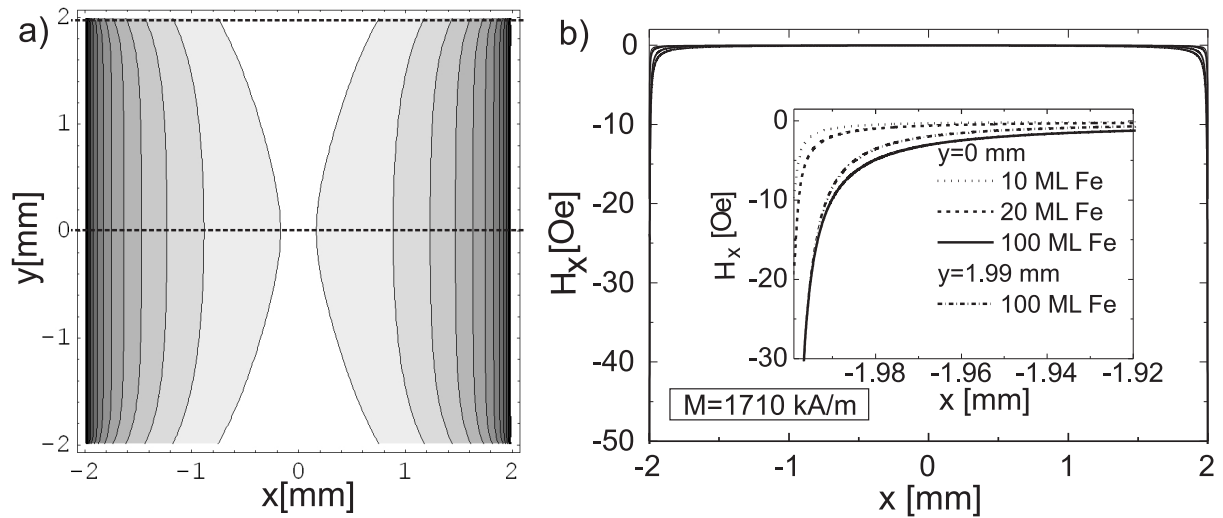


Fig. 4.13.: (a) Contour plot of the H_x -component of the demagnetizing field (logarithmic spacing of the contour lines). (b) H_x profiles along the two dashed lines in (a) for Fe films of different thicknesses.

where δ is the *Dirac Delta function*. This integral was analytically evaluated by using 'Mathematica' [106]. The solution was expanded in a series for $d \ll L$ and its final form can be found in the appendix Eq. (A.7). Note that in this 2D continuum approach the volume magnetization transforms to an area magnetization $M \cdot d$. Figure 4.13 (a) shows a qualitative contour plot of the H_x component of the demagnetizing field inside a film of $4 \times 4 \text{ mm}^2$ size. Quantitative line scans along the x -direction are found in Fig. 4.13 (b) for three different film thickness: 10, 20 and 100 ML. For the 100 ML film, the line scans were calculated in the middle of the film, e.g. $y = 0 \text{ mm}$, and $10 \text{ }\mu\text{m}$ away from the edge of the film at $y = 1.99 \text{ mm}$. These line scans are illustrated as dashed lines in Fig. 4.13 (a). However, no significant difference is seen. The other film thicknesses are only shown for $y = 0$. The thicker the films, the larger the demagnetizing fields in the interior.

To estimate the influence of the demagnetizing fields on the magnetization at the edges, one can regard the coercive field H_c . For thin films, typical coercive fields applied along the easy axis are in the order of 10 Oe. Therefore, we calculate the distance x from the sample

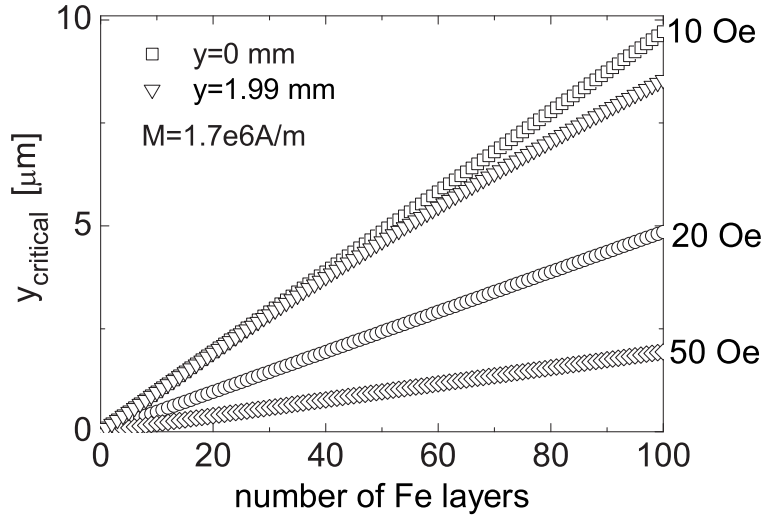


Fig. 4.14.: Numerical calculation of the demagnetizing field range $y_{critical}$ (measured from the sample edge) as a function of Fe film thickness where it drops below a critical value (10, 20 or 50 Oe).

edge where the demagnetizing field has dropped below this value. The result of this numerical calculation is presented in Fig. 4.14. The symbols represent the distance from the sample edges up to which the demagnetizing field exceeds the hypothetical coercive fields of 10 Oe as a function of film thickness. Assuming a coercive field of 10 Oe, different symbols (triangles and squares) indicate H_x line profiles along the x -direction, that are parallel shifted along the y -direction. Data for $y = 0$ and $y = 1.0$ mm fall on top of each other. Only very near the sample edge (here 10 μm away from the edge) can deviations be found. In this case, the critical field range at the sample edge is even smaller compared to scans across the middle. The critical field range for higher coercive fields as indicated in the plot becomes smaller. For an Fe film thickness up to 50 ML, the maximum range of the demagnetizing field is below 5 μm compared to the lateral film dimensions of 4 mm. Even if one assumes the extreme case that all the magnetization is reversed inside the critical range, the stray field at the SQUID position will only be reduced by 0.5%. This error is smaller than other experimental errors (see Sec. 4.1.8). To show that this consideration is an upper estimate for the 'worst case', experiments to i) find a reduction of the remanent magnetization (by MOKE) and ii) to observe domains (by Magnetic Force Microscopy and Kerr Microscopy) have been performed (Sec. 4.2 and Sec. 4.3).

The situation changes when the film thickness is 100 nm or larger. In this limit, demagnetizing effects might reduce the 'far away' stray field at the SQUID position such that the magnetization values determined from stray field data are virtually reduced.

To summarize this section:

- Demagnetizing fields arise from the magnetic poles of a sample and are opposed to the magnetization direction.
- At the sample edges (magnetic poles) the magnitude of demagnetizing fields is large and drops fast in the interior of the film.
- The magnitude and range of demagnetizing fields depend linearly on the magnetization M and thickness d of the film.
- For a critical field strength, e.g. 10 Oe, the edge area over which demagnetizing fields for films up to 100 ML thickness must be considered is limited to a few μm . This implies that for macroscopic films of a few mm size the lateral *macroscopic shape* (square, circle) does not influence the development of domains in these samples.
- A decrease in thickness near the sample edge or a corrugated border as experimentally expected will *reduce* the magnetostatic potential (due to the scalar product $\vec{n} \cdot \vec{M}$ in Eq. (2.6)) and therefore the formation of domains gets even less favorable.
- In the calculation, the magnetization at the sample edges (magnetic poles) is considered unchanged by the demagnetizing field \vec{H}_d . If, however, a part of the magnetization at the edges was reversed by \vec{H}_d , the demagnetizing effects would even become further reduced.

4.1.6. Influence of surface roughness on the magnetic stray field

BRUNO investigated the influence of surface roughness on the demagnetizing field theoretically and could show that it can give rise to an effective perpendicular anisotropy whose magnitude can be calculated using roughness parameters [107]. Experimental work on the influence of interfacial roughness was carried out for Co/Au sandwich structures [108] and for Ni/Cu(001) [109]. Since magnetization measurements in this thesis use the magnetic stray field of FM films, the question is how the surface roughness can influence the magnetic stray field. An *ad hoc* consideration might come to the conclusion that the magnetic flux which emerges at roughness features of a thin film forms closed flux lines as indicated in Fig. 4.15. The roughness is characterized by the so-called roughness correlation length ξ (see Fig. 4.15). It is implied that the surface roughness does not change the average magnetization of the film and that its orientation remains unchanged near roughness features. To confirm the last point, we consider the island sizes of Fe grown on GaAs. THIBADO investigated the size of Fe islands on GaAs(001)-(2 \times 4) at 175° C by STM. At a coverage of 1 ML, the average island width \times length is about 35 \times 90 Å. A 35 ML Fe film exhibits rectangular islands of approximately 50 \times 80 Å (elongated along $[\bar{1}10]$) on average and a height of 3 ML. Another STM study of 150 Å Fe/GaAs shows

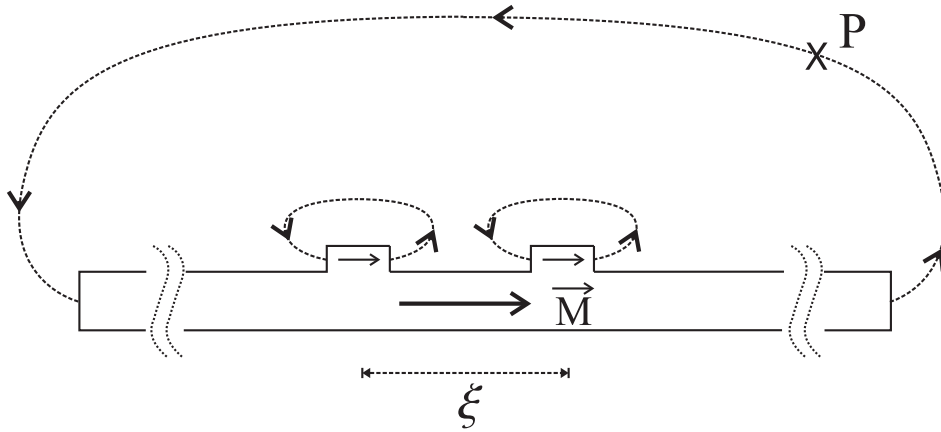


Fig. 4.15.: *Ad hoc* consideration of the influence of surface roughness on the magnetic stray field. The film roughness with correlation length ξ gives rise to localized closed flux lines. The magnetic stray field of the whole in-plane magnetized film at point P is regarded.

island-like undulations about 10 \AA high and about 150 \AA in diameter [110]. Considering the Fe exchange length $\delta_{ex} \approx 21 \text{ nm}$, it is therefore unlikely that the magnetization in the islands is laterally tilted out-of-plane due to surface anisotropy effects. This is because a tilt of magnetic moments at a length scale comparable to δ_{ex} would be very costly with regard to the energy. Under these premises, one may argue that the magnetic flux is lost at an observation point P and the magnetic flux density is reduced at P . The consequence of this scenario would be an erroneous reduction of the magnetization value of the film from SQUID analysis. However, it is proven in the following that mesoscopic roughness does not influence the magnetic stray field at typical distances of a few mm from the film.

This can be shown strictly assuming that the roughness does not change the in-plane magnetization orientation of the layer. Namely, the stray field of a rough film can be evaluated as a field of 'magnetic charges' appearing on the film surface because the magnetization projection on the surface normal is not zero when a surface roughness is present (this is the situation depicted in Fig. 4.15). Expanding the surface density of these charges into a Fourier series and substituting this expansion into the standard Poisson equation for the scalar magnetic potential shows that the potential of each individual harmonic decays exponentially with the decay length proportional to the spatial wave vector k of this harmonic. This calculation is carried out in appendix A.4. Further, the net 'magnetic charge' of a film surface remains zero (assuming that on average the film magnetization remains in-plane), so that the constant contribution to the stray field from $k = 0$ is absent. Hence, one finds that the total stray field from an in-plane magnetized film with a rough surface decays exponentially with the decay length corresponding to the spatial wave vector for which the Fourier component of the surface roughness profile is maximal. This means, in turn, that the decay length of the stray field is about the typical roughness wavelength, which is much smaller than the distance between sample and SQUID.

In a PhD thesis [111], it was shown that the deviation of the magnetic stray field originating from discrete spins at the position of regular lattice sites drops exponentially to zero when compared to continuum theory. The modelling of the surface roughness can be transferred to this situation.

4.1.7. Asymmetric magnetic stray field shapes of in-plane magnetized films

Asymmetries in B_z line scans for in-plane magnetized films can have different origins. In the following a checklist is given to account for possible experimental errors in the analysis of M :

- A *ferromagnetic background* signal of the sample holder can make it impossible to evaluate the stray field data. Even measuring the background stray field of the magnetized sample holder with a subsequent subtraction from the film's signal will not yield a satisfactory result. The magnitude and shape of the background signal depends on the position and can be different from the configuration during the measurement of a ferromagnetic film. Therefore, ferromagnetic contamination of the sample holder must be avoided! Additionally, the recommendations given in the appendix A.6 concerning the sample holder materials and the cleaning procedure should be followed.
- A *tilt of the sample surface* with respect to the x - y plane causes an asymmetric B_z profile. An asymmetric line shape can be observed because of the effect of distance on the stray field. Extreme care should be taken to align the sample holder such that it does not include an angle with the surface parallel to the x - y plane.
- An *angle α between magnetization M and scanning direction x* will also lead to asymmetric scans along x (Sec. 4.1.4). The in-plane angle, however, can be determined and used in the analysis. In order to find the center of the film ($y = 0$) y should be varied until the asymmetry vanishes.
- A *non-uniform magnetization over the film area* can also give rise to asymmetries. This possibility includes the formation of magnetic domains and a locally reduced magnetization which can arise from a rough topography of the underlying substrate. It might also be possible that a part of the film was inadvertently deposited on the sample holder, not the substrate.

4.1.8. Accuracy limitations for the magnetization determination

The individual factors determining the accuracy of the magnetization analysis of the present SQUID setup are listed below:

4. Results and discussion

Origin of errors		$M_{exp} - \Delta M/M_{exp}$
SQUID calibration		1.0%*
deviation from sample center \diamond	$\Delta y = 0.5$ mm	1.3%* (1.6%)
y=0	$\Delta y = 1.0$ mm	5.3% (6.1%)
height determination \diamond	$h_0 = 5$ mm, $\Delta h = 0.1$ mm	5.0%* (5.5%)
film thickness calibration		5%*
edge domains		negligible
surface roughness		negligible
tilt of the sample		rectifiable
(FM background signal)		(variable)
maximum total error*		12.3%

Table 4.1.: Error contributions to the magnetization. The total error is the sum of the values marked by (*)

\diamond The estimates are made for a square shaped film with a side length of $L=4$ mm. For $L=3$ mm the errors increase and are given in parentheses.

This conservative estimate yields a total uncertainty of about 12%. The center of the film needs to be found within $\Delta y = 0.5$ mm. Interestingly, the accuracy, with regard to the height determination and to the deviation in y , increases as the film size increases from 3×3 (values in parenthesis) to 4×4 mm². This is understandable to some extent from regarding the stray field geometry in units of the sample length, i.e. the rescaled variables introduced in Sec. 2.3.1 since in rescaled lengths the deviation for a larger film are smaller. The errors arising from an inaccuracy in height determination can be reduced by a factor of 2, using the calibration loop which is described in Sec. 4.1.2. One main error contribution comes from the uncertainty of film thickness measurements by means of a quartz oscillator. Using MEED (or RHEED) oscillations is considered to be the most accurate method to determine the film thickness in UHV as is demonstrated for e.g. Ni on Cu [112]. However, it would only slightly improve the thickness accuracy and we were not able to see any MEED oscillations for Fe on GaAs(001). Sec. 4.1.5 showed that the formation of magnetic domains is negligible, and that the surface roughness does not modify the magnetic stray field in the far field (see Sec. 4.1.6). A tilted substrate or sample holder (tilt angle $\beta < 1^\circ$) with respect to the scanning direction x results in asymmetric B_z line shape. A simplified approach to correct this effect is to substitute $z = z_0 + x \sin(\beta)$ in the stray field formulas.

Special care must be taken to avoid ferromagnetic background signals, since they can make stray field analysis impossible. The cleaning procedure to remove FM impurities from the surface of the Cu sample holder is explained in appendix A.6.

4.2. Magnetization of Fe monolayers on GaAs(001)

4.2.1. Substrate preparation and growth of Fe films

GaAs(001) substrates are first cleaned with acetone and isopropanol in an ultrasonic bath for 5 minutes until an optical microscope reveals a clean surface. The surface roughness is checked with an atomic force microscope (AFM) revealing an RMS (root mean square) roughness of typically 0.4 nm. In the UHV chamber, the substrate is sputtered with Ar^+ ions at an Ar pressure of 1×10^{-5} mbar and an ion energy of 500 eV until no contaminations of carbon are visible with AES. Then, the substrate temperature is increased to 600° C while the substrate is sputtered as mentioned above for about 30 minutes. After 2 to 3 cycles of this procedure, AES reveals a clean GaAs surface. Figure 4.16 (a) and (b) show the Auger spectra before and after the substrate preparation. Before the Ar etching carbon ($E=272$ eV) and oxygen ($E=503$ eV) can be found, whereas finally, only Ga and As peaks are visible. This treatment results in a clean $\{4 \times 6\}$ -reconstructed GaAs(001) surface [14]. A typical LEED image of this GaAs surface is shown in Fig. 4.17 on the left hand side. A schematic sketch of the diffraction pattern is drawn on the right with corresponding crystallographic directions. Big spots originate from the GaAs cubic unit cell with the lattice constant a . The smaller spots along $[1\ 1\ 0]$ corresponds to a surface reconstruction along this direction with a periodicity of $6a$, and $4a$ in the $[1\ \bar{1}\ 0]$ -direction.

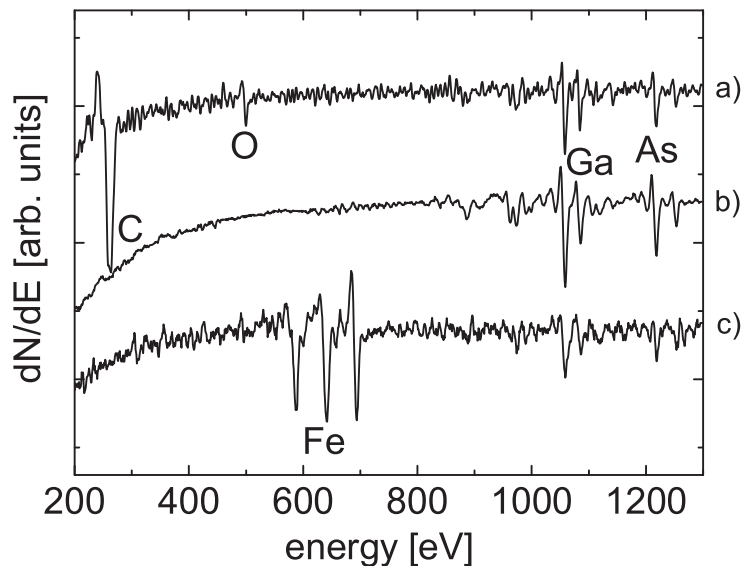


Fig. 4.16.: (a) AES of an GaAs substrate before Ar ion etching, and (b) after Ar ion etching at $p = 10^{-5}$ mbar with $E = 500$ eV for 30 minutes. (c) AES of 3 ML Fe deposited on a clean GaAs substrate.

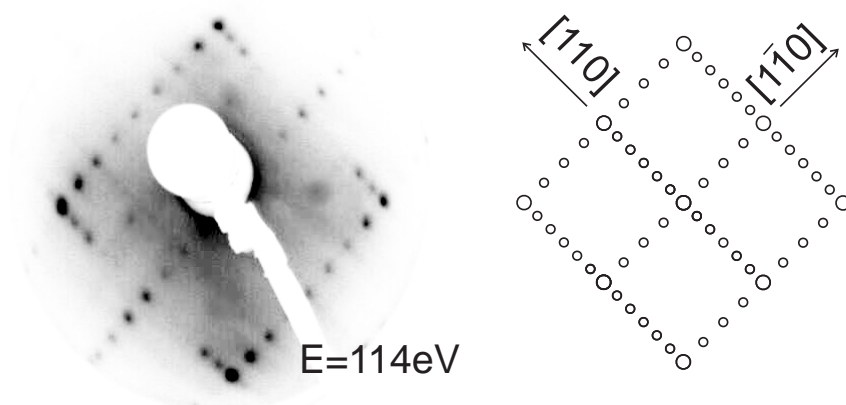


Fig. 4.17.: Left side: LEED image of a $\{4 \times 6\}$ -reconstructed GaAs(001) surface. Right side: Schematic drawing of the LEED spots.

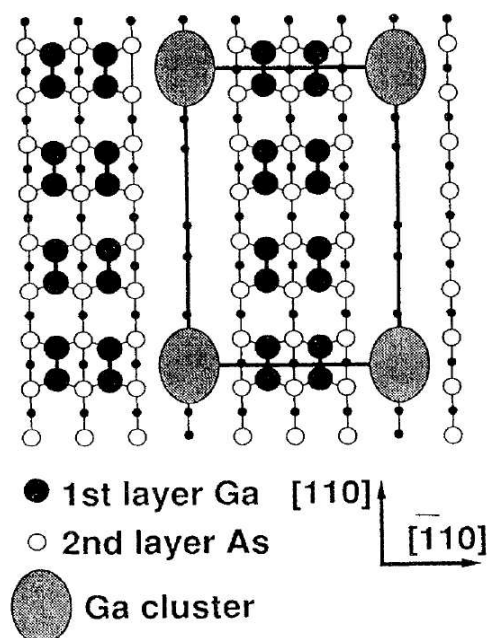


Fig. 4.18.: Proposed atomic structure model of the $\{4 \times 6\}$ -reconstructed GaAs(001) surface taken from Ref. [22].

BIEGELSEN *et al.* [113] observed coexisting phases of GaAs(001)- (4×2) and (2×6) which explain a 'pseudo' $\{4 \times 6\}$ -reconstructed surface obtained from LEED investigations. However, XUE *et al.* [22] reported on an additional 'genuine' GaAs(001)- (4×6) surface based on scanning tunneling microscopy investigations in combination with a first-principles total-energy calculation, which is reprinted in Fig. 4.18. The authors assume that the Ga clusters consist of 6 to 8 atoms. This is one of the most Ga rich surface of GaAs(001) known.

Fe was deposited by electron beam evaporation at deposition rates of about 1 ML/min at room temperature. The pressure did not exceed 1×10^{-9} mbar. The relative partial pressures

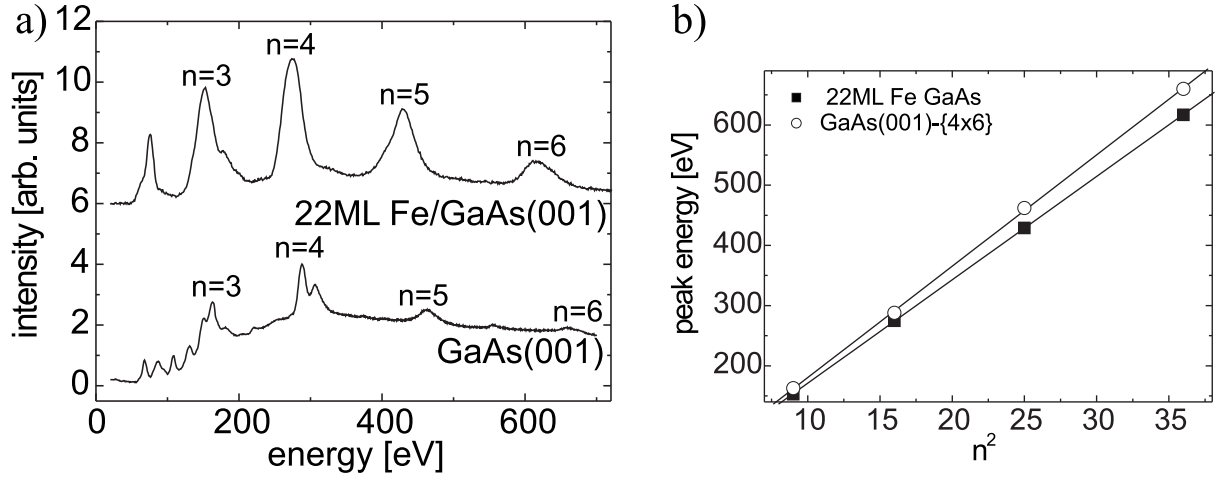


Fig. 4.19.: (a) (0,0)-LEED spot intensity as a function of electron energy of a $\{4\times 6\}$ -reconstructed GaAs(001) substrate and a 22 ML Fe film which has been deposited on the same substrate at 300 K. (b) Plot of the Bragg peak energies shown in (a) as a function of Bragg order squared.

during evaporation were about 37% 2 amu (atomic mass units) (H_2), 27% 28 amu (N_2 and CO) and about 7% 18 amu (H_2O). Molecular oxygen (32 amu) only contributes to 0.7 %. Figure 4.16 (c) shows an AES spectrum of 3 monolayer Fe deposited on a clean GaAs(001) substrate. It has 3 distinct peaks at $E = 598, 651$ and 703 eV characteristic for Fe. At this Fe coverage Ga and As peaks of the underlying substrates are still visible.

The lattice mismatch between bcc Fe and GaAs gives rise to considerable compressive in-plane strain in the Fe film. As a consequence, the Fe film expands in the vertical direction (i.e. along the film normal) to minimize the elastic energy. We studied this vertical expansion by IV-LEED as a function of film thickness. Figure 4.19 shows the IV-LEED spectrum of the (0,0) spot of a $\{4\times 6\}$ -reconstructed GaAs substrate and a 22 ML Fe film deposited onto this substrate. From the energy of the Bragg peaks as a function of the order of diffraction n squared (Fig. 4.19 (b)), the interplanar distance d_{inter} according to Eq. (3.7) of GaAs $d_{inter} = 1.407 \pm 0.0035$ Å is calculated. This corresponds to a lattice constant of 5.628 ± 0.014 Å for the cubic unit cell. This value is -0.5 % smaller than the literature value for GaAs bulk ($a_{GaAs} = 5.653$ Å). The slight decrease of the vertical interplanar spacing for the $\{4\times 6\}$ -reconstructed surface compared to bulk GaAs might be due to missing neighbors of the GaAs surface atoms which lead to a contraction of the topmost layers.

The difference between the out-of-plane interplanar spacings of Fe and GaAs is evident from the shift of the peak position of the Fe film to lower energies (\equiv larger interplanar distance) and from the different slopes of the Bragg peaks in Fig. 4.19 (b). Figure 4.20 shows the vertical interplanar spacing of Fe films on GaAs(001) as a function of film thickness. Up to a thickness of about 22 ML Fe, we find a 3% vertical expansion in comparison to the interplanar spacing of $\{100\}$ atomic planes in bulk α -Fe. This yields a tetragonal distortion of

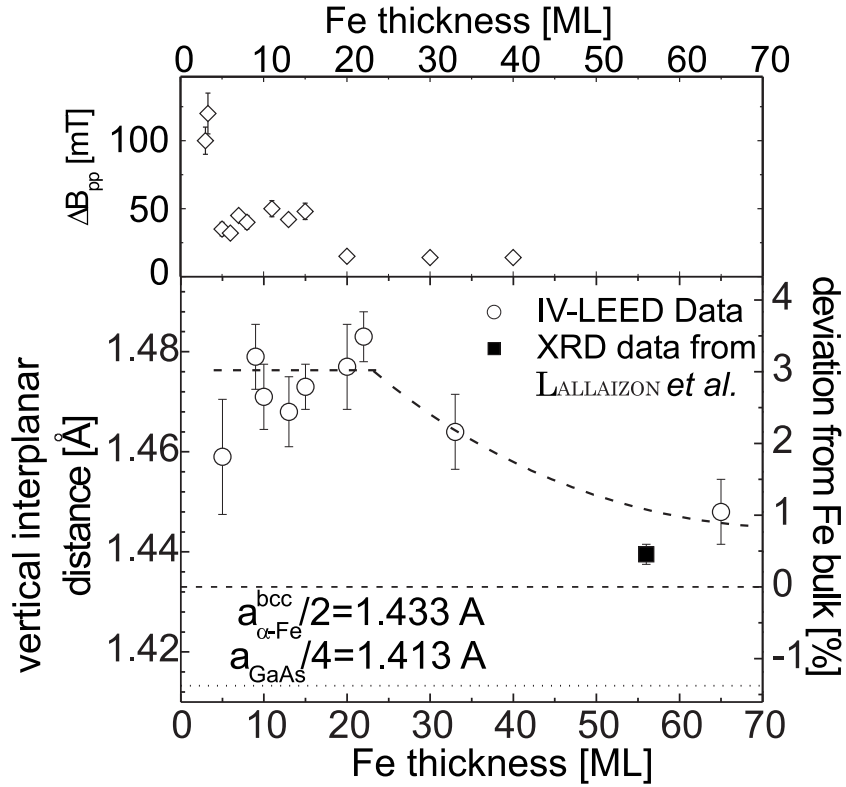


Fig. 4.20.: (lower panel) Vertical Fe interplanar distance determined from IV-LEED experiments for various film thicknesses on $\{4 \times 6\}$ -reconstructed GaAs(001). Data from LALLAIZON *et al.* [114] measured on 80 nm Fe/GaAs(001) is plotted in addition. The bulk interplanar distances for bcc Fe and GaAs are plotted as horizontal lines. (upper panel) FMR line width with the external magnetic field applied along the $[1 \bar{1} 0]$ -direction as a function of film thickness taken from Ref. [115].

$a_{Fe\perp}/a_{Fe\parallel} = 1.045$. Note, that at 5 ML thickness the penetration depth of electrons during the IV-LEED experiments is larger than the Fe thickness. Hence, a part of the measured vertical distance originates from the GaAs substrate which decreases the measured interplanar distance on average. The apparent decrease for 5 ML Fe may also be assisted from the corrugation of thin Fe films, i.e. a thickness fluctuation, as was reported earlier in this thesis. Thus, also for the 5 ML Fe film, it is reasonable to assume the same 3% vertical strain. The volume of the tetragonally distorted unit cell of the Fe film up to 22 ML is conserved and is the same as for bulk α -Fe. Above 22 ML, the vertical strain continuously relaxes as the data points show for 33 ML and 65 ML thick Fe films. But even in the 65 ML Fe film, a vertical strain of 1% persists. The strain relaxation mechanism likely proceeds via the formation of misfit dislocations. LALLAIZON *et al.* [114] measured the out-of-plane lattice constant $a_{Fe\perp}$ using XRD on a 80 nm (~ 56 ML) thick Fe/GaAs film. They found a significant relaxation of the vertical expansions and their value has also been plotted in Fig. 4.20. However, it indicates an Fe film which is even more relaxed than was found from our IV-LEED experiments. Perhaps the GaAs substrate from [114] was not prepared as well as the ones we used since a more defective surface might

ease the incorporation of misfit dislocations. Furthermore, XRD probes the whole Fe film and not only the top surface layers as of our IV-LEED experiments do. The Rutherford backscattering spectrometry (RBS) experiments of the same authors report a significant relaxation of the uppermost 30 nm of the Fe film considering the penetration depth of their method. Further experimental indications make the authors propose that 'most of the interface defects are located in the substrate side'. Our measurements indicate a slightly varying distortion of the top layers up to about 22 ML Fe, followed by a relaxation to the bulk value above this thickness due to the enhanced incorporation of misfit dislocations. However, the average vertical strain relaxes more slowly for thicker films and is observed up to a thickness of about 160 ML [11]. The sudden relaxation around 20 ML Fe is reflected in the line width ΔB_{pp} of FMR spectra which have been recorded with the magnetic field applied along the $[1 \bar{1} 0]$ -direction as a function of film thickness [116]. The result of these measurements are plotted in the upper panel of Fig. 4.20. Starting at 3 ML, ΔB_{pp} drops to about 50 mT at an Fe film thickness of 5 ML. The broad FMR lines below 5 ML are due to the existence of a superparamagnetic phase (close to the percolation limit) or magnetic inhomogeneities [117,118] resulting from the island formation in films < 5 ML. Up to 20 ML, the line width stays nearly constant before suddenly dropping to 15 mT, which is approximately the thickness where IV-LEED data show the vertical relaxation of the Fe film. A reason could be the decrease of the Gilbert damping constant α , which directly influences the line width ΔB_{pp} . α is governed by the spin-orbit (SO) interaction which couples phonons to the spin-system, i.e. the stronger the SO interaction the more energy is dissipated thus damping the precession of the spins. In a perfect cubic environment, the orbital contribution to the total magnetic moment is quenched to first order perturbation theory. This situation is reflected in the g-factor of cubic bcc Fe, $g=2.09$, which is close to the value for pure spin magnetism ($g=2.0023$). Since the IV-LEED investigations show a tetragonally distorted film below 20 ML Fe, an increased orbital contribution is very likely. This assumption is corroborated by CLAYDON *et al.* [35] who found an orbital enhancement of about 300% for Fe films on GaAs(001)-(4 \times 6) up to 10 ML from XMCD measurements. The incorporation of misfits leading to the relaxation of the Fe film might, therefore, directly reduce the Gilbert damping parameter α due to reducing the SO interaction. Generally, the line width is directly related to the relaxation rate. Since the change of the line width by a factor of three is rather large, it is presumably not exclusively explained by a change of the intrinsic relaxation rate between 15 and 20 ML. A more detailed answer could only be given if frequency dependent measurements were performed. It is likely that up to 15 ML Fe, magnetic inhomogeneities lead to a broadening of ΔB_{pp} .

The experimental distortion data can be compared to calculated data using the continuum elasticity theory. The mismatch-induced vertical strain at the interface between the deposit and the substrate is given by $\epsilon_{33} = -c_{12}/c_{11}(\epsilon_{11} + \epsilon_{22})$ [119], where $\epsilon_0 = \epsilon_{11} = \epsilon_{22} = -0.014$ is the

isotropic lattice mismatch of bulk Fe and bulk GaAs, and $c_{11} = 229$ GPa and $c_{12} = 134$ GPa are the bulk Fe elastic constants [28]. This gives the expected out-of-plane strain $\epsilon = 1.6\%$ and a tetragonal distortion of $a_{Fe\perp}/a_{Fe\parallel} = 1.030$. Hence, this theory cannot explain the observed larger tetragonal distortion 1.045. To reconcile the experimental vertical expansion with the continuum elasticity theory, one might choose different elastic constants, since the bulk values may not be adequate in the thin film regime. As the ratio c_{12}/c_{11} determines the vertical strain, c_{12} needs to be bigger or c_{11} smaller. In addition, the lattice mismatch might be different as the $\{4\times 6\}$ -reconstructed semiconductor surface can have differing in-plane lattice constants in the surface plane compared to the bulk values. They might even be different along the $[1\ 1\ 0]$ and $[1\ \bar{1}\ 0]$ -directions. However, a detailed study on the surface in-plane lattice constant by either GIXS (Grazing Incidence X-ray Scattering) or EXAFS analysis (Extended X-Ray Absorption Fine Structure) does not exist to the author's knowledge.

The evolution of the film magnetization as a function of film thickness is the subject of this section. Since the stray field calculations assume a uniformly magnetized FM film with no external magnetic field applied, we begin with the experimental confirmation that the FM Fe films are, in fact, single domain. In Sec. 4.1.5, it was shown that the formation of domains due to demagnetizing fields was only expected near the magnetic poles at the very edges of the film. Experimental proof for this prediction can be obtained from magneto-optic Kerr effect measurements which can be carried out in the UHV system. Figure 4.21 (a) shows the MOKE hysteresis loop of a 5 ML Fe film measured in longitudinal geometry with the magnetic field applied along the $[1\ \bar{1}\ 0]$ -direction using p-polarized light. The original MOKE data are plotted in Fig. 4.21 (b) and exhibit a superposition of the FM hysteresis loop with a linear background signal. It can be identified with the Faraday effect, since the laser beam is transmitted through

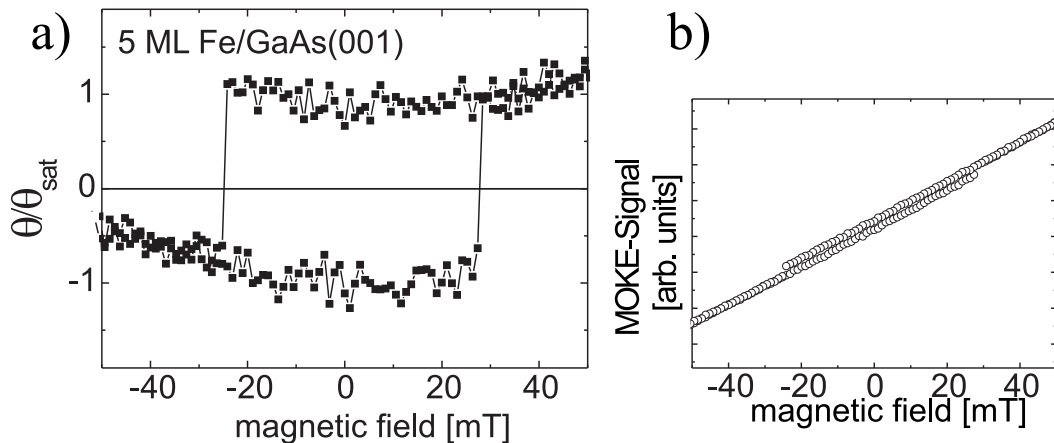


Fig. 4.21.: (a) MOKE hysteresis loop of a 5 ML Fe film deposited on GaAs(001) measured at room temperature with the magnetic field applied along the $[1\ 1\ 0]$ -direction. (b) The original data which includes the Faraday effect caused by the glass finger.

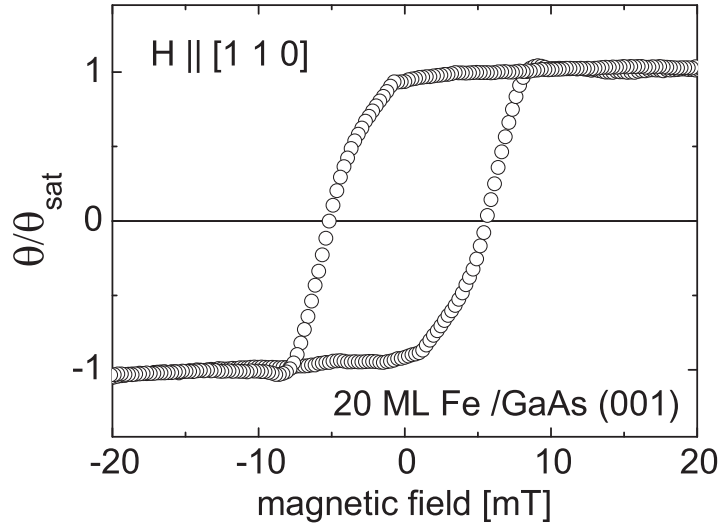


Fig. 4.22.: MOKE hysteresis loop of a 20 ML Fe film deposited on GaAs(001) measured at room temperature with the magnetic field applied along the $[1\ 1\ 0]$ -direction.

the glass finger with the external magnetic field applied substantially along the transmission direction of the light beam. Because of its linearity with the magnetic field, this effect could be subtracted from the original data to yield the hysteresis loop displayed in (a). It represents a square shaped hysteresis which is typical for magnetization measurements along the easy axis of magnetization. If at zero external magnetic field the magnetization were decomposed into magnetic domains, one would expect a reduced Kerr signal which is not the case. The squareness of the hysteresis loop is consequently a proof for a homogeneously magnetized film within the spot size of the laser. The coercive field of this 5 ML Fe film is $H_c = 26 \pm 1$ mT.

The hysteresis loop of a 20 ML Fe film on GaAs measured with *in situ* MOKE is shown in Fig. 4.22 after subtracting the linear background signal. Here, the external magnetic field was also applied along the $[1\ \bar{1}\ 0]$ direction although at this thickness an in-plane reorientation of the easy axis from $[1\ \bar{1}\ 0]$ to $[1\ 0\ 0]$ and $[0\ 1\ 0]$, respectively, is expected. Hence, the remanent magnetization along $[1\ \bar{1}\ 0]$ is only $0.9 M_s$. The coercive field $H_c \approx 6$ mT of this thicker Fe film is reduced compared to the 5 ML which indicates better growth conditions for this film.

Figure 4.23 shows the z -component of the magnetic stray field across the center of an 8 ML Fe/GaAs(001) film of square shape. The fit to the experimental data is also plotted using Eq. (A.4) and gives the best agreement for $h = 5.1$ nm and $M = (1.79 \pm 0.09) \times 10^6$ A/m which is only 4.5 % larger than the bulk value at 295 K.

Figure 4.24 shows the remanent magnetization of Fe monolayers on $\{4 \times 6\}$ -reconstructed GaAs at room temperature as a function of film thickness. Fe was deposited at 300 K as de-

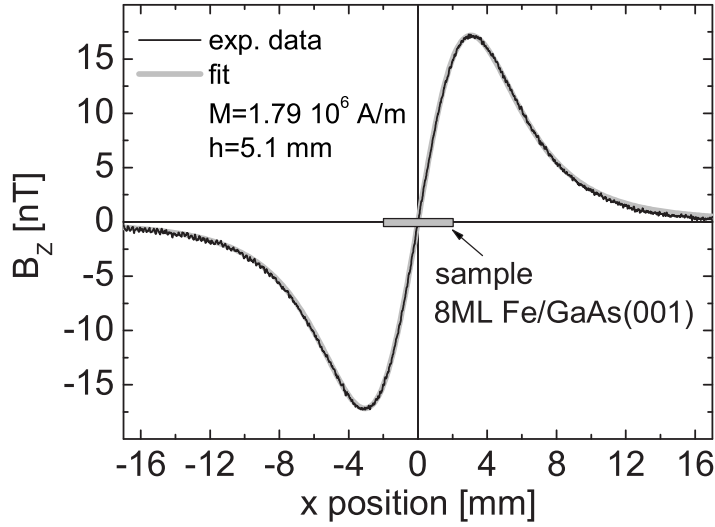


Fig. 4.23.: Experimental B_z line scan across the center of an 8 ML Fe/GaAs(001) film and a fit to the data for a height $h = 5.1$ mm and a magnetization $M = 1790$ kA/m.

scribed above. The compilation of data includes films which were grown in a single evaporation step, and films which were prepared by stepwise evaporation on top of previously measured films at a pressure of 1×10^{-9} mbar during evaporation (base pressure 2×10^{-10} mbar). Below 3 ML Fe, the magnetization is zero at room temperature and sets in between 3 and 4 ML. Up to 5 ML, its value is significantly reduced with respect to the Fe bulk value. Interestingly, at 5 ML Fe film thickness, one observes two trends of the remanent magnetization. Either it has fully evolved to the bulk value or it is reduced by about 25%. Additional Fe deposition on a film which already has the full bulk magnetization at 5 ML does not change the magnetization value. Otherwise, increasing the Fe film thickness of a film which does not have the full bulk magnetization at 5 ML will only gradually increase its magnetization to finally yield the bulk magnetization value at about 10 ML. To get an estimate of how many layers contribute to the FM signal the non FM layers $d_{\text{non-fm}}$ from all thicknesses with a reduced magnetization ($M < M_{\text{bulk}}$) are calculated using $d_{\text{non-fm}} = d_{\text{Fe}}(1 - M/M_{\text{bulk}})$, where d_{Fe} is the nominal thickness of the Fe film, M is the measured remanent magnetization and $M_{\text{bulk}} = 1714$ kA/m is the Fe bulk magnetization at room temperature. The result of this calculation can be taken from Fig. 4.25. With increasing Fe coverage, the number of non-ferromagnetic layers continuously decreases from about 2 non-FM layers at around 4 ML Fe thickness to about 0.5 at a thickness of 10 ML. The two data points (\bullet) from 12 and 20 ML thick Fe films indicate 1 non-FM layer each. They were measured 24 h after they had been prepared. During that time, the chemisorption of residual gases inside the UHV chamber (base pressure 2×10^{-10} mbar), mainly O_2 and

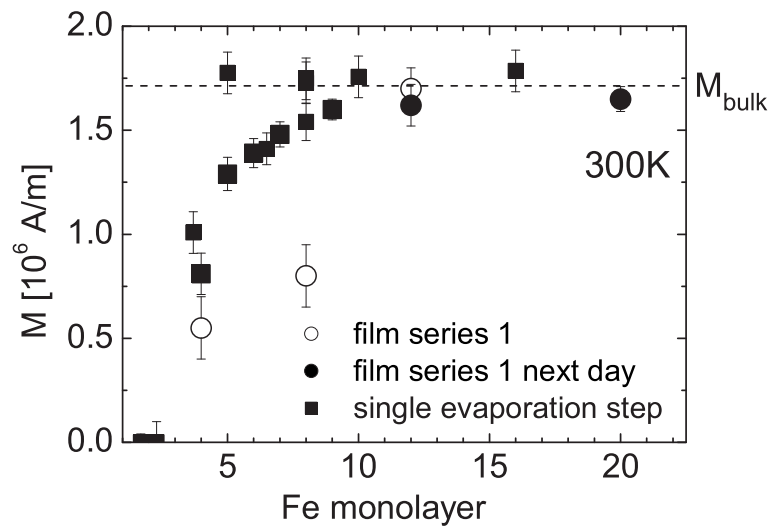


Fig. 4.24.: Remanent magnetization of Fe monolayers on GaAs(001) as a function of film thickness.

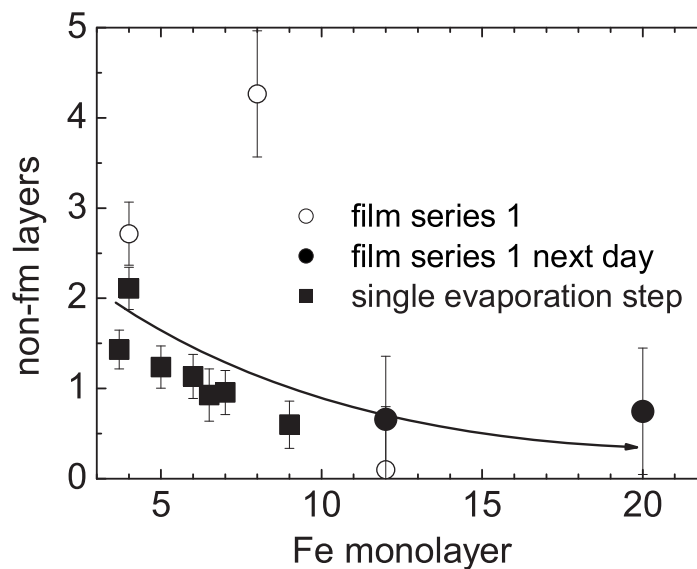


Fig. 4.25.: Calculated non-ferromagnetic (non-fm) layer equivalents from remanent magnetization data of figure 4.24.

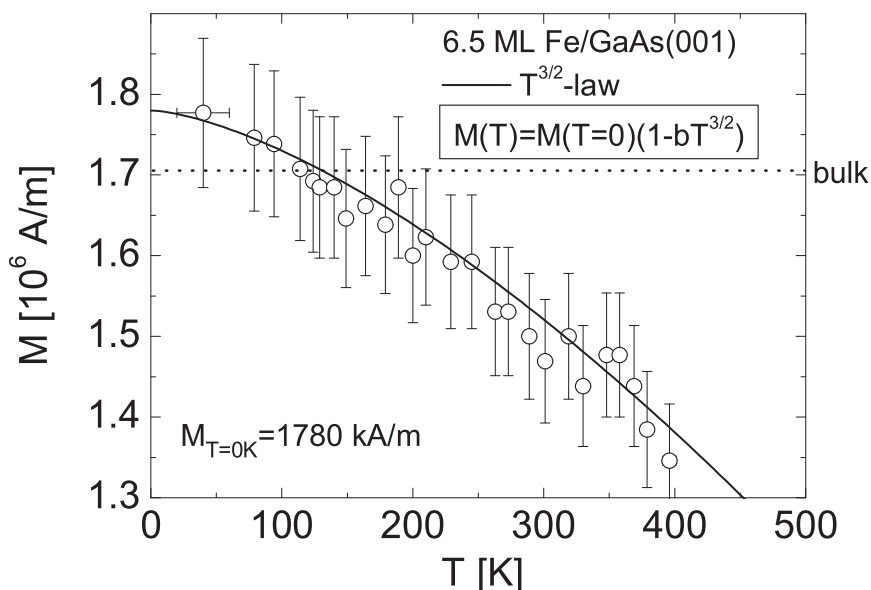


Fig. 4.26.: Remanent magnetization plotted vs. temperature. Fit with spin wave law is plotted as a solid line: $M_{T=0K} = 1780$ kA/m, $B = (2.85 \pm 0.35) \times 10^{-5} \text{ K}^{-3/2}$.

CO, probably had been incorporated into the Fe film and reduced the magnetization. A systematic study on the influence of oxygen exposure on the remanent magnetic signal will be given in Sec. 4.5. It should be noted that one film at a thickness of 8 ML (\circ) has a reduced magnetization with respect to the other films. However, after depositing additional 4 ML Fe the magnetization of this 12 ML Fe film equals the bulk value. Therefore, one must conclude that the 8 ML Fe film was incidently not magnetized before the measurements and not in a single domain magnetic state. The decrease of M for several Fe films at low Fe coverage is most likely be influenced by a rough surface topography of the substrate which 'delays' the coalescence of the iron islands. In Ref. [13] it was reported that this island coalescence governs the onset of the FM phase. The magnetization serves as a measure of how much of the Fe islands are interconnected. In conclusion, the formation of intermetallic compounds at the interface can be excluded since the magnetization recovers the Fe bulk value around 10 ML, which indicates the absence of non-FM interface layers.

In Fig. 4.26 the remanent magnetization of 6.5 ML Fe on GaAs(001) is presented as a function of temperature for $40 \text{ K} < T < 400 \text{ K}$. With increasing temperature the magnetization decreases and can be described with the so-called $T^{3/2}$ spin wave law (Bloch's law) which is explained further down (see Eq. (4.10)) and includes the Bloch constant B . It is plotted as a solid line in the figure. The fit yields a Bloch constant of $B = (2.85 \pm 0.35) \times 10^{-5} \text{ K}^{-3/2}$ and

the ground state magnetization $M(T = 0) = (1.78 \pm 0.06) \times 10^6$ A/m. The bulk ground state magnetization (T=0 K) of Fe is about 1.746×10^6 A/m [120]. Hence, the measured value is increased by about 2.0% with respect to the bulk value. There are two possible reasons for this finding. a) The thickness of the Fe film is wrong by 5 %; which is possible due to the error bar of the quartz microbalance. However, several films show a slight increase of the magnetization similarly to the one above. Within the error bar, the enhancement of M might be due to an over-estimation of d . b) Fe magnetic moments on the Fe/vacuum interfaces are enhanced. *Ab initio* calculations using the full potential linearized augmented plane wave (FLAPW) method on the magnetic properties of seven monolayer thick Fe(100) predict increased magnetic moments of $3.01 \mu_B$ in the first monolayer (vacuum interface layer), $2.36 \mu_B$ in the second and after all $2.42 \mu_B$ in the third layer [121]. Assuming that all remaining layers below have bulk-like magnetic moments of $2.22 \mu_B$, including the layer at the Fe/GaAs interface the total magnetization of the 6.5 ML Fe film is 1.833×10^6 A/m. This value is even 5.0% bigger than the Fe-bulk value. Yet one should also consider that the calculated surface magnetic moments emanate from a perfectly ordered, not strained and abrupt interface which is only conditional applicable for Fe films on GaAs. Therefore, an increase of magnetic moments for a not perfect surface probably turns out smaller. A clear answer of which both possibilities are true cannot be given.

At 400 K, the remanent magnetization is reduced by about 25 % with respect to 0 K. M of bulk Fe decreases by only 3 % in the same temperature interval. This stronger decrease in 6.5 ML Fe is attributed to the finite size effect, i.e. a decrease of T_C with decreasing film thickness. Within this model, the Curie temperature as a function of film thickness d can be expressed by a scaling law with the critical exponent ν , i.e. $T_C(d)/T_C(\text{bulk}) = 1 - C \cdot d^{1/\nu}$, where C is a constant [122]. However, this model is not applicable for the Fe/GaAs system where the onset of ferromagnetism is governed by a percolation phenomenon. To describe the thickness dependence of the Curie temperature a power law was proposed $T_C(p) \propto (p/p_C - 1)^\phi$ with a percolation parameter $p > p_C$ and a critical exponent ϕ [47]. To avoid interdiffusion, the magnetization of a 6.5 ML Fe film could not be measured up to $T_C(6.5 \text{ ML})$. However, for thinner films, measurements have been carried out up to and above T_C .

The remanent magnetization vs. T of a 3.7 ML Fe film is shown in Fig. 4.27. The double logarithmic plot of M/M_0 over $(T_C - T)/T$ was chosen to find the critical exponent β , since near the paramagnetic-ferromagnetic phase transition at T_C the magnetization should follow the relation²:

$$M(T) = M(0)(1 - (T/T_C))^\beta \quad (4.9)$$

The magnetization vanishes at around $392 \text{ K} \pm 5 \text{ K}$. To determine T_C more accurately, the magnetization data in Fig. 4.27 are plotted for 5 different T_C between 389 K and 393 K. The data are linearly fitted from T_C to $0.1 T_C$ and the slope yields the experimental critical exponent

²A short review on the physical meaning of critical exponents is given in the appendix A.5

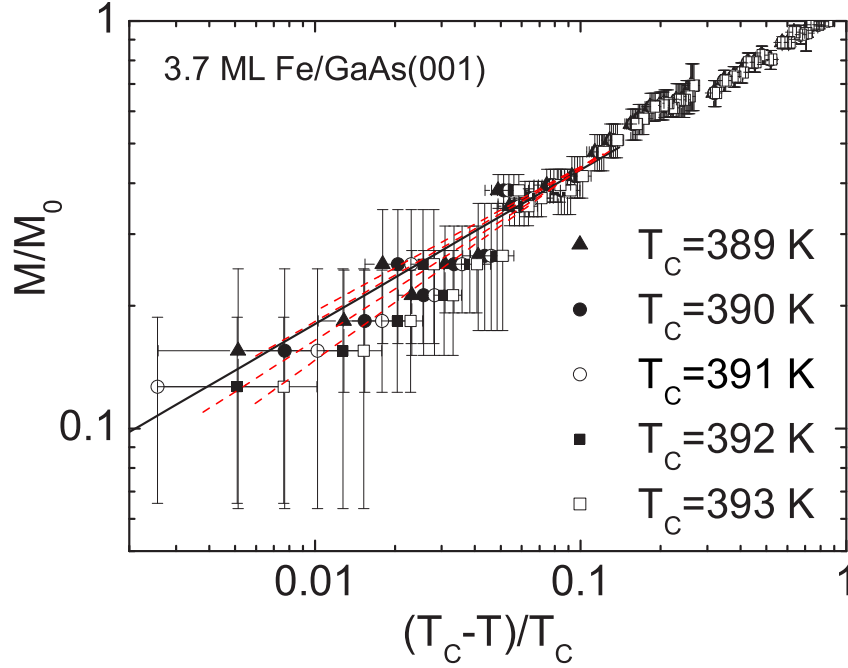


Fig. 4.27.: Double logarithmic plot of the remanent magnetization vs. reduced temperature $(T_C - T)/T_C$. The same data are plotted for different T_C with linear fits within an interval from T_C to $0.1 T_C$.

T_C	β	error
389 K	0.36	± 0.132
390 K	0.38	± 0.127
391 K	0.38	± 0.112
392 K	0.42	± 0.124
393 K	0.47	± 0.158

Table 4.2.: Critical exponent β from linear fits of data points in Fig. 4.27 in a temperature interval from T_C to $0.1 T_C$.

β . The Curie temperature yielding the smallest difference of the linear fit with the experimental data is chosen. It corresponds to $T_C = 391$ K with $\beta = 0.38$ ($10^{-2} < (T_C - T)/T < 10^{-1}$). In Tab. 4.2.1, the critical exponents are shown for various Curie temperatures. BENSCH *et al.* [47] measured the critical exponent of a 3.4 ML Fe film on GaAs(001)-(2 \times 6) with MOKE and found an exponent $\beta = 0.26 \pm 0.02$ ($10^{-3} < (T_C - T)/T < 10^{-1}$), which is very close to the effective critical exponent of a 2D-XY model of finite size ($\beta = 3\pi/128 \approx 0.23$) [123]. In Fig. 4.28, $M(T)$ for the 3.7 ML Fe film is plotted on a linear scale. In addition, power laws for different critical exponents β are plotted. The $T^{3/2}$ -law, which is discussed further down, is also plotted but can strictly only be applied from 0 to $0.3 T_C$. The experimentally obtained $\beta = 0.38$ from SQUID analysis is significantly bigger than the prediction of the 2D-XY model, but also too small to be explained by mean field theory. If one compares the measured data to

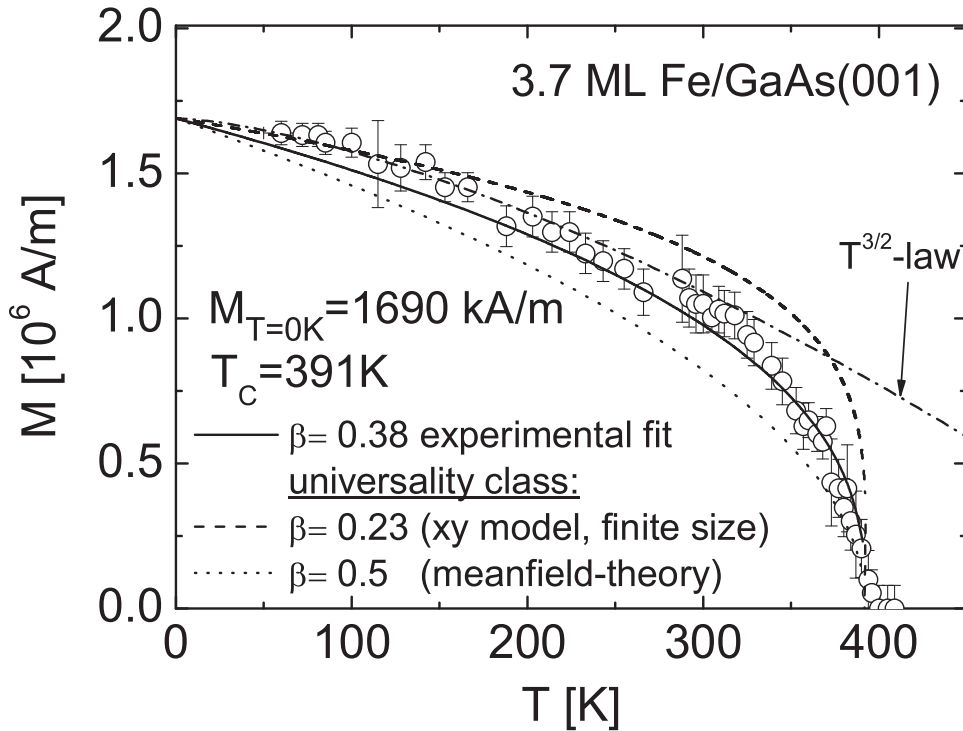


Fig. 4.28.: Remanent magnetization plotted vs. temperature. Fits are given for different universality classes and the spin wave law.

the predictions of the 2D-XY model it is obvious that the remanent magnetization above 200 K, and especially in the vicinity of T_C , is significantly smaller. The discrepancy in the difference of $M(T)$ behavior might be due to a temperature dependent domain formation, since the film was not re-magnetized before the measurements at each temperature.

At a film thickness of 2.3 ML Fe, the Curie temperature is decreased to $T_C = 170 \text{ K} \pm 6 \text{ K}$ (see Fig. 4.29). A fit using Bloch's $T^{3/2}$ -law yields $M(T=0) = 0.76 \pm 0.03 \cdot 10^6 \text{ A/m}$, which is a reduction of 57% with respect to the bulk value. In the model of percolating Fe islands, one can conclude that the coalescence of islands is not yet finished and roughly half of the islands do not touch each other. The percolation of the islands, on the other hand, switches on the direct exchange and causes the abrupt onset of ferromagnetism. The determination of a critical exponent of the magnetization data is not meaningful due to the relative large spread of the data points and to few data near T_C . The reduction of M with T is even less abrupt than for the 3.7 ML Fe film, which as well can be explained by temperature dependent domain formation which here starts at an even lower temperatures. An initial fit with a power law dependence yielded a nonphysical exponent $\beta = 0.7$ and is therefore not shown. The fit for the mean field theory value of $\beta = 0.5$ is presented but does not show good accordance to the data.

The temperature dependence of the spontaneous magnetization $M_s(T)$ for $T < 0.5T_C$ for

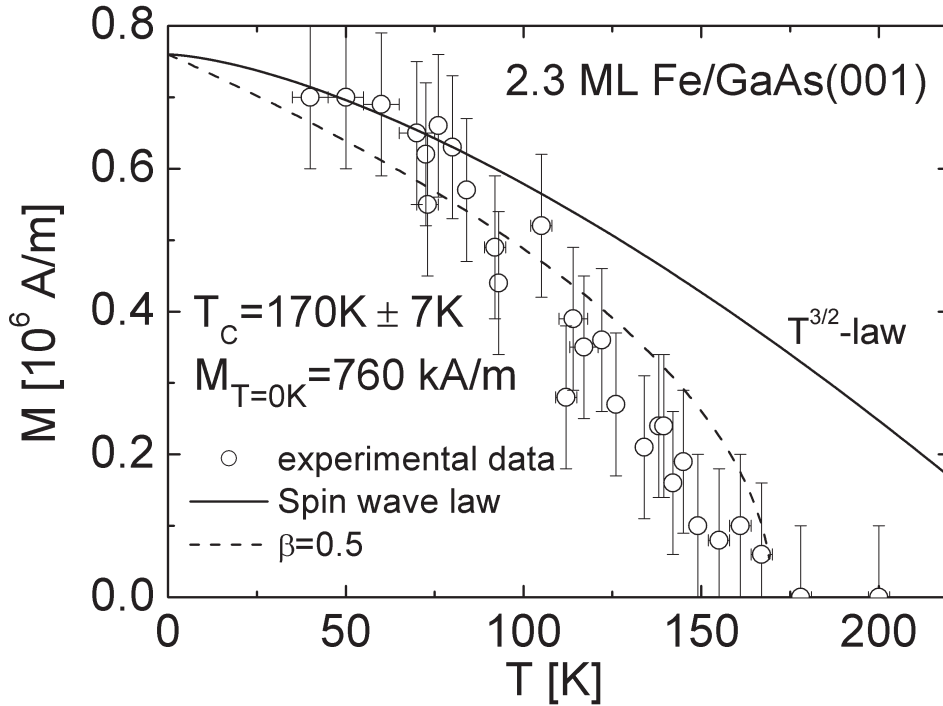


Fig. 4.29.: Remanent magnetization plotted vs. Temperature. Fits are plotted for a critical exponent $\beta = 0.5$ (mean-field theory) and the spin wave law.

the most bulk ferromagnetic materials can be described with Bloch's law

$$M_s(T) = M_s(0) (1 - BT^{3/2}) \quad (4.10)$$

Bloch's law results from a linearized spin-wave theory neglecting higher order terms in the magnon dispersion relation. Many experimental investigations show that the temperature dependence of the spontaneous magnetization of high-quality continuous thin films can be also well described by a $T^{3/2}$ -law, although no theories predict this behavior for a 2D system [124,125,126]. However, it has been shown by MATHON and AHMAD that an 'effective $T^{3/2}$ -law' is valid for two-dimensional system in a certain temperature range [127].

In Fig. 4.30, the temperature dependence of the remanent magnetization of continuous 3.7 and 6.5 ML Fe films is presented as a function of $T^{3/2}$ for a temperature range from 40 to 400 K. The remanent magnetization was measured along the easy [1 1 0] direction and the remanent magnetization is assumed to be equal to the saturation magnetization. The magnetization values were normalized to the value at $T = 0$ K, which was obtained from fits according to Bloch's law.

The data can be well described by Eq. (4.10). The spin wave Bloch parameter B and the ground state magnetization were determined from the fits and are presented in Table 4.3. The data for bulk-Fe are also given.

Fig. 4.31 shows the spin wave Bloch parameter B as a function of the inverse thickness $1/d$. The solid squares are the Bloch parameters obtained in this work while the circles represent

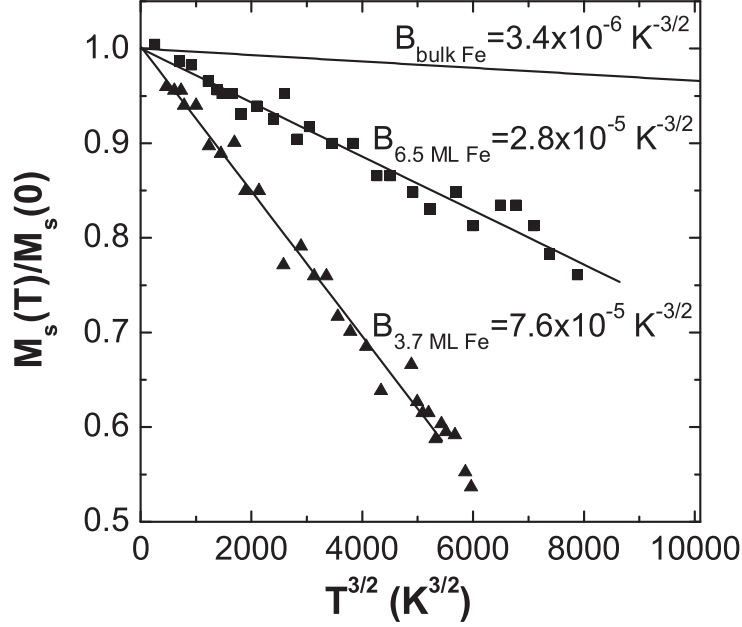


Fig. 4.30.: Temperature dependence of the normalized spontaneous magnetization for 3.7 and 6.5 ML of Fe on GaAs (001). The solid lines are fits according to Bloch's $T^{3/2}$ -law. The corresponding Bloch parameters B are shown for each film thickness. The temperature dependence of bulk-Fe with $B = 3.4 \times 10^{-6} \text{ K}^{-3/2}$ (Ref. [128]) is also represented.

sample	$M_s(0 \text{ K})$ [10^6 A/m]	B [$10^{-5} \text{ K}^{-3/2}$]	D [$\text{meV}\text{\AA}^2$]
3.7 ML Fe/GaAs	1.71 ± 0.07	7.5 ± 0.4	36.37
6.5 ML Fe/GaAs	1.78 ± 0.06	2.85 ± 0.35	70.21
bulk-Fe	1.746 (Ref. [120])	0.34 ± 0.02 (Ref. [128])	290.1

Table 4.3.: Ground state spontaneous magnetization $M_s(0 \text{ K})$ and the Bloch parameter B determined from fits according to Bloch's spin wave law. The spin wave stiffness constant D calculated according to Eq. (4.11) is also presented.

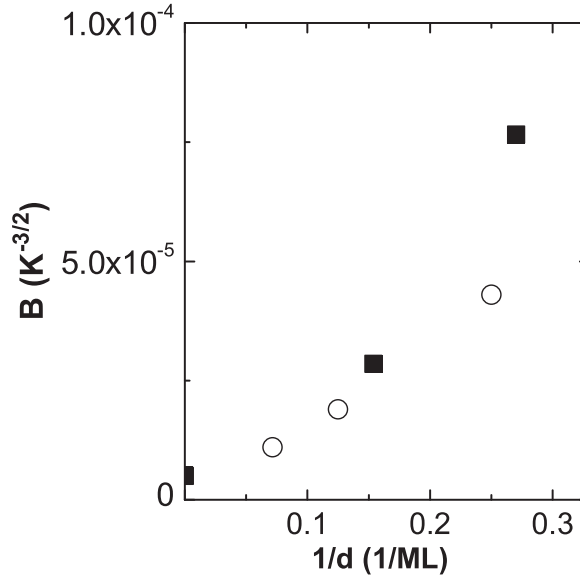


Fig. 4.31.: Spin wave Bloch parameter as a function of the inverse thickness d for Fe thin films deposited on GaAs (001). The solid squares are the Bloch parameters determined in this work. The circles are taken from Ref. [126].

data from Ref. [126]. The data from this work are in agreement with the earlier ones. The spin wave Bloch parameter increases with decreasing thickness. It does not scale linearly with $1/d$ as it was observed for thin films with very weak anisotropies, such as Fe on Au(001) [129] and $\text{Fe}_{70}\text{Co}_{30}$ on Au(001) [130]. A linear dependence $B(1/d)$ is expected for the case that the energy of the lowest spin wave mode is independent of the film thickness. This is only true in the absence of large anisotropies [131]. The presence of a large anisotropy in Fe/GaAs(001) films causes a thickness dependence of low spin wave energies and, hence, a non-linear $B(1/d)$ dependence.

The spin-wave parameter or the Bloch parameter B is related to the spin wave stiffness constant D through the expression [132]

$$D = \frac{k_B}{4\pi} \left(\frac{\zeta(3/2)g\mu_B}{M_s(0)B} \right)^{2/3} \quad (4.11)$$

where $\zeta(3/2)$ is the Riemann zeta function, g is the spectroscopic splitting factor which is equal 2.09 for Fe, μ_B is the Bohr magneton, and k_B is the Boltzmann constant. The spin wave stiffness constant D is calculated and the results are presented in Table 4.3. We observe a strong decrease of the spin wave stiffness constant with decreasing Fe thickness. The spin wave stiffness constant is proportional to the exchange coupling energy between neighboring spins and measures the energy of spin waves. Because of a reduced coordination number of the surface spins, the

exchange energy per spin at the surface is smaller than in the volume. Hence, the energy of a spin wave with a given wave vector \vec{k} is lower.

4.3. Magnetization reversal of Fe films on GaAs

In order to study the details of magnetization reversal of thin Fe films on GaAs, a Pt capped 15 ML Fe film was measured by Kerr microscopy at room temperature. Figure 4.32 shows a hysteresis loop which has been recorded using the longitudinal magneto-optical Kerr Effect with p-polarized light. The external magnetic field was applied along the [1 1 0] direction of the substrate. Basically, a square hysteresis is observed, which, however, show a rather smooth approach to saturation after magnetic field reversal (marked by (*)). Square shaped magnetization curves are typical for measurements along the easy axis of magnetization. The coercive field is found at about $H_c = 4$ Oe. The same sample has also been investigated by Kerr *microscopy* with the magnetic field applied along the easy axis, i.e. the [1 1 0] direction. The magnetization reversal process typically commences somewhere in the center of the film. The domains nucleate in the direction of the reversed magnetic field (Fig. 4.33 (a)) and grow by domain wall displacement in all directions (Fig. 4.33 (b)). One may note the zig-zag walls between the oppositely oriented domains. The formation of 'head-on' magnetic domains in thin films results in a high 'magnetic charge' density. By configuring a zig-zag shaped wall, the charge density is reduced [133]. By increasing the zig-zag angle, the charge density decreases at the expense of wall surface. Another Kerr microscopy image shows an area of the film close to the film edge. Part of the substrate is also visible in the upper area of the image. One notices that the

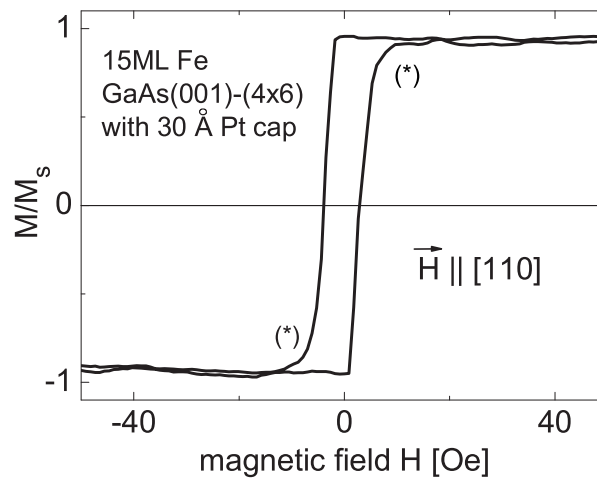


Fig. 4.32.: Longitudinal MOKE measurement along the [1 1 0] direction.

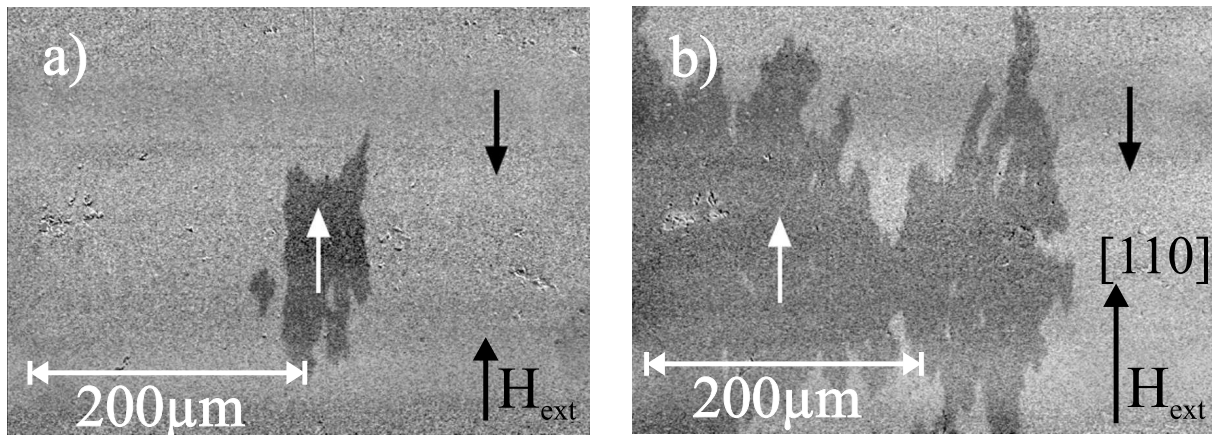


Fig. 4.33.: Kerr microscopy images of a 15 ML Fe film with 30 Pt deposited on $\{4 \times 6\}$ -reconstructed GaAs(001). (a) nucleation of a domain (white arrow) in the direction of the reversed magnetic field. b) same sample position with increased field strength. Note, that the field strength was not quantified.

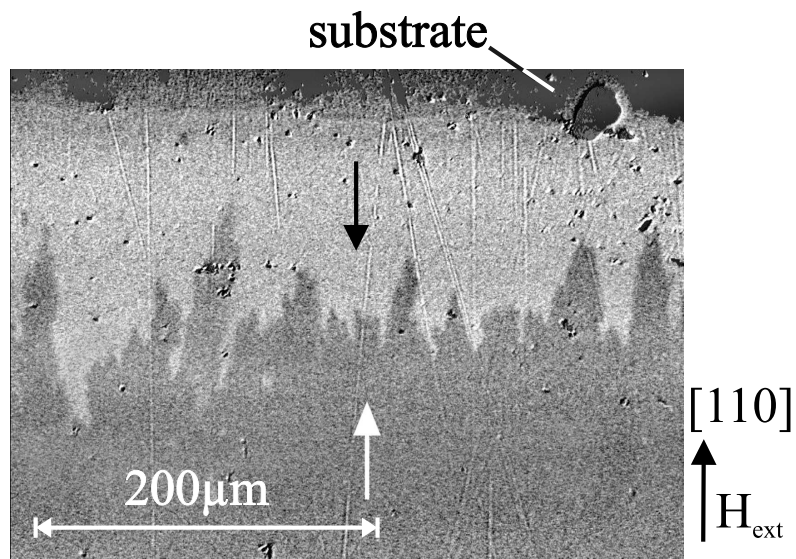


Fig. 4.34.: Kerr microscopy image similar as in Fig. 4.33 but taken at the edge of the Fe film in the presence of a reversed magnetic field.

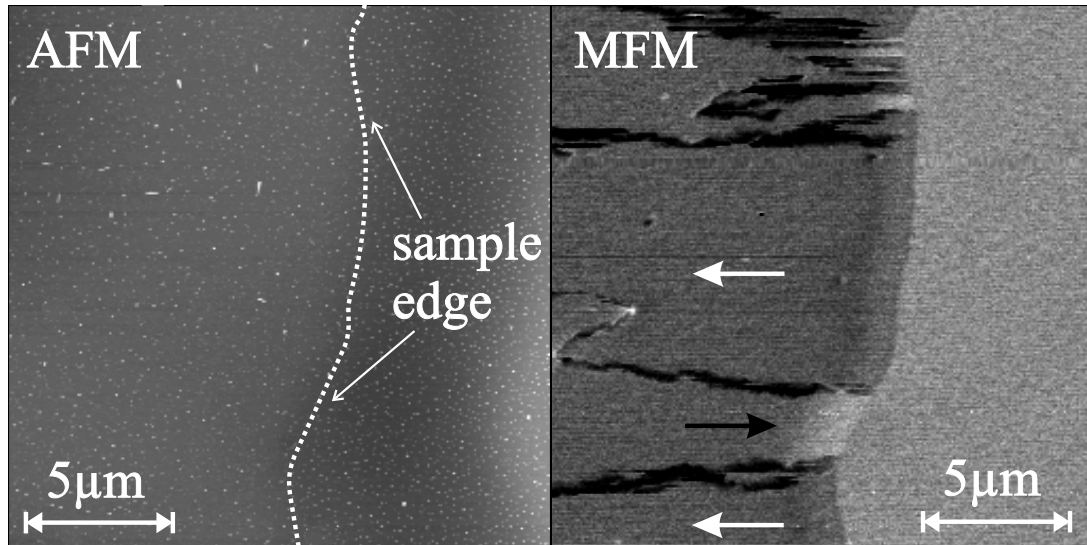


Fig. 4.35.: MFM image of a 15 ML Fe film on $\{4 \times 6\}$ GaAs(001) with 30 Pt cap layer. The MFM tip was magnetized along the $-z$ -direction prior to measurement. Arrows indicate the magnetization direction of the domains.

magnetization reversal does not start from the edge of the sample, but the reversed magnetic domain approaches the sample edge from the middle of the sample. At first glance, this is surprising since, as shown in Sec. 2.2, the demagnetizing field which emerges from the sample edge should lower the energy barrier for the reversal of M near the edge. However, one has to consider that the evaporation through an aperture yields a continuously varying thickness near the edges. This reduces demagnetizing effects at the film boundaries. Secondly, the film boundary is corrugated on a $\approx 10 \mu\text{m}$ scale which also reduces demagnetizing effects.

Kerr microscopy images were also taken in the magnetic remanent state of the sample. Notably, no magnetic domains were observed after the film has been saturated, which justifies the assumption of single domain magnetic films for the stray field calculation in Sec. 2.3.

Magnetic domain images with higher resolution ($\approx 50 \text{ nm}$) were obtained by magnetic force microscopy [134]. Since in the magnetically saturated state MFM was not capable of visualizing magnetic domains the sample was demagnetized in an alternating magnetic field along the easy axis with continuously reduced field amplitude. Figure 4.35 shows an MFM image of the capped 15 ML Fe sample on GaAs(001)- (4×6) taken close to the film edge (dotted line). The AFM image shown on the left was simultaneously recorded when the MFM image was taken. The film edge is difficult to see in the left image, but runs from the top to the bottom as indicated. It becomes more obvious in the MFM image, where a sharp change in contrast is visible at the sample edge. The easy axis of magnetization is along the vertical direction (arrows). Before recording the image, the magnetic tip was magnetized along the $-z$ -direction as indicated in Fig. 4.36. Attractive interaction between tip and sample is visualized by dark image contrast whereas repulsive interaction is shown with bright contrast.

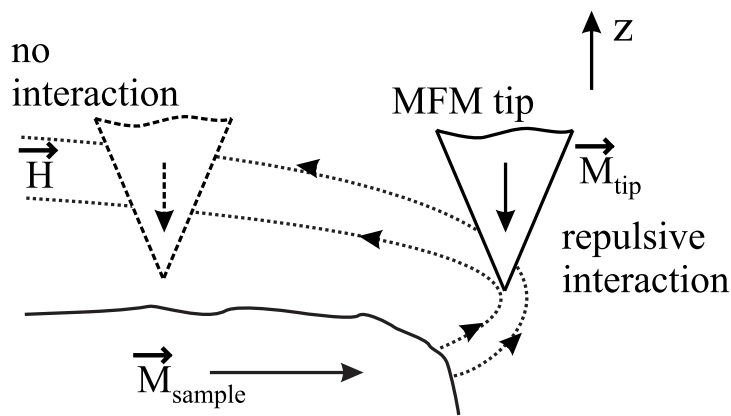


Fig. 4.36.: An MFM tip is magnetized along the $-z$ -direction, the sample in the plane of the film. The magnetic stray field gives rise to repulsive interaction at the sample edge and to no interaction above the film.

In Fig. 4.36, a magnetic domain at the sample edge points to the right. The schematic stray field is also indicated by the dashed line. Near the sample edge, the stray field will have a dominating z -component which in the present case will result in a repulsive interaction between tip and sample (bright contrast in the MFM image). Above the in-plane magnetized sample, $\vec{M}_{tip} \cdot \vec{H} \approx 0$ and therefore, no contrast is expected. The bright-dark contrast variation (Fig. 4.35) at the film boundary can now be attributed to different magnetization directions of the domains. The magnetization directions are shown by the black and white arrows in the image. Note that the domain walls in Fig. 4.35, which are probably of Néel type, have an attractive interaction with the MFM tip. This interaction is understandable from the interaction of the tip's stray field with the sample. At a lift scan height of $d = 90$ nm, the tip's stray field is about 100 Oe [135]. Consequently, the tip's stray field forces the magnetic moments in the domain wall to turn out-of-plane during the measurement which always results in an attractive interaction. After the MFM tip moves away from the domain wall, the magnetic moments in the domain wall rotate back to their original orientations. Like in many investigations of soft magnetic materials, the magnetic microstructure is influenced during the measurement by the MFM tip.

Figure 4.37 shows an MFM image taken at the center area of the film. The two features marked by a (*) represent small reversed magnetic domains, within which the magnetization is pointing into the exact opposite direction as the magnetization direction of the surrounding magnetic domain (white arrow). The center of the MFM image shows a domain wall generally extending from left to right, separating two magnetic domains which are oriented to the left and to the right, respectively. Note the alternating bright and dark image contrast along sections of the domain wall. Here, the observed change in contrast implies that the magnetic moments within the domain wall are obviously much less affected by the stray field of the magnetic tip

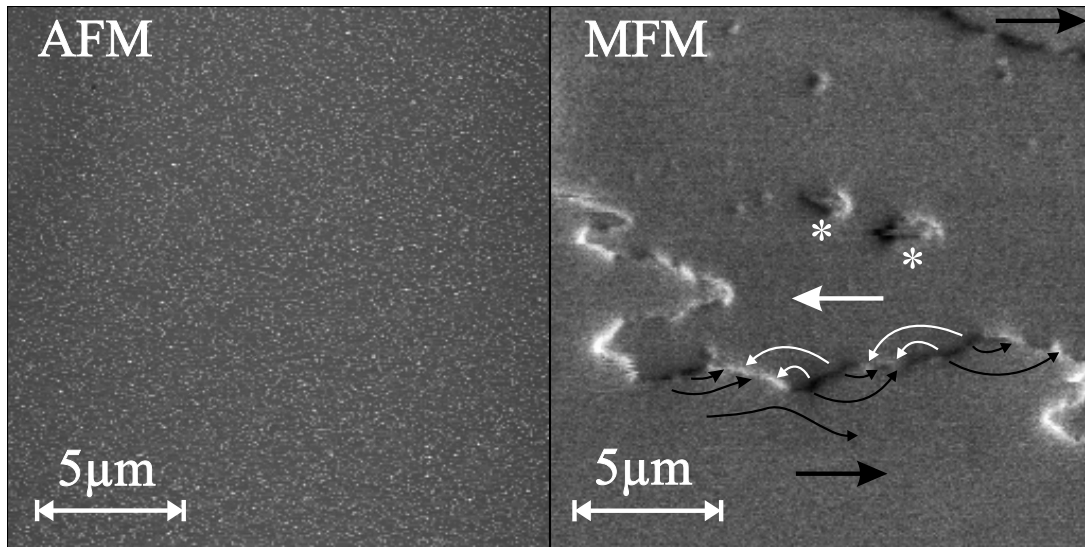


Fig. 4.37.: MFM image of the same sample as in Fig. 4.35 but imaged in the middle of the film.

than in the case as discussed above for the domain wall close to the sample edge. The observed contrast results from an alternating attractive (dark) and repulsive (bright) interaction of magnetic moments within the wall with the magnetic tip. Such a contrast may only occur if the arrangement of magnetic moments within the domain wall is much more stable, whereby the magnetic moments do not follow the stray field of the magnetic tip (as discussed above). Taking into account the direction of the magnetization within the tip (being oriented into the $-z$ direction), the contrast change along the domain wall can be interpreted by assuming a magnetization orientation close to the domain wall, as indicated within Fig. 4.37 by black and white arrows. Here, any 'head-to-head' orientation of the magnetization represents a source of magnetic stray field emerging from the sample in $+z$ direction, and thus leading to a repulsive interaction with the magnetic tip (bright image contrast). A 'tail-to-tail' orientation of the magnetization produces a sink of magnetic stray field where the magnetic field is oriented in $-z$ direction above the sample, and thus leading to an attractive interaction with the magnetic tip (dark image contrast). The resulting 'waviness' of the magnetization, which certainly extends into the areas above and below the domain wall, resembles the magnetization distribution close to a so-called 'cross-tie' wall [136]. The 'zig-zag'-like domain wall can be thought of as a precursor of such a cross-tie wall where within the white and black areas, the magnetization is starting to turn upwards and downwards respectively, thereby forming the later 'Bloch-lines' of the cross-tie wall. Future Lorentz-microscopy investigations could help to confirm the character of such a domain wall which is typical for the cross-over region with respect to the film thickness between pure Bloch-like and Néel-like domain walls.

4.4. In-plane spin reorientation transition for Fe/GaAs films

The magnetic anisotropy of a few monolayers of Fe on GaAs(001) is dominated by a strong uniaxial anisotropy ($K_{2||} < 0$) with easy in-plane axis along the $[1\ 1\ 0]$ -direction which stems from the Fe/GaAs interface [24,45]. Because this interface anisotropy contribution depends on $K_{2||}/d$ according to Eq. (2.14), it becomes less and less important with increasing film thickness d . The influence of the fourfold anisotropy $K_4 > 0$ will increase steadily. The easy axes of magnetization of this volume anisotropy are along the $\langle 1\ 0\ 0 \rangle$ -directions. Since the uniaxial out-of-plane anisotropy $K_{2\perp} > 0$ is small compared to the shape anisotropy F_{shape} , the magnetization will always lie in the film plane with no external field applied. Therefore, it is expected that the easy axis of magnetization will rotate from the $[1\ 1\ 0]$ direction (thin film limit) to either the $[1\ 0\ 0]$ or $[0\ 1\ 0]$ -direction with increasing film thickness. To illustrate this situation, a sketch of the free energy density as a function of in-plane angle is plotted in Fig. 4.38 according to Eqs. (2.11) and (2.13) ($\delta = \pi/4$ and $\theta = \pi/2$). In (a) the fourfold (K_4) and uniaxial in-plane ($K_{2||}$) anisotropy energy is plotted separated. The minima of the energy are the easy directions of the magnetization and marked by black dots. In the uniaxial case, the equivalent equilibrium angles are 45° and 225° . This also applies to the fourfold anisotropy equilibrium angles $0^\circ/90^\circ/180^\circ/270^\circ$. Here, the superposition of both anisotropies is plotted for different ratios $K_4/K_{2||} < -1$. With increasing $K_4/K_{2||}$, the minimum shifts from the $[1\ 1\ 0]$ direction (135°) toward the $[0\ 1\ 0]$ - and $[1\ 0\ 0]$ -directions, respectively and two local minima (black and white dots) are observed. The following discusses the reorientation from $[1\ 1\ 0]$ to $[1\ 0\ 0]$. Figure 4.38 (b) shows the calculated equilibrium angle ϕ vs. the ratio of the anisotropy constants $|K_4|$ and $|K_{2||}|$. As long as $|K_4|$ is smaller than the twofold anisotropy constant $|K_{2||}|$ the easy axis of magnetization is the $[1\ 1\ 0]$ direction. Above $|K_4/K_{2||}| > 1$, the easy axis continuously rotates quickly towards the $[1\ 0\ 0]$ direction for $|K_4/K_{2||}|$ only slightly larger than 1. For larger $|K_4/K_{2||}|$, the $[1\ 0\ 0]$ direction is asymptotically approached and never fully reached.

Table 4.4 lists the anisotropy constants $K_{2||}$ and K_4 given in Ref. [45] which contain both, volume and interface contributions, for different thickness of the Fe layers on $\{4 \times 6\}$ -reconstructed GaAs(001) at 300 K. The values are derived from angular dependent FMR measurements under UHV conditions. Also given are the respective anisotropy fields which are direct fit parameters from the angular dependence. Up to a thickness of at least 7 ML Fe no fourfold anisotropy can be measured. Only from about 11 ML Fe onwards the fourfold anisotropy sets in and reaches the bulk value at about 20 ML Fe film thickness. At this thickness, just a small value of $K_{2||} = -0.042 \times 10^5 \text{ J/m}^3$ is measurable. It increases by a factor of more than 20 in the case of a 5 ML Fe film, since it is mainly an GaAs-Fe interface contribution. We use these values to calculate equilibrium angles ϕ by minimizing the free energy arising from the

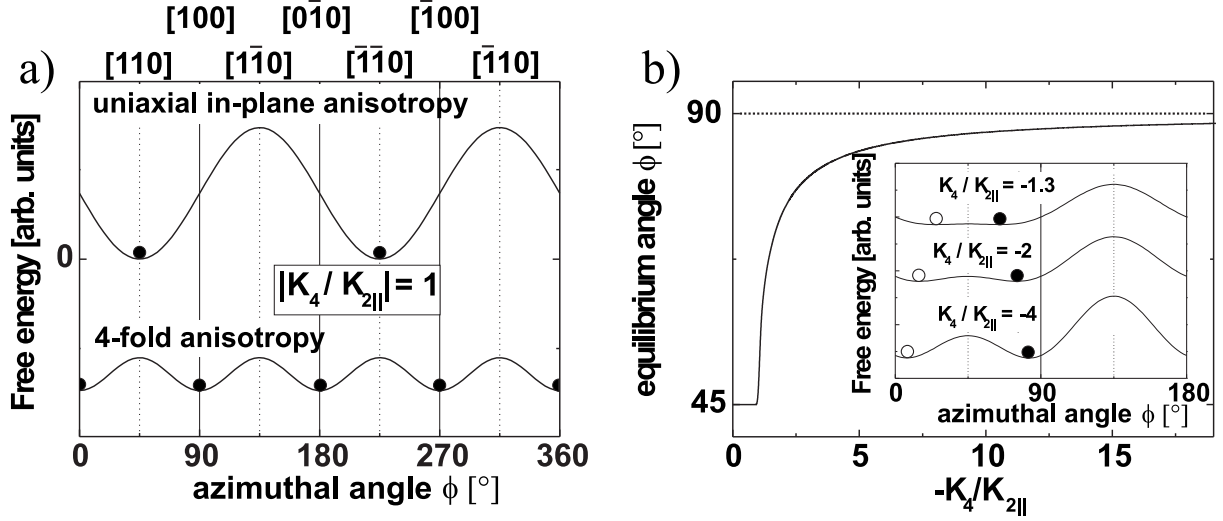


Fig. 4.38.: (a) Free Energy density F as a function of azimuthal (in-plane) angle ϕ for the uniaxial in-plane and fourfold anisotropy contribution ($K_4 > 0$, $K_{2||} < 0$). (b) Calculated equilibrium angle ϕ as a function of $-K_4/K_{2||}$. Superposition of $K_{2||}$ and K_4 for various ratios $|K_4/K_{2||}|$ (inset).

sum of Eqs. (2.11) and (2.13) for the in-plane case. The results of this calculation are shown graphically in Fig. 4.39 as solid squares. Up to 7 ML Fe, the easy axis of magnetization is along $[1\ 1\ 0]$ since $K_4 = 0$. As K_4 increases, the reorientation of the easy axis toward the $[1\ 1\ 0]$ -direction starts from about 10 ML and finishes at about 20 ML. The line in the graph is plotted as a guide to the eye. This expected behavior was independently confirmed by measuring the in-plane angle of \vec{M} by the SQUID method presented in Sec. 4.1.4. The open symbols in Fig. 4.39 show the results, which are in reasonable agreement to the angles determined from the FMR analysis. The small difference might be due to the different modes of film preparation, i.e. for SQUID measurements by stepwise deposition on thinner layers. The reorientation of the

Thickness (ML)	K_4 (10^5 J/m 3)	$K_{2 }$ (10^5 J/m 3)	$\frac{K_4}{M}$ (mT)	$\frac{K_{2 }}{M}$ (mT)
bulk	0.47	-	27.5	-
20	0.46	-0.043	27	-2.5
15	0.44	-0.08	26	-4.7
11	0.3	-0.29	17.6	-17
7	0	-0.59	0	-34
6	0	-0.85	0	-50
5	0	-1.02	0	-60

Table 4.4.: Anisotropy constants and fields at 300 K measured with FMR for various film thicknesses from Ref. [45].

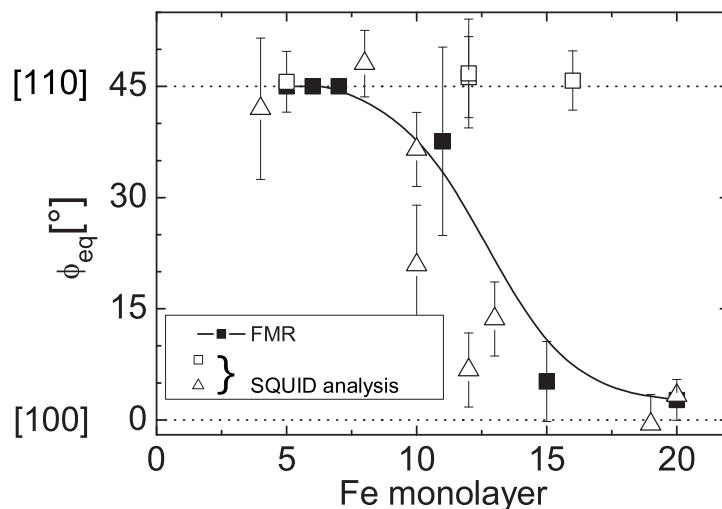


Fig. 4.39.: Calculated in-plane equilibrium angles from magnetic anisotropy constants measured with FMR (Ref. [45]) and measured equilibrium angles from SQUID data analysis.

film series measured with FMR starts at a thickness above 7 ML and is completed at about 20 ML Fe. The SQUID data (Δ) of some Fe films show a reorientation starting at slightly lower Fe thickness. Measurements of other Fe films with SQUID (\square) still exhibit a [1 1 0]-easy axis of magnetization at a thickness of 16 ML. Contrarily, in the literature, Fe films showed the in-plane reorientation at 40 to 50 ML [24,21,44,137,138], which are different from the results in Ref. [45] and the present SQUID measurements. The critical Fe film thickness seems to depend on the individual substrate preparation. It is worth noting that the present measurements, as well as the ones in Ref. [45], use the same substrate several times. After the measurements, the films are sputtered and the substrate is prepared as described in Sec. 4.2. After several preparation cycles, the GaAs surface roughness is likely to increase, which may result in a reduced interface anisotropy contribution of $K_{2||}$ and might explain that for films with smaller $K_{2||}$ the reorientation occurs at lower film thickness.

It should be noted that the easy axis of magnetization is defined by the minimum of the free energy (see Fig. 4.38 (b)) and depends on the exact value of the anisotropy constants. Another point is the presence of two symmetric in-plane easy axes which are energetically equally favorable. If the magnetic field for sample saturation is not aligned perfectly along [1 1 0], which may be the case in the experiment, one axis is preferred. In the case of a 'perfect' alignment of the magnetic field, the sample magnetization could break up into domains oriented along both symmetry axes.

4.5. Influence of oxygen exposure on the magnetic properties of Fe films

The physical properties of iron oxides have been studied for more than half a century [139]. Among the most important stoichiometric iron-oxygen compounds - there exist a total of 16 iron oxides including hydroxides and oxide hydroxides - are wüstite (FeO), haematite (α -Fe₂O₃), maghemite (γ -Fe₂O₃) and magnetite (Fe₃O₄). An overview of the physical properties of these iron oxides is given in Tab. 4.5. Wüstite is a black iron oxide which only contains divalent Fe. Normally, it is found to be nonstoichiometric with a deficiency in cations (Fe_{1-x}O). Haematite prevails in nature and is of significant importance as a principal component in ore, spread in industrial processes. It exists in the corundum structure with an hcp anion packing. It is also an extremely stable iron oxide and often the final product of iron oxide transformations. The ferromagnetic magnetite contains both divalent (Fe²⁺) and trivalent ions (Fe³⁺) in equal amounts, and has an inverse spinel structure. Isostructural with magnetite, maghemite contains only trivalent Fe³⁺, but with a deficiency of cation sites.

Haematite (α -Fe₂O₃) films with low crystallinity can be fabricated by ion beam induced chemical vapor deposition on various substrates [141]. Magnetite films can be obtained by the following two step process [142]. First, an Fe oxide film is grown by co-deposition of atomic oxygen and iron from a Knudsen cell at a substrate temperature of approximately 450 K, re-

	iron (Fe)	wüstite (FeO)	haematite (α -Fe ₂ O ₃)	maghemite (γ -Fe ₂ O ₃)	magnetite (Fe ₃ O ₄)
M_s @ 300 K (kA/m)	1717	AF	1.6 or AF	340	471
$T_C/(T_N)$ (K)	1044	(198)	956	1020	850
crystal symmetry	cubic (bcc)	cubic	trigonal	inverse spinel-cubic or tetragonal	inverse spinel-cubic
cell dimen- sions (Å)	a=2.866	a=4.302 -4.275	a=5.0340 c=13.752	a=8.34	a=8.39
colour	metallic-grey	black	reddish, black	reddish-brown	black
density (g cm ⁻³)	7.874	5.9-5.99	5.26	4.87	5.18
ionic state	-	Fe ²⁺ , O ²⁻	Fe ³⁺ , O ²⁻	Fe ³⁺ , O ²⁻	Fe ²⁺ , Fe ³⁺ , O ²⁻

Table 4.5.: Physical properties of selected stoichiometric iron oxides taken from Ref. [140].

sulting in a nonstoichiometric $\text{Fe}_{3-\delta}\text{O}_4$. The chemical composition is checked by AES during the initial growth and the oxygen partial pressure is accordingly controlled. Post-annealing of this slightly over oxidized film at 900 K for 1 h reduces the film to stoichiometric magnetite with high crystallographic quality. Electron beam evaporation of iron in a plasma oxygen environment of 1×10^{-5} Torr at a substrate temperature of about 520 K [143] and rf sputter deposition from a target consisting of a mixture of Fe_3O_4 and Fe_2O_3 [144] are other ways to create polycrystalline Fe_3O_4 films. Epitaxial maghemite ($\gamma\text{-Fe}_2\text{O}_3$) films on MgO are fabricated using oxygen-plasma-assisted MBE while the substrate is held at temperatures between 520 and 770 K [145]. All these methods are used to fabricate films in the order of 100 nm. Well ordered *ultrathin* films of Fe_2O_3 are fabricated by PFLITSCH *et al.* [146] by oxidizing a 5 ML Fe film epitaxially grown on Cu(110) (deposition and oxidation at 130 K) and subsequent annealing between 400 and 550 K.

These authors address the question of how the properties of Fe films are affected by the controlled oxygen exposure, which is important for the understanding of corrosion phenomena [147]. During the gas phase oxidation of metal surfaces, the following steps have to be considered [148]: the transport of the oxygen to the metal surface, followed by the adsorption, dissociation and ionization of the adsorbate (oxygen). Moreover, the growth of the oxide layer involves the transport of material (i.e. ions and electrons). The FROMHOLD and COOK-model, which is reviewed in Ref. [149], considers coupled currents of ions and electrons due to concentration gradients, homogeneous electric fields across the oxide layer and tunneling of electrons through the potential barrier of the oxide film. At elevated temperatures, an electron flux - due to thermal emission - is included in this approach. ^{18}O tracer experiments corroborated that Fe atom transport contributes to at least 80% of the oxidation [150]. Therefore, the cationic transport dominates over the anionic one during the oxidation, which might be related to the larger ionic radius of O^{2+} . A great deal of effort has been devoted to understanding the initial step of oxidation to elucidate the growth process of iron oxide. BLOŃSKI *et al.* [151] predict a preferential adsorption of oxygen atoms at the fourfold hollow sites of the Fe(100) surface at an oxygen coverage of 0.25 ML by *ab initio* calculations. This is equivalent to the $c(2 \times 2)$ -reconstructed surface observed by LEED on Fe(100) surfaces at an oxygen exposure of about 1-2 Langmuir (L) at room temperature [152]. These authors find a gradual change in the range of 0-1.5 L oxygen in the LEED pattern from $p(1 \times 1)$ of the clean (001) surface to $c(2 \times 2)$ -O. Additional exposure of 4 L total leads to the disappearance of the $c(2 \times 2)$ features. More exposure gradually fades out all diffraction spots at 7 L. However, other authors could either not observe the superstructure [153] or attribute it to a contamination with e. g. carbon or sulfur [154,155,156]. An electron-energy-loss-spectroscopy study at room temperature on the Fe(001) surface reveals (i) dissociative chemisorption of the oxygen up to 3 L, (ii) incorporation of oxygen adatoms between 3 and 20 L and (iii) oxidation above 20 L [157].

Although a lot of literature exists on oxidized iron films, the magnetization and the magnetic anisotropy have not been as intensively investigated as the chemical, structural and electronic properties. The reason for this is the need for *in situ* magnetic investigation techniques with monolayer sensitivity and calibration in absolute units. The $c(2 \times 2)$ -O surface reconstruction is accompanied by an increase of the magnetic moment of the top most Fe layer of up to 25% and also of the subjacent layer to a minor extent as is found in a theoretical study [151]. Investigations of the Fe surface with spin polarized He* de-excitation spectroscopy by SALVIETTI *et al.* [158] yield at 3-4 L oxygen a non-magnetically ordered surface layer evidenced by the disappearance of the asymmetry of the spin-selected density-of-states at T=120 K. In addition, the polarization of the oxygen is investigated by spin-polarized AES. The O KLL lines show a positive spin polarization for the singlet final state, which is indicative for a parallel alignment of the oxygen magnetic moment with the one of the magnetized Fe(001) substrate [159]. This result is confirmed by spin resolved photoelectron spectroscopy. It reveals an exchange splitting of the O $2p_x$ level which is characteristic for an induced magnetic moment in the adsorbed oxygen layer [160]. However, none of these studies give values on the magnetization in absolute units [A/m] or magnetic anisotropy constants of iron films during the exposure to oxygen. Only the scanning SQUID technique used in this work, which measures the remanent magnetization quantitatively *in situ*, can provide this information. It turns out that a quantitative analysis of the magnetic anisotropy of the Fe films is only possible through the combination of FMR and SQUID under UHV conditions.

For the oxidation experiments, a contamination free $\{4 \times 6\}$ -reconstructed GaAs(001) surface was prepared, as discussed previously. Fe films between 5 and 16 ML were deposited at 300 K using an electron beam evaporator at growth rates of 1 ML/min. After the film growth, the epitaxial quality of the Fe film was checked again by LEED. AES detected traces of oxygen corresponding to a coverage below 0.1 ML, only. Pure oxygen (99.998%; supplier *Messer*) was dosed by means of a leak valve in exposure times of 200 sec. To get various oxygen doses, the pressure was varied from $5 \cdot 10^{-9}$ to $5 \cdot 10^{-5}$ mbar.

For the FMR experiments, the sample was moved into the quartz glass finger as shown in Fig. 3.1. The cavity was shoved over the glass finger which was positioned between the pole shoes of the external magnet with the magnetic field direction along y . The GaAs(001) substrate was oriented with the $[1\ 1\ 0]$ direction parallel to x , the axial direction of the sample manipulator. The sample could be rotated about the x -axis for angular dependent FMR measurements. Measurements could be carried out at two microwave frequencies ($f = 4$ and 9.3 GHz) using different microwave cavities and generators. The SQUID measurements were performed as described earlier (see Sec. 4.2).

The structural effects of the oxidation will be discussed first in this section. A typical LEED image of 10 ML Fe is shown in Fig. 4.40. It has a cubic $p(1 \times 1)$ symmetry characteristic for a bcc

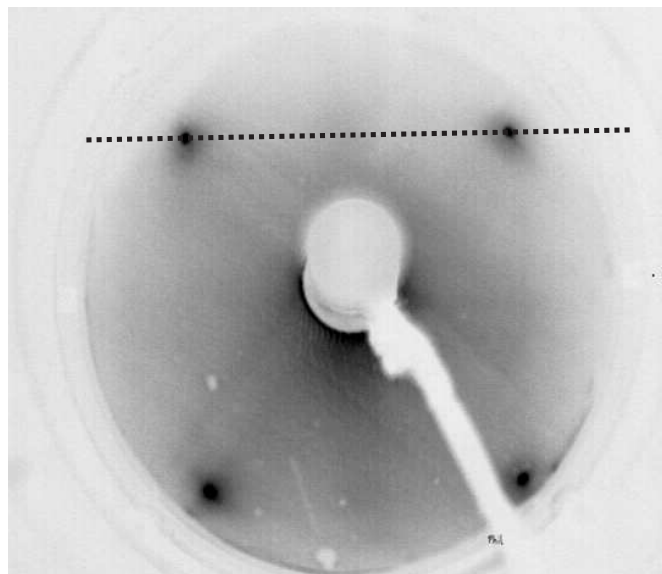


Fig. 4.40.: LEED image of 10 ML Fe on GaAs(001) before exposure to oxygen taken at an electron energy of $E=124$ eV. The dashed line tags the intensity scanning line, which is used in Fig. 4.41 during oxidation.

(001) face. During the oxidation of a 33 ML Fe film, the LEED intensity has been tracked along the dashed line indicated in Fig. 4.40 as a function of oxygen exposure by taking LEED images at constant time intervals of 10 seconds at an oxygen pressure of 10^{-8} mbar. Immediately after the exposure starts, the brightness of the diffraction spots decreases, as can be observed in the intensity line scans along the $[1\ 0\ 0]$ -direction displayed in Fig. 4.41 (a) for three oxygen doses between 0.15 and 0.675 L. The normalized intensity of the (1,1) LEED spot as a function of oxygen exposure is plotted in Fig. 4.41 (b). The data points show good agreement with an exponential function fit. From this finding, one can conclude that the cubic translational symmetry of the Fe surface layer is destroyed within the transfer width (coherence length) of the low energy electron beam. This indicates the formation of a structurally disordered oxide. Residual Fe diffraction spots can be observed up to exposures of about 6 L, which is close to the value of 7 L that is reported by BRUCKER *et al.* [161]. At very low exposure (0.15 L) (Fig. 4.41 (a)), an extra spot evolves halfway between the diffraction spots originating from the Fe atoms. The center part of the line profiles is multiplied by a factor of five for better visualization of this effect. The appearance of this extra spot indicates the formation of the $c(2\times 2)$ superstructure. However, the intensity at 0.15 L is only about 5% of the $(1,\bar{1})$ -spot intensity, and further oxidation removes the reconstruction below 1 L. This can be explained by Fe cation transport during the oxidation which implies that the oxidation process affects both the ordered Fe surface and the initial reconstruction of oxygen atop the Fe surface. This observation differs from what has been reported by SAKISAKA *et al.* [157], who found dissociative chemisorption at exposures up to 3 L. This deviation may be explained by differing surface morphologies of the samples.

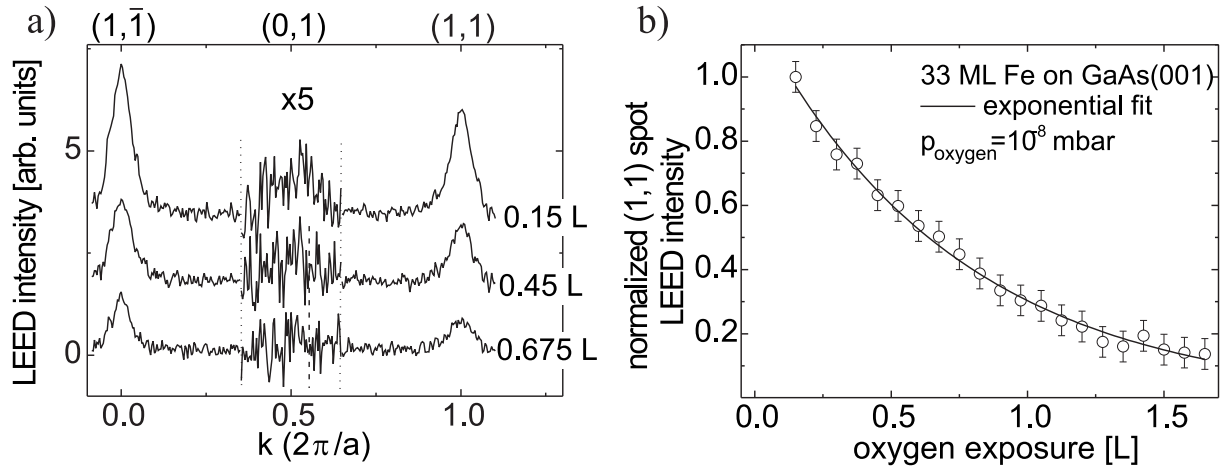


Fig. 4.41.: (a) Line scan of LEED intensity along the line of Fig. 4.40 for various oxygen doses of a 33 ML Fe film on GaAs(001). (b) (1,1) LEED spot intensity as a function of oxygen dose.

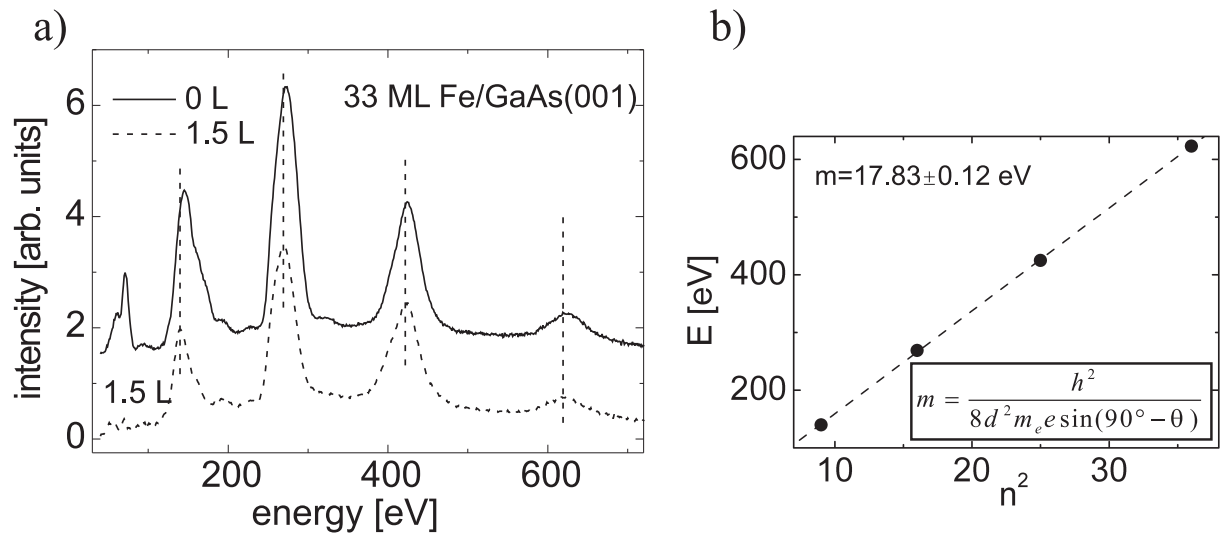


Fig. 4.42.: (a) (0,0)-LEED reflex intensity as a function of electron energy on a 33 ML Fe film after film preparation and after exposure to 1.5 L oxygen. (b) Energy position of the peaks for 1.5 L exposure as a function of n^2 . The slope of the fit m is used to determine the interplanar distance d according to Eq. (3.7).

Here, two possible explanations are given. (i) The motion of oxygen along the edges of the Fe islands on GaAs is less costly in energy when compared to the motion on a smooth surface and might ease oxide formation [162,163]. (ii) The rougher surface of our Fe/GaAs films exhibits a larger number of low coordinated Fe atoms which can easier form chemical bonds to oxygen.

The effect of oxygen adsorption on the vertical interplanar spacing of the Fe(001) film has been investigated by IV-LEED. Figure 4.42 (a) shows the intensity of the (0,0)-LEED spot as a function of electron energy of a 33 ML Fe film without oxygen and after exposure to 1.5 L oxygen. This film exhibits peaks which are at slightly higher energies in comparison to the film

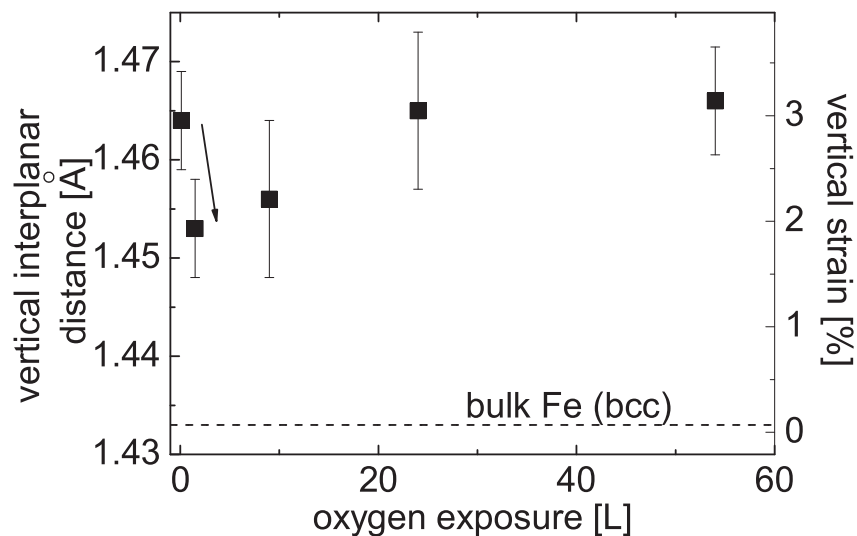


Fig. 4.43.: Vertical interplanar distance determined from IV-LEED experiments on 33 ML Fe on GaAs(001). The arrow indicates the sudden decrease of the interplanar spacing after exposure of 1.5 L.

exposed to oxygen. The vertical dashed lines located at the peak position of the film exposed to 1.5 L oxygen serve as a guide to the eye. Additional small peaks, at energies of $E=55, 70, 96, 196$ and 229 eV for the 1.5 L film, which are not Bragg-peaks, are probably due to multiple scattering of the electrons and are not considered in the simple evaluation employed here. The peak positions are plotted vs. n^2 , n being the order of the Bragg reflection (Fig. 4.42 (b)) for the 1.5 L film. The slope yields the vertical interplanar spacing $d = 0.1453 \pm 0.0005$ nm. Figure 4.43 shows the results at different oxygen dosages up to 50 L oxygen. At even higher oxygen dosages, the intensity variations get smaller and make the evaluation of the IV-LEED data impossible. The film of 33 ML thickness has an enhanced vertical interplanar distance d of 2.2%, compared to the bulk value (see Sec. 4.2). After exposure to only 1.5 L oxygen, d decreases by about 0.7%. This reduces the vertical strain by more than 30%, or in other words, this is a significant relaxation of the film. A reason for this effect might be either the charge transfer from the Fe atoms to the adsorbed oxygen atoms after they dissociated at the Fe surface or an oxygen induced incorporation of misfits dislocations into the Fe film. At higher oxygen exposure (50 L), one finds an increase in the vertical interplanar distance d even slightly exceeding the value at 0 L, since the oxidation sets in in this range. The formation of iron oxides is accompanied by a change in the lattice constant, since oxygen ions have larger ionic radii than Fe ions (Tab. 4.6). In particular, divalent oxygen anion diameters are about twice as large as Fe cation diameters. Trivalent Fe ions possess even smaller diameters than divalent ones. It will be shown later that the thickness of the oxide layer at 50 L oxygen cannot exceed a thickness of 2 ML. Electrons with energies of up to 600 eV have penetration depths of about 10 ML (Fig. 3.4). One therefore measures an averaged interplanar distance of the surface iron oxide and of

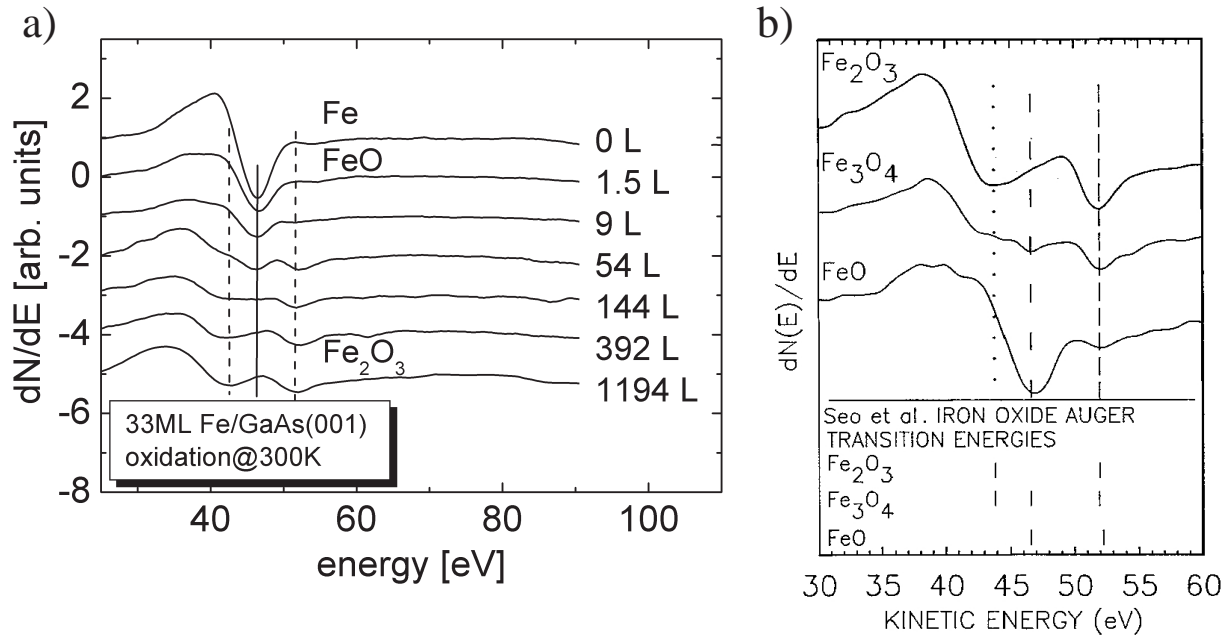


Fig. 4.44.: (a) Low energy AES spectra measured on a 33 ML Fe/GaAs(001) film after different oxygen dosage. (b) Reference AES spectra taken from Ref. [164]. The Auger transition energies reported by SEO *et al.* [165] for the three selected iron oxides species are also shown.

the metallic iron below. Consequently, the measured interplanar distance $d = 1.466 \text{ \AA}$ at e.g. 50 L is much smaller than the one of the iron oxides, i.e. $d = a/2$ for wüstite and $d = a/4$ for magnetite, respectively (a is the dimension of the cubic unit cell given in Tab. 4.5).

In an effort to understand the evolution of the chemical composition of the iron oxide, AES measurements of the $M_{2,3}VV$ Auger lines were taken. These low energy electron transitions probe the valence states of the Fe and thus, are valuable tools to get insight into the chemical bonds of the Fe atoms. Auger spectra taken from a 33 ML Fe/GaAs(001) film after exposure to oxygen dosages up to about 1000 L are presented in Fig. 4.44 (a). One sees a continuous change in the line shapes with increasing exposure. The low energy Auger electron spectra for various Fe oxides (FeO, Fe₂O₃ and Fe₃O₄) have been investigated previously [164], reference AES spectra are also shown in Fig. 4.44 (b). The clean Fe film exhibits a peak minimum at 46.5 eV. After exposure to only 1.5 L oxygen, a plateau evolves at the maximum peak position of the clean Fe film. This is a characteristic feature of wüstite. In agreement with Ref. [157],

	O ²⁻ anionic	Fe ²⁺ cationic	Fe ³⁺ cationic
ion radius (nm)	0.14	0.082	0.065

Table 4.6.: Ion radius of oxygen and Fe taken from Ref. [140]

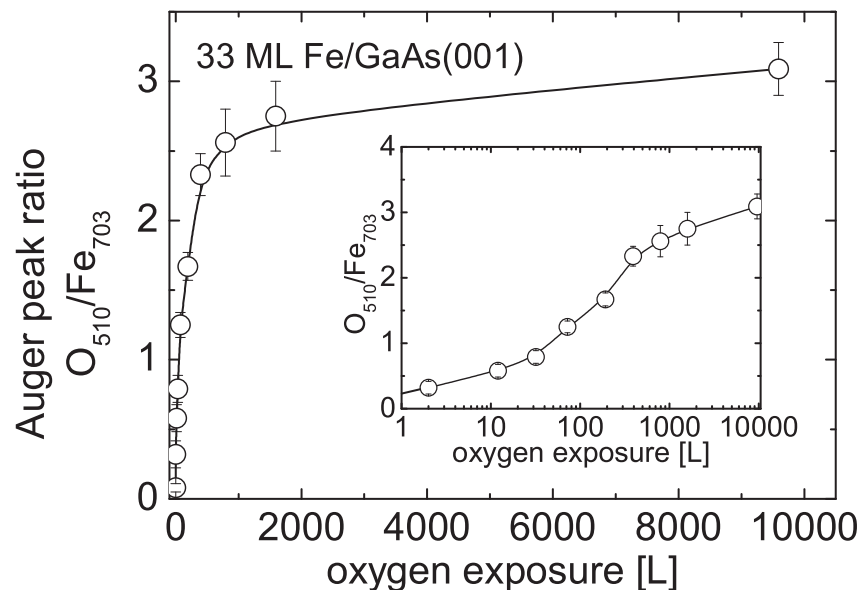


Fig. 4.45.: Auger peak ratio O_{510}/Fe_{703} of a 33 ML Fe film on GaAs as a function of oxygen dosage at 300K. The inset shows the same plot with logarithmic x axis.

this exposure corresponds to an oxygen coverage of about 0.25 ML. In addition, there is good agreement with STM investigations on an Fe(110) surface from WIGHT *et al.* [166], who found evidence for the formation of FeO at an oxygen coverage above 0.25 ML. At an exposure of about 50 L oxygen the line shape resembles the one of magnetite (Fe_3O_4), but changes upon further oxidation to the one of Fe_2O_3 at 1000 L. Continuous dosage up to 25000 L no longer changes the line shape. As listed in Tab. 4.5, Fe_2O_3 , regardless of the presence of haematite or maghemite, only consists of trivalent Fe ions, and the Fe atoms are in a higher oxidation stage than in magnetite.

Figure 4.45 shows the development of the Auger amplitude ratio s of the oxygen and the Fe Auger peak at $E=510$ eV and $E=703$ eV, respectively. At first, the Auger amplitude ratio O_{510eV}/Fe_{703eV} takes a steep increase up to an exposure of about 1000 L and has a value of ≈ 2.5 . A decuple increase at this exposure will only slightly raise s to about 3. SEO *et al.* [165] report that to a first approximation, the amplitude ratio O_{510eV}/Fe_{703eV} is proportional to the relative content of Fe and O atoms in the iron oxides. The only exception to this rule of thumb is haematite, which has the same stoichiometry as maghemite (composition ratio $N_O/N_{Fe}=1.5$), but has an s value about 5% larger than maghemite. These authors find a value $s \approx 2.3$ ($s \approx 2.45$) for γ - Fe_2O_3 (α - Fe_2O_3) and therefore, similar values at our exposures of about 1000 L. Although the low energy Auger line shapes already indicate the formation of Fe_2O_3 below 1000 L, there is still an increase of s by more than 15% at higher exposures. The only oxide which has a greater compositional ratio of oxygen and Fe is lepidocrocite (γ - $FeOOH$) with $s \approx 2.8$, which can be excluded due to the small partial H_2O pressure in the UHV chamber

($p_{H_2O} < 10^{-9}$ mbar) during oxygen exposure. Consequently, the higher ratio s originates from chemisorbed oxygen on top of the Fe oxide film surface that did not form any chemical bonding with the Fe.

However, AES cannot distinguish between haematite and maghemite, since they are chemically equivalent. They do differ in their crystal structure (see Tab. 4.5). Consequently, a 20 ML Fe/GaAs(001) film was oxidized inside the vacuum chamber at an exposure of 20000 L and taken out of the chamber to perform XRD measurements.

The X-ray diffraction pattern of the oxidized Fe film measured with a $\Theta - 2\Theta$ diffractometer³ is shown in Fig. 4.46 (upper curve) in comparison to a clean GaAs(001) substrate (lower curve). The peaks correspond to polycrystalline γ -Fe₂O₃, but have different relative intensities in comparison to the intensities given in the literature measured on polycrystalline bulk γ -Fe₂O₃. The derivation of single diffraction peak positions from a bulk reference sample is within $\pm 3\%$. Note that magnetite and maghemite are difficult to distinguish in XRD measurements, for both have an inverse spinel-cubic lattice with almost the same lattice constants (deviation of 0.6%). Due to the small signal of our thin film (here ≈ 3 nm), the analysis is even more complicated. By combining the two results from AES which indicate the Fe₂O₃ state and XRD, one can conclude that the final oxidation stage of thin Fe films on GaAs is γ -Fe₂O₃ (maghemite).

The line width of XRD spectra is a measure for the crystallite sizes of the sample. The average crystallite size D can be calculated from the full width at half maximum of a distinct XRD peak using the Scherrer equation [167]:

$$D = \frac{k \cdot \lambda}{\beta_c(2\theta) \cos \theta} \quad (4.12)$$

$\beta_c(2\theta)$ is the full width at half maximum of the peak at diffraction angle 2θ in radians corrected for instrumental broadening. k is the shape factor which accounts for the shapes of the crystallites. Figure 4.47 shows the deconvolution of the experimental line width, exemplary for the γ -Fe₂O₃ (430) peak. Two gaussian functions with an amplitude ratio of 2 are used. A line width of $w_1 = 0.126^\circ$ for the K_{α_1} peak is obtained. By using Eq. (4.12) with a typical value of $k = 0.9$ and the peak position at $2\theta = 66.82^\circ$, one obtains an average crystallite size of 85 nm. A small instrumental broadening is not considered, i.e. the 'genuine' crystallite size D is larger. Also, the effect of strain, which leads to an additional broadening of the XRD peaks [168], is not included. This in turn might lead to overestimated crystallite sizes. Using the simplified approach above, different reflexes were investigated yielding crystallite sizes in the range of 75 to 90 nm.

³The XRD experiments were performed using a $\Theta - 2\Theta$ diffractometer with a Co K_α source with a weighted average wavelength of $\lambda = 1.7902 \text{ \AA}$ (The individual wavelengths are $\lambda_{K_{\alpha_1}} = 1.7889 \text{ \AA}$ and $\lambda_{K_{\alpha_2}} = 1.7928 \text{ \AA}$). An iron filter was placed in the diffracted beam path to suppress the K_β radiation. The detector used was the X-Celrator, i.e. an ultra-fast X-ray detector based on the Real Time Multiple Strip (RTMS) technology characterized by its high efficiency.

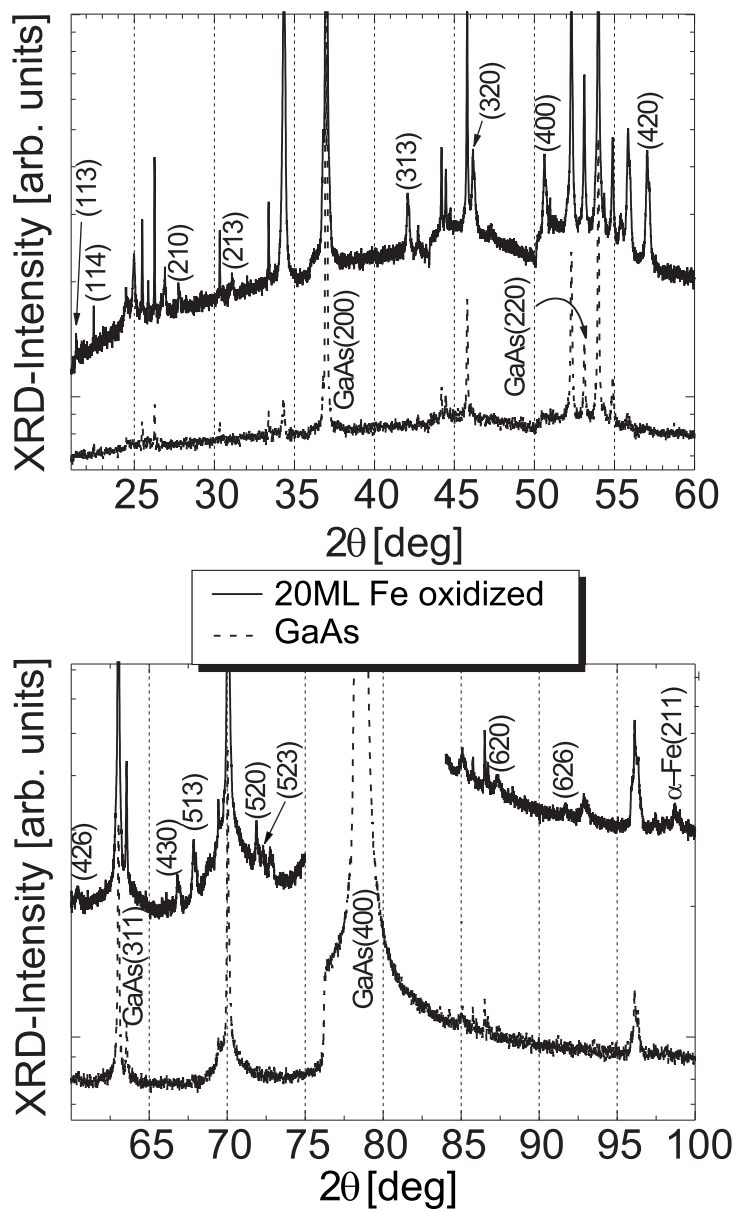


Fig. 4.46.: XRD data of a 20 ML Fe film on GaAs(001) exposed to ambient atmosphere for a GaAs(001) substrate (lower curve).

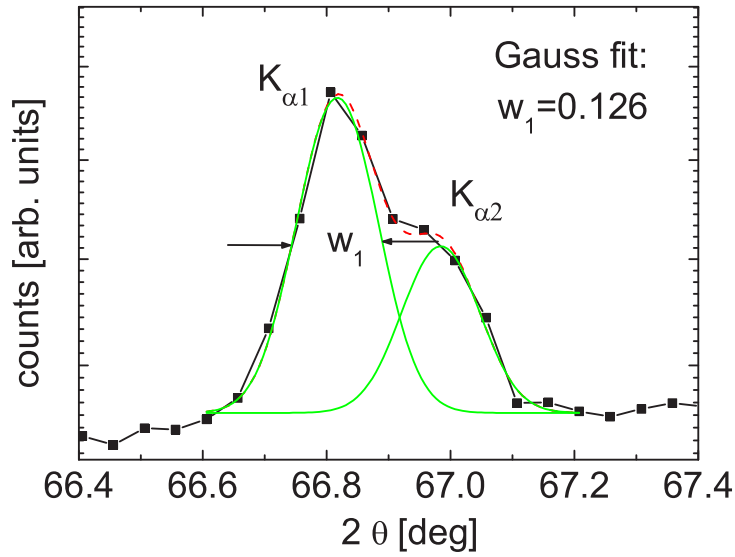


Fig. 4.47.: Line width analysis of the XRD (430) peak. Two gaussian curves are superposed to fit the double peak which arises from the $CoK_{\alpha 1}$ and $CoK_{\alpha 2}$ radiation.

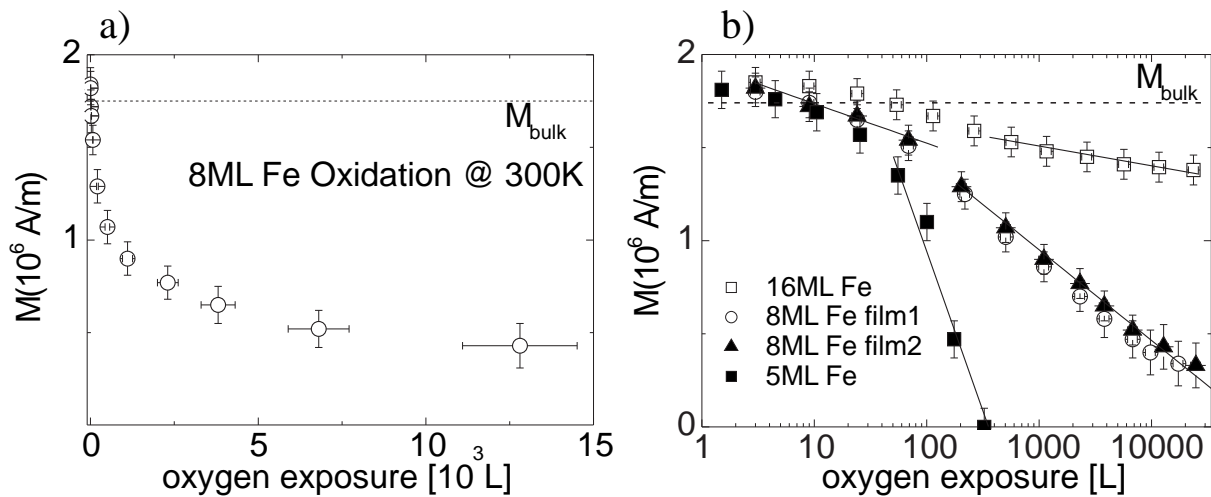


Fig. 4.48.: (a) Remanent magnetization of an 8 ML Fe/GaAs(001) film during successive steps of oxygen exposure. (b) Remanent magnetization of a 5, 8 and 16 ML Fe film plotted over a logarithmic exposure axis. An 8 ML Fe film has been measured twice.

This is contrary to the LEED results which were carried out at low exposures and showed a structural surface disorder within the transfer width of the LEED optics (10 nm). Consequently, the 75 to 90 nm crystallites grow at higher oxygen exposure. Note that the Scherrer equation (4.12) can strictly be applied only for isotropic crystalline shapes that is obviously not the case in our naturally oxidized Fe film.

From the magnitude of the remanent magnetization at room temperature of the 5, 8 and 16 ML Fe which equals the Fe bulk value within the error bar, one can conclude that no non-ferromagnetic layer forms at the Fe/GaAs interface. In Fig. 4.48 (a), the remanent magnetization

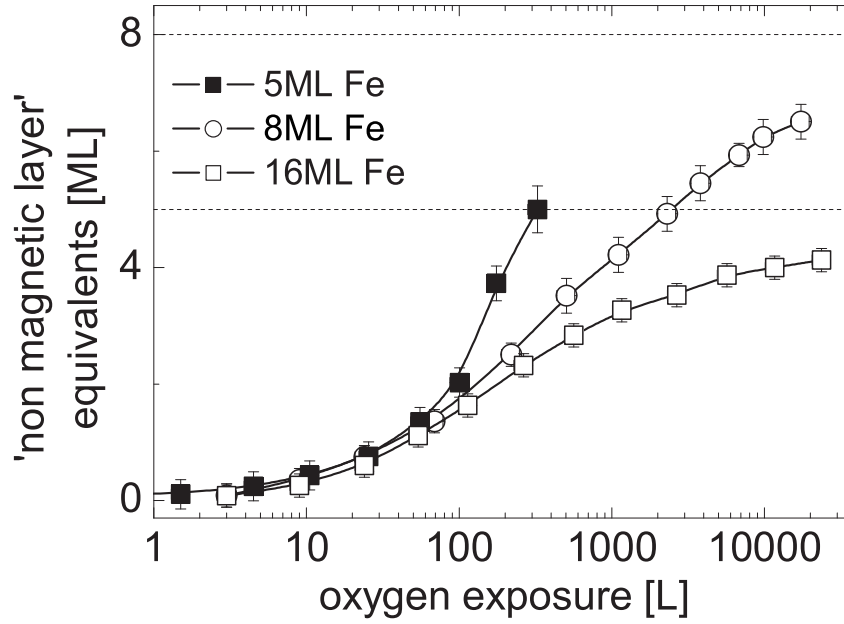


Fig. 4.49.: Calculated non-magnetic layer equivalents of the 5, 8, and 16 ML Fe/GaAs(001) film of Fig. 4.48 taking into consideration the individual film thicknesses.

of an 8 ML Fe film is plotted versus the exposure to oxygen at room temperature. After an initial fast decrease of the remanent magnetization with increasing oxygen exposure, the reduction slows down and has a value of about 25% of the bulk magnetization at an exposure of around 13000 L. It seems that the remanent magnetization approaches a saturation limit at high exposure. The slowing down of the magnetization decrease with oxygen exposure is a motivation to plot the abscissa in a logarithmic scale as done in 4.48 (b). Here, the magnetization data from 5, 8, and 16 ML Fe films are plotted in the same diagram. To show the reproducibility of the measurements, an 8 ML film was measured twice. Each measured film exhibits a decrease of magnetization which can be divided into two sections with different slopes. Below 100 L, the slope of the data points declines more gently than it does at higher exposures. The slope at higher exposures becomes the steeper, the thinner the Fe thickness. The 5 ML Fe film has a vanishing remanent magnetization at only 300 L oxygen. After the magnetization disappeared, the film was magnetized again in a magnetic field, but it did not regain a remanent magnetization. On the other hand, the 8 and 16 ML Fe films still had a remanent magnetization of 65% and 85% M_{bulk} , respectively, at 300 L. It seems that the remanent magnetization of the thickest Fe film is least influenced by the oxygen. However, one has to include the individual thicknesses of the films, as magnetization is defined as magnetic moment per volume. It was discussed previously, that γ -Fe₂O₃ forms at higher oxygen exposures. The ferrimagnet γ -Fe₂O₃ has about 20% of the magnetization of Fe bulk and will most likely be further reduced when the oxide is not in a single crystalline phase. The same argument applies for the ferrimagnet magnetite (27% of M_{bulk}^{Fe}) which was observed for exposures below 1000 L. Therefore, in a first approach, one

can neglect the contribution of the Fe oxide to the magnetic signal and calculate the number of oxidized Fe layers as shown in Fig. 4.49. The dashed horizontal lines indicate the thicknesses of the 5 and 8 ML Fe film. Up to about 70 L oxygen, only two ML of Fe are oxidized and the films behave identically. Above 70 L the curves split up, indicating a faster increase in 'non magnetic layer equivalents' for the 5 ML Fe film, as already seen from Fig. 4.48 (b). But also when comparing the 8 ML and 16 ML Fe film in this 'thickness corrected plot', a faster decrease of M of the thinner film is evident. Here, the 16 ML Fe film clearly shows a saturation behavior. At 25000 L oxygen only 4 ML of the 16 ML Fe film have been oxidized, indicating the formation of a passivating oxide layer on top of the Fe film. As the main reason for the reduction of remanent magnetization, one can assume the disordered growth of iron oxide. Due to the preferential cation transport (Fe atoms) during the oxidation, the topmost Fe atoms leave their regular lattice positions and form a disordered iron oxide layer. The loss of the LEED diffraction spots during the oxidation procedure supports this finding. Further confirmation is also given in the literature by SHINJO *et al.* [169], who observed a spin-glass-like frustrated state in a thin oxide layer on an Fe film which had been exposed to air using conversion electron Mössbauer spectroscopy (CEMS). An important result is the above mentioned increase of apparent non-magnetic oxide layers as a function of oxygen exposure, which is faster for thinner films. One can discuss different reasons for this behavior: (i) the finite size effect, (ii) a roughness dependent oxidation process and (iii) a thickness dependent relaxation of the strained Fe film when oxygen is dosed.

(i) In the thin film limit, the Curie temperature generally decreases with respect to the bulk material. BENSCH *et al.* [47] extrapolated the Curie temperature for Au capped Fe/GaAs(001) films to 0 K and found a critical film thickness of 2.5 ML where ferromagnetism sets in. Above 2.5 ML Fe, these authors found a strong increase of the Curie temperature of approximately 270 K/ML. At room temperature, the critical thickness was 3.6 ML. Note that these results are influenced by the Au capping layer, which were used for *ex situ* characterization. Uncapped Fe films in UHV on the other hand - as shown in Sec. 4.2 - exhibit a critical film thickness below 2.5 ML at 0 K. Uncapped 2.3 ML Fe has a $T_C \approx 170$ K. Concerning the 5 and the 8 ML Fe films, this finite size effect cannot be neglected, since the formation of iron oxide is in fact thinning the Fe film.

(ii) The roughness of Fe/GaAs(001) decreases with the film thickness. It has been suggested and later validated by STM investigations that the Fe growth on Ga-rich GaAs substrates proceeds via a 3D Volmer-Weber mode, starting with the formation of Fe islands which coalesce at a thickness of 3.5 ML to finally form a homoepitaxial film on the GaAs substrate (e.g. Refs. [13,12]). During the Fe deposition, one observes a gradual sharpening of the LEED images (Fig. 4.50) shown for 5 and 16 ML Fe films. The shapes of the Fe islands which form at low coverage, lead to a rough Fe surface as the islands coalesce (see schematics of Fig. 4.50 for the 5 ML film). It is not until the film thickness increases that the roughness gradually lessens. The smoother surface offers a lower number of low coordinated Fe atoms, which are

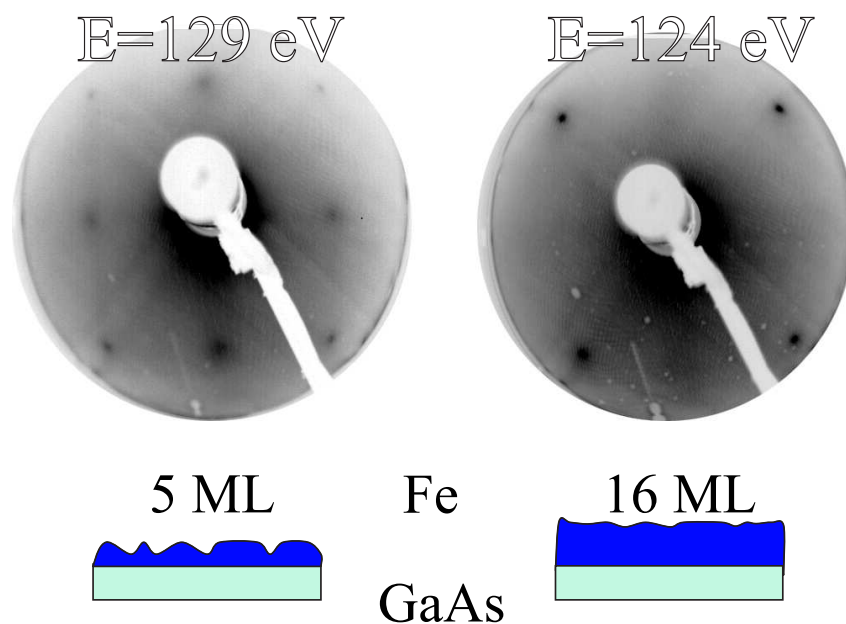


Fig. 4.50.: LEED images of a 5 and a 16 ML Fe film on $\{4\times 6\}$ -reconstructed GaAs(001) at quoted electron energies. The schematic picture illustrates the continuous smoothing of the film surface with increasing Fe thickness.

susceptible to easier oxide formation. (iii) Enhanced oxidation might also be due to a strained state of the Fe film, which may weaken the bonding strength of surface atoms. A vertical strain of about 3% in the topmost Fe layers (Sec. 4.2) is found for all films up to about 20 ML Fe. The vertical strain of a 33 ML Fe film (2.2%) is reduced by 30% after exposure to 1.5 L oxygen. This behavior is expected for other film thicknesses as well. The thinnest films of this oxidation study (5 and 8 ML) might not show the same strong reduction of the surface strain upon oxygen adsorption because they are too thin to allocate the relaxation across the film thickness. The resulting larger strain may cause an enhanced oxidation rate.

At this point, a remark should be made concerning the various partial pressures oxygen during the oxidation experiments. As depicted earlier, the diverse oxygen doses (pressure \times time) were achieved by changing the oxygen pressure and maintaining the exposure time. It is worth mentioning that in general the formation of the iron oxide *depends* on the pressure of the oxygen. However, ROOSEDAAL *et al.* [170] found by XPS that iron oxides, which have been prepared between 10^{-8} and 10^{-6} mbar oxygen (the pressure range used in the present study), but with the same coverage, have the same ratio of di- and trivalent ionized Fe atoms ($N_{Fe^{2+}}/N_{Fe^{3+}}$). Hence, in the discussion one can neglect the pressure dependence.

The following examines the influence of oxygen on the magnetic anisotropy. With the magnetic field applied along the $[1\bar{1}0]$ -direction, the hard magnetic in-plane axis, the resonance

condition for the FMR experiment according to Ref. [45] is:

$$\left(\frac{\omega}{\gamma}\right)^2 = \left(B_r^{\parallel} - \frac{2K_4}{M} - \frac{2K_{2\parallel}}{M}\right) \left(B_r^{\parallel} - M_{\text{eff}} + \frac{K_4}{M}\right) \quad (4.13)$$

Here, ω is the microwave frequency, γ is the gyromagnetic ratio, B_r^{\parallel} is the resonance field, M is the magnetization, and $M_{\text{eff}} = 2K_{2\perp}/M - \mu_0 M$ is the effective out-of-plane anisotropy field. The anisotropy constants K_i have been described earlier (see Sec. 2.2.2). Figure 4.51 shows FMR spectra for oxygen exposures between 0 L and 204 L, measured on a 10 ML Fe film on GaAs(001). The magnetic field was applied along the hard in-plane axis ($[1 \bar{1} 0]$ -direction) and a microwave frequency of $f = 9.3$ GHz was used. The shift of the resonance field is sensitive to the three anisotropy constants and the magnetization. Without oxygen, the resonance field is equal to 1.75 kOe and shifts to 1.55 kOe at about 10 L. At higher oxygen dosages, the resonant field increases and even crosses the value without oxygen at an exposure of 204 L. In addition, the resonance lines broaden and decrease in amplitude. To understand the observed shift of the resonance field and to find the individual anisotropy constants, angular dependent FMR experiments were performed. The angular dependent measurements are presented in Fig. 4.52 for (a) the polar angular dependent investigation with the magnetic field changed from the $[1 \bar{1} 0]$ towards the $[0 0 1]$ -direction and (b) the in-plane angular dependency within a small angular variation of 6° around the $[1 \bar{1} 0]$ -direction (hard in-plane axis). The polar dependency

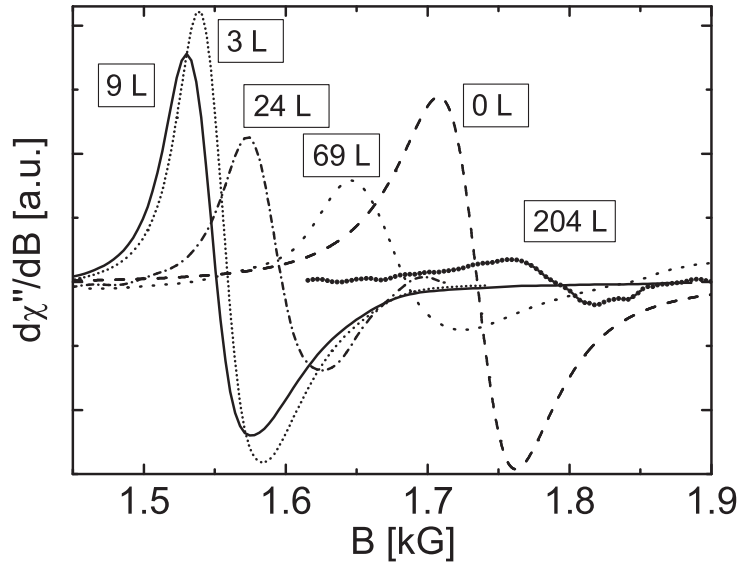


Fig. 4.51.: Ferromagnetic Resonance spectra of a 10 ML Fe film on GaAs(001) for various oxygen dosage measured at a microwave frequency of $f = 9$ GHz and the magnetic field applied along the $[1 \bar{1} 0]$ -direction.

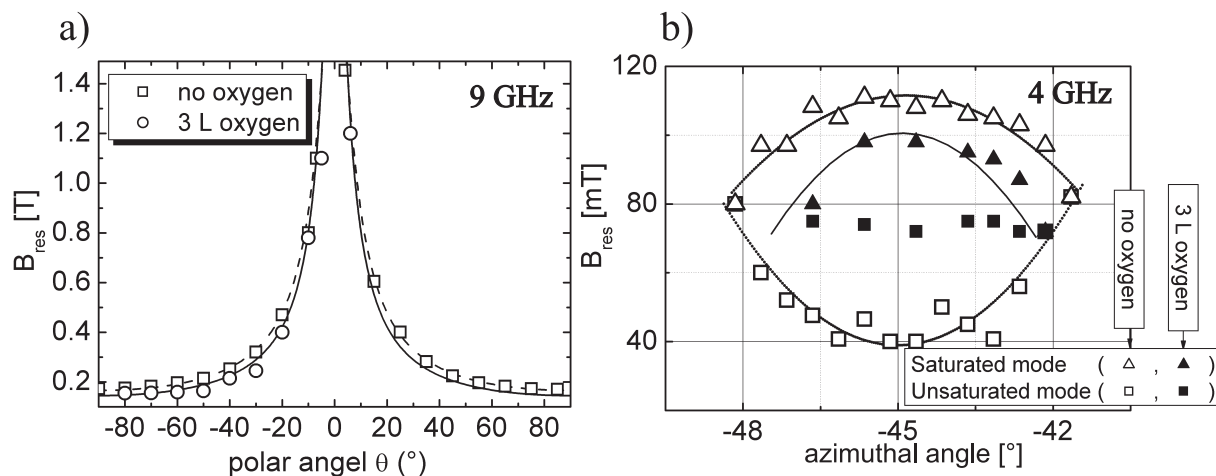


Fig. 4.52.: (a) Polar angular dependence of the resonance field B_{res} of a 10 ML Fe film on GaAs, measured from $[1 \bar{1} 0]$ towards the $[0 0 1]$ -direction. The dependencies are shown for as-prepared samples and after exposure to 3 L oxygen. (b) Corresponding in-plane dependencies measured around the $[1 \bar{1} 0]$ -direction showing a saturated and an unsaturated mode. The error bar is smaller than the symbol size. The lines correspond to fits according to the resonance conditions as described in the text.

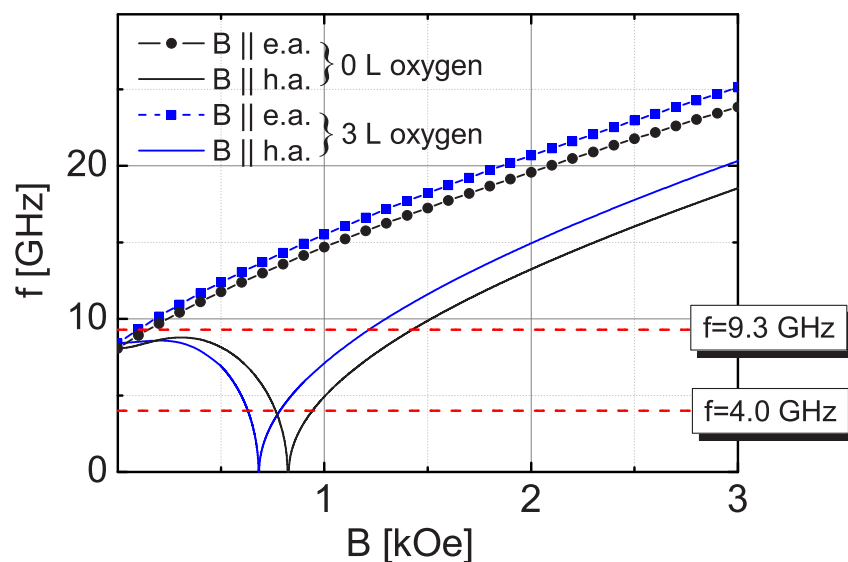


Fig. 4.53.: Dispersion relation of a 10 ML Fe film on GaAs(001) with experimental anisotropy constants without oxygen and after exposure to 3 L oxygen for the magnetic field B applied along the easy axis (e. a.) and the hard axis (h. a.) of magnetization. The available microwave frequencies of our setup are given by the dashed horizontal lines.

is shown for 0 L and 3 L with corresponding fits according to the resonance equations given in Ref. [45]. The shape of the angular dependency is mainly determined by the twofold out-of-plane anisotropy constant $K_{2\perp}$ whereas $K_{2\parallel}$ and K_4 only have minor effects. To find $K_{2\parallel}$ and K_4 the in-plane field was varied, since these two anisotropy constants mainly affect the azimuthal dependence. At a microwave frequency of $f = 4$ GHz, two resonance modes occur, the so-called saturated mode and the unsaturated mode at a lower resonance field. Figure 4.52 (b) shows data for an as-prepared sample and after oxygen exposure of 3 L. In addition, fits according to an equation presented in Ref. [45] are shown. The unsaturated resonance mode is a resonant precession of the magnetization about an axis defined by the film anisotropies, whereas in the saturated mode, the magnetization precesses about the applied magnetic field direction. The dispersion relation is shown in Fig. 4.53 for the experimentally obtained magnetization and anisotropy constants at 0 L and 3 L oxygen. It clarifies the occurrence of resonance fields for different microwave frequencies for the magnetic field applied along the in-plane easy axis $[1\ 1\ 0]$ and the in-plane hard axis $[1\ \bar{1}\ 0]$. This relation is obtained by plotting Eq. (4.13) for the hard axis direction and an equation given in Ref. [45] for the easy axis. The experimentally used microwave frequencies $f = 9.3$ and 4.0 GHz are also shown as horizontal lines in the plot. Resonance fields are found at the intersection of these frequencies with the dispersion relation. The higher microwave frequency is slightly too high to observe an unsaturated mode. An FMR measurement along the easy axis with the available microwave frequencies does not lead to reasonable results. B_r of the low resonances cannot be evaluated accurately, since the line width is too broad. Thus, it is helpful to use two microwave frequencies, since the derived anisotropy constants must yield consistent results within both sets of experimental data.

The magnetic anisotropy constants from the angular dependent measurements are plotted in Fig. 4.54. The analysis was performed at 0, 3, 9, and 24 L oxygen on the 10 ML Fe film on GaAs(001). The biggest influence is seen in the twofold out-of-plane anisotropy constant $K_{2\perp}$, which decreases from 5.0 to 3.0×10^5 J/m³ already at 3 L oxygen exposure. More oxygen only slightly decreases $K_{2\perp}$ to 2.8×10^5 J/m³ at 24 L. $K_{2\perp}$ of the clean Fe film was found to be mainly due to the Fe-vacuum interface [45]. Obviously, it is this anisotropy contribution which experiences the biggest effect. The fourfold anisotropy constant K_4 decreases from 1.5 to 1.0×10^4 J/m³. The twofold uniaxial in-plane anisotropy $K_{2\parallel}$ decreases by about 10%, as it is identified to be mainly an Fe-GaAs interface effect, which is not influenced by the oxygen on the Fe top surface. Please note that for the determination of the anisotropy constants K_i the measured magnetization values have been included in the analysis.

In order to investigate the passivating effect of an oxide layer atop a FM Fe film, a 20 ML Fe film on GaAs was exposed to air, and measured at 300 K with a commercial SQUID system (Quantum Design). In Fig. 4.55, the magnetization M is plotted as a function of H for the external magnetic field H applied along the $[1\ 1\ 0]$ -direction. As discussed in Sec. 4.4, a 20 ML

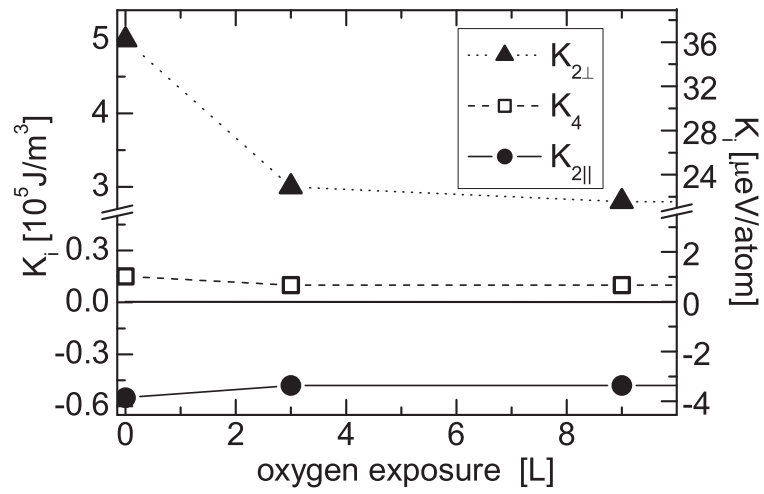


Fig. 4.54.: Magnetic anisotropy constants of a 10 ML Fe film on GaAs(001) as a function of oxygen exposure derived from angular dependent FMR experiments.

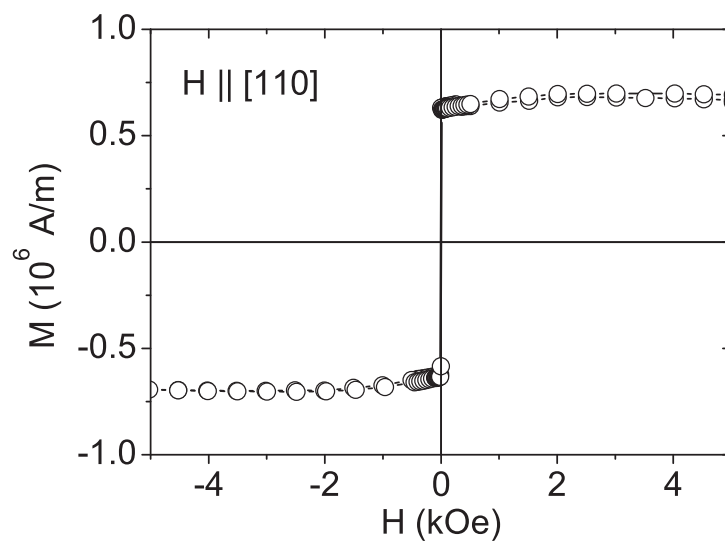


Fig. 4.55.: Hysteresis loop of a 20 ML Fe film on GaAs(001) exposed to air.

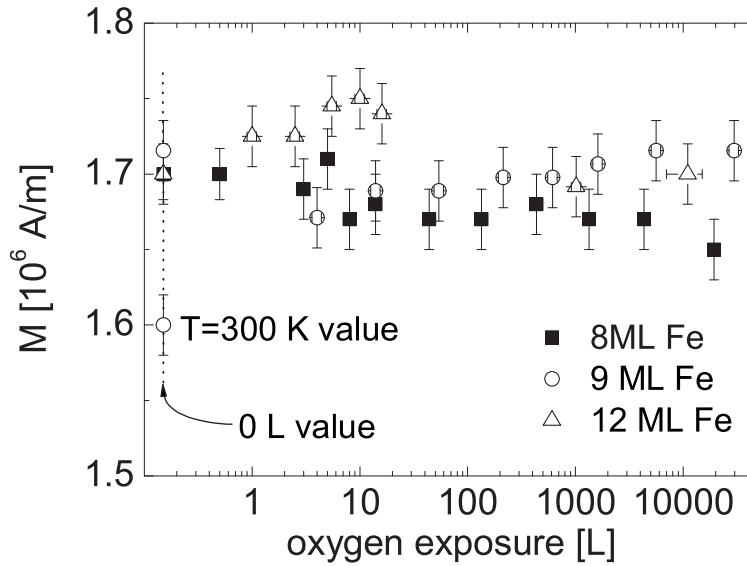


Fig. 4.56.: Remanent magnetization of an 8, 9 and 12 ML Fe film on GaAs(001) which has been exposed to oxygen at $T=40$ K. The magnetization values without oxygen exposure (0 L values) are plotted on a vertical dotted line.

Fe film on GaAs has an easy axis along a $\langle 100 \rangle$ in-plane direction. Hence, the remanence of the magnetization M_r is reduced with respect to the saturation magnetization $M_s = 697$ kA/m ($\pm 4\%$) by 11%. Since the Fe film was exposed to air containing H_2O vapor, the formation of FeOOH is possible, whose modifications are mostly antiferromagnetic. Water at the Fe surface can enhance the material transport of the Fe cations, which is the well known phenomenon of corrosion.

Assuming that the oxidized Fe does not contribute to the magnetization, the saturation magnetization of (bulk) Fe at 300 K is $M_{s,Fe} = 1714$ kA/m [28]. About 8 ML Fe contribute to the ferromagnetic signal, whereas 12 ML of the Fe film are oxidized.

Since oxidation of Fe is a thermal activated process [171], the oxidation process can be slowed down at low temperatures. At room temperature, oxygen exposure below 10 L destroys the ordering of the Fe(100) surface due to the cation (Fe) transport induced by the oxygen. The question arises if at low temperature the mass transport can be suppressed and therefore ease the formation of the $c(2 \times 2)$ superstructure mentioned previously. In this case, an increase of the surface magnetic moments should be observed according to Ref. [151]. Figure 4.56 shows the remanent magnetization of 8, 9 and 12 ML Fe films as a function of oxygen exposure at 40 K. Magnetization values at 0 L are also plotted on the logarithmic abscissa and are explicitly labelled. In addition, the 9 ML Fe film is measured at room temperature before the oxygen

exposure and shows an increase of magnetization of about 6% when cooled down to $T=40$ K. In contrast to the room temperature oxidation experiments, the magnetization values at $T=40$ K are only slightly influenced by the oxygen exposure. However, no general tendency in the data is found. The magnetization of the 9 ML Fe film is reduced by 2.5% at 4 L oxygen, but recovers to the 0 L value at an exposure of 30000 L. The trend of the 8 ML Fe film is a continuous decrease with oxygen by 3% in comparison to the as-prepared state of the film. Interestingly, the 12 ML Fe film exhibits an increased magnetization at 10 L by 3%. However, this value is reduced again at exposures above 1000 L. In conclusion, no clear trend of the remanent magnetization as a function of oxygen exposure at $T=40$ K can be found. It should be noted that the LEED pattern of the Fe film vanishes in consequence of oxygen exposure similar to the room temperature exposure and no distinct $c(2\times 2)$ superstructure is observed.

4.5.1. Temperature driven reorientation transition of an oxidized Fe film

Spin reorientation transitions are phenomena which can occur in thin magnetic films and are governed either by the temperature, the thickness of the film or by (non-magnetic) capping layers [172,173,174]. Some authors address the question of how gas adsorbates can influence a spin reorientation transition. For ultrathin Ni films on Cu, the spin reorientation as a function of film thickness from an in- to an out-of-plane orientation of the magnetization occurs at 5 ML on a pre-oxidized Cu substrate in contrast to a critical film thickness of 11 ML for a clean substrate [175], for example.

Throughout the literature, the Fe/GaAs thin film system is known to have an in-plane easy axis which is lying in the plane of the film either along the $[1\ 1\ 0]$ direction for thin films or along the in-plane $\langle 1\ 0\ 0 \rangle$ directions for thicker films. This section shows that an out-of-plane reorientation of the sample magnetization can be found on an oxidized Fe film at low temperature.

An oxidized 8.6 ML Fe film deposited on GaAs showed a spin reorientation transition from in-plane to out-of-plane when measured as a function of temperature. The film had been exposed to 25000 L oxygen which had reduced the remanent magnetization to $M = 350 \pm 40$ kA/m. 15 hours after the oxygen exposure the remanent magnetization at room temperature was essentially unchanged and the sample was cooled to $T = 40$ K. Without saturating the sample in a magnetic field, SQUID measurements were continuously performed with increasing temperature. The B_z profiles are presented in Fig. 4.57 for selected temperatures. At temperatures up to 175 K, the shape of the stray field is the one of an out-of-plane magnetized sample as shown in Sec. 2.3.1 and has a distinct maximum. Above $175\text{ K} \pm 10\text{ K}$, the signal continuously transforms to an in-plane stray field signal which is characterized by the existence of a minimum and a maximum. The out-of-plane to in-plane reorientation is finished at $250\text{ K} \pm 10\text{ K}$.

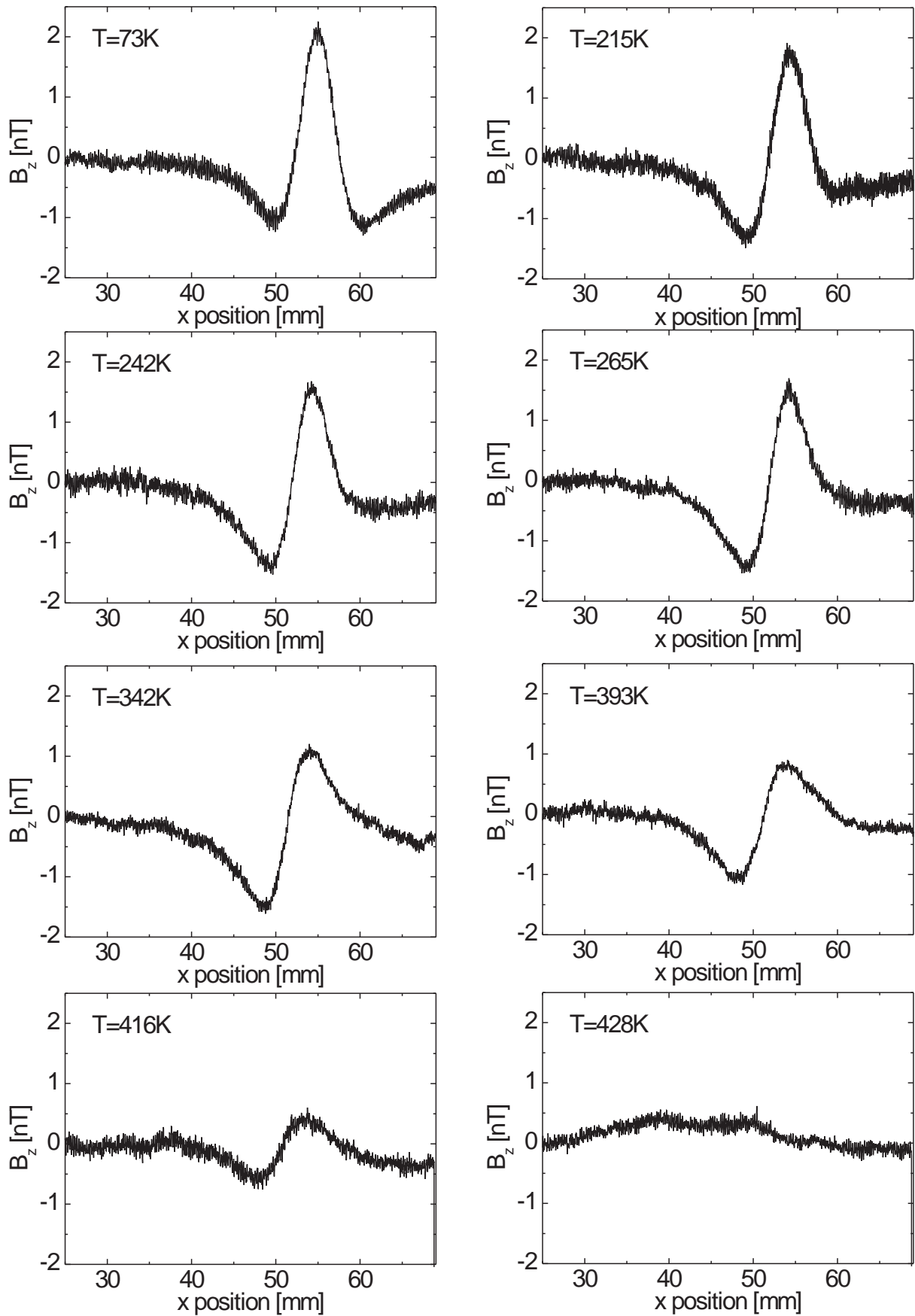


Fig. 4.57.: B_z line scans of an oxidized 8 ML Fe film for increasing temperature showing a reorientation from out-of-plane to in-plane.

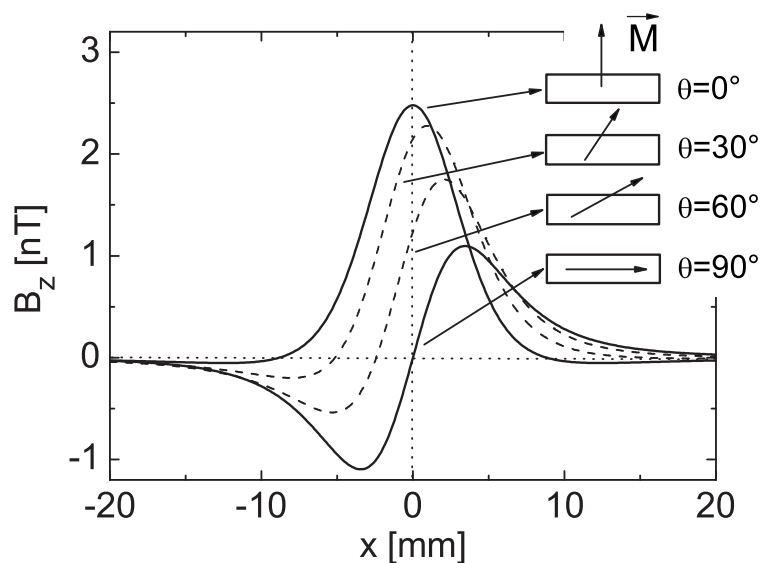


Fig. 4.58.: Calculated z -component of the magnetic stray field of a square film during reorientation of the magnetization from an out-of-plane orientation $\parallel z$ ($\theta = 90^\circ$) to an in-plane magnetization direction $\parallel x$ ($\theta = 0^\circ$). A magnetization $M = 180$ kA/m of an 8 ML thick Fe film enters the calculation.

A further increase of the temperature will reduce the stray field amplitude, and above the Curie temperature of $422 \text{ K} \pm 6 \text{ K}$, B_z vanishes.

The magnetic stray field component B_z during a reorientation from an out-of-plane to an in-plane magnetization direction has been modelled using Eq. (2.24) and is shown in Fig. 4.58. The respective polar angles θ are given in the figure, whereas the in-plane angle was chosen to have an in-plane magnetization projection which is parallel to the scanning direction x . For the calculation of the stray field we chose a typical SQUID-sample distance of $h = 5$ mm and a magnetization of $M = 180$ kA/m to fit the observed peak height. The calculated stray field for different θ qualitatively shows good agreement to the experimental stray field data confirming the continuous change of θ . (compare Figs. 4.57 and 4.58). Deviations from the stray field of an ideally out-of-plane magnetized sample may be explained by not magnetizing the sample out-of-plane prior to the SQUID measurements. Therefore, a minor part of the film can incidentally be magnetized opposed to the main magnetization direction of the film. In comparison to the measured remanent magnetization of $M = 350$ kA/m at room temperature, it is corroborated that the spontaneously reoriented film at low temperature is not in a single domain state. Note that the 'unnatural' line shapes of B_z impede a proper analysis of the magnetization. Besides, a careful examination of the experimental stray field yields a temperature driven shift of the stray field signal to smaller x values, e.g. at $T = 73 \text{ K}$, $x_{max} = 55$ mm and $T = 416 \text{ K}$, $x_0 = 50.8$.

This effect is exclusively explained from a length expansion of the cryostat and the sample holder.

In the following, the reorientation will be explained by the temperature dependence of the anisotropic part of the free energy density. The equilibrium angle of the magnetization of a FM sample can be calculated by minimizing the free energy density with respect to the spherical coordinates. The total free energy density for thin Fe films on GaAs is [45]:

$$\begin{aligned}
 F = & \left(\frac{\mu_0}{2} M^2 - K_{2\perp} - K_4 \right) \cos^2 \theta \\
 & + K_{2\parallel} \cos^2(\phi - \delta) \sin^2 \theta \\
 & - \frac{K_4}{8} (7 + \cos 4\phi) \sin^4 \theta
 \end{aligned} \tag{4.14}$$

Here, the Zeeman energy is omitted since measurements are carried out without external magnetic field. All other notations are the ones of Sec. 2.2.2. In a first approach, we do not consider the fourfold anisotropy contribution K_4 which is rather small in thin films. Also negligible is the twofold uniaxial anisotropy contribution $K_{2\parallel}$, which is about one order of magnitude smaller than the out-of-plane anisotropy contribution $K_{2\perp} > 0$, being by far the dominating term for the film thicknesses under consideration. Although the oxygen reduces the perpendicular twofold anisotropy at the initial step of oxidation (≤ 24 L), $K_{2\perp}$ of a 10 ML film still has about 50% of the value prior to the oxygen exposure (Sec. 4.5). Finally, Eq. (4.14) reduces to

$$F = \left(\frac{\mu_0}{2} M^2(T) - K_{2\perp}(T) \right) \cos^2(\theta) \tag{4.15}$$

The magnetization M and the twofold anisotropy constant $K_{2\perp}$ are functions of the temperature T which will both decrease as T rises. For $\mu_0/2M^2(T) - K_{2\perp} > 0$, the shape anisotropy dominates and the magnetization will lie in the plane of the film ($\theta = \pi/2$) to minimize the free energy. An out-of-plane alignment of the magnetization ($\theta = 0$) is anticipated if $K_{2\perp}$ outbalances the shape anisotropy.

ZAKERI *et al.* [176] measured the temperature dependence of M and $K_{2\perp}$ for a 5 ML Fe film on GaAs and compared it to a model by CALLEN AND CALLEN [177]. They found the following experimental relation for the 5 ML Fe/GaAs:

$$\frac{K_{2\perp}(T)}{K_{2\perp}(0)} \propto \left(\frac{M(T)}{M(0)} \right)^{2.9 \pm 0.2} \tag{4.16}$$

This relationship implies a faster decay of the anisotropy constant $K_{2\perp}$ in comparison to the magnetization.

First, we discuss the in-plane alignment of the magnetization at room temperature of the oxidized 8.6 ML Fe film. Using $M(T=300 \text{ K})$, the shape anisotropy energy density is calculated to $7.7 \times 10^4 \text{ J/m}^3$. On the other hand, $K_{2\perp}$ for a 10 ML Fe film at 24 L oxygen is $2.8 \times 10^5 \text{ J/m}^3$ (see Sec. 4.5). However, these values cannot explain an in-plane magnetization and therefore,

$K_{2\perp}$ must be at least a factor of 4 smaller. This seems to be very likely since the Fe film was oxidized much stronger (~ 25000 L). Regrettably, FMR spectra were not evaluable at oxygen exposures > 204 L to observe the further decrease of $K_{2\perp}$. At low temperature, the magnetization is not significantly enhanced as can be concluded by similar stray field amplitudes between $T=40$ K and $T=300$ K. According to Eq. (4.16), $K_{2\perp}$ increases more strongly with decreasing temperature and causes the reorientation below $T=175$ K.

Although the reorientation transition as a function of temperature is understandable from the temperature dependence of M and $K_{2\perp}$, it cannot explain the continuous reorientation. If $\mu_0/2M^2(T) - K_{2\perp}$ changes sign, the equilibrium angle will only change discontinuously between $\theta = 0$ and $\theta = \pi/2$ with no intermediate settings. In a theoretical study by ERICKSON and MILLS [178] considering a twofold anisotropy contribution only, it was predicted that the reorientation of magnetization as a function of temperature occurs via a loss of long-range order for a system with a ground state easy axis perpendicular to the film plane. Since we observe a continuous transition with no vanishing stray field during the reorientation, one can conclude that other anisotropy contributions stabilize the ferromagnetic order of the sample when the dipolar contribution and the contribution from $K_{2\perp}$ compensate for each other during the reorientation.

These anisotropy contributions, separated in surface and volume contributions, were derived from thickness dependent FMR investigations of Fe films on GaAs in Ref. [45]. For thin films, the volume contribution to the fourfold anisotropy can be neglected, but a small surface contribution of $K_4^{s,eff} = -6.1 \times 10^{-5}$ J/m² is observed. Since a negative $K_4^{s,eff}$ yields an easy axis of magnetization along the $\langle 1\ 1\ 0 \rangle$ -directions, it may explain the continuous transition.

A measurement of the same film after 36 h yielded an in-plane remanent magnetization with a value of 660 ± 50 kA/m at room temperature. This is about twice the earlier value. After cooling down the film again, no out-of-plane reorientation could be observed. The increase of magnetization with time indicates that the *in situ* oxidized Fe film is not in a thermodynamic stable state and subject to chemical and/or structural rearrangements. Unfortunately, this experimental result could not be reproduced by oxidizing Fe films of comparable thickness with the same process parameters. This can be understood from the delicate dependence on the two energy contributions discussed above. To observe the temperature driven reorientation, these contributions have to be quite similar and slight variations of process parameters can become decisive. Incidentally, $K_{2\perp}$ was bigger than the shape anisotropy energy $\mu_0 M^2$ for the oxidized film which showed the reorientation. All other oxidized Fe films, which were in-plane at all temperatures, obviously had an even smaller $K_{2\perp}$.

5. Conclusion and outlook

In the present work, the growth and the magnetic properties of ultrathin Fe films on GaAs(001)-(4×6) are investigated, particularly with regard to the magnetization. The magnetic stray field of a magnetized film is scanned using an *in situ* rf SQUID and is compared to stray field calculations, which are carried out for different sample geometries and magnetization orientations. The sample magnetization is determined in absolute units with a resolution limit of a fraction of a monolayer. The demagnetizing fields for thin films are calculated and the range of these fields within the sample is estimated as a function of the Fe film thickness. It turns out that for thin films ($d < 10$ nm) with a lateral size of several millimeters, the demagnetizing effects are found only at the magnetic poles of the film and can influence the sample magnetization only in the μm -range away from the film edges. Thus, the reduction of the magnetic stray field due to demagnetizing effects in a typical SQUID to sample distance of $h = 5$ mm is negligible and does not influence the magnetization measurement. The demagnetizing effect at the sample edge is studied by Kerr microscopy on a 15 ML Fe/GaAs(001) film covered with 3 nm Pt and no evidence for domains in remanence are found. Additionally, it is shown in this work that the roughness of magnetic films, which at low thicknesses can be quite pronounced in the case of Fe on GaAs, does not alter the sample stray field under the reasonable assumption that the roughness does not change the magnetization direction. A detailed discussion on the factors which limit the accuracy in the determination of M is given. It turns out that the distance between sample and SQUID, h , has the greatest influence on the accuracy of the determination of M from the stray field data; $\Delta M/M = 5\%$. To minimize this contribution, a current loop integrated in the sample holder is used to extract h from the loop's stray field.

Fe films are deposited on Ga-rich {4×6}-reconstructed GaAs at room temperature and the magnetization M in remanence of up to 20 ML Fe is determined. Below a coverage of 2 ML none of the prepared films are ferromagnetic even at a temperature of $T=40$ K. Different behavior of the magnetization is observed depending on the substrate preparation and the experimental parameters. For some Fe films, M at a thickness from 5 ML upwards is bulk-like at room temperature. Other films show a gradual increase of M , starting from a film thickness of 3-4 ML to the Fe bulk value at a thickness of 10 ML. The decrease of M at low Fe coverage is most likely to be influenced by a rough surface topography of the substrate which 'delays' the coalescence of the iron islands. The magnetization serves as a measure of how much of the Fe islands are in-

terconnected. The formation of intermetallic compounds at the interface can be excluded since the magnetization recovers around 10 ML to the Fe bulk value. This indicates the absence of 'magnetic dead layers' which have been reported in the literature. IV-LEED measurements are used to probe the vertical interplanar distance d_{inter} of the surface layers of the Fe/GaAs(001) film. d_{inter} is increased to about 3% with respect to bulk α -Fe up to a film thickness of around 20 ML due to the epitaxial growth on GaAs(001). Above 20 ML, the film relaxes via incorporation of misfit dislocations. Interestingly, the line width ΔB_{pp} of FMR lines shows a decrease of a factor of about 3 for the same thickness. This finding is attributed to a decrease of the Gilbert damping constant α of the same order of magnitude. Temperature dependent measurements ($40 \text{ K} < T < 400 \text{ K}$) on 2.3, 3.7 and 6.5 ML Fe films show a reduced Curie temperature T_C with respect to bulk α -Fe which indicates the finite size effects for decreasing film thickness. For the 3.7 ML Fe film, the phase transition from the ferromagnetic to the paramagnetic regime occurs around $391 \text{ K} \pm 5 \text{ K}$. The determination of the spin wave Bloch parameter B for the 3.7 ML Fe/GaAs film yields a value which is increased by a factor 22 with respect to the Fe-bulk value. The data from different film thicknesses in this work together with values taken from the literature show a non-linear $B(1/d)$ dependence which probably results from the strong uniaxial anisotropy in thin Fe/GaAs films.

The thickness dependent reorientation which occurs between 7 and 20 ML due to the interplay of K_4 and $K_{2||}$ is studied using SQUID data, and in comparison to the results of the FMR measurements, both methods show good agreement.

Fe/GaAs films of 5 to 33 ML thickness are exposed to various oxygen doses (up to 30000 Langmuir (L)¹) at room temperature while the structural, chemical and magnetic properties are investigated. The vanishing of the $p(1 \times 1)$ LEED spots of the Fe(001) surface indicates a disordered growth of Fe oxide. Only at very low exposures a very weak $c(2 \times 2)$ superstructure is visible. It is found that at low exposures ($< 10 \text{ L}$) FeO forms which modifies after further oxygen exposure ($> 1000 \text{ L}$) to Fe_2O_3 . XRD measurements on a 20 ML Fe film which is exposed to air confirms the formation of γ - Fe_2O_3 (maghemite) and yields crystallite sizes in the range of 75 to 90 nm. Therefore, one can conclude that with increasing oxygen exposure a transition from disordered to polycrystalline Fe oxide occurs and the crystallites grow in size. The vertical strain of a 33 ML Fe film is considerably reduced after the film is exposed to only 1.5 L oxygen. The magnetization of 5, 8 and 16 ML Fe films is measured as a function of oxygen exposure and a reduction of M is found which is attributed to the disordered growth of Fe oxide. It is found that M , which is corrected for the individual film thickness, of the thinner films decreases more quickly with oxygen exposure. This might be either caused by a roughness dependent oxidation process, the finite size effect or a thickness dependent relaxation of the Fe films during initial oxygen exposure. It is found that the 16 ML Fe film develops a passivating oxide layer consist-

¹ 1 L = 10^{-6} Torr sec

ing of 4 former Fe layers at 25000 L. To investigate the influence on the different anisotropy constants angular dependent FMR measurements were carried out on a 10 ML Fe film. In the initial stage of oxidation the perpendicular uniaxial anisotropy $K_{2\perp}$ is reduced by 40 % at 3 L O_2 at which the other anisotropies are hardly affected. A moderate oxygen exposure of up to 24 L has nearly no further effect on any of the anisotropy constants. Furthermore, the oxidation of Fe films at $T=40$ K can be effectively suppressed.

Finally, when a heavily oxidized (25000 L) 8.6 ML Fe film was cooled it exhibited an out-of-plane magnetization for $T < 175$ K. This has never been observed for Fe films on GaAs(001) since the dominating shape anisotropy $F_{shape} = \mu_0 M^2 \cos(\theta)/2$ always favors an in-plane orientation of M . Since oxygen exposure can dramatically reduce M in thin films (and thus shape anisotropy), other anisotropies are able to dominate. With increasing temperature M rotates back in the plane of the film between 175 and 250 K. This continuous reorientation transition is governed by the interplay of $M(T)$ and $K_{2\perp}(T)$. The latter must therefore decrease more rapidly with increasing temperature. Unfortunately, this surprising spin reorientation transition could not be reproduced but may be worthwhile to look for in a new project.

The following remarks give an outlook on issues which can be associated to this work. The operation of a SQUID magnetometer is often perturbed by environmental noise whose origin is quite far away from the SQUID (in the range of m, rather than the typical mm spacing between SQUID and sample). However, the gradient of disturbing electromagnetic fields becomes smaller at greater distances. Using a SQUID gradiometer (which measures e.g. dB/dx), the noise sensitivity is decreased whereas the stray field gradient from a magnetized sample prevails. Since all stray fields in this thesis are calculated analytically, it is easy to transfer them to the gradiometer method which comprises higher SQUID stability and even better resolution.

The *in situ* Kerr effect setup, which was built as part of the work of this thesis, uses the longitudinal MOKE with the magnetic field applied along the y -direction (see Figs. 3.1 and 3.3). However, the SQUID measurements are usually carried out with the easy axis of the magnetic film oriented along the scanning direction of the SQUID, i.e. the x -direction. It would be desirable to perform the MOKE measurements along this direction (x). This is in fact possible by applying the transverse Kerr effect (T-MOKE), which gives rise to an intensity change of the incident light rather than a Kerr rotation, to record magnetic hysteresis loops. It can be demonstrated that the magnetic hysteresis using T-MOKE measured on a 30 ML Fe/GaAs film which has been exposed to air, yields a signal to noise ratio of better than 40:1 while being measured repeatedly for 2 minutes. Although these measurements are carried out *ex situ*, they demonstrate the applicability in UHV where the light has to pass through the glass finger. Another side-effect of T-MOKE is the absence of the Faraday effect which superimposes the Kerr rotation in longitudinal geometry and therefore is not conducive to precise analysis.

A. Appendix

A.1. Magnet used for magneto-optic Kerr effect

For the *in situ* MOKE measurements, a magnet was designed which can be mounted around the glass finger of the UHV system to perform Kerr effect measurements in longitudinal geometry. A sketch of the magnet which has been fabricated from a Pertinax[©] rod is sketched in Fig. A.1. Proper mounts (not shown here) have been built to attach the magnet to the glass finger. The bore parallel to the long axis of the magnet is tapered at the ends to allow for longitudinal MOKE measurements with a laser beam. For the electrical winding, an isolated Cu wire with a cross section of $A=0.8 \text{ mm}^2$ was used with about 600 turns on each side of the coil bobbin. The resistance of the coil is about $R=4 \text{ } \Omega$ and the calibration factor is 8.76 mT/A .

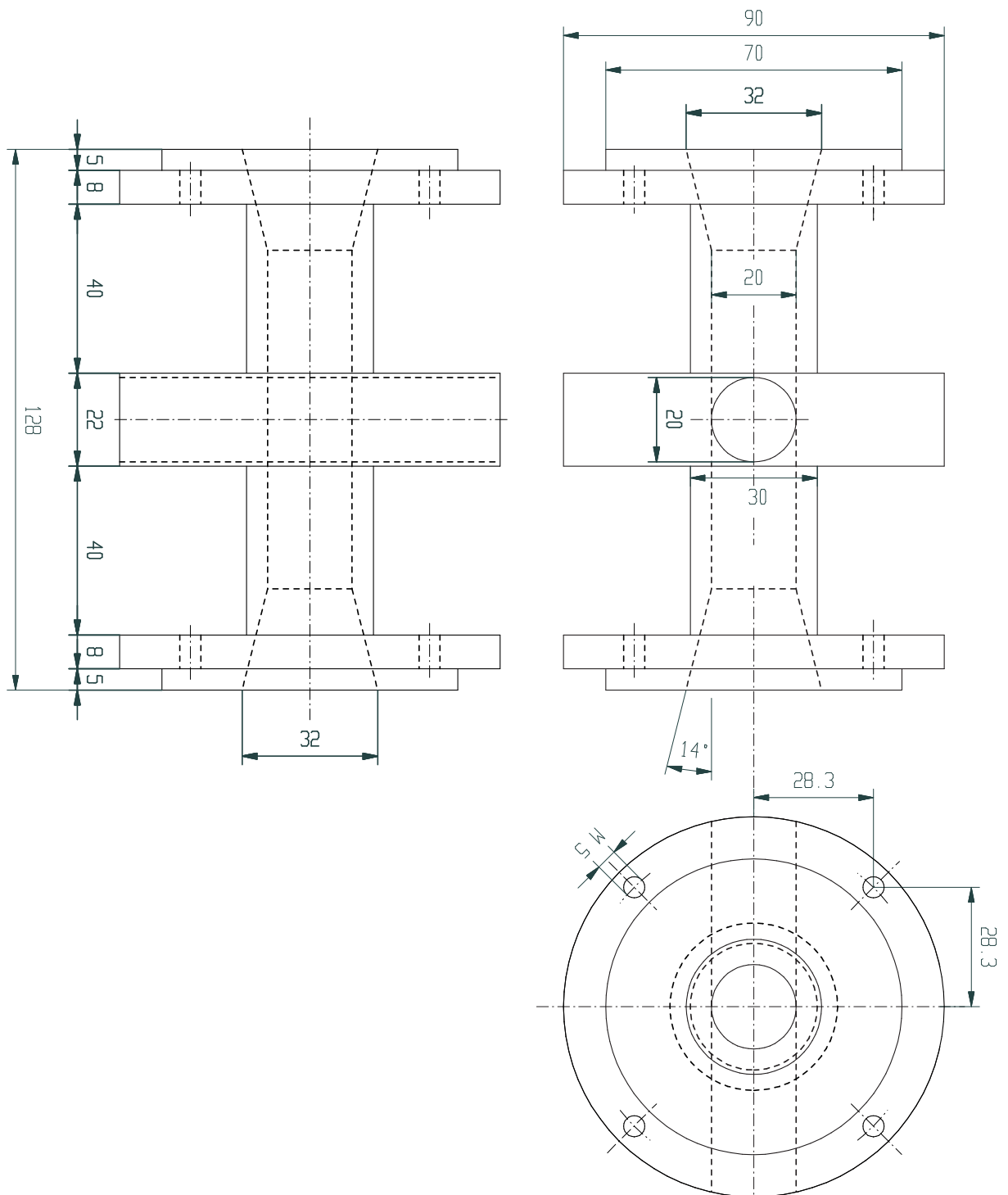


Fig. A.1.: Engineering drawing of the magnet used for magneto-optical Kerr effect from different views.

A.2. Magnetic field pulse box

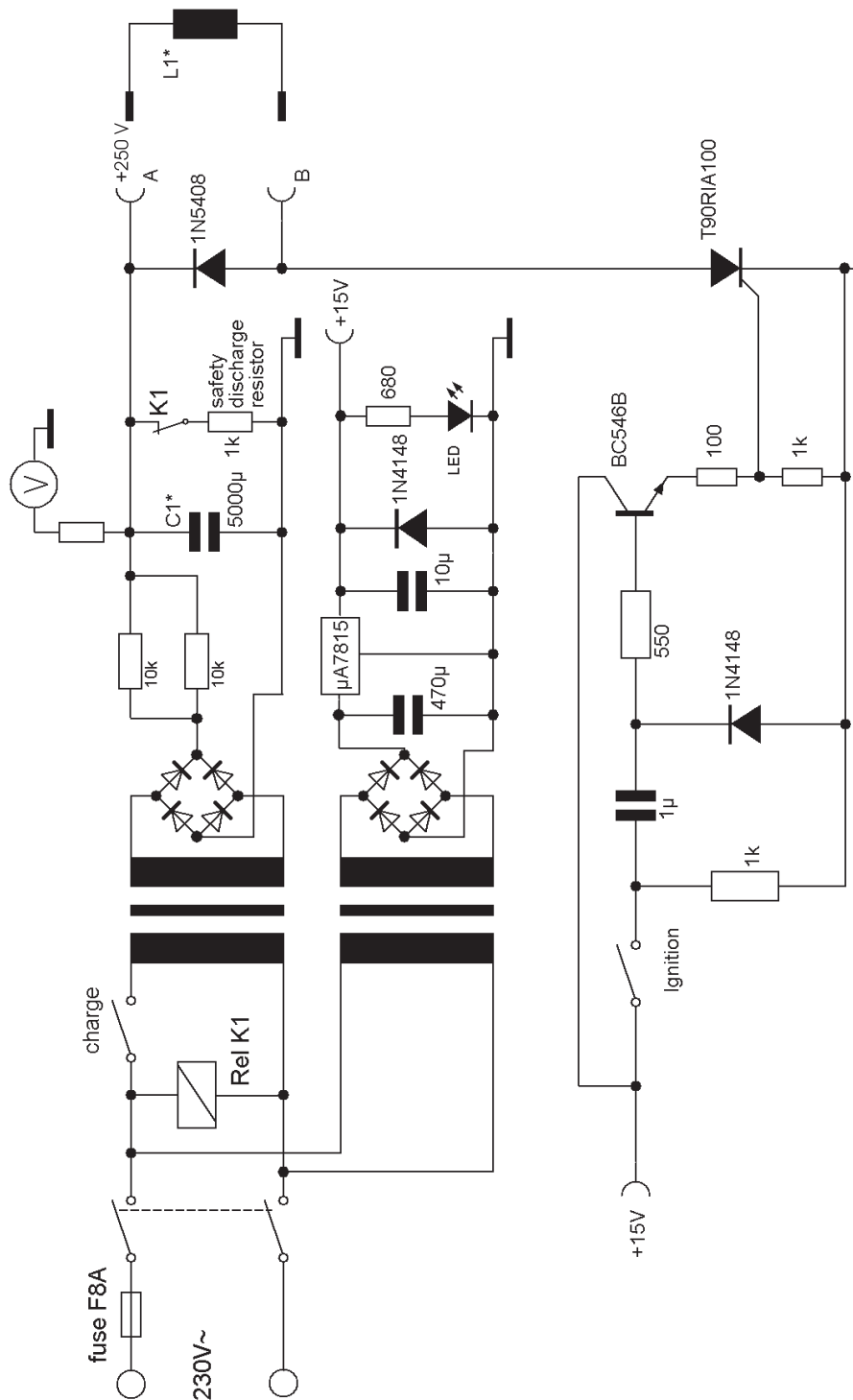


Fig. A.2.: Electrical circuitry of the pulse box to generate pulsed magnetic field.

Figure A.2 shows the circuit diagram of the pulse box to generate pulsed magnetic fields. These fields exceed the fields of a given coil compared to 'conventional' dc laboratory power supplies many times over. It consists of a capacitor bank which is charged as long as the 'charge

switch' is pressed. The charging current is limited by the two $10k\Omega$ resistors. A maximum voltage of approximately $250V$ can be achieved when the 'charge switch' is pressed for 5 minutes. If the 'ignition switch' is pushed the thyristor *T90RIA100* discharges the capacitors via the electromagnet *LI* attached to the connectors *A* and *B*. In this thesis, the MOKE magnet from A.1 is used, as well as a second 'pulse magnet', which is lighter for more secure fixing to UHV glass finger. Figure A.3 shows the magnitude of the current as a function of time for both magnets. The current-magnetic flux coefficient for the MOKE magnet is 8.76 mT/A and yields a maximum field of $B_{max} = 0.49 \text{ T}$. Even in the case of the 'pulse magnet' (30.26mT/A) with much higher resistance $R \approx 30 \Omega$, the maximum field is $B_{max} = 0.26 \text{ T}$ when the capacitors are fully loaded. A security feature of the pulse box is the 'self holding' relay *Rel KI*, which retains relay contact *KI* as long as the main power is turned on. As the main power is switched off, *KI* will be closed and the capacitor bank will be discharged via a $1k$ high power ceramic resistor.

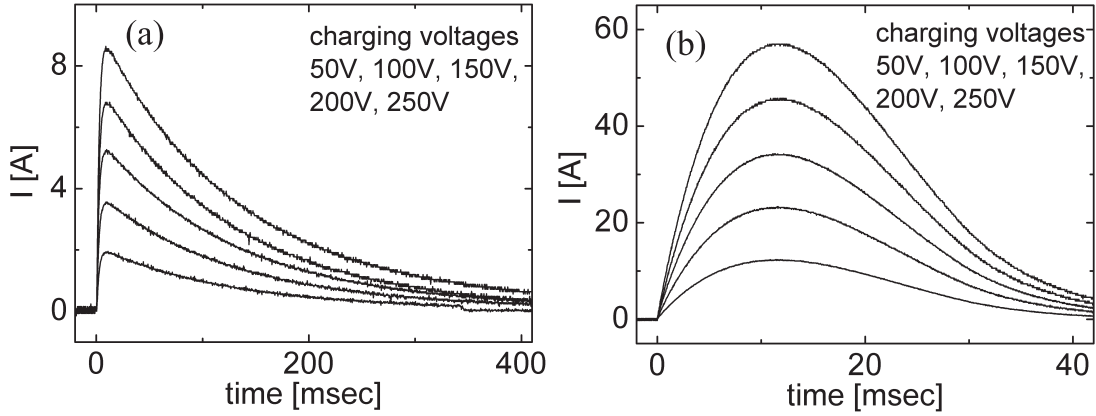


Fig. A.3.: Evolution of the currents generated by the pulse box with various voltages are shown for (a) the 'pulse box magnet' and (b) the MOKE magnet.

A.3. Analytic expressions for the magnetic stray field

A.3.1. Rectangular shaped current loop

Consider the site of wire 1 in Fig. 4.6 where it is parallel to the x -axis at distance a within the $x - y$ plane. Consequently, substitution of $y_p \rightarrow y_p + a$ in Eq. 4.6 leads to

$$B_{z_1} = \frac{\mu_0}{4\pi} \frac{I}{\sqrt{(y_p+a)^2+z_p^2}} \frac{1}{\sqrt{1+\frac{z_p}{y_p+a}}} \left[\sin \left(\arctan \left(\frac{x_e-x_p}{\sqrt{(y_p+a)^2+z_p^2}} \right) \right) - \sin \left(\arctan \left(\frac{x_a-x_p}{\sqrt{(y_p+a)^2+z_p^2}} \right) \right) \right] \quad (\text{A.1})$$

In the case of wire 3, we can proceed similarly, but due to the opposite direction of the current in $-x$ -direction we include a minus and replace $y_p \longrightarrow y_p - a$

$$B_{z3} = -\frac{\mu_0}{4\pi} \frac{I}{\sqrt{(y_p-a)^2+z_p^2}} \frac{1}{\sqrt{1+\frac{z_p}{y_p-a}}} \left[\sin \left(\arctan \left(\frac{x_e-x_p}{\sqrt{(y_p-a)^2+z_p^2}} \right) \right) - \sin \left(\arctan \left(\frac{x_a-x_p}{\sqrt{(y_p-a)^2+z_p^2}} \right) \right) \right] \quad (\text{A.2})$$

Wire 2 lies along the y -axis and has a length of $2a$ which leads to both the commutation of x_p and y_p and the determination of the start and end points of the wire $x_a = a$ and $x_e = -a$. Therefore, we get:

$$B_{z2} = \frac{\mu_0}{4\pi} \frac{I}{\sqrt{x_p^2+z_p^2}} \frac{1}{\sqrt{1+\frac{z_p}{x_p}}} \left[\sin \left(\arctan \left(\frac{y_p-a}{\sqrt{x_p^2+z_p^2}} \right) \right) - \sin \left(\arctan \left(\frac{y_p+a}{\sqrt{x_p^2+z_p^2}} \right) \right) \right] \quad (\text{A.3})$$

A.3.2. In-plane magnetized square shaped film

The z -component of the rescaled magnetic field with an in-plane magnetization of arbitrary in-plane angle α with respect to the x -axis was calculated within this thesis. Please note that the Cartesian coordinates given here are in rescaled lengths \tilde{r} . To calculate the physical stray field, one substitutes back to Cartesian coordinates $\tilde{r}_i = 2r_i/L$ with $i=1,2,3$ and multiplies the expression given below with $3\mu_0 \cdot M \cdot d/4\pi$ as shown in Sec. 2.3.5. d is the thickness of the film and M the (volume) magnetization:

$$B_{z,square}^{resc,in-plane}(\alpha, \tilde{x}, \tilde{y}, \tilde{z}) = \frac{2\tilde{z}}{L(1-2\tilde{x}+\tilde{x}^2+\tilde{z}^2)(1+2\tilde{x}+\tilde{x}^2+\tilde{z}^2)} \left\{ \frac{1}{ABC} \left[-(1-\tilde{y})A(\tilde{x}^2(B-C) + (1+\tilde{z}^2)(B-C) - 2\tilde{x}(B+C)) \cos \alpha + \right. \right. \\ \left. \left. - D(B+C+\tilde{x}(B-C)) \sin \alpha \right] + \frac{1}{EFG} \left[(-1-\tilde{y})E(\tilde{x}^2(F-G) + (1+\tilde{z}^2)(F-G) - 2\tilde{x}(F+G)) \cos \alpha + \right. \right. \\ \left. \left. - D(F+G+\tilde{x}(F-G)) \sin \alpha \right] \right\} \quad (\text{A.4})$$

where

$$\begin{aligned}
A &= 1 - 2\tilde{y} + \tilde{y}^2 + \tilde{z}^2 \\
B &= \sqrt{2 - 2\tilde{x} + \tilde{x}^2 - 2\tilde{y} + \tilde{y}^2 + \tilde{z}^2} \\
C &= \sqrt{2 + 2\tilde{x} + \tilde{x}^2 - 2\tilde{y} + \tilde{y}^2 + \tilde{z}^2} \\
D &= \tilde{x}^4 + 2\tilde{x}^2(-1 + \tilde{z}^2) + (1 + \tilde{z}^2)^2 \\
E &= 1 + 2\tilde{y} + \tilde{y}^2 + \tilde{z}^2 \\
F &= \sqrt{2 - 2\tilde{x} + \tilde{x}^2 + 2\tilde{y} + \tilde{y}^2 + \tilde{z}^2} \\
G &= \sqrt{2 + 2\tilde{x} + \tilde{x}^2 + 2\tilde{y} + \tilde{y}^2 + \tilde{z}^2}
\end{aligned}$$

A.3.3. Out-of-plane magnetized square shaped film

In this section, the z -component of the rescaled magnetic stray field for an out-of-plane magnetized film of square shape is given. In order to obtain the stray field in physical units, follow the instructions given in Sec. A.3.2 of this appendix.

$$\begin{aligned}
B_z(\tilde{x}, \tilde{y}, \tilde{z}) &= -\frac{(-1 + \tilde{y})}{L(1 - 2\tilde{y} + \tilde{y}^2 + \tilde{z}^2)} \left(-\frac{(-1 + \tilde{x})(2 - 2\tilde{x} + \tilde{x}^2 - 2\tilde{y} + \tilde{y}^2 + 2\tilde{z}^2)}{(1 - 2\tilde{x} + \tilde{x}^2 + \tilde{z}^2)\sqrt{2 - 2\tilde{x} + \tilde{x}^2 - 2\tilde{y} + \tilde{y}^2 + \tilde{z}^2}} + \right. \\
&\quad \left. \frac{(1 + \tilde{x})(2 + 2\tilde{x} + \tilde{x}^2 - 2\tilde{y} + \tilde{y}^2 + 2\tilde{z}^2)}{(1 + 2\tilde{x} + \tilde{x}^2 + \tilde{z}^2)\sqrt{2 + 2\tilde{x} + \tilde{x}^2 - 2\tilde{y} + \tilde{y}^2 + \tilde{z}^2}} \right) + \\
&\quad -\frac{(1 + \tilde{y})}{L(1 + 2\tilde{y} + \tilde{y}^2 + \tilde{z}^2)} \left(-\frac{(-1 + \tilde{x})(2 - 2\tilde{x} + \tilde{x}^2 + 2\tilde{y} + \tilde{y}^2 + 2\tilde{z}^2)}{(1 - 2\tilde{x} + \tilde{x}^2 + \tilde{z}^2)\sqrt{2 - 2\tilde{x} + \tilde{x}^2 + 2\tilde{y} + \tilde{y}^2 + \tilde{z}^2}} + \right. \\
&\quad \left. \frac{(1 + \tilde{x})(2 + 2\tilde{x} + \tilde{x}^2 + 2\tilde{y} + \tilde{y}^2 + 2\tilde{z}^2)}{(1 + 2\tilde{x} + \tilde{x}^2 + \tilde{z}^2)\sqrt{2 + 2\tilde{x} + \tilde{x}^2 + 2\tilde{y} + \tilde{y}^2 + \tilde{z}^2}} \right). \tag{A.5}
\end{aligned}$$

A.3.4. In-plane magnetized circular film

In this section, the z -component of the rescaled magnetic stray field component B_z for a magnetic circular film with radius R and in-plane magnetization along the x -direction is given. Using the analytic expression Eq. (2.26) in cylindrical coordinates and inserting the transformation instruction Eq. (2.28) yields the analytic expression in rescaled coordinates. In order to obtain the stray field in physical units, follow the instructions given in Sec. A.3.2 of this

appendix.

$$\begin{aligned}
B_{z,circle}^{resc}(\tilde{x}, \tilde{y}, \tilde{z}) = & \\
& \frac{2\tilde{x}\tilde{z}}{R(\tilde{x}^2 + \tilde{y}^2) \left(\left(-1 + \sqrt{\tilde{x}^2 + \tilde{y}^2} \right)^2 + \tilde{z}^2 \right)^{3/2}} \sqrt{1 - 4 \frac{\sqrt{\tilde{x}^2 + \tilde{y}^2}}{\left(1 + \sqrt{\tilde{x}^2 + \tilde{y}^2} \right)^2 + \tilde{z}^2}} \\
& \left((1 + \tilde{x}^2 + \tilde{y}^2 + \tilde{z}^2) \text{EllipticE} \left(2 \sqrt{\frac{\sqrt{\tilde{x}^2 + \tilde{y}^2}}{\left(1 + \sqrt{\tilde{x}^2 + \tilde{y}^2} \right)^2 + \tilde{z}^2}} \right) - \right. \\
& \left. \left(\left(-1 + \sqrt{\tilde{x}^2 + \tilde{y}^2} \right)^2 + \tilde{z}^2 \right) \text{EllipticK} \left(2 \sqrt{\frac{\sqrt{\tilde{x}^2 + \tilde{y}^2}}{\left(1 + \sqrt{\tilde{x}^2 + \tilde{y}^2} \right)^2 + \tilde{z}^2}} \right) \right) \quad (\text{A.6})
\end{aligned}$$

A.3.5. The demagnetizing field of a square shaped film

Consider a rectangular shaped film of thickness d and magnetization M . Its length along the x -direction is L_x and along the y -direction L_y . Let the film be homogenously magnetized along x and consider it thin compared to its lateral dimensions. Then, the x -component of the magnetic field inside the film can be calculated analytically:

$$\begin{aligned}
H_d^x(x, y, L_x, L_y, M, d) = & -\frac{Md}{2\pi} \\
& \left\{ \frac{L_y - y}{(L_x - x) \sqrt{L_y^2 + L_x^2 - 2L_y y + y^2 - 2L_x x + x^2}} + \right. \\
& \frac{L_y + y}{(L_x - x) \sqrt{L_y^2 + L_x^2 + 2L_y y + y^2 - 2L_x x + x^2}} + \\
& \frac{L_y - y}{(L_x + x) \sqrt{L_y^2 + L_x^2 - 2L_y y + y^2 + 2L_x x + x^2}} + \\
& \left. \frac{L_y + y}{(L_x + x) \sqrt{L_y^2 + L_x^2 + 2L_y y + y^2 + 2L_x x + x^2}} \right\} \quad (\text{A.7})
\end{aligned}$$

where M is in A/m and all lengths in m. The demagnetizing field in the formula above is then given in A/m.

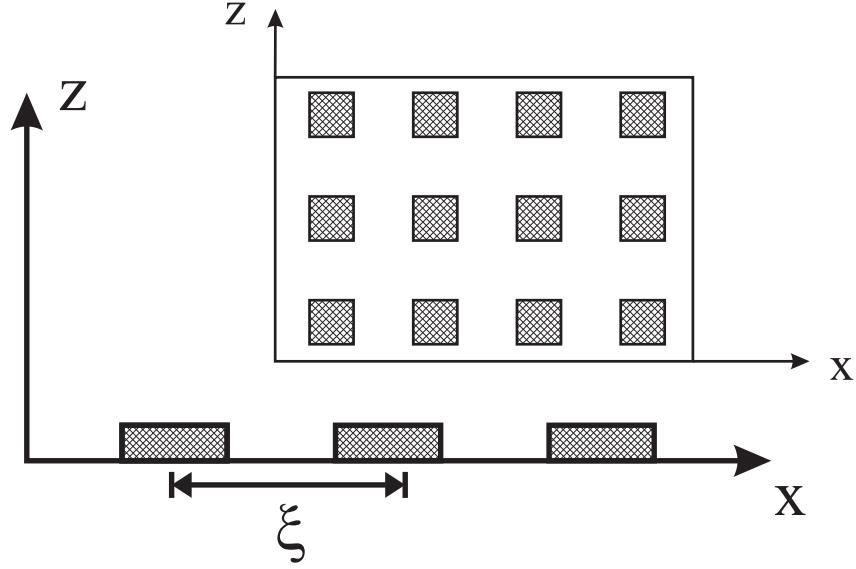


Fig. A.4.: An infinitely expanded film with periodic surface roughness gives rise to a periodic magnetic charge density in the x - y -plane. ξ is the periodicity length along x and y .

A.4. Calculation of the magnetostatic potential for periodic surface charges

Let us compute a magnetostatic field from a rough surface with periodic roughness as shown in Fig. A.4. The surface magnetic charge density $\sigma_{mag_{m,n}}$ for such a system with periodicity in x and y directions can be expanded in a Fourier series:

$$\sigma_{mag_{m,n}} = \sum_{-\infty}^{\infty} \sum_{-\infty}^{\infty} c_{m,n} \exp \left[\frac{im\pi}{\xi} x + \frac{in\pi}{\xi} y \right] \quad (\text{A.8})$$

where ξ is the periodicity length of the surface charge and $c_{m,n}$ is the Fourier transform which is given by the following equation:

$$c_{m,n} = \frac{1}{(2\pi)^2} \int_{-\xi/2}^{\xi/2} \int_{-\xi/2}^{\xi/2} \sigma_{mag_{m,n}} \exp \left[-\frac{im\pi}{\xi} x - \frac{in\pi}{\xi} y \right] dx dy \quad (\text{A.9})$$

In analogy to electrostatics, the scalar magnetic potential can be expressed by a surface magnetic charge density and in addition, the Laplace equation must be fulfilled. Furthermore, the magnetostatic potential $\phi_{m,n}$ must be valid at the boundary ($z = 0$).

$$\nabla^2 \phi_{mag_{m,n}} = 0 \quad (\text{A.10})$$

$$\nabla \phi|_{z=0} = -\sigma_{mag_{m,n}} \quad (\text{A.11})$$

where $\sigma_{mag_{m,n}}$ is the surface charge density of Eq. (A.8). A possible solution for the magnetostatic potential is:

$$\phi_{mag_{m,n}}(x, y, z) = \sum_{-\infty}^{\infty} \sum_{-\infty}^{\infty} \phi_{m,n} \exp \left[\frac{im\pi}{\xi} x + \frac{in\pi}{\xi} y \right] \exp[-P_{m,n}z] \quad (\text{A.12})$$

where $P_{m,n}$ can be expressed as following:

$$P_{m,n} = \frac{\sqrt{m^2 + n^2}\pi}{\xi} \quad (\text{A.13})$$

It is important to note that $P_{m,n}$ is positive and scales inversely with ξ . Consequently, the scalar magnetic potential can be conveniently written as

$$\phi_{mag_{m,n}}(x, y, z) = \sum_{-\infty}^{\infty} \sum_{-\infty}^{\infty} \phi_{nm} \exp \left[-\frac{im\pi}{\xi} x - \frac{in\pi}{\xi} y \right] \exp \left[-\frac{\sqrt{m^2 + n^2}\pi}{\xi} z \right] \quad (\text{A.14})$$

The magnetic field can be calculated by $H = \nabla \phi_{mag_{m,n}}$. Therefore, the magnetic field due to a periodic magnetic charge density decreases exponentially with increasing distance z . The fundamental harmonic ($n,m=0$) does not exist due to the absence of a net surface charge. Although the calculation is carried out for a periodic surface roughness, it can also be applied for a non-periodic rough surface (see main text).

A.5. Remarks on phase transitions and the critical exponent β

The appearance of a spontaneous magnetization below a critical temperature is a characteristic feature of a phase transition, namely the transition from a non-ordered paramagnetic state into a ferromagnetic state below the Curie temperature T_C . The order parameter, which decides whether or not a system is in an ordered state, is the magnetization of the system. The onset of ferromagnetism is accompanied by the breaking of the symmetry which the system had in the non-ordered state above T_c , i.e. the rotational symmetry in the paramagnetic state. Simple models of magnetism can be taken into consideration to discuss the implications which the symmetry breaking brings about. As a simple example, the Landau theory of magnetism expands the free energy as a power series in M containing only even powers up to the order of four. Minimization of this free energy expression $\partial F/\partial M = 0$ yields $M = \pm const \cdot (T_C - T)^{1/2}$ for $T < T_C$. Since this approach of describing phase transitions assumes an identical averaged exchange field produced by neighboring spins, it is called a *mean-field theory*. However, mean field theory neglects correlations and fluctuations of the order parameter which become very important near T_C . Therefore, predictions from this theory near T_C must be handled with care.

In real systems, admittedly, the magnetization behaves as $(T_C - T)^\beta$ near the Curie temperature with β not necessarily equal to $1/2$. β is one among other critical exponents and gives experimental valuable information about the nature of the phase transition. Albeit the type of phase transition, e.g. liquid-gas, ferromagnetic-paramagnetic or any other, the critical exponents arising in different systems often possess the same set of critical exponents. This phenomenon is known as *universality*. Thus, for a continuous phase transition, the critical exponents depend only on the dimensionality of the system, the symmetry of the order parameter and whether the forces are short or long range.

A.6. Details of the sample holder

The sample holder for the SQUID measurements needs to satisfy several requirements. Its length is determined by the maximum travel distance of the UHV manipulator on the one hand, and the FMR measuring position with fully extended manipulator on the other hand.

It turned out that OFHC (oxygen-free high conductivity) Cu, which is normally used in UHV applications, has FM impurities which can easily exceed the magnetic stray field signal of an ultrathin magnetic film. This is a solvable problem for FMR experiments, since often the resonance fields of these impurities are different from the resonance fields of the ferromagnetic sample. In the stray field analysis from SQUID data, however, it is hard to distinguish between the FM background and the FM signal from a sample. Therefore, we use Cu with a high purity of 99.9999%. The fabrication procedure of the sample holder involves drilling and milling procedures which can contaminate the sample holder with FM grit of the tools. Thus, a precautionary etching procedure of the final sample holder is followed, using a mixture of hydrochloric acid (HCl) and water in a mixing ratio of 1:2 (≈ 1 minute). Adding a few drops of hydrogen peroxide (H_2O_2) can intensify the chemical reaction. Care should be taken that threads and thin parts of the sample holder are not strongly affected by the etching. Finally, the sample holder is rinsed in water and acetone.

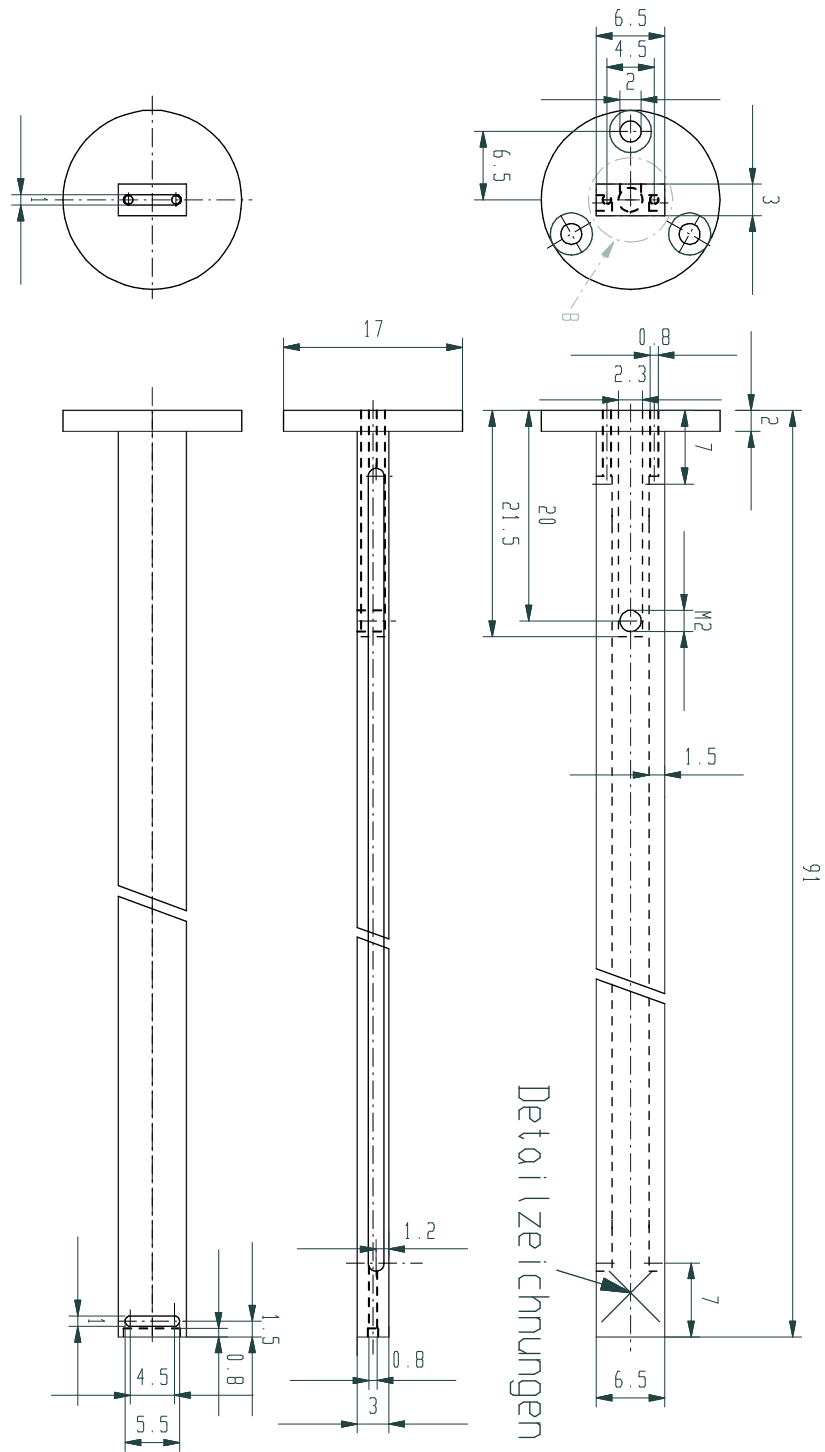


Fig. A.5.: Sketch of the sample holder's forepart. All lengths are given in mm.

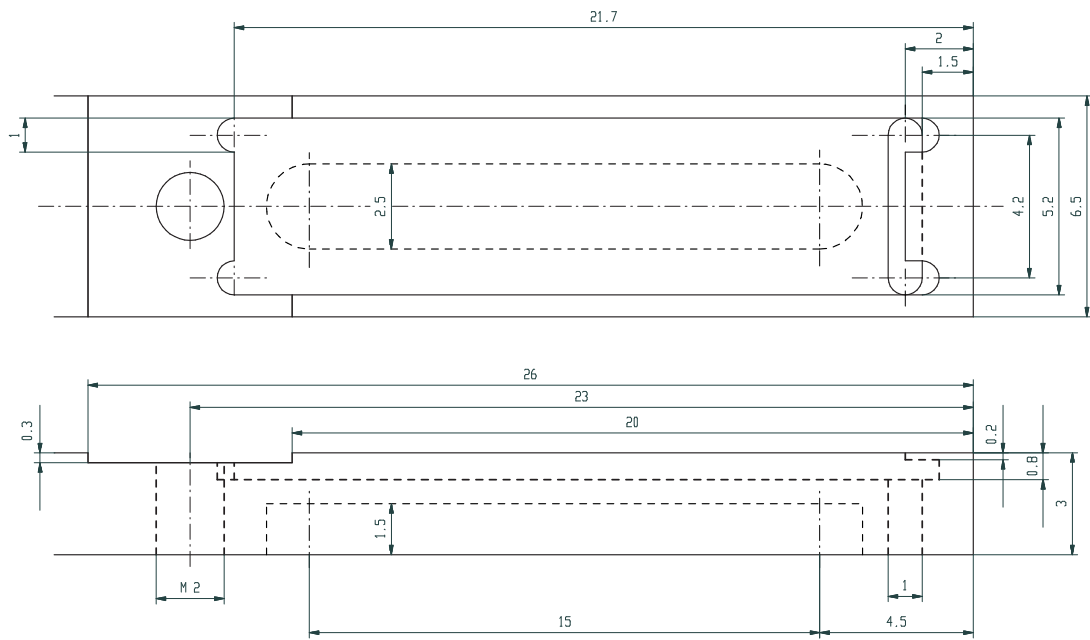


Fig. A.6.: Detailed drawing of the top side of the front part of the sample holder

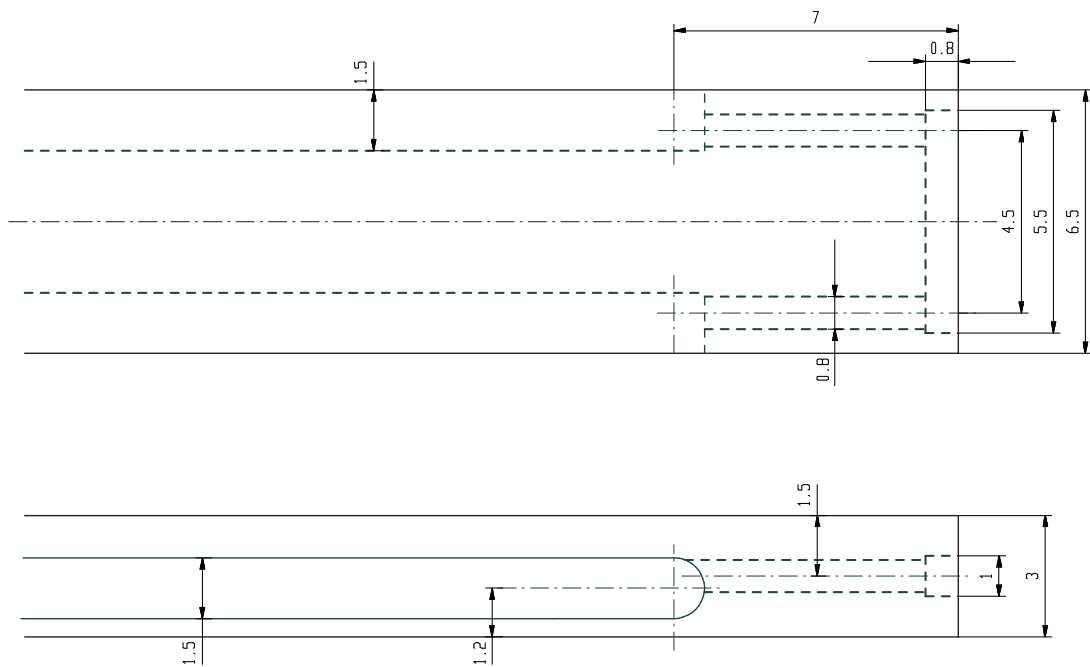


Fig. A.7.: Detailed drawing of the rear side of the front part of the sample holder

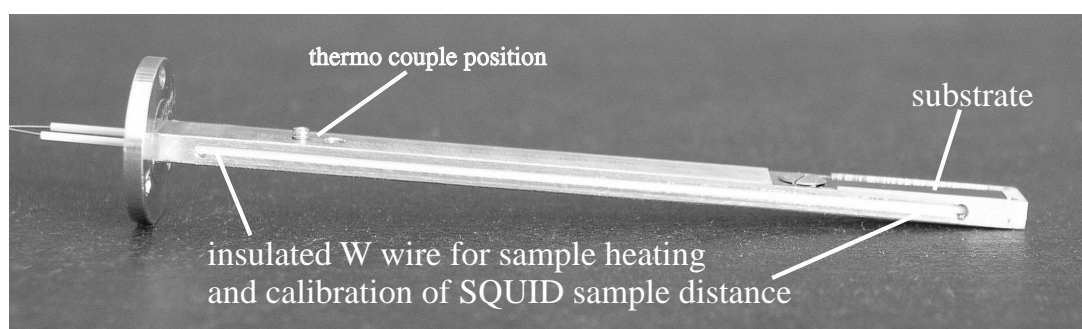


Fig. A.8.: Photograph of the sample holder used for the UHV experiments.

List of Figures

2.1.	Surface free energy polar plots of the magnetic anisotropy	16
2.2.	Sketch of a square film of length L with coordinate system	19
2.3.	Rescaled stray fields for square shaped in-plane magnetized films	20
2.4.	B_z line scan	21
2.5.	Rescaled stray fields for square shaped out-of-plane magnetized films	23
2.6.	Sketch of a circular film of radius R with coordinate system	24
2.7.	Coordinate system rotation for circular shaped films	25
2.8.	Rescaled stray fields for circular shaped in-plane magnetized films	26
2.9.	Comparison of the stray fields of a square film, a circular film and a point dipole	28
2.10.	Scheme of the stray field simulation for simple domain configurations	29
2.11.	Stray field simulation for a simple domain configuration	31
3.1.	Sketch of the UHV-chamber	34
3.2.	Configuration of the evaporator, thickness monitor and aperture	35
3.3.	<i>In situ</i> setup of longitudinal MOKE	37
3.4.	Experimental data of the mean free path of electrons in a solid	38
3.5.	Ewald sphere in a 2D lattice	39
3.6.	Reflection of a plane wave from a single crystal	40
3.7.	Atomic model for the Auger process	41
3.8.	Schematics of a dc SQUID	43
3.9.	Basic circuitry of an rf SQUID	44
3.10.	rf SQUID flux-voltage transfer function	46
3.11.	Photograph of the SQUID electronics and electrical shielding	47
3.12.	Experimental 2D B_z field distribution of a 20 ML Fe film	48
3.13.	SQUID calibration	50
4.1.	Experimental $B_z(x)$ of a 40 ML Fe film for various heights h	54
4.2.	Shape of sample stray fields for various heights h	55

4.3. Peak to peak distance of B_z as a function of height h for in-plane magnetized films	55
4.4. Sketch for the calculation of the magnetic field \vec{B} for a wire of finite length in 2-dimensions	57
4.5. Sketch for the calculation of the magnetic field \vec{B} for a wire of finite length in cartesian coordinates	58
4.6. Arrangement of the rectangular loop used for the height calibration of the SQUID to sample distance h	59
4.7. Calculated and experimental stray field of the rectangular calibration loop . . .	60
4.8. Experimental B_z line scans across the calibration loop's center and experimental height dependence of B_z	61
4.9. Determination of the in-plane angle of magnetization with the scanning SQUID	64
4.10. Schematic stray field distribution of an in-plane magnetized film	65
4.11. Determination of the in-plane angle of magnetization on an 8 ML Fe film on GaAs(001)	66
4.12. The demagnetizing field at the sample edges	67
4.13. Demagnetizing field component H_x of a square shaped sample with magnetization along x	67
4.14. Range of the demagnetizing field in the interior of a magnetic sample	68
4.15. Influence of surface roughness on the magnetic stray field	70
4.16. AES of unclean/clean GaAs and 3 ML Fe/GaAs	73
4.17. LEED image of $\{4 \times 6\}$ -reconstructed GaAs(001)	74
4.18. Atomic structure model of the $\{4 \times 6\}$ -reconstructed GaAs(001) surface	74
4.19. IV-LEED spectra of a GaAs(001) substrate and a 22 ML Fe/GaAs film	75
4.20. Vertical Fe interplanar distance as a function of film thickness on GaAs(001) . .	76
4.21. MOKE hysteresis loop of 5 ML Fe on GaAs(001)	78
4.22. MOKE hysteresis loop of 20 ML Fe on GaAs(001)	79
4.23. Magnetization determination of an 8 ML Fe/GaAs(001) film	80
4.24. Remanent magnetization vs. film thickness of Fe films on GaAs(001)	81
4.25. Non FM layers equivalents of Fe films on GaAs as a function of film thickness .	81
4.26. M(T) of 6.5 ML Fe on GaAs(001)	82
4.27. M(T) of 3.7 ML Fe on GaAs(001) in a double logarithmic plot	84
4.28. M(T) of 3.7 ML Fe on GaAs(001)	85
4.29. M(T) of 2.3 ML Fe on GaAs(001)	86
4.30. Determination of the Bloch parameters from M(T) curves of 3.7 and 6.5 ML Fe.	87
4.31. Spin wave Bloch parameter vs. inverse thickness of Fe/GaAs films.	88
4.32. MOKE hysteresis loop of 15 ML Fe/GaAs with 30 Å Ag cap	89

4.33. Magnetization reversal imaged with Kerr microscopy	90
4.34. Kerr microscopy image near the sample edge	90
4.35. MFM image of a 15 ML Fe/GaAs film at the sample edge	91
4.36. MFM contrast mechanism at the sample edge of in-plane magnetized films . . .	92
4.37. MFM image of a 15 ML Fe/GaAs film in the middle of the film	93
4.38. Change of Free Energy during in-plane reorientation transition	95
4.39. Measured in-plane equilibrium angles vs. film thickness	96
4.40. LEED image of 10 ML Fe on GaAs prior to oxygen exposure	100
4.41. Online monitoring of LEED intensity during oxidation of 33 ML Fe/GaAs . . .	101
4.42. IV-LEED spectrum of 33 ML Fe without and with 1,5L oxygen exposure . . .	101
4.43. Interplanar distance of 33 ML Fe during oxidation	102
4.44. Low energy AES of 33 ML Fe/GaAs(001) exposed to oxygen	103
4.45. Auger ratio O_{510}/Fe_{703} of 33 ML Fe/GaAs vs. oxygen exposure	104
4.46. XRD data of 20 ML Fe on GaAs(001) oxidized in air	106
4.47. XRD line width of 20 ML Fe/GaAs(001) oxidized in air	107
4.48. Remanent magnetization of a 5, 8 and 16 ML Fe/GaAs(001) film during oxygen exposure	107
4.49. Calculated non-magnetic layer equivalents of a 5, 8 and 16 ML Fe/GaAs(001) film	108
4.50. LEED image of 5 and 16 ML Fe on GaAs(001)	110
4.51. FMR spectra of 10 ML Fe/GaAs(001) exposed to oxygen	111
4.52. Angular dependence of the resonance field of 10 ML Fe/GaAs(001) exposed to oxygen	112
4.53. Dispersion relation $B(f)$ for the MAE constants of 10 ML Fe/GaAs	112
4.54. Change of MAE of 10 ML Fe/GaAs(001) after exposure to oxygen	114
4.55. $M(H)$ of 20 ML Fe/GaAs(001) exposed to air	114
4.56. Remanent magnetization of 8, 9, and 12 ML Fe/GaAs(001) vs. oxygen exposure at T=40 K	115
4.57. Temperature driven out-of-plane in-plane reorientation of 8.6 ML Fe/GaAs . .	117
4.58. Calculated stray field $B_z(x)$ during out-of-plane in-plane reorientation	118
A.1. Engineering drawing of the magnet used for MOKE	126
A.2. Electrical circuitry of the pulse box	127
A.3. Evolution of the current from the pulse box for two different magnets	128
A.4. Periodic roughness of a magnetic film in the x - y -plane	132
A.5. Sketch of the sample holder	135
A.6. Sample holder details, top side	136
A.7. Sample holder details, rear side	136

A.8. Photograph of the sample holder 137

List of Tables

2.1. Properties of bulk α Fe at room temperature	7
2.2. Fe/GaAs magnetic moments	9
2.3. Fe spin and orbital magnetic moments	10
4.1. Error contributions to the magnetization measurement	72
4.2. Critical exponent β for 3.7 ML Fe/GaAs(001) for different Curie temperatures .	84
4.3. Experimental Bloch parameters and spin wave stiffness constants.	87
4.4. Anisotropy constants of Fe/GaAs(001) for various film thicknesses	95
4.5. Physical properties of selected iron oxides	97
4.6. Ion radius of oxygen and iron	103

Bibliography

- [1] S.A. Wolf, D.D. Awschalom, R.A. Buhrmann, J.M. Daughton, S. von Molnár, M.L. Roukes, A.Y. Chtchelkanova and D.M. Treger, *Science* **294**, 1488 (2001)
- [2] Igor Zutíć, J. Fabian and S. Das Sarma, *Rev. Mod. Phys.* **76**, 323 (2004)
- [3] M.N. Baibich, J.M. Broto, A. Fert, F. Nguyen van Dau, F. Petrolt, P. Etienne, G. Creuzzet, A. Friedrich and J. Chazelas, *Phys. Rev. Lett.* **61**, 2472 (1988)
- [4] G. Binash, P. Grünberg, F. Sauernbach, W. Zinn, *Phys. Rev. B* **39**, 4828 (1989)
- [5] S. Datta and B. Das, *Appl. Phys. Lett.* **56**, 665 (1990)
- [6] R. Fiederling, M. Keim, G. Reuscher, W. Ossau, G. Schmidt, A. Waag and L.W. Molenkamp, *Nature (London)* **402**, 787 (1999)
- [7] Y. Ohno, D.K. Young, B. Beschoten, F. Matsukura, H. Ohno and D.D. Awschalom, *Nature (London)* **402**, 790 (1999)
- [8] P.R. Hammar, B.R. Bennett, M.J. Yang and M. Johnson, *Phys. Rev. Lett.* **83**, 203 (1999)
- [9] H.J. Zhu, M. Ramsteiner, H. Kostial, M. Wassermeier, H.-P. Schönherr and K.H. Ploog, *Phys. Rev. Lett.* **87**, 016601 (2001)
- [10] A.T. Hanbicki, B.T. Jonker, G. Itskos, G. Kioseoglou and A. Petrou, *Appl. Phys. Lett.* **80**, 1240 (2002)
- [11] A. Filipe, A. Schuhl and P. Galtier, *Appl. Phys. Lett.* **70**, 129 (1997)
- [12] M. Zölfl, M. Brockmann, M. Köhler, S. Kreuzer, T. Schweinböck, S. Miethaner, F. Bensch and G. Bayreuther, *J. Magn. Magn. Mat.* **175**, 16 (1997)
- [13] Y.B. Xu, E.T.M. Kernohan, D.J. Freeland, A. Ercole, M. Tselepi and J.A.C. Bland, *Phys. Rev. B* **58**, 890 (1998)

- [14] M. Doi, B. Roldan Cuenya, W. Keune, T. Schmitte, A. Nefedov, H. Zabel, D. Spodding, R. Meckenstock and J. Pelzl, *J. Magn. Magn. Mat.* **240**, 407 (2002)
- [15] B. Roldan Cuenya, M. Doi, W. Keune, S. Hoch, D. Reuter, A. Wieck, T. Schmitte and H. Zabel, *Appl. Phys. Lett.* **82**, 1072 (2003)
- [16] H. Ohno, K. Yoh, T. Doi, A. Subagyo, K. Sueoka and K. Mukasa, *J. Vac. Sci. Technol. B* **19**, 2280 (2001)
- [17] L. Ruppel, G. Witte, Ch. Wöll, T. Last, S. F. Fischer and U. Kunze, *Phys. Rev. B* **66**, 245307 (2002)
- [18] J.R. Waldrop and R.W. Grant, *Appl. Phys. Lett.* **34**, 630 (1979)
- [19] J.J. Krebs, B.T. Jonker and G.A. Prinz, *J. Appl. Phys.* **61**, 2596 (1987)
- [20] J.M. Florczak and E.D. Dahlberg,, *Phys. Rev. B* **44**, 9338 (1991)
- [21] C. Daboo, R.J. Hicken, E. Gu, M. Gester, S.J. Gray, D.E.P. Eley, E. Ahmad and J.A.C. Bland, *Phys. Rev. B* **51**, 15964 (1995)
- [22] Q. Xue, T. Hashizume, J.M. Zhou, T. Sakata, T. Ohno and T. Sakurai, *Phys. Rev. Lett.* **74**, 3177 (1995)
- [23] P.M. Thibado, E. Kneedler, B.T. Jonker, B.R. Bennett, B.V. Shanabrook and L.J. Whitman, *Phys. Rev. B* **53**, R10481 (1996)
- [24] M. Gester, C. Daboo, R.J. Hicken, S.J. Gray, A. Ercole and J.A.C. Bland, *J. Appl. Phys.* **80**, 347 (1996)
- [25] E. Kneedler, B.T. Jonker, P.M. Thibado, R.J. Wagner, B.V. Shanabrook and L.J. Whitman, *Phys. Rev. B* **56**, 8163 (1997)
- [26] Y.B. Xu, E.T.M. Kernohan, D.J. Freeland, M. Tselepi, A. Ercole and J.A.C. Bland, *J. Magn. Magn. Mat.* **198**, 703 (1999)
- [27] M. Brockmann, M. Zöfl, S. Miethaner and G. Bayreuther, *J. Magn. Magn. Mat.* **198**, 384 (1999)
- [28] G. Wastlbauer and J.A.C. Bland, *Advances in Physics* **45**, 137 (2005)
- [29] F. Bensch, R. Moosbühler and G. Bayreuther, *J. Appl. Phys.* **91**, 8754 (2002)
- [30] Ch. Kittel, *Einführung in die Festkörperphysik*, R. Oldenbourg Verlag, München, Wien (1999), 12. Auflage

- [31] G.A. Prinz and J.J. Krebs, *Appl. Phys. Lett.* **39**, 391 (1981)
- [32] G. Schmidt, D. Ferrand, L.W. Molenkamp, A.T. Filip and B.J. van Wees, *Phys. Rev. B* **62**, R4790 (2000)
- [33] H.-P. Schönherr, R. Nötzel, W. Ma and K.H. Ploog, *J. Appl. Phys.* **89**, 169 (2001)
- [34] R.M. Stroud, A.T. Hanbicki, Y.D. Park, G. Kioseoglou, A.G. Petukhov and B.T. Jonker, *Phys. Rev. Lett.* **89**, 166602 (2002)
- [35] J.S. Claydon, Y.B. Xu, M. Tselepi, J.A.C. Bland and G. van der Laan, *Phys. Rev. Lett.* **93**, 037206 (2004)
- [36] K. Sano and T. Miyagawa, *Jap. J. Appl. Phys.* **30**, 1434 (1991)
- [37] T.L. Monchesky, B. Heinrich, R. Urban, K. Myrtle, M. Klaua and J. Kirschner, *Phys. Rev. B* **60**, 10242 (1999)
- [38] E. Kneedler, P.M. Thibado, B.T. Jonker, B.R. Bennett, B.V. Shanabrook, R.J. Wagner and L.J. Whitman, *J. Vacuum Science and Technology B* **14**, 3193 (1996)
- [39] C. Lallaizon, B. Lépine, S. Ababou, A. Schussler, A. Quémerais, A. Guivarc'h, G. Jézéquel, S. Députier and R. Guérin, *Appl. Surf. Sci.* **123/124**, 319 (1998)
- [40] S.C. Erwin, S.-H. Lee and M. Scheffler, *Phys. Rev. B* **65**, 205422 (2002)
- [41] S.C. Hong, M.S. Chung, B.-G. Yoon and J.I. Lee, *J. Magn. Magn. Mat.* **239**, 39 (2002)
- [42] J.A.C. Bland and B. Heinrich, Hrsg., *Ultrathin Magnetic Structures Vol. 1 and Vol. 2*, Springer-Verlag, Berlin (1994)
- [43] W. Jantz, G. Rupp, R.S. Smith, W. Wetzling and G. Bayreuther, *IEEE Tran. Magn. MAG* **19**, 1859 (1983)
- [44] C. Daboo, M. Gester, S.J. Gray, J.A.C. Bland, R.J. Hicken, E. Gu, R. Ploessl and J.N. Chapman, *J. Magn. Magn. Mat.* **148**, 262 (1995)
- [45] Kh. Zakeri, Th. Kebe, J. Lindner and M. Farle, *J. Magn. Magn. Mat.* **299**, L1 (2006)
- [46] S.J. Steinmuller, M. Tselepi, V. Strom and J.A.C. Bland, *J. Appl. Phys.* **91**, 8679 (2002)
- [47] F. Bensch, G. Garreau, R. Moosbühler, G. Bayreuther and E. Beaurepaire, *J. Appl. Phys.* **89**, 7133 (2001)
- [48] J.W. Freeland, I. Coulthard, W.J. Antel Jr and A.P. Stampfl, *Phys. Rev. B* **63**, 193301 (2001)

- [49] S. Mirbt, B. Sanyal, C. Isheden and B. Johansson, *Phys. Rev. B* **67**, 155421 (2003)
- [50] C.L. Fu, A.J. Freeman and T. Oguchi, *Phys. Rev. Lett.* **54**, 2700 (1985)
- [51] H.-J. Elmers, *J. Mod. Phys. B* **9**, 3115 (1995)
- [52] V. Crisan and P. Entel, *Phase Transitions* **76**, 385 (2003)
- [53] Y.B. Xu, M. Tselepi, C.M. Guertler, C.A.F. Vaz, G. Wastlbauer, J.A.C. Bland, E. Dudzik and G. van der Laan, *J. Appl. Phys.* **89**, 7156 (2001)
- [54] J.S. Claydon, Y.B. Xu, M. Tselepi, J.A.C. Bland and G. van der Laan, *J. Appl. Phys.* **95**, 6543 (2004)
- [55] B.T. Thole, P. Carra, F. Sette and G. van der Laan, *Phys. Rev. Lett.* **68**, 1943 (1992)
- [56] P. Carra, B.T. Thole, M. Altarelli and X. Wang, *Phys. Rev. Lett.* **70**, 694 (1993)
- [57] M. Ysumi, R. Taharo, and Y. Nakamura, *J. Phys. Soc. Jpn.* **48**, 1937 (1980)
- [58] C.T. Chen, Y.U. Idzerda, H.J. Lin, N.V. Smith, G. Meigs, E. Chaban, G.H. Ho, E. Pellegrin and F. Sette, *Phys. Rev. Lett.* **75**, 152 (1995)
- [59] P. Weiss, *J. de Phys. Rad.* **6**, 661 (1907)
- [60] L.D. Landau and E. Lifshitz, *Phys. Z. Sowjetunion* **8**, 153 (1935)
- [61] A.H., Morrish, *The physical Principles of Magnetism*, John Wiley & Sons, Inc. (1965)
- [62] L.A. Zhenga and E.V. Barrera and R.D. Shull, *J. Appl. Phys.* **97**, 094309 (2005)
- [63] P. Vavassori, D. Bisero, F. Carace, A. di Bona, G.C. Gazzadi, M. Liberati and S. Valeri, *Phys. Rev. B* **72**, 054405 (2005)
- [64] A. Aharoni, *Introduction to the Theory of Ferromagnetism*, Clarendon Press (1996)
- [65] J.D. Jackson, *Klassische Elektrodynamik*, de Gruyter (1983)
- [66] I.N. Bronstein, K.A. Semendjajew, *Taschenbuch der Mathematik*, Verlag Harri Deutsch, Frankfurth am Main, Thun (1997), 3. Auflage, p. 603
- [67] M. Farle, A. Berghaus and K. Baberschke, *Phys. Rev. B* **39**, 4838 (1989)
- [68] P. Bruno, *Phys. Rev. B* **39**, 865 (1989)
- [69] N.D. Mermin and H. Wagner, *Phys. Rev. Lett.* **17**, 1133 (1966)

-
- [70] M. Bander and D.L. Mills, *Phys. Rev. B* **38**, 12015 (1988)
- [71] M. Farle, *Rep. Prog. Phys.* **61**, 755 (1998)
- [72] J. Lindner, P. Pouloupoulos, R. Nünthel, E. Kosubek, H. Wende and K. Baberschke, *Surf. Sci. Lett.* **523**, L65 (2003)
- [73] A. Zieba and S. Foner, *Rev. Sci. Instrum.* **53**, 1344 (1982)
- [74] O.V. Snigirev, K.E. Andreev, A.M. Tishin, S.A. Gudoshnikov and J. Bohr, *Phys. Rev. B* **55**, 14429 (1997)
- [75] A. Ney, P. Pouloupoulos, M. Farle and K. Baberschke, *Phys. Rev. B* **62**, 11336 (2000)
- [76] A. Beyer, *Zur Berechnung des magnetischen Feldes homogen und inhomogen magnetisierter Körper*, Verlag H. Wolff (1986)
- [77] Wolfram Research, Inc., *Mathematica Help Browser*, Champaign, IL 61820, USA (1986), computational algebra system
- [78] R. Ramchal, *PhD thesis* (2004), Universität Duisburg-Essen
- [79] J. Kerr, *Phil. Mag.* **3**, 321 (1877)
- [80] M. Faraday, *Phil. Trans. Royal Soc. (London)* **136**, 1 (1846)
- [81] W. Voigt, *Nachr. Kgl. Ges. Wiss. Göttingen, Math.-Phys. Kl.* **4**, 355 (1898)
- [82] L.D. Landau and E.M. Lifshitz, *Electrodynamics of Continuous Media*, Pergamon, Oxford (1984), 2nd ed.
- [83] W. H. Kleiner, *Phys. Rev.* **142**, 318 (1966)
- [84] Y. Suzuki, T. Katayama, K. Tanaka and K. Sato, *Phys. Rev. Lett.* **68**, 3355 (1992)
- [85] H. Ebert, *Rep. Prog. Phys.* **59**, 1665 (1966)
- [86] C.-Y. You and S.-C. Shin, *J. Appl. Phys.* **84**, 541 (1998)
- [87] W. Reim and J. Schoenes, *Ferromagnetic Materials* **5**, 133 (1990)
- [88] K. Oura, V.G. Lifshits, A.A. Saranin, A.V. Zotov and M. Katayama, *Surface Science - An Introduction*, Springer, Berlin, Heidelberg, New York (2003)
- [89] J.B. Pendry, *Low-Energy Electron Diffraction*, Academic, London (1974)
- [90] W.C. Lin, C.C. Kuo, C.L. Chiu and Minn-Tsong Li, *Surf. Sci.* **478**, 9 (2001)

- [91] G.E. McGuire, *Auger Electron Spectroscopy Reference Manual - A Book of Standard Spectra for Identification and Interpretation of Auger Electron Spectroscopy Data* (1979)
- [92] C.C. Chang, *Surf. Sci.* **25**, 53 (1971)
- [93] <http://www.lfu.baden-wuerttemberg.de> (2005), Landesanstalt für Umweltschutz, Baden-Wuerttemberg
- [94] B.D. Josephson, *Phys. Rev. Lett.* **1**, 251 (1962)
- [95] J. Clarke, *Phil. Mag.* **13**, 115 (1966)
- [96] J.E. Zimmerman and A.H. Silver, *Phys. Rev.* **141**, 367 (1966)
- [97] A.I. Braginski, *SQUID Sensor: Fundamentals Fabrication and Application*, Kluwer, Dordrecht (1996), NATO ASI, Series
- [98] W. Buckel, R. Kleiner, *Superconductivity*, Wiley-VCH, Berlin (2004)
- [99] G. Suran, A. Stankoff and F. Hoffmann, *Phys. Rev. B* **8**, 1109 (1973)
- [100] R. Meckenstock and J. Pelzl, *J. Appl. Phys.* **81**, 5259 (1997), and references therein
- [101] J. Lindner and K. Baberschke, *J. Phys.: Condens. Matter* **15**, R193 (2003)
- [102] J. Smit and H. G. Beljers, *Phillips Res. Rep.* **10**, 113 (1955)
- [103] H. Suhl, *Phys. Rev.* **97**, 555 (1955)
- [104] B.D. Cullity, *Introduction to Magnetic Materials*, Addison-Wesley, Reading, MA (1972)
- [105] J.R. Kirtley and J.P. Wikswo, Jr., *Annu. Rev. Mater. Sci.* **29**, 117 (1999)
- [106] Wolfram Research, Inc., *Mathematica Vers. 5.2*, Champaign, IL 61820, USA (1986), computational algebra system
- [107] P. Bruno, *J. Appl. Phys.* **64**, 3153 (1988)
- [108] C. Chappert and P. Bruno, *J. Appl. Phys.* **64**, 5736 (1988)
- [109] P. Pouloupoulos, J. Lindner, M. Farle and K. Baberschke, *Surf. Sci.* **437**, 277 (1999)
- [110] E. Gu, J.A.C. Bland, C. Daboo, M. Gester and L.M. Brown, *Phys. Rev. B* **51**, 3596 (1995)
- [111] A. Hucht, *PhD thesis* (1999), Universität Duisburg
- [112] J. Lindner, *PhD thesis* (2002), Freie Universität Berlin

-
- [113] D.K. Biegelsen, R.D. Bringans, J.E. Northrup and L.E. Swartz, *Phys. Rev. B* **41**, 5701 (1990)
- [114] C. Lallaizon, B. Lépine, S. Ababou, A. Guivarc'h, S. Députier, F. Abel and C. Cohen, *J. Appl. Phys.* **86**, 5515 (1999)
- [115] Kh. Zakeri, Th. Kebe, J. Lindner and M. Farle, *Superlattices and Microstructures* (in press)
- [116] Kh. Zakeri, Th. Kebe, J. Lindner, C. Antoniak, M. Farle, K. Lenz, T. Toliński and K. Baberschke, *Phase Transition* **79**, 793 (2006)
- [117] Y. Li and K. Baberschke, *Phys. Rev. Lett.* **68**, 001208 (1992)
- [118] S.M. Rezende, A. Azevedo, M.A. Lucena and F.M. Aguiar, *Phys. Rev. B* **63**, 214416 (2001)
- [119] D. Sander, *J. Phys.: Condens. Matter* **16**, R603 (2004)
- [120] L.J. Swartzendruber, *J. Magn. Magn. Mat.* **100**, 573 (1991)
- [121] A.A. Ostroukhov, V.M. Floka, V.T. Cherepin, *Surf. Sci.* **331** (1995)
- [122] G.A.T. Allan, *Phys. Rev. B* **1**, 352 (1970)
- [123] S.T. Bramwell and P.C.W. Holdsworth **5**, L53 (1993)
- [124] G. Lugert and G. Bayreuther, *Phys. Rev. B* **37**, 660 (1988)
- [125] M. Przybylski, J. Korecki and U. Gradmann, *Appl. Phys. A.: Solid Surf.* **52**, 33 (1991)
- [126] W. Kipfert, M. Dumm, M. Rahm and G. Bayreuther, *J. Appl. Phys.* **93**, 7601 (1993)
- [127] J. Mathon and S.B. Ahmad, *Phys. Rev. B* **37**, 660 (1988)
- [128] B.E. Argyle, S.H. Charap and E.W. Pugh, *Phys. Rev.* **132**, 2051 (1963)
- [129] W.Kipferl, M. Sperl, T. Hagler, R. Meier and G. Bayreuther, *J. Appl. Phys.* **97**, 10B313 (2005)
- [130] M. Sperl, W. Kipferl, M. Dumm and G. Bayreuther, *J. Appl. Phys.* **99**, 08J703 (2006)
- [131] R. Swirkowicz, J. Korecki and M. Przybylski, *J. Magn. Magn. Mat.* **123**, 87 (1993)
- [132] U. Krey, *Z. Phys. B.* **31**, 247 (1978)
- [133] L.A. Finzi and J.A. Hartmann, *IEEE Tans. Magn.* **4**, 662 (1968)

- [134] P. Glijer, E.N. Abarra, H. Kisker and T. Suzuki, *IEEE Trans. Magn.* **32**, 3557 (1996)
- [135] S. Kirsch, *PhD thesis* (2003), Universität Duisburg-Essen
- [136] E.E. Huber, Jr., D.O. Smith, J.B. Goodenough, *J. Appl. Phys.* **29** (1958)
- [137] C. Daboo, R.J. Hicken, D.E.P. Eley, M. Gester, S.J. Gray, A.J.R. Ives and J.A.C. Bland, *J. Appl. Phys.* **75**, 5586 (1994)
- [138] R.J. Hicken, D.E.P. Eley, M. Gester, S.J. Gray, C. Daboo, A.J.R. Ives and J.A.C. Bland, *J. Magn. Magn. Mat.* **145**, 278 (1995)
- [139] A.M. Horgan and D.A. King, *Surf. Sci.* **23**, 259 (1970), and references therein
- [140] R.M. Cornell and U. Schwertmann, *The Iron Oxides*, VCH Verlagsgesellschaft mbH (1996)
- [141] F. Yubero, M. Ocaña and A. Justo, *J. Vac. Sci. Technol. A* **18**, 2244 (2000)
- [142] F. Schedin, E.W. Hill, G. van der Laan and G. Thornton, *J. Appl. Phys.* **96**, 1165 (2004)
- [143] Y. Zhou, Xuesong Jin and I.V. Shvets, *J. Appl. Phys.* **95**, 7357 (2004)
- [144] Y. Peng, C. Park and D.E. Laughlin, *J. Appl. Phys.* **93**, 7957 (2003)
- [145] Y. Gao, Y.J. Kim, S. Thevuthasan, S.A. Chambers and P. Lubitz, *J. Appl. Phys.* **81**, 3253 (1996)
- [146] Ch. Pflitsch, R. David, L.K. Verheij and R. Franchy, *Surf. Sci.* **488**, 32 (2001)
- [147] P. Marcus, *Electrochim. Acta* **43**, 109 (1998)
- [148] S.J. Roosendaal, J.P.R. Bakker, A.M. Vredenberg and F.H.P.M. Habraken, *Surf. Sci.* **197** (2001)
- [149] P.C.J. Graat, M.A.J. Somers, A.M. Vredenberg and E.J. Mittemeijer, *J. Appl. Phys.* **82**, 1416 (1997)
- [150] G.W.R. Leibbrandt, G. Hoogers and F.H.P.M. Habraken, *Phys. Rev. Lett.* **68**, 1947 (1992)
- [151] P. Bloński, A. Kiejna and J. Hafner, *Surf. Sci.* **590**, 88 (2005)
- [152] C.F. Brucker and T.N. Rhodin, *Surf. Sci.* **57**, 523 (1975)
- [153] K.O. Legg, F. Jona, D.W. Jepsen and P.M. Marcus, *Phys. Rev. B* **16**, 5271 (1977)
- [154] P.B. Sewell, D.J. Mitchell and M. Cohen, *Surf. Sci.* **33**, 535 (1972)

-
- [155] C. Leygraf and S. Eklund, *Surf. Sci.* **40**, 609 (1973)
- [156] T. Matsudaira, M. Watanabe and M. Onchi, *Japan. J. Appl. Phys. Suppl.* **2**, 181 (1974)
- [157] Y. Sakisaka, T. Miyano and M. Onchi, *Phys. Rev. B* **30**, 8649 (1984)
- [158] M. Salvietti, P. Ferro, R. Moroni, M. Canepa and L. Mattera, *Surf. Sci.* **377** (1997)
- [159] R. Allenspach, M. Taborelli and M. Landolt, *Phys. Rev. Lett.* **55**, 2599 (1985)
- [160] M. Getzlaff, J. Bansmann and G. Schönhense, *J. Magn. Magn. Mat.* **192**, 458 (1999)
- [161] C.F. Brucker and T.N. Rhodin, *Surf. Sci.* **57**, 523 (1976)
- [162] R.L. Schwoebel, *J. Appl. Phys.* **37**, 3682 (1966)
- [163] Z.-J. Tian and T.S. Rahman, *Phys. Rev. B* **47**, 9751 (1992)
- [164] V.S. Smentkowski and J.T. Yates, Jr., *Surf. Sci.* **232**, 113 (1990)
- [165] M. Seo, J.B. Lumsden and R.W. Staehle, *Surf. Sci.* **55**, 541 (1975)
- [166] A. Wight, N.G. Condon, F.M. Leibsle, G. Worthy and A. Hodgson, *Surf. Sci.* **331** (1995)
- [167] H.P. Klug and I.E. Alexander, *X-Ray Diffraction Procedures*, Wiley, New York (1974), Chapter 9
- [168] B.D. Cullity, *Elements of X-ray Diffraction*, Addison-Wesley, Reading, MA (1978)
- [169] T. Shinjo, T. Iwasaki, T. Toshihiko and T. Takada, *Jap. J. Appl. Phys.* **23**, 283 (1984)
- [170] S.J. Roosendaal, B. van Asselen, J.W. Elsenaar, A.M. Vredenberg and F.H.P.M. Habraken, *Surf. Sci.* **442**, 329 (1999)
- [171] A. Atkinson, *Rev. Mod. Phys.* **57**, 437 (1985)
- [172] G. Garreau, E. Beaurepaire, K. Ounadjela and M. Farle, *Phys. Rev. B* **53**, 1083 (1996)
- [173] M. Farle, W. Platow, A.N. Anisimov, B. Schulz and K. Baberschke, *J. Magn. Magn. Mat.* **165**, 74 (1997)
- [174] K.D. Usadel and A. Hucht, *Phys. Rev. B* **66**, 024419 (2002)
- [175] R. Nünthel, T. Gleitsmann, P. Pouloupoulos, A. Scherz, J. Lindner, E. Kosubek, Ch. Litwinski, Z. Li, H. Wende, K. Baberschke, S. Stolbov and T.S. Rahman, *Surf. Sci.* **531**, 53 (2003)

- [176] Kh. Zakeri, Th. Kebe, J. Lindner and M. Farle, *Phys. Rev. B* **73**, 052405 (2006)
- [177] H.B. Callen and E. Callen, *J. Phys. Chem. Solids* **27**, 1271 (1966)
- [178] R.P. Erickson and D. L. Mills, *Phys. Rev. B* **46**, 861 (1992)

Publications

I. Articles

1) Th. Kebe and A. Carl

Calibration of magnetic force microscopy tips by using nanoscale current-carrying parallel wires, Appl. Phys. Reviews

J. Appl. Phys. **95**, 775 (2004)

2) Th. Kebe, Kh. Zakeri, J. Lindner and M. Farle

Combined in-situ SQUID magnetometry and FMR study on magnetic properties of thin Fe/GaAs(001) films exposed to oxygen

J. Phys.: Condens. Matter **18**, 8791 (2006)

3) Kh. Zakeri, Th. Kebe, J. Lindner and M. Farle

Magnetic anisotropy of Fe/GaAs(0 0 1) ultrathin films investigated by in situ ferromagnetic resonance

J. Magn. Magn. Mater. **299**, L1-L10 (2006)

4) Kh. Zakeri, Th. Kebe, J. Lindner and M. Farle

Power-Law Behavior of the Temperature Dependence of Magnetic Anisotropy of uncapped ultrathin Fe Films on GaAs(001)

Phys. Rev. B **73**, 052405 (2006)

5) Kh. Zakeri, Th. Kebe, J. Lindner, C. Antoniak, M. Farle, K. Lenz, T. Tolínski and K. Baberschke

Magnetic Anisotropy in the nanoscaled materials probed by Ferromagnetic Resonance

Phase Transitions **79**, 793 (2006)

6) Kh. Zakeri, Th. Kebe, J. Lindner and M. Farle

Correlation between structure and magnetism in epitaxial Fe monolayers on GaAs(001)

Superlattices and Microstructures (2006), *accepted for publication / in press*

II. Talks

1) Th. Kebe and A. Carl

Kalibrierung von MFM-Spitzen mit stromführenden parallelen Leiterbahnen

Frühjahrstagung der Deutschen Physikalischen Gesellschaft in Dresden (2003)

2) Th. Kebe, Kh. Zakeri and M. Farle

In situ ferromagnetische Resonanz und Magnetometrie an epitaktischen Fe/HL Grenzflächen

Klausurtagung des Sfb491 in Lennestadt (April 2004)

3) Th. Kebe, Kh. Zakeri, J. Lindner and M. Farle

UHV-SQUID Magnetometrie an Fe Monolagen auf GaAs(001)

Klausurtagung des Sfb491 in Lennestadt (März 2005)

4) Th. Kebe, Kh. Zakeri, J. Lindner and M. Farle

SQUID Magnetometrie im UHV

Frühjahrstagung der Deutschen Physikalischen Gesellschaft in Berlin (2005)

5) Th. Kebe, Kh. Zakeri, J. Lindner and M. Farle

The effect of oxygen adsorption on the magnetization of Fe monolayers on {4×6}-reconstructed GaAs(001)

Frühjahrstagung der Deutschen Physikalischen Gesellschaft in Dresden (2006)

III. Posters

1) Th. Kebe, Kh. Zakeri, J. Lindner and M. Farle

In situ ferromagnetische Resonanz und Magnetometrie an epitaktischen Fe/Halbleitergrenzflächen

Präsentation zur Evaluierung des Sfb491 / Antrag der nächsten Förderperiode (Juni 2005)

2) Th. Kebe, Kh. Zakeri, J. Lindner and M. Farle

Scanning SQUID magnetometry on ultrathin Fe films on GaAs(001) in UHV

Workshop: "Magnetic imaging" in Bochum (November 2005)

3) Th. Kebe, Kh. Zakeri, J. Lindner and M. Farle

In situ UHV SQUID magnetometry on ultrathin Fe films on GaAs(001)

364. Heraeus-Seminar "Nanoscale Magnets - Top-down meets Bottom-up" in Bad Honnef
(Jan. 2006)

Curriculum vitae

I. Persönliche Daten

Name: Thomas Kebe
Nationalität: deutsch
Geburtsort und -tag: Duisburg, 18.07.1976
Anschrift: Universität Duisburg-Essen,
Institut für Physik, Lotharstr. 1, D-47048 Duisburg
Tel.: +49-203-379 2075, Fax.: +49-30-379 5110,
e-mail: tkebe@agfarle.uni-due.de

II. Schulausbildung

1985-1988 Grundschule Koopmannstrasse, Duisburg
1988-1996 Max-Planck-Gymnasium, Duisburg
1996 Abitur

III. Zivildienst

1996-1997 Kaiser-Wilhelm-Krankenhaus, Duisburg

IV. Hochschulausbildung

1997-2001 Physikstudium an der Universität Duisburg
2001-2002 Diplomarbeit "*Magnetkraftmikroskopische Untersuchungen an stromführenden parallelen Leiterbahnen*"
an der Universität Duisburg
in der Arbeitsgruppe von Prof. Dr. E. F. Wassermann
Nov. 2002 Diplom in Physik
seit 2003 Doktorarbeit an der Universität Duisburg-Essen
in der Arbeitsgruppe von Prof. Dr. M. Farle

Acknowledgment

An dieser Stelle möchte ich all denen danken, die durch ihre Hilfe und Engagement zum erfolgreichen Entstehen dieser Arbeit beigetragen haben. Ohne ihren Einsatz würde die Arbeit in der hier vorliegenden Form nicht existieren. Insbesondere gilt mein Dank:

Prof. Dr. Michael Farle für die Möglichkeit in einem spannenden Forschungsfeld zu arbeiten, für seine Unterstützung und für viele hilfreiche Diskussionen.

Dr. Jürgen Lindner, der stets ein guter Motivator war und großes Interesse für das Vorankommen der Arbeit zeigte. Sein fachliches Wissen hat viel zur Qualität dieser Arbeit beigetragen.

Khalil Zakeri Lori, mit dem ich etliche Stunden im Labor verbrachte. Seine freundliche Art und Hilfsbereitschaft bei experimentellen und wissenschaftlichen Fragestellungen war stets eine Bereicherung für diese Arbeit.

Horst Zähres für Tipps und Unterstützung bei nahezu allen Fragestellungen rund um das Labor.

Dr. Marina Spasova für ihre Diskussionsbereitschaft im Hinblick auf eine Vielzahl von Fragestellungen in dieser Arbeit und für ihre Hilfe bei SQUID-Messungen (Quantum Design).

Dr. Axel Carl für seine Diskussionsbereitschaft und kritische Durchsicht des Manuskripts.

Dr. Andreas Ney ebenfalls für seine kritische Durchsicht des Manuskripts und für viele hilfreiche Diskussionen.

Dr. Robert Ramchal, von dem ich gerade in der Anfangszeit viel über UHV lernen konnte.

Dieter Schädel für schnelle und perfekt ausgeführte Werkstattarbeiten.

Dr. Alfred Hucht, der bei der Herleitung der analytischen Streufeldformeln eine große Hilfe war.

Ellen Schuster für die Herstellung der Fe/GaAs *ex situ* Proben und ihre Diskussionsbereitschaft.

Dr. Rudolf Schäfer für die Kerrmikroskopiemessungen.

Dr. Dmitri Berkov für die Diskussion und Hilfestellung bezüglich des Einflusses von Rauigkeitseffekten auf das magnetische Steufeldsignal, sowie die Durchsicht der entsprechen-

den Stellen des Manuskripts.

Florian Römer für viele Programmierarbeiten zur Motorsteuerung und Datenaufnahme.

Thorsten Krenke, Burkhard Stahlmecke und Dr. Eyup Duman, die stets zu einer tolle Arbeitsatmosphäre beigetragen haben.

Michael Vennemann für alles was irgendwie mit Computern zu tun hatte, und ebenso für die Durchführung von Röntgenmessungen.

Dr. Ramona Nünthel für die Hilfestellung bei den IV-LEED Messungen und ihre Diskussionsbereitschaft.

Dem Sekretariat: Sabina Grubba, Gudrun Ciolek, Helga Mundt und Thomas Fridrich dafür, dass sie viele anfallende Verwaltungsaufgaben schnell und unproblematisch gelöst haben.

Der Firma **JSQUID**, die viel zur technischen Verbesserung des SQUID-Aufbaus beigetragen hat.

Carolin Antoniak, Christian Raeder und Dr. Ralf Meckenstock danke ich für Diskussionen und Hilfe verschiedenster Art.

Stephan Buschmann und **Dr. David Schmooll** für ihre Hilfsbereitschaft beim Korrekturlesen.

*I would like to express my deep appreciations to **Tamara Machac** and **Rachel Kim** for their dedicated work on proofreading the manuscript.*

Allen anderen namentlich nicht genannten Mitgliedern der Arbeitsgruppe Prof. Farle danke ich für das angenehme Arbeitsklima und ihre Hilfsbereitschaft.

Zuletzt möchte ich meiner Familie einen herzlichen Dank aussprechen für ihren Zuspruch und für ihr Interesse am Fortkommen meiner Arbeit. Insbesondere danke ich meiner Frau **Jessica** und meinem Sohn **Phil** für ihr Verständnis dafür, dass ich oft wenig Zeit für sie hatte.